Flow-Directed Solution Self-Assembly of Block Copolymers in Microfluidic Devices

by

Joe Chih-Wei Wang
B.Sc., University of British Columbia, 2002
M.Sc., University of Victoria, 2005

A Dissertation Submitted in Partial Fulfillment of the
Requirements for the Degree of

DOCTOR OF PHILOSOPHY

in the Department of Chemistry

Supervisory Committee

Flow-Directed Solution Self-Assembly of Block Copolymers in Microfluidic Devices

by

Joe Chih-Wei Wang
B.Sc., University of British Columbia, 2002
M.Sc., University of Victoria, 2005

Supervisory Committee

Dr. Matthew G. Moffitt, Department of Chemistry (UVic)
Co-Supervisor

Dr. Dave Sinton, Department of Mechanical Engineering (UT)
Co-Supervisor

Dr. Thomas Fyles, Department of Chemistry (UVic)
Departmental Member

Dr. Peter Oshkai, Department of Mechanical Engineering (UVic)
Outside Member

Supervisory Committee

Dr. Matthew G. Moffitt, Department of Chemistry (UVic)
Co-Supervisor

Dr. Dave Sinton, Department of Mechanical Engineering (UT)
Co-Supervisor

Dr. Thomas Fyles, Department of Chemistry (UVic)
Departmental Member

Dr. Peter Oshkai, Department of Mechanical Engineering (UVic)
Outside Member

Abstract

The self-assembly of polystyrene-stabilized cadmium sulfide nanoparticles (PS-CdS) with amphiphilic stabilizing chains of polystyrene-*block*-poly(acrylic acid) (PS-*b*-PAA) into colloidal quantum dot compound micelles (QDCMs) is studied on two-phase gas-liquid segmented microfluidic reactors. The resulting particle sizes are found to arise from the interplay of shear-induced coalescence and particle breakup, depending on a combination of chemical and flow conditions. Variation of water content, gas-to-liquid ratio, and total flow rate, enable control of QDCM sizes in the range of 140 – 40 nm.

The flow-variable shear effect on similar microfluidic reactors is then applied to direct the solution self-assembly of a PS-*b*-PAA block copolymer into various micelle morphologies. The difference between off-chip and on-chip morphologies under identical chemical conditions is explained by a mechanism of shear-induced coalescence enabled by strong and localized on-chip shear fields, followed by intraparticle chain rearrangements to minimize local free energies. Time-dependent studies of these nanostructures reveal that on-chip kinetic structures will relax to global equilibrium given sufficient time off-chip. Further investigations into the effect of chemical variables on on-chip shear-induced morphologies reveal a combination of thermodynamic and kinetic effects, opening avenues for morphology control via combined chemical (bottom-up) and shear (top-down) forces. An equilibrium phase diagram of off-chip micelle morphologies is constructed and used in conjunction with kinetic considerations to rationalize on-chip

mechanisms and morphologies, including cylinders and vesicles, under different chemical conditions.

Finally, we extend our strategy of two-phase microfluidic self-assembly of PS-*b*-PAA to the loading of fluorescent hydrophobic probes (pyrene and naphthalene) with different affinities for the PS core. The on-chip loading approach provides a fast alternate to the slow off-chip method, with implications for the potential development for point-of-care devices for drug loading. On-chip loading results indicate that loading efficiencies are dependent on water content and, to a lesser extent, on flow rate; the results also suggest that the on-chip morphologies of the PS-*b*-PAA micelles are an important factor in the loading efficiencies.

Table of Contents

List of Figures

List of Schemes

List of Tables

Acknowledgements

First and foremost, I would like to express my most sincere gratitude to my two supervisors, Professors Matthew Moffitt and Dave Sinton, for the precious opportunity to work with them in such a fascinating hybrid project. I am very grateful for their constant support and encouragement, endless patience, infectious enthusiasm and utmost optimism. I am deeply thankful for everything I learned from them, let it be in academic or in real life. Without their tremendous efforts and understating, the completion of the thesis is not possible.

I cannot give enough thanks to my parents for their unconditional love and support over the last few years. Their consistent encouragement was what made it possible to complete this thesis. I would also like to thank my younger brother for taking care of the family while I am away. Without his help to look after the parents, I would certain not have the luxury to the time and space I needed to finish this work.

Words cannot even describe my utmost appreciation for all the hard work and sacrifices that my wife Lainie has made over the years in order for me to finish my work. She has always been there for me during all the ups and downs throughout the years. She is my most caring best friend; her endless bounds of optimism have made me see a lot of things from a very positive perspective. Thank You My Dear Wife.

In addition, I would like to thank:

My chemistry group members past and present Yunyong Guo, Gavin Phinney, Saman Harirchian-Saei, Amandeep Bains, and post-doctoral fellow, Dr. Celly Izumi for all their help and support over the years.

My engineering group members past and present: Paul wood, Brent Scaff, Carlos Escobedo, Ali Oskooei for their help on microfabrication and operation of microfluidic reactors.

Last but not the least, all the Chemistry faculty and staff, and fellow graduate students in the Petch lab, for making the five years of my PhD studies, a truly great experience.

CHAPTER 1

GENERAL INTRODUCTION

1.1. Background and Motivation

Microfluidics is the study and manipulation of small amounts of liquids (10^{-9} to 10^{-8} litres) in confined environments with length scales on the order of tens to hundreds of microns and smaller.[1, 2] In general, fluidic systems with characteristic dimensions greater than 1 mm are considered to be macroscale. Flow characteristics at the microscale are very different from their macroscale counterparts.[3, 4] As a result of shrinking the length scale, the surface-to-volume ratio increases, so that surface forces become dominant over body and inertial forces. The miniaturization of length scale also translates into improved heat dissipation, lower consumption of reagents, and shorter processing times.

The research in the area of microfluidics has advanced significantly in the last decade, owing to the development of soft lithography technology by Whitesides and others.[5] In addition, process parameters such as flow characteristics, flow rate, temperature and pressure gradients, residence time and residence time distribution, which are of crucial importance to numerous applications, can be easily controlled in microfluidics.[6-11] Microfluidics, with its unique ability to deliver, sample, react, separate and detect small fluid volumes, has found many applications in biology, biochemistry, analytical chemistry and material synthesis.[12-14] Multiphase microfluidic reactors, particularly gas-liquid multiphase microfluidic reactors, have been attracting increased attention in particle synthesis as they offer several key advantages over single phase reactors: improved mixing, and constant recirculation, which effects to better size control and narrower polydispersity.[6-8, 10, 11, 15] In gas-liquid multiphase reactors, the interface between liquid plugs and gas bubbles leads to flow-variable high shear regions in the

corners of the liquid plugs.[6, 7, 16] Thus far, the effect of these high shear regions on particle processing (shear-induced coalescence and breakup) has not been explored.

This thesis will investigate for the first time microfluidic self-assembly in two different systems that have been studied extensively in the bulk: 1. quantum dot compound micelles (QDCMs) and 2. amphiphilic block copolymer micelles. In the first system, blends of hydrophobic block copolymer-stabilized cadmium sulfide quantum dots (CdS QDs) with an external polystyrene (PS) brush layer (PS-CdS) and polystyrene-*block*-poly(acrylic acid) (PS-*b*-PAA) stabilizing chains co-dissolved in dimethylformamide (DMF) organize into spherical assemblies termed quantum dot compound micelles (QDCMs) upon addition of water.[17] Quantum dot compound micelles are promising candidates for biological and photonic applications, due to their size-dependent CdS emission, stability in aqueous media, complex structural hierarchy, and functional surface groups. However, for various applications, control of QDCM sizes and polydispersities represents a significant challenge, as these sizes are entirely kinetically determined and self-assembly occurs far from thermodynamic equilibrium. In the second system, amphiphilic block copolymers assemble into diverse micelle morphologies due to a combination of thermodynamic and kinetic factors.[18-22] A key challenge in utilizing block copolymer micelles in applications such as drug delivery, sensing and medical imaging is controlling the morphology.

The main goal of this thesis work was to develop a combined top-down and bottom-up methodology for directing the self-assembly of amphiphilic block copolymers in solution, and thus to establish new control handles on particle morphology and size. Specifically, we used gas-liquid multiphase microfluidic reactors, in which

compartmentalized liquid plugs are segmented by a regular stream of gas bubbles, to self-assemble various systems of block copolymers. In the aforementioned self-assembling systems, we show that flow-variable high shear regions in the corners of the liquid plugs strongly influence particle sizes and morphologies via competing mechanisms of shear-induced coalescence and breakup. These outcomes point to a new avenue to guide polymer self-assembly via flow-variable shear forces. The reminder of the present chapter is divided into seven sections. Section 1.2 provides a basic background to polymer science. Section 1.3 is devoted to the formation of block copolymer micelles, including a description of thermodynamic and kinetic factors that govern micellization; the same section also contains a survey of the existing literature data on morphological variability and delivery applications of block copolymer micelles. Section 1.4 describes the basic concepts of small-scale fluid flow and multiphase microfluidic reactors. In section 1.5, a detailed description of key microfluidic methodologies germane to this thesis, including soft lithography, fluid and gas delivery, and flow control is presented. Section 1.6 discusses the important characterization tools applied in this work. Finally, section 1.7 provides a summary of the content of the remaining chapters of the thesis.

1.2. General Introduction to Polymers

1.2.1. Definition and Terminology

A polymer is a large molecule, synthetic or natural, made up of smaller structural units called monomers covalently joined together.[23, 24] When monomers are connected to form a polymer, they are called repeat units, and the average number of repeat unit in a polymer chain is called the degree of polymerization. Depending on the connectivity of

monomers, polymers may be categorized as linear, branched, or network polymers.[24-26] Linear polymers, as the name suggests, have a linear skeletal structure. Branched polymers, on the other hand, have side chains or "branches" that are connected to the main polymer backbone chain at branch points. Network polymers have a three-dimensional structure in which polymer chains are interconnected via many junction points.

In addition, polymers can be classified according to the number of types of monomers that are used to form the polymer. When there is only a single type of monomer in a polymer, it is called a homopolymer. If there is more than one type of monomer in a polymer, the polymer is termed a copolymer. Copolymers can be divided into four main categories depending on the arrangement of monomers: random copolymers, block copolymers, alternating copolymers and graft copolymers (Figure 1.1). Random copolymers are also called statistical copolymers as the distribution of monomers along the chain is statistical, or random. Block copolymers are copolymers made up of long sequences (or blocks), each made up of one type of monomer, covalently connected to other sequences made up of different monomer types. If there are only two blocks in the chain, the copolymer is called a diblock copolymer. Alternating copolymers as its name suggests have an alternating arrangement of the repeat units along the chain. Graft copolymers are branched copolymers that consist of blocks of one type of repeat units being grafted onto the backbone of another type of repeat unit

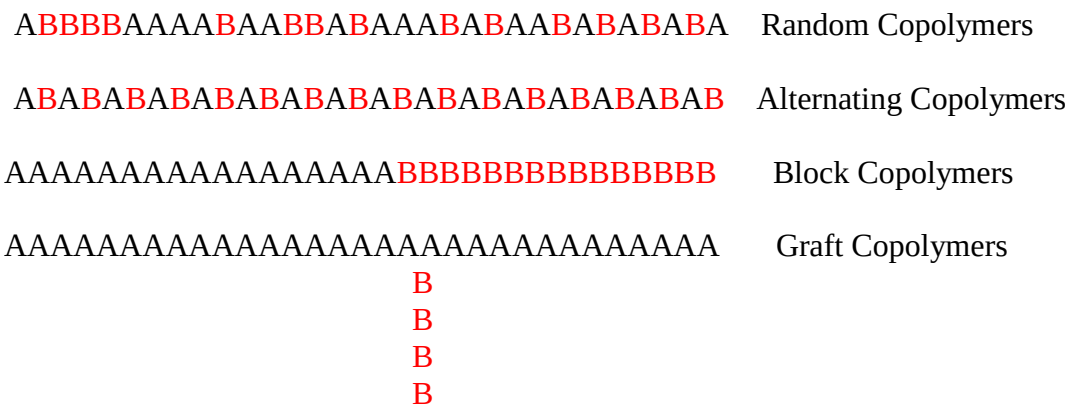

Figure 1.1. Types of copolymers formed from A and B repeat units.

1.2.2. Molecular Weight Distributions

An important characteristic of any polymer sample is the average molecular weight, as this parameter strongly influences the properties of the material. Unlike small molecules, polymers do not have a single molecular weight; rather, a distribution of molecular weights arises from the statistical nature of the polymerization process. A typical distribution of molecular weights is provided in Figure 1.2.

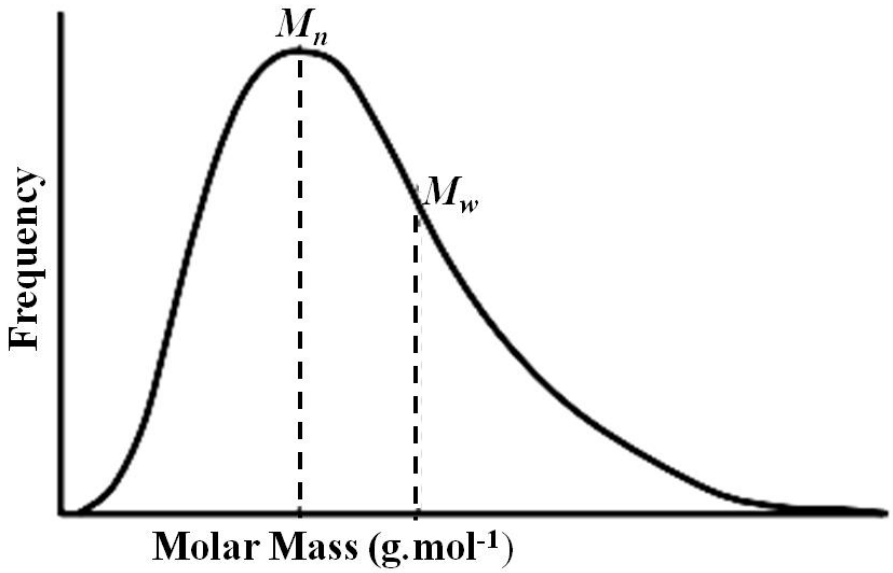

Figure 1.2. Molecular weight distribution of a theoretical polymer sample highlighting the position of different types of average molecular weights.[23]

As suggested by the figure, there is more than one way of defining the average molecular weight for polymers. These values differ in the way they average the distribution of polymer chains. The number-average molecular weight (M_n) is defined by taking the weight of the entire polymer sample and dividing this by the total number of molecules present in the sample (Equation 1.1)

$$M_n = \frac{\sum_i N_i M_i}{\sum_i N_i} \qquad \textbf{(1.1)}$$

where N_i is the number of molecules of species i with molecular weight M_i. M_n can be determined from characterization methods sensitive to the total number of molecules in the system (i.e. colligative methods) such as osmotic pressure, vapor pressure lowering, boiling point elevation and freezing point depression.

Another average value that is commonly used is the weight-average molecular weight, M_w. M_w is generally determined by analytical methods that are sensitive to the size of molecules in solution, the most important method for polymers being light scattering techniques. As a result, larger molecules in the distribution contribute more to M_w than M_n . M_w is defined as:

$$M_w = \frac{\sum_i w_i M_i}{\sum_i w_i} = \frac{\sum_i N_i M_i^2}{\sum_i N_i M_i} \qquad \textbf{(1.2)}$$

where w_i is the weight of all molecules of species i with molecular weight M_i. These two values are used hand in hand to give information on the distribution of molecular weights. The ratio of the weight-average molecular weight (M_w) and the number-average molecular weight (M_n) is used to characterize the width of the molecular weight distribution for a polymer sample; this ratio is commonly known as the polydispersity index, *P.I.* (Equation 1.3):

$$P.I. = \frac{M_w}{M_n} \qquad \textbf{(1.3)}$$

Polymers with *P.I.* values approaching unity are said to have low polydispersity whereas polymers with large *P.I.* values have high polydispersity. In general, synthetic polymer samples have *P.I.* > 2 with varying polydispersities depending on the type of polymerization method. The theoretical limit of *P.I.* = 1 defines a monodisperse sample;

however, this is never achieved in synthetic polymers. Certain polymerization methods such as anionic polymerization offer superior polymerization control and lower *P.I.* values (down to 1.01).[27] On the other hand, step-growth polymerization methods, such as condensation reactions, result in a theoretical *P.I.* of 2.0, and thus produce relatively broad size distributions of chains.[24]

In this thesis, the number-average degree of polymerization (x_n) per chain is used to describe the average polymer chain lengths and is defined as:

$$x_n = \frac{M_n}{M_o} \qquad \textbf{(1.4)}$$

where M_0 is the molecular weight of single repeat unit.

1.3. Block Copolymer Micelles

1.3.1. Formation of Block Copolymer Micelles

The most intriguing property of block copolymers is their ability to undergo self-assembly in solid and solution state into various shapes and forms, making them an ideal candidate for fundamental study and practical applications. For example, block copolymer have been used in a variety of fields including lubrication,[28] adhesion,[29] and polymer-mediated drug delivery.[30] As well, block copolymers have been used in the templated synthesis of inorganic nanoparticles (NPs).[31-36]

The ability of diblock copolymers to undergo self-assembly stems from their unique molecular architecture, involving covalent connectivity between chemically

incompatible and distinct blocks.[37-41] When diblock copolymers are dissolved above a critical micelle concentration (cmc) in a solvent medium that is thermodynamically compatible with one block and not the other (a selective solvent), the insoluble blocks will strive to minimize enthalpically unfavorable interactions with the solvent by spontaneously associating to form the core of a block copolymer micelle, with the surrounding soluble blocks forming the micelle corona. This process is analogous to the well-known formation of micelles of relatively low-molecular weight surfactants (e.g. soap molecules in water).[37-41] For historical reasons, if the micelles are formed in an aqueous solvent with a hydrophobic core and a hydrophilic corona, they are referred to as regular micelles. Conversely, if the micelles are formed in organic solvent, with a hydrophilic core and a hydrophobic corona, they are known as reverse micelles. Furthermore, if the corona-forming block is large with respect to the core-forming block, the micelles are known as "star-like", and if the reverse is true they are described as "crew-cut" micelles. These classification schemes are represented pictorially in Figure 1.3.

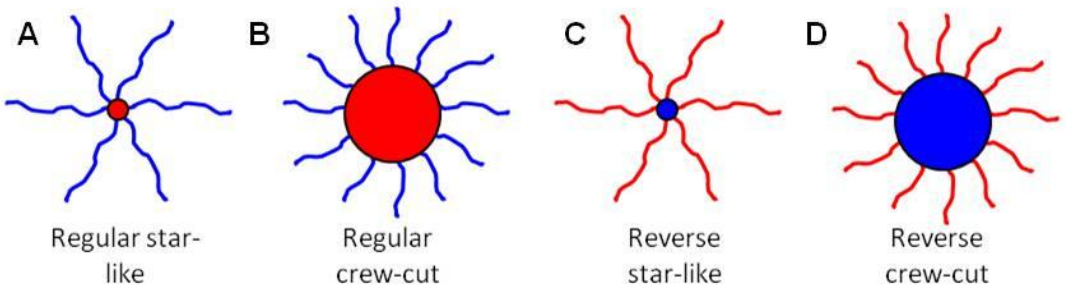

Figure 1.3. Illustrations of the various definitions of amphiphilic diblock copolymer micelles in aqueous solvent (A, B), and organic solvent (C, D). Red indicates relatively hydrophobic block and blue represents relatively hydrophilic block, respectively.[42]

1.3.2. Thermodynamics and Kinetics of Block Copolymer Micelles

The interaction of polymer chains in liquid media is of considerable interest from both a practical and theoretical point of view. In any spontaneous process at constant pressure (p) and temperature (T), a system seeks to achieve a minimum of Gibbs free energy, G. The fundamental thermodynamic equation relating the change in G with the changes in enthalpy and entropy, H and S, is:[24]

$$\Delta G = \Delta H - T\,\Delta S \qquad \textbf{(1.5)}$$

The thermodynamics of micellization in organic solvents has been investigated for several block copolymer systems. Price and co-workers used calorimetric technique to study polystyrene-*b*-polyisoprene (PS-*b*-PI) and polystyrene-*b*-poly(ethylene/propylene) (PS-*b*-PEP) in various organic solvents and found that in these systems micellization is an enthalpically-driven process, with negative ΔH and negative ΔS determined for micellization.[43-48] The negative ΔH results from the exothermic interchange energy, as a result of exchanging high energy polymer/solvent interactions with low energy polymer/polymer interactions for the core-forming block.[37-40] For the same block copolymer systems, Price and co-workers also determined that ΔG became significantly more negative as the length of the core-forming block increased, while for the corona-forming block, the effect of the block length on ΔG was a small effect.[43-48] These authors inferred from the data the loss in entropy accompanying the micellization process to two contributions: 1) chain stretching of the core- and corona-forming blocks

within the micelle (loss of conformational entropy) and 2) localization of block junctions at the core/corona interface (loss of translational entropy).

The micellization of block copolymers in aqueous media has also been studied extensively.[20-22, 49-61] In contrast to micellization of block copolymers in organic solvents, the micellization process in water is entropically-driven, similar to that in small molecule surfactant systems.[37-40, 62-64] In general, micellization of block copolymer molecules in aqueous media reduces their entropy; the driving force for the process is the overall increase in the entropy of the water molecules (hydrophobic effect). Introducing hydrophobic polymer blocks into water forces the water molecules to reconstruct their hydrogen bonds by building water "cages" around the blocks, leading to significant reduction in the entropy of the water molecules. The entropy of the water thus increases significantly when the micelles form and the hydrophobic blocks are removed from the water and into the core.

Micellization of block copolymers in mixtures of polar organic solvents (e.g. DMF, dioxane, THF) and water are of particular relevance to this thesis. Eisenberg and co-workers have studied the thermodynamics of crew-cut micelle formation of polystyrene-*b*-poly(acrylic acid) PS-*b*-PAA diblock copolymers in various DMF/water mixtures by using statistic light scattering technique to monitor the temperature-induced micellization.[18] They found that at low water contents (4.3 – 5.0 wt%), the driving force for micellization comes from the negative enthalpy, which is due to the change from unfavourable interactions between polystyrene segments and solvent to the more favourable interactions of polystyrene/polystyrene and solvent/solvent interactions accompanying the micellization process. However, at relatively high water content (15

wt %), enthalpy exchange is positive. Despite the positive enthalpy change at high water content, the entropy change is positive enough to outweigh the unfavorable enthalpy change. The authors concluded from their data that the higher the water content, the stronger hydrophobic interactions between the polymer chains and the water molecules and the more ordered the water structure before micellization. Upon micelle formation, more normal water structure is regenerated, resulting in a substantial increase in the entropy. They also pointed out that between low and high water content, both negative ΔH and positive ΔS drive micellization of block copolymers.

Micellization of block copolymer systems is strongly influenced by the kinetic of micellization process. Small molecular surfactants have transitional movement on a fast time scale (on the order of μS to mS) as a result of their small size; therefore, their micellization kinetic are fast and systems quickly equilibrate.[65] Polymers, on the other hand, have large size, which leads to strong chain entanglements and slow molecular dynamics in micellization process (time scale ~0.1 s to several tens of hours).[66] This often leads to micelle systems that are not equilibrated.[61, 66-71] A number of studies have been conducted aimed at measuring the exchange dynamics of polymer chains between the solvent and the micelles.[21, 72-75] A general conclusion of these studies is that chain dynamics are greatly influenced by the nature of the solvent and the interaction between the solvent molecules and the polymer chains. Tian et al. determined that in the case of polystyrene-based copolymers micelles (prepared using dissolution method) in various dioxane/water mixtures, the dynamics of micelle hybridization (obtained from sedimentation velocity measurement) are directly related to the solvent swelling of the PS core of the micelles.[73] They found that the higher the solvent content in the micellar core,

the faster the dynamics of chain exchange. However, if the amount of nonsolvent (e.g. H_2O) in the core increases, the core tends to become glassy and the exchange between chains between micelles slows down.

A similar study to determine the dynamics of micelle hybridization was performed by Zhang et al.[21] In their study, they mixed two solutions of micelles of different sizes (which had been prepared separately from different copolymers) at different water content. If the dynamics of polymer chain is significant at a particular water content, chain exchange between different micelles will change the size of the micelles over the time scale of the experiment. On the other hand, if the dynamic of polymer chain is slow, this will lead to a slow chain exchange and micelles will retain their structural integrity. The mixed populations micelles were stirred for 1 day to allow polymer chain exchange and partition over that time scale, and the resulting micelles were analyzed by transmission electron microscopy (TEM) to determine micelle sizes. They concluded that water content has a significant effect on the chain exchange within the polymer phase, due to differing extents of plasticization by the organic solvent. As the water content increases, the effect of chemical potential gradients drives organic solvents out of the core. For their specific system (PS-*b*-PAA in DMF), they identified that chain exchange is fast at a water content of 6 wt% so that the micelles are formed under equilibrium condition. However, as the water content is increased to 11 wt %, the copolymer chain exchange becomes negligible.

1.3.3. Multiple Morphologies of Block Copolymer Micelles

The interest in using polymeric micelles is motivated by the broad range of their morphologies, their biocompatibility, and by the variety of their potential applications.[60, 76, 77] In 1995, Eisenberg et al. published the first paper that demonstrated the ability to obtain block copolymer micelles of different morphologies from polystyrene-*b*-poly(acrylic acid) in a solvent mixture.[19] Since then, extensive research efforts have been devoted to controlling the morphologies of block copolymers in solution. For example, the same research group have use other highly asymmetric amphiphilic diblock copolymers such polystyrene-b-polyethylene(PS-*b*-PEO), polystyrene-*b*-poly(4-vinylpridine), and polybutadiene-*b*-poly(acrylic acid) to form micelles of multiple morphologies in solutions.[18-22, 49-60, 76-92] To date, more than 30 morphologies have been identified by research groups around the world, including spheres, rods, vesicles, compound micelles, tubes, disks, toriods, plumber's nightmare, onions, entrapped vesicles, bowl-shaped and needle morphology just to name a few.[18-22, 49-61, 67, 68, 71, 76-97] Many of these morphologies are governed by thermodynamics, but some of these are under kinetic control.

In the course of block copolymer micelle formation, the specific morphologies and sizes of micelles are governed by an interplay of three thermodynamic factors: (1) the chain stretching of the core-forming block (entropic factor), (2) the interfacial tension at the core-corona interface (enthalpic factor) and (3) the chain stretching in the corona (entropic factor). Experimentally, a large of number of chemical parameters will influence the balance of these thermodynamic factors and therefore allow these morphologies to be tuned. These variables include the block copolymer composition,

choice of solvent systems, presence of added ions and small molecules, the polymer concentration. In general, variables that increase interfacial tension will effect to an increase in aggregation number and therefore micelle size, at the entropic cost of increased chain stretching.

The influence of block copolymer composition on the morphology of the aggregates has received considerable attention. Liu and co-workers have studied extensively polystyrene-*block*-poly(2-cinnamoylethyl methacrylate) (PS-*b*-PCEMA) and polyisoproene-*block*-poly(2-cinnamoylethyl methacrylate) (PI-*b*-PCEMA) in various organic blends, and observed multiple morphologies including egglike and onionlike particles, and semi-shaved and fully shaved hollow nanospheres.[98-100] The group of Maskos has examined the concept of using block copolymers with one of the blocks still carries available polymerizable groups to generate block copolymer micelles with highly complex and yet stable morphologies.[101, 102] They have shown that by using suitable block copolymers such as poly(dimethylsiloxane)-*block*-poly(ethylene oxide) and poly(1,2-butadiene)-*block*-(ethylene oxide) and cross-linking of micellar structures formed from these polymers, exotic and stable morphologies such as double-shell vesicles, strings of vesicles and filaments were observed. Meier et al have synthesized an ABA triblock with polymerizable end groups, poly(2-methyloxazoline)-*block*-poly(dimethylsiloxane)-*block*-(2-methyloxazoline) (PMOXA-*b*-PDMS-*b*-PMOXA).[103, 104] They were able to generate vesicles structures in dilute aqueous solution, and the size of which can be tuned from 50 nm up to 500 nm. In the other study by Meier's group, giant vesicles (1-2 μm) formed from same type of ABA triblock copolymer with the incorporation of an ionophore selective for calcium transport can be used to control

calcium concentration during the precipitation of calcium phosphate. Kickelbick et al studied short-chain amphiphilic polysiloxane-b-poly(ethylene oxide) ($PDMS_4$-*b*-PEO_{12} and $PDMS_{10}$-*b*-PEO_{12}), and successfully observed spontaneous multi-lamellar vesicles formation in aqueous solution.[105] Harris et al. have prepared poly(ethylene oxide)-*block*-poly(butylene oxide) oligomers with ethylene oxide repeating units ranging from 6-24 and butylenes oxide repeating units ranging from 10-12.[106] They also observed spontaneous generation of multilamellar vesicles in aqueous solution. Discher et al. synthesized poly(ethyleneoxide)-*b*-poly(ethylethylene) (PEO_{42}-*b*-PEE_{37}) and formed vesicles of different sizes (from <200 nm to 20-50 μm), which they called polymersomes.[94] They have shown that these polymersomes are tougher and at least 10 times less permeable to water than common phospholipid bilayers. Toroidal micelle morphology or ring-like micelles have also been observed.[95, 107, 108] For example, Cui et al. demonstrated toroidal micelle formation from the self-assembly of poly(acrylic acid)-*block*-poly(methyl acrylate)-*block*-poly(styrene) (PAA-*b*-PMA-*b*-PS) via interaction with organic diamines in mixed THF/water.[95] Foster et al. investigated the association behavior of charge block copolymer micelles made from poly(ethylethylene-*block*-styrenesulfonic acid) (PEE-*b*-PSSH) and successfully observed that spherical micelles can be fused into vesicles or toroidal structures.[108] The Pluronics series tri-block poly(ethylene oxide)-*block*-poly(propylene oxide)-*block*-poly(ethylene oxide) and di-block poly(propylene sulfide)-block-poly(ethylene glycol) also have received a great deal interest.[109-113] Aggregates of various shapes such as spheres, rods, vesicles and multi-lamellar vesicles (onions) were observed.

Control of morphology through polymer-solvent interactions in crew-cut micelles has been demonstrated. Desbaumes et al. demonstrated crew-cut micelles of different morphologies can be achieved from PS-*b*-PAA copolymer a through single solvent method.[83] Low alkanols (i.e.., methanol to n-butanol) were used as solvents. The block copolymers were dissolved at elevated temperature, and upon cooling, the decrease in temperature induces self-assembly. They were able to obtain a number of different morphologies using this single solvent method: tubules (in methanol), vesicles (in ethanol), interconnected vesicles (in propanol) and solid spheres (in butanol). In another work, Yu et al. showed that an array of different morphologies (from spheres to cylinders, to vesicles) can be obtained by progressively changing the solvent composition from 0/100 w/w THF/DMF to 50/50 w/w THF/DMF.[53]

The morphogenic effect of ionic additives on crew-cut micelles has been investigated in great detail.[18, 21, 22, 51, 90] This method provides a simple and effective avenue to tune the morphologies of the aggregates. Thus far, the level of morphological complexity achieved by ionic additives is astonishing. A great deal of work has been done on polystyrene-block-poly(acrylic acid) and polystyrene-block-poly(4-vinylpyridine) due to their ionic blocks between which electrostatic repulsion is operative. It was found that by controlling the molar ratio (*R*) of the number of added ions to the repeat units in the partially ionized corona, the morphology can be tuned. For example, in the study carried out by Zhang et al, the morphologies of the aggregates progress from spheres to cylinders, to vesicles and finally to large compound vesicles (LCV) with increasing NaCl concentration.[21, 22, 51] The cause of the added NaCl effect on the aggregate morphology is rationalized in terms of the screening effect provided by the

salt. The screening effect reduces the interchain repulsion between partially ionized chains within the corona, such that the aggregate sizes can increase in order to reduce the interfacial tension between the core and the solvent. The core-forming block must stretch more as the size of the aggregates becomes larger. However, there is an entropic penalty associated with chain stretching of the core-forming block, and at some point when size of the aggregates becomes large enough, the aggregates change their morphologies from sphere to cylinder, and to bilayer in order to reduce entropy penalty due to the core-forming block stretching

For copolymer systems containing ionic block such as PS-*b*-PAA, the effect of pH on the morphology has been investigated.[51] When a strong acid such as HCl is added to the system, it protonates the partially ionized carboxylic acid units of the PAA blocks, reducing the total charge density on the corona. The end result is the overall (both electrostatic and steric) repulsion on the corona reduces, which promotes aggregation. Hence, increasing the molar ratio of added HCl progressively leads to the formation of rods, vesicles and LCV. In contrast, when a strong base such as NaOH is used as an additive, the morphology changed in the opposite direction. Strong base serves to deprotonate the PAA segments and as a result, the degree of ionization increases, which leads to an increase in the repulsion among the PAA corona chains and consequently a decrease in the aggregation number.

Several studies have been devoted to examining the influence of small molecule additives on block copolymer morphologies.[85, 114, 115] Kabanov et al. introduced various cationic surfactants to the diblock copolymer poly(ethylene oxide)-*block*-poly(sodium methacrylate) (PEO-*b*-PMANa), and observed the spontaneous formation of vesicles

from complexes of surfactants and ionic block copolymers.[85] Onion types micelles (three-layer micelles) were prepared by Talingting et al from the system of polystyrene-*block*-poly(2-vinylpridine) (PS-*b*-PVP) in methanol/dioxane/water mixture.[115] They found that with the aid of another polymer additive, poly (2-vinylpridine)-*block*-poly(ethylene oxide) (PVP-*b*-PEO) and at appropriate pH condition, the synergistic self-assembly can transform spherical micelles into multilayer vesicles. The research team led by Davis has investigated the morphology of mixed systems of nonionic surfactants and nonionic amphiphilic copolymers.[114] The experiments demonstrated that the shapes of mixed micelles changed from cylinders to spheres with increasing surfactant-to-copolymer ratio. It was found that the nonionic surfactants could interact with corona of the micelles, acting as spacers between the polymer chains surface and increasing their conformational entropy.

Motivated by diversity of block copolymer micelle morphologies, several groups have utilized them in templated synthesis for functional materials. For example, various novel nanostructures from organometallic-inroganic block copolymer were observed by the groups of Manners and Winnik.[116-118] They observed long rodlike micelles from poly(ferrocenyldimethylsilane)-*block*-poly(dimethylsiloxane) (PFS-*b*-PDMS) (block ratio = 1:6) in hexane solution.[118] By adjusting the ratio of PFS to PDMS from 1:6 to 1:13, they were able to obtain organometallic nanotubes.[116] Moller and co-workers prepared different lengths of ion-containing nanowires by treating spherical micelles assembled from polystyrene-*block*-poly(2-vinylpridine) with different ratio of $HAuCl_4$.[119]

1.3.4. Delivery Applications of Block Copolymer Micelles

Drug delivery is the process of administering certain therapeutic compound to achieve therapeutic effects in living species. Morden drug delivery technologies aimed at modifying drug release profile, absorption, and distribution for the benefit of improving therapeutic effect and safety. Block copolymer micelles have been studied as potential drug delivery vehicles because they 1) can be biocompatible/and or biodegradable, 2) have small tuneable sizes, and morphologies, 3) their ability to load different hydrophobic and hydrophilic, and 4) their potential to allow further surface modifications on the corona to target specific delivery site.

The loading and releasing of drugs such as cancer combating drugs, doxorubicin (DXR) and docetaxel (Dtxl), in block copolymer micelles have been studied.[13, 120-124] However, these kinds of studies are often impeded by the high cost of the drugs. Therefore, as a model system for drug encapsulation study in block copolymer micelles, various probes are often used as stand-ins for potential drug targets. These probes are cheaper, more accessible and can be measured with more sensitivity, e.g. fluorophores. For example, Soo et al. studied the loading and release of hydrophobic probes to/from the hydrophobic micelle cores formed from poly(caprolactone)-*block*-poly(ethylene oxide) with implications for drug delivery.[77] From their experimental results, they were able to evaluate the loading efficiency, partition coefficient and release profiles, which all play critical roles in micellar drug delivery. With the potential application of drug delivery in mind, the final chapter of this thesis will investigate the loading of two hydrophobic fluorescent probes (pyrene and naphthalene) in block copolymer micelles formed on a two phase reactors and factors that govern their loading efficiency.

A critical issue in using block copolymer micelles as drug carrier vehicles is the controlling of aggregate morphology, size and size distribution.[76, 125-128] These parameters are believed to play a key role in bio-transport, biodistribution and circulation times. For example, for intravenous injections, phagocytic cells in the liver and spleen do not uptake efficiently particles which are less than 200 nm.[76, 126] In contrast, for topical drug formulation, particles greater than 200 nm have shown to exhibit enhanced transport through the skin.[76, 126] In addition, the size of the carrier vehicle can also influence the mechanism of its uptake by cells, which in turn affects the uptake kinetics and levels. Also, a broad size distribution of carrier vehicles would likely result in a broad distribution of circulation times, which might not be favourable.[76] Hence, there remains a strong need to search for a new self-assembly method that can address the shape, size and size distribution of the drug carrier vehicles in an efficient way.

1.4. Introduction to Microfluidics

1.4.1. Basic Concepts

As mentioned previously, flow characteristic at the microscale are very different from their macroscale counterparts. As a direct consequence of miniaturization, the surface area-to-volume ratio increases. Surface tension and viscous forces, which are both inversely proportional to the channel diameter, d, (or hydraulic diameter, d_H, for non-circular channels), will dominate over inertial and gravity forces for small-dimension channels. Flow characteristic at the microscale can be gauged by the dimensionless Reynolds number (Re), which is a measure of the ratio of inertial forces to viscous forces.[129] The *Re* number is defined as

$$Re = \frac{\rho U d_H}{\mu} \quad \textbf{(1.6)}$$

where ρ is the fluid density, U is the characteristic fluid velocity and d_H is the characteristic channel diameter, and μ is the dynamic viscosity of the fluid. Because of the small dimensions associated with microfluidics, the Reynolds number is normally on the order of unity or less, which characterizes laminar flow.[130] Within the laminar flow regime, fluid elements move slowly in parallel ordered streamlines. In contrast, fluid flow at the macroscale frequently has high a Reynolds number and falls within the turbulent flow regime where flow is fast and chaotic. The absence of inertia in microfluidic flow makes the flow effectively instantaneous, meaning that no momentum can be stored and hence the fluid's motion is not influenced by any forces exerted previously.[131] Another direct consequence of microscale flow is the enhanced heat and mass transfer which are crucial to most applications.

Microscale flow is usually achieved by means of mechanical pumping (pressure-driven flow), though for water and other very polar solvents, an applied electrical field can also be used for fluid transport (electro-osmotic flow).[4] Pressure-driven flow (Poiseuille flow) is well understood, and is generally characterized by a parabolic flow velocity profile, as shown in Figure 1.4., over the cross section of the channel with a maximum velocity at the channel's center and zero velocity near the walls (no-slip boundary condition).[4] The nonuniformity in the flow speed over the cross section is a result of the interaction of the liquid with the wall: the imposed pressure exerts a uniform force over the cross-sectional area of the channel, but momentum is lost at the walls due to interaction with solid boundaries.[4, 5] The consequence of this is that different volume

elements of the fluid travel at different speeds in the channel, resulting in different residence times of fluid elements in the channel, and as characterized by the residence time distribution (RTD). This dispersion process is called Taylor dispersion.

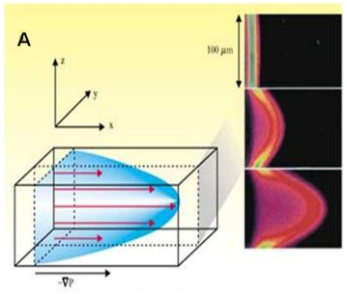

Figure 1.4. Flow profiles in microchannels. (A) A pressure gradient, $-\nabla P$, along a channel generates a parabolic or Poiseuille flow profile in the channel. The velocity of the flow varies across the entire cross-sectional area of the channel. On the right is an experimental measurement of the distortion of a volume of fluid in a Poiseuille flow. The frames show the state of the volume of fluid 0, 66, and 165 ms after the creation of a fluorescent band of dye.[5]

1.4.2. Multiphase Microfluidics Reactors

While single phase reactors have been widely employed in material synthesis, multiphase microfluidic reactors have been attracting increased attention in material synthesis. .[6-9, 15] In single phase reactors, mixing is slow due to the absence of turbulence and generating turbulence in microchannels requires extremely high flow rates (~10 ms^{-1}). Reaching such flow rates requires undesirably high reagent consumption and high pressure.[4] In addition, the cross-stream variation in flow velocity, characteristic of pressure-driven flow, results in a wide variance of residence time (broadened residence time distribution) and increased polydispersity in material synthesis in general. These two problems can be eliminated by introducing a second immiscible stream of fluid (gas

or liquid) into the system such that the immiscible interface results in the generation of a succession of immiscible fluid segments.[6-8, 10, 11, 15, 132]

Multiphase microfluidic reactors in general can be divided into two types: droplet reactors (liquid-liquid flow) and gas-liquid segmented reactors.[6-8, 10, 11, 15, 132] In droplet reactors, (Figure 1.5A) discrete liquid droplets are encapsulated by a carrier fluid that wets the microchannel. The relative interfacial tension of the fluids with the channel surface determines which fluid which will be the major phase (continuous phase) and which fluid will be the minor phase (dispersed phase).[6, 8, 11] The phase that has higher interfacial tension with the channel wall, i.e., the less wetting phase, will form droplets or bubbles. The sizes of droplets or bubbles formed with respective to the continuous phase are primarily a function of flow rates. The reagents in the case of droplet reactors are compartmentalized within the nanoliter-sized droplets and do not come into contact with the channel surface, and are transported through the channel without dispersion. In the gas-liquid segmented reactor (Figure 1.5B), the liquid "plugs" are the continuous phase and are separated by discrete gas bubbles. In this case, reactions occur in the continuous phase, and the liquid plugs are connected by a thin liquid film surrounding the gas (dispersed) phase.

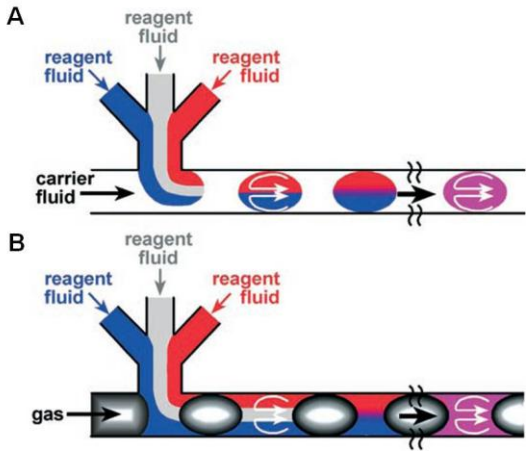

Figure 1.5. Reactions can be studied in two types of segmented flows in microfluidic channels. A) Discrete liquid plugs are encapsulated by an immiscible continuous phase (for example, a fluorocarbon-based carrier fluid). Reactions occur within the dispersed phase (within the plugs). Owing to the surface properties of the microchannel walls, these walls are preferentially wet by the continuous phase. B) Aqueous plugs are separated by another immiscible phase (for example, discrete gas bubbles). Reactions occur within the continuous phase (i.e., within the plugs).[8]

Both types of multiphase microfluidic reactors (droplet and gas-liquid) have been widely used in particle synthesis and each has its own advantages and disadvantages.[8] Since the work in thesis was done exclusively using gas-liquid segmented flow reactors, the discussion here shall focus on this type of reactor. The advantages of gas-liquid segmented flow reactors are bubbles can be generated in a variety of geometry of microfluidic reactor and do not require the use of surfactants. Usually no separation step is required to remove the gas phase from the resulting product. However, other aspects of gas-liquid segmented flow reactors should also be considered. The liquid plugs in such reactors physically contact the reactor wall and the adjacent plugs, allowing for some dispersion through the thin film connecting liquid plugs, and particles contact with the surface and thus particle-surface interactions must be considered.[6, 7]

In the field of microfluidics, there remains a need for techniques that allow for highly controlled formation of droplets and bubbles.[133-136] As well, there has been research interest in understanding the mechanism behind droplet and bubble formation inside microchannels. The mechanisms depend on the values of the capillary number.[137] The capillary number is a dimensionless quality describing the ratio of viscous forces to surface tension forces and is given by equation 1.7:

$$Ca = \frac{\mu U}{\gamma} \qquad (\mathbf{1.7})$$

where μ is the viscosity, and U is the mean speed of the carrier fluid and γ is the interfacial tension. In microchannels, Ca is typically small ($Ca < 10^{-2}$).[137] In this regime, the breakup of droplets (or bubbles) is not caused by shear stresses but is rather dominated by drops in pressure, which arise across the emerging droplet (or bubble). A schematic illustrating this process is shown in Figure 1.6. A typical process of formation of droplets (or bubbles) begins with two immiscible liquid phases merging at the junction of the inlet and main channel. The stream of the droplet phase penetrates into the main channel containing the continuous phase, and a droplet starts growing (Figure 1.6A). In the meantime, as the droplet grows to cover the entire cross-section of the main channel, the pressure in the inhibited flow upstream of the emerging droplet rises (Figure 1.6B). Finally, at a critical pressure, the neck connecting the droplet to its inlet channel breaks and the droplet moves downstream (Figure 1.6C and D). The formation of bubbles in gas-liquid segmented reactors follows the same mechanism.[137]

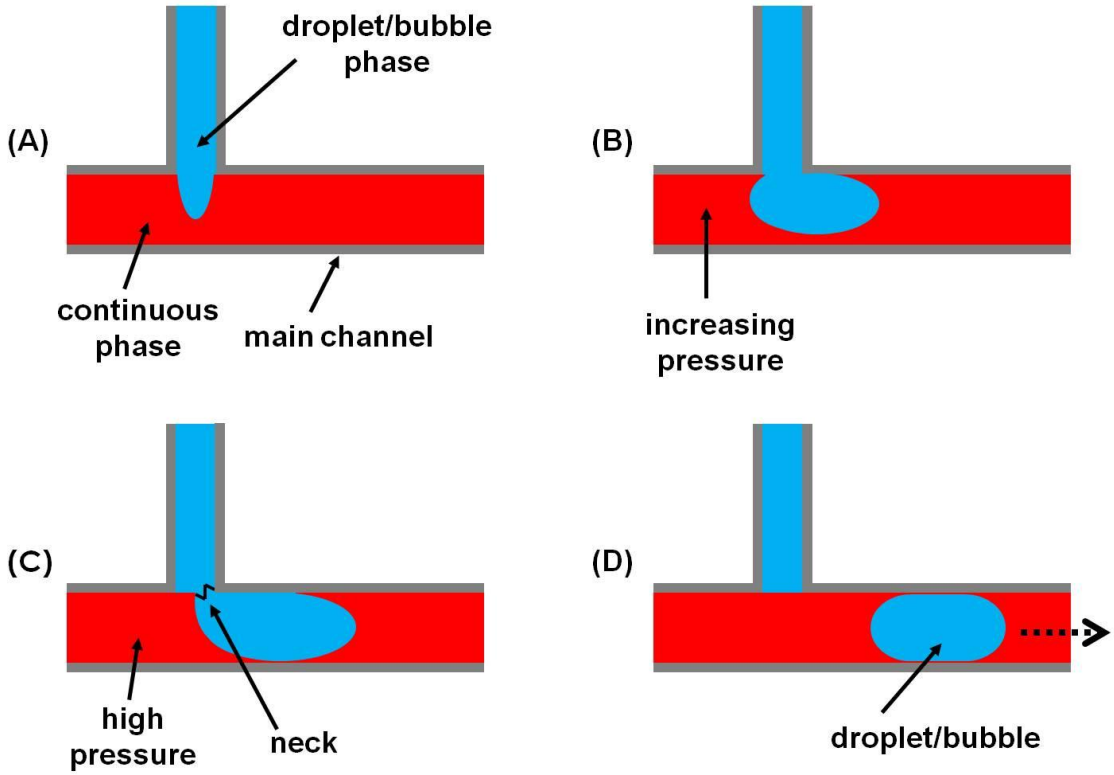

Figure 1.6. Schematic illustration of droplet/bubble formation in microchannels. (A) The droplet/bubble phase enters the main channel. (B) The droplet begins to form and grows downstream. (C) The droplet grows to cover the entire cross-section of the main channel, increasing the pressure in the continuous phase until the neck of the droplet breaks. (D) The droplet moves downstream and the cycle is repeated.

One of the appealing characteristics of multiphase microfluidic reactors is the recirculation flow that is induced in droplets travelling through the microfluidic channels.[7-11, 15] The recirculation in droplets occurs in the form of a pair of counter-rotating vortices, one in the left half and the other one in the right half of the plug (Figure 1.7A). The recirculation in the droplets can greatly enhance mixing and reduces axial dispersion of concentration. Similar motion is also induced within the plugs of the carrier

fluids.[7-11, 15] In addition, mixing in multiphase reactors can be further increased by utilizing a sinusoidal channel, which will generate time-dependent variation in streamline patterns of the vortices (Figure 1.7B).

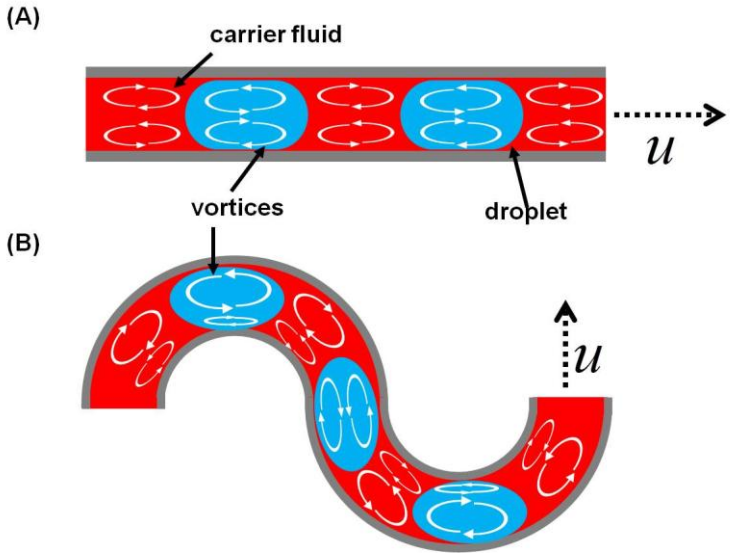

Figure 1.7. Schematic showing mixing patterns inside droplets/plugs moving downstream with velocity u. (A) straight channel and (B) sinusoidal channel. The mixing effect is greatly enhanced for droplets/plugs moving in sinusoidal channel (B), which will generate time-dependent variation in streamline patterns

1.5. Methodologies

1.5.1. Microfabrication

In the 1970's, when the field of microfluidics was starting to attract research interest, the first microfluidic devices were made of silicon and glass.[138, 139] Most of the early methods for fabricating microfluidic systems were based on available and highly

developed method such as micromachining, photolithography and etching.[138, 139] Both silicon and glass are not ideal candidates as materials for microfabrication. Silicon is relatively expensive, and has the major disadvantage of being opaque in the visible/UV region of the spectrum, making it unsuitable for optical detection. Glass, on the other hand, is transparent, but, due to its amorphous properties, itching in vertical side wall is more difficult in comparison with Si. Furthermore, the commonly used methods to seal these materials typically require high voltage or high pressure and a clean room environment. These early methods were time-consuming and expensive, and the mechanical properties of the materials imposed challenges during the fabrication process and limited the range of geometries that could be made. Hence, there was a need for new materials as well as new fabrication methods to produce the next generation of microfluidic devices.

Soft polymeric materials were used as a new material for microfluidics since the early 90s.[138-140] They were a promising alternative to former materials due to their relatively low cost, tunable physical and chemical properties, and their potential for mass fabrication. Soft lithography was then developed and was very popular among researchers. The success of soft lithography depends on the ability to produce a flawless master, as any surface defects on the master will be passed on to the polymers, and hence great care must be taken during the master fabrication stage. The entire process can be done in as little as one day, and routine access to a clean room is not necessary. Soft lithography is a suite of nonphotolithographic methods for replicating a pattern, which is done in two stages: rapid prototyping and replica molding.

1.5.2. Rapid Prototyping

The first step in rapid prototyping begins with the design of channels for the microfluidic device using a computer aided design (CAD) program. The design is then printed on a transparency using a commercial printer, and the transparency is then called the photomask. The desired pattern in the photomask is transparent while the rest of the design is hatched to black in order to block the UV exposure. In the second step, a negative master of the microchannels is fabricated using photolithography (shown schematically in Figure 1.8). Photolithography is a process whereby the 2-dimensional features of the channel are transferred onto a photoresist though light exposure.[138, 139] A photoresist is a light sensitive material whose physical properties are altered upon exposure with light of specific wavelength. A thin layer of photoresist is deposited on a substrate (typically silicon wafer or glass) (Figure 1.8B). The substrate is then heated (pre-exposure bake) to evaporate the solvent; then it is slowly cooled down to room temperature to allow the photoresist to harden. The deigned photomask is then placed on top of the photoresist, and is subsequently exposed to UV light (Figure 1.8C). The type of photoresist used in this thesis is a negative photoresist SU-8, in that the areas of the substrate which are exposed to UV light will polymerize after a post-exposure bake. In addition, the post-exposure bake step also serve to enhance structural rigidity and adhesion to the substrate. The photoresist is then cooled down to room temperature before being placed in a developer solution, and the unexposed area is washed away and the master is ready (Figure 1.8D and E). It should be noted that SU-8 is an epoxy based photoresist that is chemically, thermally and structurally stable, and that it can be used indefinitely. The size of the features obtainable with rapid prototyping is between 50-100

µm, which fits most microfluidic applications. The height of the microchannel can be adjusted by choosing SU-8 with appropriate viscosity.

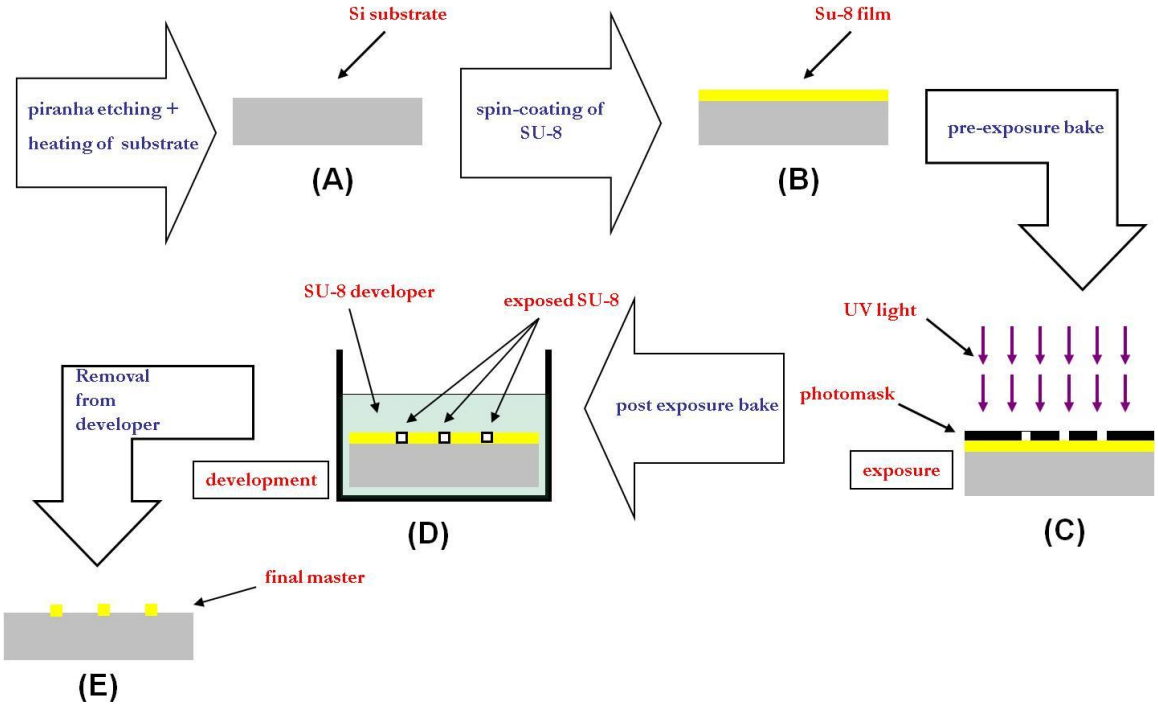

Figure 1.8. Fabrication of a negative SU-8 mater of a microfluidic chip on a silicon wafer using photolithography. A cross-sectional schematic of the microfluidic device at the various stages in the process is shown: cleaning and heating of the substrate (A); spin-coating of SU-8 onto the substrate (B); pre-exposure bake and UV light exposure (C); post-exposure bake and developing (D); washing with isopropanol to obtain the clean, final master (E).

1.5.3. Replica Molding

Once a master is finished, the microfluidic device can be fabricated using replica molding. Replica molding is a process whereby a prepolymer is added to the master, and a negative replica of the master is generated in the polymer. The steps involved in replica molding are schematically shown in Figure 1.9. Of all the available polymers,

polydimethylsiloxane (PDMS) has become a very popular choice among researchers. It has many appealing characteristics that make it an excellent candidate for microfluidic applications.[138, 139] It is a relatively inexpensive material and features on the micron scale can be reproduced very well with replica molding. It is suitable for optical detection methods such as UV-Vis absorbance and fluorescence as it is optically transparent down to 280 nm. It can be cured at both low and high temperatures. It is nontoxic and can be deformed reversibly. It can be sealed reversibly or irreversibly to many materials depending on the applications. Its surface chemistry can be easily altered using well-developed techniques. It is resistant to water and compatible with many organic solvents. However, there are also some drawbacks. It cannot withstand high temperature which is required in some material synthesis applications; it is air-permeable and absorption of particles is common; it can become swollen in certain solvents.[141]

Once molded and cured, the PDMS is removed from the master. Although PDMS forms reversible bonding to glass or a PDMS coated glass substrate by van der waals interactions, the seal can only withstand pressures of less than 5 Psi, which is not sufficient for most microfluidic applications. For higher pressure application, a strong permanent bond is required. This is done by treating PDMS surface with oxygen plasma. It has been shown that the treatment oxidizes the surface methyl groups (Si-CH_3) and generates silanol groups (Si-OH).[142] After oxygen plasma treatment, PDMS can be bonded irreversibly to a whole range of substrates including glass and itself. For glass and PDMS the reaction produces Si-O-Si bond after loss of water. Further, this oxygen plasma treatment makes the PDMS surface hydrophilic rending it useful for applications where aqueous solution is needed.[143] However, over time, the surface does revert back to

its original state. The tunable surface properties of PDMS make PDMS well-suited for different applications. Figure 1.10 shows the images of the finished components during the microfabrication process.

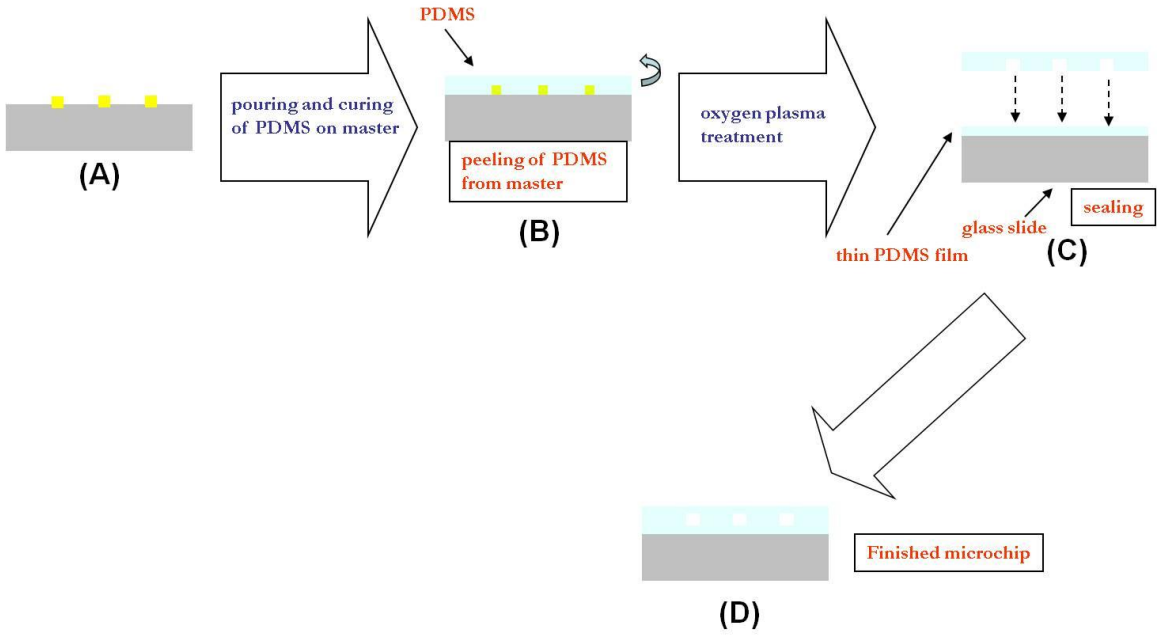

Figure 1.9. A cross-sectional schematic of the microchip during the replica molding and the sealing process at different stages of fabrication: the negative master prior to pouring of PDMS (A); the cured and peeled off PDMS (B); oxygen plasma treatment of the PDMS chip and the PDMS-coated substrate and then sealed to one another (C): the finished microchip ready to be used (D).

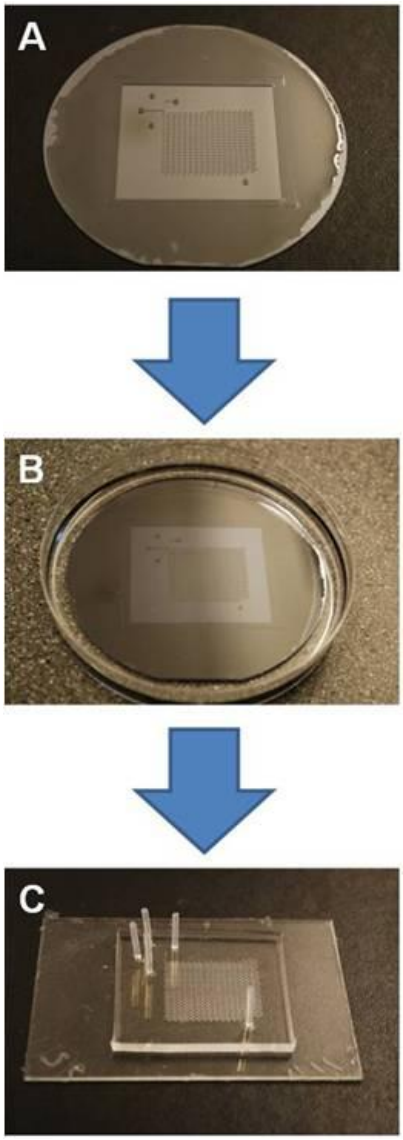

Figure 1.10. Pictures of finished products at different stages of the microfabrication process: finished negative SU-8 master on a silicon wafer (A); silicon wafer submerged in cured PDMS in a petri dish (B); and cut-out and sealed PDMS microchip ready to be used (C).

1.5.4. Fluid Delivery and Control

The experimental apparatus and set up for fluid delivery and control is shown in Figure 1.11. The microchip was mounted on an inverted microscope (DMI 6000B, Leica). Gas tight syringes (Hamilton gastight series, NV) and syringe pumps (Harvard, Apparatus, QC) were used to the deliver solutions to the microchannels. Two sizes of syringes were used (250 µl and 1000 µl) in this thesis. Holes were punched through the inlet and the outlets of the microchip using of the microchip using a NWSL sensipress. Teflon tubing (Scientific Products and Equipments, ON) with a $1/16^{th}$ inch outer diameter was used to connect the syringes to the inlets of the microchip. The holes were smaller than the Teflon tubing and elasticity of the PDMS provided a friction-fit of the Teflon tubing to the chip. Argon gas was delivered to the microchip via a pressure regulator (Johnston Control Inc) connected to a Q-sized argon tank (Praxair Inc, ON). The flow conditions on chip were captured using a charge-couple device (CCD) camera (Orca AG) installed on the microscope.

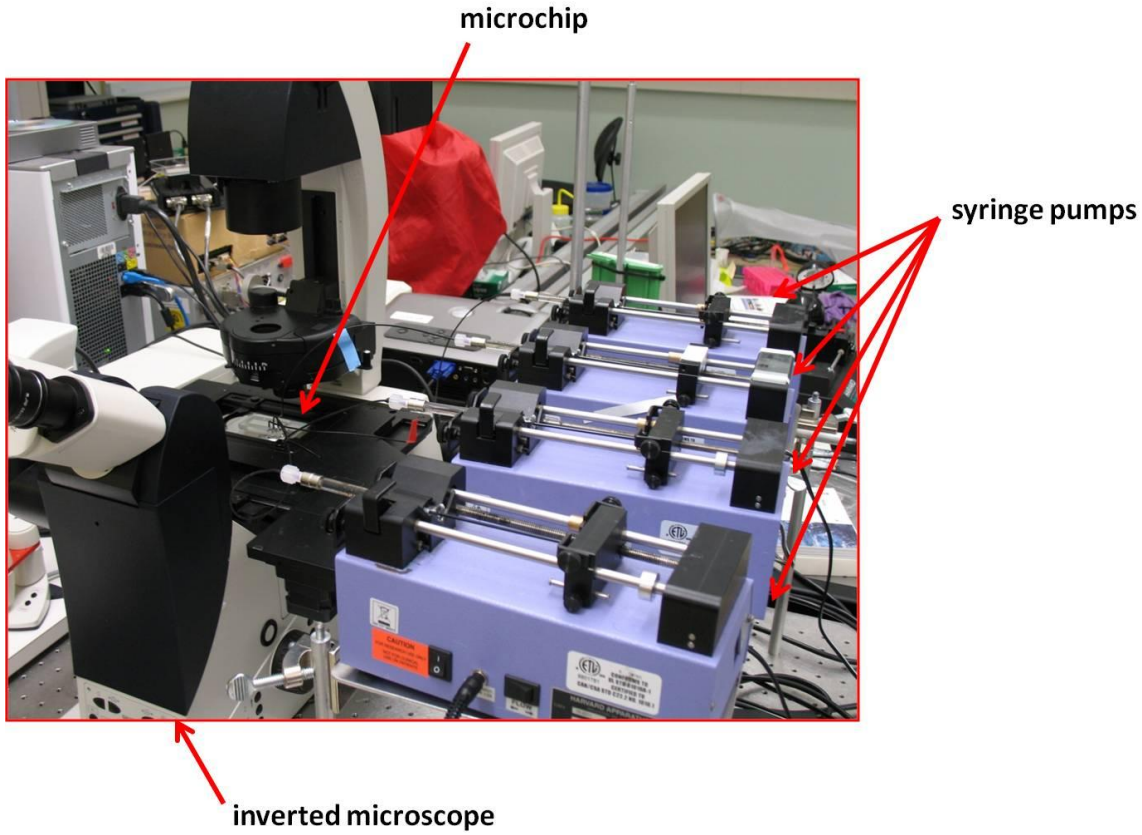

Figure 1.11. The experimental set up used in this thesis. The microchip is mounted on a inverted microscope (DMI 6000B microscope) (left) and connected to gas tight syringes mounted on syringe pumps via Teflon tubing (right).

1.6. Characterization Tools

1.6.1. Transmission Electron Microscopy

To characterize the structures of the various micelles morphologies, transmission electron microscopy (TEM) was routinely employed. In 1924, De Broglie proposed the theoretical ideas that are the foundation of TEM, an instrument that has allowed scientists to image structures on the nanoscale for the first time.[144] He proposed that an accelerated electron beam has an effective wavelength according to the following relationship:

$$\lambda = \frac{h}{mv} \qquad \textbf{(1.8)}$$

where λ is the wavelength of an electron of mass *m* travelling at velocity *v*. For the typical accelerating voltage (75 kV) used in this thesis, this yields a theoretical resolution of ~5 pm. Therefore, in principle, an electron microscope should be capable of imagining structures with atomic resolution, if one only considers the wavelength limitation (or the diffraction limit). For the TEM that was used in this thesis, a Hitachi H-700 electron microscopy, a spatial resolution of 1 nm is achievable;[145] the cause for the lower resolution than what the diffraction limit allowed comes from the technological limit in manufacturing the TEM at the time. Figure 1.12 is a typical schematic of a transmission electron microscope (TEM).

The electron gun in TEM fires a monochromatic stream of electrons that passes through a series of condenser lenses. These electrons then strike the sample and are scattered at different angles depending on the electron density of the region they encounter in the sample. These electrons can either be (A) undeflected, (B) deflected

without loss of energy (elastically scattered), or (C) deflected with significant loss of energy (inelastically scattered).[144] These various processes will govern the amount of electrons that pass or not pass the through the objective. The relative brightness of the image in each region is related to number of unscattered electrons which passes through the objective aperture. Regions of the specimen that are consisted of light atoms such as carbon will transmit more electrons and appear bright, while for heavy atoms such as iron the regions will for appear dark due to more electrons being deflected away.

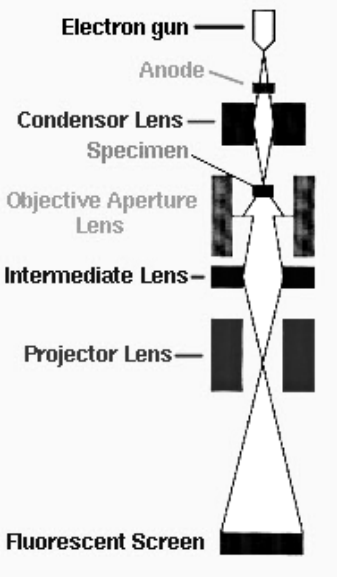

Figure 1.12. Schematic representation of transmission electron microscope (TEM).[144]

1.6.2. Photoluminescence (PL) Spectroscopy

Since photoluminescence (PL) spectroscopy is being employed to characterize loading efficiency of hydrophobic fluorescent probes in PS-*b*-PAA crew-cut micelles in chapter 5, a brief discussion on the theoretical background will be given here. The whole photoluminescence process is depicted in a simplified Jablonski diagram (Figure 1.13). Photoluminescence is an optical phenomenon whereby the excited states are generated using photons, and upon returning from initial high energy to lower energy states, photons are emitted.[146] Generally, photoluminescence can be divided into two categories: fluorescence and phosphorescence.[146] In fluorescence, when a fluorescent molecule (a fluorophore) absorbs light of specific wavelength, the electron in the lower energy orbital are excited to the higher energy orbital, while maintaining its spin orientation. Namely, the electrons in the higher energy orbitals have the opposite spin orientation as the electrons in the lower energy orbitals and this is termed a singlet excited state. These two electrons are also said to be paired. After a very brief moment, the electron in the excited state relaxes back to the ground state, releasing energy in the form of emitted photons. Since this kind of process does not require the electron in the excited state to change its spin orientation, this transition is quantum mechanically "allowed" and the fluorescence life time is typically near 1 to 10 ns. As for phosphorescence, the excited electrons in the higher energy orbitals (T_1) have the same spin orientation as the electrons in the lower energy orbitals, i.e., electrons are unpaired and this is termed a excited triplet state. In such case, electrons returning from excited state (triplet state) to ground state (singlet state) need to change its spin orientation, and the transitions are not allowed and the life time ranges from ms to s.

A common phenomena that happens in photoluminescence is the Stokes' shift where the photons been emitted is at higher wavelength than the photons absorbed. Following photon absorption, a fluorophore is usually excited to some higher vibration level of either S_1 or S_2, and the molecules quickly relax to the lowest vibration level of S_1. This is called internal conversion, which happens on the order of 10^{-12} sec. Then the molecules can further relax from the lowest vibration level of S_1 to the lowest vibration level of S_0, emitting photons in the process. In addition, molecules can decay to the excited vibrational level of S_0, causing a further loss of vibrational energy. Common causes for Stokes' shift include collisions between the molecules themselves and interactions between the solvents and the molecules.

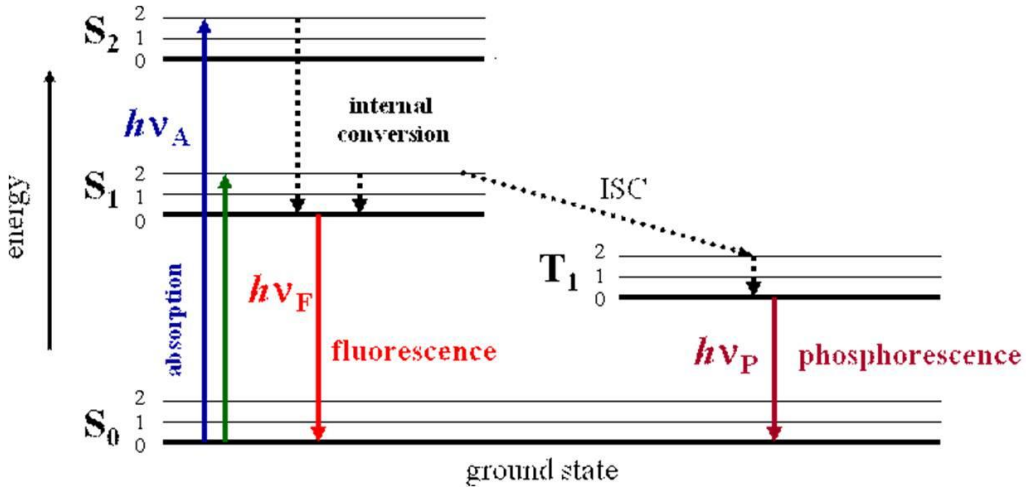

Figure 1.13. Simplified Jablonski diagram. The sequence of events leading the fluorescence and phosphorescence are shown. S_0 is the ground state, and S_1 and S_2 are excited singlet states. T_1 is the excited triplet states. 0, 1, 2 represent different vibration energy level.[147]

1.7. Content of the Thesis

The remainder of this thesis consists of four chapters, each exploring a distinct aspect of block copolymer self-assembly using top-down gas-liquid segmented microfluidic reactors. The content of these four chapters is as follows:

Chapter 2 focuses on the size control of quantum dot compound micelle assemblies (QDCMs) consisting of polystyrene-coated CdS QSs and polystyrene-*block*-poly(acrylic acid) stabilizing chains. Specifically, the shear effect in the corner of the liquid plugs has been utilized to tune the QDCMs sizes. Chemical parameters such as water contents and flow parameters such as the effect of gas-to-liquid ratio and total flow rate were investigated. The size and size distribution for each experimental condition was analyzed by TEM image analysis. This work has been previously published.[148]

Chapter 3 describes a new and versatile method of directing block copolymer micelle morphologies via shear forces that are operative on gas-liquid microfluidic reactor. The interplay between two mechanisms, shear-induced coalescence and shear-induced breakup, was used to direct the morphologies. The relative magnitude of these two competing mechanisms can be adjusted by on-chip flow condition. As well, the effect of water contents on the aggregate morphologies was investigated. A mechanism for the morphological transformation was proposed in the way of an energy diagram. The relaxation of the kinetic morphology formed on-chip back to their equilibrium morphology was tracked at various stages by TEM. This work has been previously published.[149]

Chapter 4 is an extension of the phenomenon described in the chapter 3 with more thorough analysis of the effect various chemical conditions. A phase diagram for the various mixed solvent systems (DMF/Dioxane) was constructed at different water

content. Phase boundaries for spherical, cylindrical, and vesicular micelles were identified. Shear forces were used to move micelle morphology in part of the phase diagram to another part of the phase diagram. The influence of the chemical parameters on the on-chip morphologies was also studied.

Finally, Chapter 5 demonstrates the applicability of shear forces on the gas-liquid segmented microfluidic reactor to influence the loading efficiency of fluorescent hydrophobic probes in block copolymer micelles. These types of loading study with hydrophobic probes could lay the foundation for potential drug delivery applications. Specifically, the effects of different hydrophobic probes and solvent conditions along with different on-chip flow conditions on the loading efficiency were studied. Photoluminescence spectroscopy was used to determine the loading efficiency.

Chapter 6 contains concluding remarks and describes the direction for future work.

1.8. References

1. Stone, H. A.; Stroock, A. D.; Ajdari, A., *Annu Rev Fluid Mech* **2004,** *36*, 381-411.

2. Whitesides, G. M., *Nature* **2006,** *442* (7101), 368-373.

3. White, F. M., *Fluid Mechanics*. 5th ed.; McGraw-Hill: Boston, Mass: London, 2003.

4. Probstein, R. F., *Physicochemical hydrodynamics: an introduction*. 2nd ed.; John Wiley&Sons: New York, 1994.

5. Whitesides, G. M.; Stroock, A. D., *Phys Today* **2001,** *54* (6), 42-48.

6. Gunther, A.; Jensen, K. F., *Lab Chip* **2006,** *6* (12), 1487-1503.

7. Gunther, A.; Khan, S. A.; Thalmann, M.; Trachsel, F.; Jensen, K. F., *Lab Chip* **2004,** *4* (4), 278-286.

8. Song, H.; Chen, D. L.; Ismagilov, R. F., *Angew Chem Int Edit* **2006,** *45* (44), 7336-7356.

9. Song, H.; Tice, J. D.; Ismagilov, R. F., *Angew Chem Int Edit* **2003,** *42* (7), 768-772.

10. Bringer, M. R.; Gerdts, C. J.; Song, H.; Tice, J. D.; Ismagilov, R. F., *Philos T Roy Soc A* **2004,** *362* (1818), 1087-1104.

11. Song, H.; Bringer, M. R.; Tice, J. D.; Gerdts, C. J.; Ismagilov, R. F., *Appl. Phys. Lett.* **2003,** *83* (22), 4664-4666.

12. Chastek, T. Q.; Iida, K.; Amis, E. J.; Fasolka, M. J.; Beers, K. L., *Lab Chip* **2008,** *8* (6), 950-957.

13. Karnik, R.; Gu, F.; Basto, P.; Cannizzaro, C.; Dean, L.; Kyei-Manu, W.; Langer, R.; Farokhzad, O. C., *Nano Lett.* **2008,** *8* (9), 2906-2912.

14. Abraham, S.; Park, Y. H.; Lee, J. K.; Ha, C. S.; Kim, I., *Adv Mater* **2008,** *20* (11), 2177-2182.

15. Song, Y. J.; Hormes, J.; Kumar, C. S. S. R., *Small* **2008,** *4* (6), 698-711.

16. Schabas, G.; Wang, C. W.; Oskooei, A.; Yusuf, H.; Moffitt, M. G.; Sinton, D., *Langmuir* **2008,** *24* (19), 10596-10603.

17. Yusuf, H.; Kim, W. G.; Lee, D. H.; Guo, Y. Y.; Moffitt, M. G., *Langmuir* **2007,** *23* (2), 868-878.

18. Shen, H. W.; Zhang, L. F.; Eisenberg, A., *J. Phys. Chem. B* **1997,** *101* (24), 4697-4708.

19. Zhang, L. F.; Eisenberg, A., *Science* **1995,** *268* (5218), 1728-1731.

20. Zhang, L. F.; Eisenberg, A., *Macromolecules* **1999,** *32* (7), 2239-2249.

21. Zhang, L. F.; Shen, H. W.; Eisenberg, A., *Macromolecules* **1997,** *30* (4), 1001-1011.

22. Zhang, L. F.; Yu, K.; Eisenberg, A., *Science* **1996,** *272* (5269), 1777-1779.

23. Carraher, J. C. E., *Polymer Chemistry*. 5th ed.; Eastern Hemisphere Distribution: New York, 2000.

24. Cowie.J.M.G., *Polymers: Chemistry & Physics of Modern Materials*. 2nd ed.; Stanley Thornes Ltd: Cheltenham, 1991.

25. Nicholson, J. W., *The Chemistry of Polymers*. 2nd ed.; The Royal Society of Chemistry: Letchworth, 1997.

26. Young, R. J.; Lovell, P. A., *Introduction to Polymers*. 2nd ed.; Chapman & Hall: New York, 1991.

27. Riess, G., *Prog. Polym. Sci.* **2003,** *28* (7), 1107-1170.

28. Raviv, U.; Giasson, S.; Kampf, N.; Gohy, J. F.; Jerome, R.; Klein, J., *Nature* **2003,** *425* (6954), 163-165.

29. Brown, H. R., *Ibm Journal of Research and Development* **1994,** *38* (4), 379-389.

30. Malmsten, M., Drugs and the pharmaceutical sciences

In *Surfactants and polymers in drug delivery*, Marcel Dekker: 2002; Vol. 122.

31. Guo, Y.; Harirchian-Saei, S.; Izumi, C. M. S.; Moffitt, M. G., *ACS Nano* **2011,** *5* (4), 3309-3318.

32. Guo, Y.; Moffitt, M. G., *Chem. Mater.* **2007,** *19* (26), 6581-6587.

33. Guo, Y.; Moffitt, M. G., *Macromolecules* **2007,** *40* (16), 5868-5878.

34. Moffitt, M.; Eisenberg, A., *Macromolecules* **1997,** *30* (15), 4363-4373.

35. Moffitt, M.; Mcmahon, L.; Pessel, V.; Eisenberg, A., *Chem. Mater.* **1995,** *7* (6), 1185-1192.

36. Wang, C. W.; Moffitt, M. G., *Langmuir* **2004,** *20* (26), 11784-11796.

37. Hadjichristidi, N.; Pispas, S.; Floudas, G., *Block Copolymers*. John Wiley & Sons, Inc: New Jersey, 2003.

38. Hamley, J. W., *The Physics of Block Copolymers*. Oxford University Press: 1998.

39. Alexandridies, P.; Lindman, B., *Amphiphilic Block Copolymers* ELSEVIER: New York, 2000.

40. Webber, S. E.; Munk, P.; Tuzar, Z., *Solvents and Self-Organization of Polymers*. Kluwer Academic Publishers: Boston, 1996.

41. Tuzar, Z.; Kratochvil, P., *In Surface and Colloid Science*. Plenum Pressure: New York, 1993; Vol. 15.

42. Cheyne, R. B. SELF-ASSEMBLY OF POLYSTYRENE-POLY(ETHYLENE OXIDE) BLOCK COPOLYMERS AND POLYMER-STABILIZED CADMIUM SULFIDE NANOPARTICLES AT THE AIR-WATER INTERFACE: PATTERNING SURFACE FEATURES FROM THE BOTTOM UP. University of Victoria, Victoria, 2005.

43. Price, C., *Pure Appl. Chem.* **1983,** *55* (10), 1563-1572.

44. Price, C.; Chan, E. K. M.; Mobbs, R. H.; Stubbersfield, R. B., *Eur. Polym. J.* **1985,** *21* (4), 355-360.

45. Price, C.; Chan, E. K. M.; Pilcher, G.; Stubbersfield, R. B., *Eur. Polym. J.* **1985,** *21* (7), 627-628.

46. Price, C.; Chan, E. K. M.; Stubbersfield, R. B., *Eur. Polym. J.* **1987,** *23* (8), 649-651.

47. Price, C.; Stubbersfield, R. B.; Elkafrawy, S.; Kendall, K. D., *British Polymer Journal* **1989,** *21* (5), 391-394.

48. Deng, Y. L.; Price, C.; Booth, C., *Eur. Polym. J.* **1994,** *30* (1), 103-111.

49. Zhang, L. F.; Eisenberg, A., *Journal of Polymer Science Part B-Polymer Physics* **1999,** *37* (13), 1469-1484.

50. Zhang, L. F.; Eisenberg, A., *J. Am. Chem. Soc.* **1996,** *118* (13), 3168-3181.

51. Zhang, L. F.; Eisenberg, A., *Macromolecules* **1996,** *29* (27), 8805-8815.

52. Yu, Y. S.; Zhang, L. F.; Eisenberg, A., *Macromolecules* **1998,** *31* (4), 1144-1154.

53. Yu, Y. S.; Eisenberg, A., *J. Am. Chem. Soc.* **1997,** *119* (35), 8383-8384.

54. Yu, K.; Zhang, L. F.; Eisenberg, A., *Langmuir* **1996,** *12* (25), 5980-5984.

55. Yu, K.; Eisenberg, A., *Macromolecules* **1998,** *31* (11), 3509-3518.

56. Yu, K.; Bartels, C.; Eisenberg, A., *Langmuir* **1999,** *15* (21), 7157-7167.

57. Yu, K.; Bartels, C.; Eisenberg, A., *Macromolecules* **1998,** *31* (26), 9399-9402.

58. Terreau, O.; Luo, L. B.; Eisenberg, A., *Langmuir* **2003,** *19* (14), 5601-5607.

59. Walther, A.; Goldmann, A. S.; Yelamanchili, R. S.; Drechsler, M.; Schmalz, H.; Eisenberg, A.; Muller, A. H. E., *Macromolecules* **2008,** *41* (9), 3254-3260.

60. Soo, P. L.; Eisenberg, A., *Journal of Polymer Science Part B-Polymer Physics* **2004,** *42* (6), 923-938.

61. Jain, S.; Bates, F. S., *Science* **2003,** *300* (5618), 460-464.

62. Lindman, B.; Wennerstrom, H., In *In Topics in Current Chemistry: Micelles*, Boschke, F., Ed. Springer-Verlag: New York, 1980; p 34.

63. Hiemenz, P. C., In *Principles of Colloid and Surface Chemistry*, 2nd ed.; Marcel Dekker: New York, 1986; p 447.

64. Hunter, R. J., In *Foundations of Colloid Science*, Oxford University Press: New York, 1987; Vol. 1, p 575.

65. Aniansson, E. A. G.; Wall, S. N.; Almgren, M.; Hoffmann, H.; Kielmann, I.; Ulbricht, W.; Zana, R.; Lang, J.; Tondre, C., *J. Phys. Chem.* **1976,** *80* (9), 905-922.

66. Honda, C.; Hasegawa, Y.; Hirunuma, R.; Nose, T., *Macromolecules* **1994,** *27* (26), 7660-7668.

67. Jain, S.; Bates, F. S., *Macromolecules* **2004,** *37* (4), 1511-1523.

68. Cui, H. G.; Chen, Z. Y.; Zhong, S.; Wooley, K. L.; Pochan, D. J., *Science* **2007,** *317* (5838), 647-650.

69. Dormidontova, E. E., *Macromolecules* **1999,** *32* (22), 7630-7644.

70. Lund, R.; Willner, L.; Richter, D.; Dormidontova, E. E., *Macromolecules* **2006,** *39* (13), 4566-4575.

71. Won, Y. Y.; Davis, H. T.; Bates, F. S., *Macromolecules* **2003,** *36* (3), 953-955.

72. Tsunashima, Y.; Kawamata, Y., *Macromolecules* **1993,** *26* (18), 4899-4909.

73. Tian, M. M.; Qin, A. W.; Ramireddy, C.; Webber, S. E.; Munk, P.; Tuzar, Z.; Prochazka, K., *Langmuir* **1993,** *9* (7), 1741-1748.

74. Kent, M. S.; Tirrell, M.; Lodge, T. P., *Journal of Polymer Science Part B-Polymer Physics* **1994,** *32* (11), 1927-1941.

75. Brown, W.; Schillen, K.; Hvidt, S., *J. Phys. Chem.* **1992,** *96* (14), 6038-6044.

76. Allen, C.; Maysinger, D.; Eisenberg, A., *Colloids and Surfaces B-Biointerfaces* **1999,** *16* (1-4), 3-27.

77. Soo, P. L.; Luo, L. B.; Maysinger, D.; Eisenberg, A., *Langmuir* **2002,** *18* (25), 9996-10004.

78. Burke, S. E.; Eisenberg, A., *Langmuir* **2001,** *17* (26), 8341-8347.

79. Burke, S. E.; Eisenberg, A., *Langmuir* **2001,** *17* (21), 6705-6714.

80. Burke, S. E.; Eisenberg, A., *Polymer* **2001,** *42* (21), 9111-9120.

81. Chen, L.; Shen, H. W.; Eisenberg, A., *J. Phys. Chem. B* **1999,** *103* (44), 9488-9497.

82. Choucair, A.; Soo, P. L.; Eisenberg, A., *Langmuir* **2005,** *21* (20), 9308-9313.

83. Desbaumes, L.; Eisenberg, A., *Langmuir* **1999,** *15* (1), 36-38.

84. Discher, D. E.; Eisenberg, A., *Science* **2002,** *297* (5583), 967-973.

85. Kabanov, A. V.; Bronich, T. K.; Kabanov, V. A.; Yu, K.; Eisenberg, A., *J. Am. Chem. Soc.* **1998,** *120* (38), 9941-9942.

86. Liu, F. T.; Eisenberg, A., *J. Am. Chem. Soc.* **2003,** *125* (49), 15059-15064.

87. Liu, X. Y.; Wu, J.; Kim, J. S.; Eisenberg, A., *Langmuir* **2006,** *22* (1), 419-424.

88. Riegel, I. C.; Eisenberg, A.; Petzhold, C. L.; Samios, D., *Langmuir* **2002,** *18* (8), 3358-3363.

89. Shen, H. W.; Eisenberg, A., *J. Phys. Chem. B* **1999,** *103* (44), 9473-9487.

90. Shen, H. W.; Zhang, L. F.; Eisenberg, A., *J. Am. Chem. Soc.* **1999,** *121* (12), 2728-2740.

91. Yu, G. E.; Eisenberg, A., *Macromolecules* **1998,** *31* (16), 5546-5549.

92. Yu, Y. S.; Zhang, L. F.; Eisenberg, A., *Langmuir* **1997,** *13* (9), 2578-2581.

93. Won, Y. Y.; Davis, H. T.; Bates, F. S., *Science* **1999,** *283* (5404), 960-963.

94. Discher, B. M.; Won, Y. Y.; Ege, D. S.; Lee, J. C. M.; Bates, F. S.; Discher, D. E.; Hammer, D. A., *Science* **1999,** *284* (5417), 1143-1146.

95. Cui, H. G.; Chen, Z. Y.; Wooley, K. L.; Pochan, D. J., *Soft Matter* **2009,** *5* (6), 1269-1278.

96. Li, Z. B.; Chen, Z. Y.; Cui, H. G.; Hales, K.; Qi, K.; Wooley, K. L.; Pochan, D. J., *Langmuir* **2005,** *21* (16), 7533-7539.

97. Li, Z. B.; Chen, Z. Y.; Cui, H. G.; Hales, K.; Wooley, K. L.; Pochan, D. J., *Langmuir* **2007,** *23* (9), 4689-4694.

98. Ding, J. F.; Liu, G. J., *Chem. Mater.* **1998,** *10* (2), 537-542.

99. Ding, J. F.; Liu, G. J., *Macromolecules* **1999,** *32* (25), 8413-8420.

100. Ding, J. F.; Liu, G. J.; Yang, M. L., *Polymer* **1997,** *38* (21), 5497-5501.

101. Maskos, M.; Harris, J. R., *Macromol. Rapid Commun.* **2001,** *22* (4), 271-273.

102. Rheingans, O.; Hugenberg, N.; Harris, J. R.; Fischer, K.; Maskos, M., *Macromolecules* **2000,** *33* (13), 4780-4790.

103. Nardin, C.; Hirt, T.; Leukel, J.; Meier, W., *Langmuir* **2000,** *16* (3), 1035-1041.

104. Sauer, M.; Haefele, T.; Graff, A.; Nardin, C.; Meier, W., *Chem Commun* **2001,** (23), 2452-2453.

105. Kickelbick, G.; Bauer, J.; Husing, N.; Andersson, M.; Palmqvist, A., *Langmuir* **2003,** *19* (8), 3198-3201.

106. Harris, J. K.; Rose, G. D.; Bruening, M. L., *Langmuir* **2002,** *18* (14), 5337-5342.

107. Yu, H. Z.; Jiang, W., *Macromolecules* **2009,** *42* (9), 3399-3404.

108. Forster, S.; Hermsdorf, N.; Leube, W.; Schnablegger, H.; Regenbrecht, M.; Akari, S.; Lindner, P.; Bottcher, C., *J. Phys. Chem. B* **1999,** *103* (32), 6657-6668.

109. Schillen, K.; Brown, W.; Johnsen, R. M., *Macromolecules* **1994,** *27* (17), 4825-4832.

110. Lehner, D.; Lindner, H.; Glatter, O., *Langmuir* **2000,** *16* (4), 1689-1695.

111. Zipfel, J.; Lindner, P.; Tsianou, M.; Alexandridis, P.; Richtering, W., *Langmuir* **1999,** *15* (8), 2599-2602.

112. Schillen, K.; Bryskhe, K.; Mel'nikova, Y. S., *Macromolecules* **1999,** *32* (20), 6885-6888.

113. Valentini, M.; Napoli, A.; Tirelli, N.; Hubbell, J. A., *Langmuir* **2003,** *19* (11), 4852-4855.

114. Zheng, Y.; Davis, H. T., *Langmuir* **2000,** *16* (16), 6453-6459.

115. Talingting, M. R.; Munk, P.; Webber, S. E.; Tuzar, Z., *Macromolecules* **1999,** *32* (5), 1593-1601.

116. Raez, J.; Barjovanu, R.; Massey, J. A.; Winnik, M. A.; Manners, I., *Angew Chem Int Edit* **2000,** *39* (21), 3862-+.

117. Massey, J. A.; Power, K. N.; Winnik, M. A.; Manners, I., *Adv Mater* **1998,** *10* (18), 1559-+.

118. Massey, J.; Power, K. N.; Manners, I.; Winnik, M. A., *J. Am. Chem. Soc.* **1998,** *120* (37), 9533-9540.

119. Spatz, J. P.; Mossmer, S.; Moller, M., *Angewandte Chemie-International Edition in English* **1996,** *35* (13-14), 1510-1512.

120. Yokoyama, M.; Kwon, G. S.; Okano, T.; Sakurai, Y.; Naito, M.; Kataoka, K., *J. Controlled Release* **1994,** *28* (1-3), 59-65.

121. Yokoyama, M.; Miyauchi, M.; Yamada, N.; Okano, T.; Sakurai, Y.; Kataoka, K.; Inoue, S., *Cancer Res.* **1990,** *50* (6), 1693-1700.

122. Yokoyama, M.; Fukushima, S.; Uehara, R.; Okamoto, K.; Kataoka, K.; Sakurai, Y.; Okano, T., *J. Controlled Release* **1998,** *50* (1-3), 79-92.

123. Kwon, G.; Naito, M.; Yokoyama, M.; Okano, T.; Sakurai, Y.; Kataoka, K., *J. Controlled Release* **1997,** *48* (2-3), 195-201.

124. Kwon, G.; Suwa, S.; Yokoyama, M.; Okano, T.; Sakurai, Y.; Kataoka, K., *J. Controlled Release* **1994,** *29* (1-2), 17-23.

125. Geng, Y.; Dalhaimer, P.; Cai, S. S.; Tsai, R.; Tewari, M.; Minko, T.; Discher, D. E., *Nat. Nanotechnol.* **2007,** *2* (4), 249-255.

126. Sentjurc, M.; Vrhovnik, K.; Kristl, J., *J. Controlled Release* **1999,** *59* (1), 87-97.

127. Coldren, B.; van Zanten, R.; Mackel, M. J.; Zasadzinski, J. A.; Jung, H. T., *Langmuir* **2003,** *19* (14), 5632-5639.

128. Pereira-Lachataignerais, J.; Pons, R.; Panizza, P.; Courbin, L.; Rouch, J.; Lopez, O., *Chem. Phys. Lipids* **2006,** *140* (1-2), 88-97.

129. Reynolds, O., *Philos. Trans. R. Soc* **1883,** *174*, pp. 935-982.

130. Reynolds, O., *Philosophical Transactions of the Royal Society of London Series a-Mathematical Physical and Engineering Sciences* **1883,** *174*, 935-982.

131. Purcell, E. M., *Am J Phys* **1977,** *45* (1), 3-11.

132. Khan, S. A.; Gunther, A.; Schmidt, M. A.; Jensen, K. F., *Langmuir* **2004,** *20* (20), 8604-8611.

133. Hosokawa, K.; Fujii, T.; Endo, I., *Anal. Chem.* **1999,** *71* (20), 4781-4785.

134. Sugiura, S.; Nakajima, M.; Iwamoto, S.; Seki, M., *Langmuir* **2001,** *17* (18), 5562-5566.

135. Ganan-Calvo, A. M., *Phys Rev E* **2004,** *69* (2).

136. Garstecki, P.; Gitlin, I.; DiLuzio, W.; Whitesides, G. M.; Kumacheva, E.; Stone, H. A., *Appl. Phys. Lett.* **2004,** *85* (13), 2649-2651.

137. Garstecki, P.; Fuerstman, M. J.; Stone, H. A.; Whitesides, G. M., *Lab Chip* **2006,** *6* (3), 437-446.

138. Duffy, D. C.; McDonald, J. C.; Schueller, O. J. A.; Whitesides, G. M., *Anal. Chem.* **1998,** *70* (23), 4974-4984.

139. McDonald, J. C.; Duffy, D. C.; Anderson, J. R.; Chiu, D. T.; Wu, H. K.; Schueller, O. J. A.; Whitesides, G. M., *Electrophoresis* **2000,** *21* (1), 27-40.

140. deMello, A. J., *Nature* **2006,** *442* (7101), 394-402.

141. Lee, J. N.; Park, C.; Whitesides, G. M., *Anal. Chem.* **2003,** *75* (23), 6544-6554.

142. Owen, M. J.; Smith, P. J., *J. Adhes. Sci. Technol.* **1994,** *8* (10), 1063-1075.

143. Ng, J. M. K.; Gitlin, I.; Stroock, A. D.; Whitesides, G. M., *Electrophoresis* **2002,** *23* (20), 3461-3473.

144. Agar, A. W.; Alderson, R. H.; Chescoe, D., *Principle and Practice of Electron Microscoope Operation*. North Holland Publishing Co: New York, 1974.

145. Gowen, B., Personal Communication. December. 2004.

146. Lakowicz, J. R., *Principles of Fluorescence Spectroscopy*. 2nd ed.; Springer: 1999.

147. http://chem.sci.utsunomiya-u.ac.jp/v13n2/22ALP_Nery/ALPNery.html.

148. Wang, C. W.; Oskooei, A.; Sinton, D.; Moffitt, M. G., *Langmuir* **2010,** *26* (2), 716-723.

149. Wang, C. W.; Sinton, D.; Moffitt, M. G., *J. Am. Chem. Soc.* **2011,** *133* (46), 18853-18864.

CHAPTER 2

CONTROLLED SELF-ASSEMBLY OF QUANTUM DOT-BLOCK COPOLYMER COLLOIDS IN MULTIPHASE MICROFLUIDIC REACTORS

2.1. Introduction

Colloidal quantum dots (QDs) and metal nanoparticles are promising nanostructured materials with size-tunable electronic and optical properties that are significantly different from their bulk counterparts. However, future applications in photonics, sensing, and biological labeling will require controlled self-assembly of nanoparticles into complex colloidal structures with hierarchical organization, in order to achieve specific collective properties arising from organization on multiple length scales.[2-11] Microfluidic reactors provide confinement and control of mass transport phenomena and have been shown to be well suited to the controlled synthesis of polymeric[12-14] and inorganic[15-20] nanoparticles. The self-assembly of various nanostructures from molecular building blocks has also been demonstrated in microfluidic environments, including core-shell organosilicon microscapsules,[21] and lipid-bilayer membranes[22] and vesicles.[23] Microfluidic environments also offer numerous advantages for the controlled self-assembly of nanoparticles into higher-order structures, since associated self-assembly events can be controlled via fine tuning of local concentrations of reagents, mixing rates, and shear forces.[24, 25]

It has been previously shown that polystyrene (PS)-stabilized cadmium sulfide (CdS) QDs (PS-CdS) and stabilizing chains of the block copolymer polystyrene-*b*-polyacrylic acid (PS-*b*-PAA) co-dissolved in polar organic solvent (e.g. dimethylformamide, DMF) undergo self-organization upon water addition to form mesoscale spherical assemblies termed quantum dot compound micelles (QDCM).[24-27]

The resulting QDCMs possess complex hierarchical structure, surface functionality for bio-conjugation, photoluminescence and water solubility, making them promising colloidal elements for photonics, bio-labeling, and sensing. The self-assembly of polymer and QD components to form QDCMs (Figure 2.1A) begins above a critical water concentration (cwc), which depends on the polymeric components, the total polymer concentration, and the solvent.[28, 29] The driving force for self-assembly is the phase separation of hydrophobic PS chains of PS-CdS and PS-*b*-PAA from solution, with the hydrophilic PAA chains of the latter component surrounding the outside of the assembly and maintaining colloidal stability. Interfacial tension drives QDCM particle growth at water concentrations above the cwc. However, as more water is added, the dynamics of QDCM growth are progressively slowed down, since DMF is forced from the polymer-rich phase, decreasing plasticization and lowering the mobility of PS chains.[28] Therefore, the average QDCM size can be kinetically tuned by controlling the rates of water addition and mixing relative to the dynamics of particle growth.[24, 25, 27, 30]

We have demonstrated QDCM formation using a single-phase flow-focusing microfluidic reactor strategy, in which PS-CdS and PS-*b*-PAA constituents in DMF are combined with water via cross-stream diffusion from a sheath stream of DMF/water solution.[24] More recently, we applied a gas-liquid multiphase microfluidic approach in which three separate liquid streams containing 1) the self-assembling constituents in DMF, 2) pure DMF (separator stream), and 3) a DMF/water mixture were combined and then segmented by gas bubbles; the resulting compartmentalized liquid plugs moved through a sinusoidal mixing channel followed by a post-formation channel of variable length. Chaotic advection in the mixing channel greatly enhanced the rate of mixing

compared to the single-phase microfluidic reactor. As well, we demonstrated that circulating flow in the post-formation channel contributes to a decrease in mean QDCM size via shear-induced particle breakup. An on-chip particle breakup mechanism was supported by the following observations: 1) a decrease in particle size with increased length of the post-formation channel under identical flow conditions, counter to expected growth due to interfacial tension and 2) a decrease in particle size with increased flow rate for similar residence times. We proposed that QDCM breakup occurs in high-shear regions in the corners of the liquid plugs, based on the above experimental results and supported by numerical analysis of flow fields and maximum shear rates within the gas-segmented reactor.[25]

In this study, we explore in detail the various chemical and flow parameters that influence mean particle size for QDCM formation in a gas-segmented microfluidic reactor, specifically water concentration, total flow rate, and gas-to-liquid flow ratio. The observed particle sizes indicate that our previously-proposed mechanism of shear-induced particle breakup is operative for all water concentrations at sufficiently high flow rate.[25] However, further to these effects, we also observe that circulating flow in gas-liquid segmented reactors can also enhance coalescence growth of particles via increased collision frequency under conditions of low water content and low flow rate. We show that by tuning the relative importance of these competing mechanisms via variable chemical and flow parameters, mean particle sizes of self-assembled block copolymer-quantum dot colloids can be effectively controlled. These results point to new avenues for top-down control of self-assembling colloidal systems via tunable shear processing in two-phase microfluidic devices.

2.2. Experimental Section

2.2.1. Materials

All block copolymer samples were synthesized via anionic polymerization of the associated polystyrene-*block*-poly(*tert*-butyl acrylate) block copolymer, followed by hydrolysis of the ester block;[31] numbers in brackets refer to number-average degrees of polymerization of each block. As described previously,[27] block copolymer-stabilized CdS QDs with an external PS brush layer (PS-CdS) were synthesized via self-assembly of a PS(300)-*b*-PAA(12) block copolymer to form reverse micelles in a hydrophobic solvent, followed by templated CdS QD synthesis in the micelle cores. Static and dynamic light scattering carried out in DMF solvent revealed that each stable PS-CdS particle is surrounded by an average of 54 ± 2 copolymer chains (kinetically frozen at the QD surface by the high T_g of the poly(cadmium acrylate), PACd, surface layer), and has a *z*-average hydrodynamic diameter of d_h = 36 ± 2 nm. QDCMs were formed via the addition of water to solutions of PS-CdS and PS(665)-*b*-PAA(68) stabilizing chains codissolved in DMF.[27]

For microfluidic self-assembly experiments, PS-CdS and PS(665)-*b*-PAA(68) stabilizing chains were dissolved separately in DMF (99.9+% HPLC grade, H_2O < 0.03%), each at a total solids concentration of 1 wt%; the solution of stabilizing chains and dispersion of PS-CdS were then combined to form a 50/50 (w/w) blend of constituents in DMF. A DMF/water mixture was created by adding 99.9% pure deionized water to DMF on a digital balance (Denver Instruments) to produce mixtures containing 24, 12, 9, and 6 wt% water, which yielded steady-state water contents of 8, 4,

3, and 2 wt%, respectively, when combined with the two other liquid streams at equal flow rate.

2.2.2. Microfluidic Chip Fabrication

Negative masters were fabricated on high-quality silicon wafers (Silicon Quest International, CA) using a negative photoresist, SU-8 (Microchem Inc., MA). Prior to use, new silicon wafers were heated on a hotplate to at 200 ºC for 20 minutes to remove all moisture. SU-8 films, 150 μm thick, were spin-coated onto the silicon wafers, then heated to 95 ºC for 60 minutes to remove residual SU-8 solvent. A photomask was placed over the film and the device was exposed to UV light for 180 s. After additional heating at 95ºC for 20 minutes, the device was submerged in SU-8 developer (Microchem, MA) until all unexposed photoresist was removed.

Microfluidic chips were fabricated from poly(dimethylsiloxane) (PDMS) using a SYLGARD 184 silicon elastomer kit (Dow Corning, MI) with an elastomer base-to-curing agent ratio of 10:1. The elastomer and curing agent were mixed together and degassed in a vacuum chamber. The degassed PDMS was poured onto the negative master in a petri dish and then degassed again until all remaining air bubbles in the PDMS were removed. The PDMS was then heated at 85 ºC until cured. The microfluidic chips were peeled off the master, and holes were punched through its reservoirs to allow for the insertion of tubing. A thin PDMS film was formed on a glass slide by spin-coating and was permanently bonded to the base of the microfluidic reactor after both components were exposed to oxygen plasma for 30 s.

2.2.3. Flow Delivery and Control

Pressure-driven flow of liquids and Ar gas to the inlets of the reactors was provided using 250 μL gastight syringes (Hamilton, NV) mounted on syringe pumps (Harvard Apparatus, MA). Flow rates were varied via the syringe pumps. The microchip was connected to the syringes with 1/16th inch (OD) teflon tubing (Scientific Products and Equipment, ON). The ratio of gas to liquid flow rate is given by Q_{gas}/Q_{liq}.

2.2.4. Sample Collection and Image Processing

Flow visualization and quantification of all the flow conditions was performed with an inverted fluorescence microscopy system with excitation/emission filter combinations for QD fluorescence (λ_{ex} = 350-400 nm, λ_{em} > 500 nm). Fluorescence images of the reactor were capture using a CCD camera (AF6000 Orca, Hamamatsu, NJ) installed on the inverted microscope (DMI 6000B, LEICA, NJ). The QD filter cube (Semrock, NY) was custom designed for CdS QDs of interest and transmitted excitation light in the range of 350-400 nm to the chip, and returning light above 500 nm to the CCD camera.

Transmission electron microscopy (TEM) of various aqueous QDCM dispersions was performed at a Hitachi H-700 electron microscope, operating at an accelerating voltage of 75 kV. For off-chip QDCM size distribution analysis, QDCM dispersions were collected from the chip following the post-formation channel into vials containing deionized water, where the particles immediately become kinetically frozen due to high water content. The final solids content of the final aqueous solution is estimated to be 0.25 mg/mL. For TEM imaging, a 10 μL drop of each QDCM dispersion was deposited onto a carbon-coated Formvar 300 mesh copper grid and then shadowed with Pt/Pd wire

for imaging. Particle size analysis and statistics were carried out on the shadowed samples, with various regions of the TEM grid randomly sampled. For each sample, the diameters of 300 QDCM particles were measured with a caliper (Mastercraft, FL) on print-outs where the particles were 40,000 times their actual size. Images of selected samples were also taken without Pt/Pd shadowing, in order to characterize the QDCM internal structure. Although TEM image analysis is time consuming, it provides a more accurate and reliable determination of size distributions than faster methods such as dynamic light scattering.

2.2.5. Calculation of parameters of gas-liquid segmented microfluidic reactor experiments (as listed in Table 2.1)

The length of the liquid plug, L_{liq}, and the length of the gas plug, L_{gas}, were determined from the fluorescence images with the convention shown in Scheme 2.1. As shown, two-phase hemispherical region was ascribed to the liquid plug length only, and thus a sum of the liquid and gas plug lengths was consistent with the reactor length.

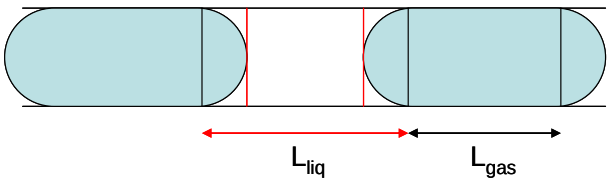

Scheme 2.1. Schematic representation showing the convention applied in determining the liquid and gas plug lengths, L_{liq} and L_{gas}, respectively. The two-phase hemispherical region was ascribed to the liquid plug length only, such that a sum of the liquid and gas plug lengths was consistent with the reactor length.

The volume of liquid plugs (V_{liq}) was calculated from the plug lengths and the known channel cross-sectional dimension. As a first order approximation, the geometry of the bubble caps were taken as hemispherical with diameter equivalent to the channel cross-sectional dimension, and the volume of the liquid film surrounding the gas bubble was ignored over the length L_{gas}. The resulting plug volumes were determined as follows:

$$V_{liq} = L_{liq} A_{c.s.} - \tfrac{4}{3}\pi r^3 \quad \textbf{(2.1)}$$

$$V_{gas} = L_{gas} A_{c.s.} + \tfrac{4}{3}\pi r^3 \quad \textbf{(2.2)}$$

Taking the liquid flow rate as programmed into the syringe pump, Q_{liq}, the gas flow rate was calculated as follows:

$$Q_{gas} = Q_{liq} \frac{V_{gas}}{V_{liq}} \quad \textbf{(2.3)}$$

The total flow rate is given by the sum of the component flow rates:

$$Q_{total} = Q_{liq} + Q_{gas} \quad \textbf{(2.4)}$$

In multiphase microfluidic reactors the presence of the interface results in high shear regions in the liquid phase. As described previously,[25] the highest shear occurs in the corners where the bubble cap meets the film, approximately at the lines delineating L_{liq} in Scheme 2.1. In reality the high shear stress region has a complex three dimensional structure on each side of the bubble, however, these regions are similar from bubble to bubble, and the number of these high shear regions is directly proportional to the number of bubbles in the system. The measure of the number of high shear 'hot spots' was thus taken to be equivalent to the number of gas bubbles in the system and calculated as follows:

$$N_{hotspot} = \frac{L_{reactor}}{L_{liq} + L_{gas}} \quad \textbf{(2.5)}$$

Table 2.1. A listing of flow parameters for gas-liquid segmented microfluidic reactor experiments described in the text.

Case	L_{liq} (μm) x 10^{-2}	L_{gas} (μm) x 10^{-2}	Q_{gas} (μL/min)	Q_{liq}[a] (μL/min)	Q_{gas}/Q_{liq}	Q_{total} (μL/min)	$N_{hotspot}$
Figure 3A, 3D	N/A	N/A	0	4.8	0	4.8	N/A
Figure 3B, 3E	6.3	4.1	2.0	2.4	0.8	4.4	1430
Figure 3C, 3F	4.1	5.1	2.0	1.2	1.6	3.2	1600
Figure 5A, 5D	4.1	5.1	1.9	1.2	1.6	3.1	1600
Figure 5B, 5E	2.4	2.6	10.6	6.0	1.8	16.6	2920
Figure 5C, 5F	2.6	2.7	19.6	12.0	1.6	31.6	2800
Figure 6A, 6D	3.3	3.7	1.9	1.2	1.6	3.1	2100
Figure 6B, 6E	2.8	4.3	13.1	6.0	2.2	19.1	2060
Figure 6C, 6F	2.8	4.6	28.9	12.0	2.4	40.9	2020

[a] The liquid flow rate is assumed to be same as the input at the syringe pump.

2.3. Results and Discussion

2.3.1. Gas-Liquid Segmented Microfluidic Strategy for QDCM Self-Assembly

The QDCM self-assembly and gas-liquid segmented microfluidic reactor strategy are depicted in Figure 2.1. A stream of DMF solution containing the self-assembly constituents (PS-CdS and PS-*b*-PAA) are combined with a DMF separator stream and a DMF/water stream. The co-laminar streams are then joined with argon gas at the injector. The introduction of argon gas serves to compartmentalize the co-laminar flow of reactants into liquid plugs, which enables fast mixing of reactants in the sinusoidal channel similar to previous microfluidic reactors.[32, 33] The reactor has a set channel depth of 150 μm, and it consists of a sinusoidal mixing channel 100 μm wide and 100 mm in length, and a post formation channel 200 μm wide and 740 mm in length. The particles exiting the post-formation channel were quenched kinetically by connecting the outlet with Teflon tubing (7 cm long, 1/16th inch OD) to a vial containing ~250 μL deionized water. Particle size analysis was done off-chip using transmission electron microscopy. In all experiments described in here, the inlet polymer solution consisted of a 50/50 (w/w) mixture of PS-CdS and PS(665)-*b*-PAA(68) dissolved in DMF to a concentration of 1 wt%; this resulted in a steady-state polymer concentration in the reactor of 0.33 wt% when the three liquid streams were combined at equal flow rate. A fluorescence image of part of the reactor in operation is shown inset in Figure 2.1B, where the observed fluorescence is that of the QDs. In that case the total flow rate and gas-to-liquid ratio were Q = 3.2 μL/min and 1.6 respectively, and the steady-state water content was 2 wt%.

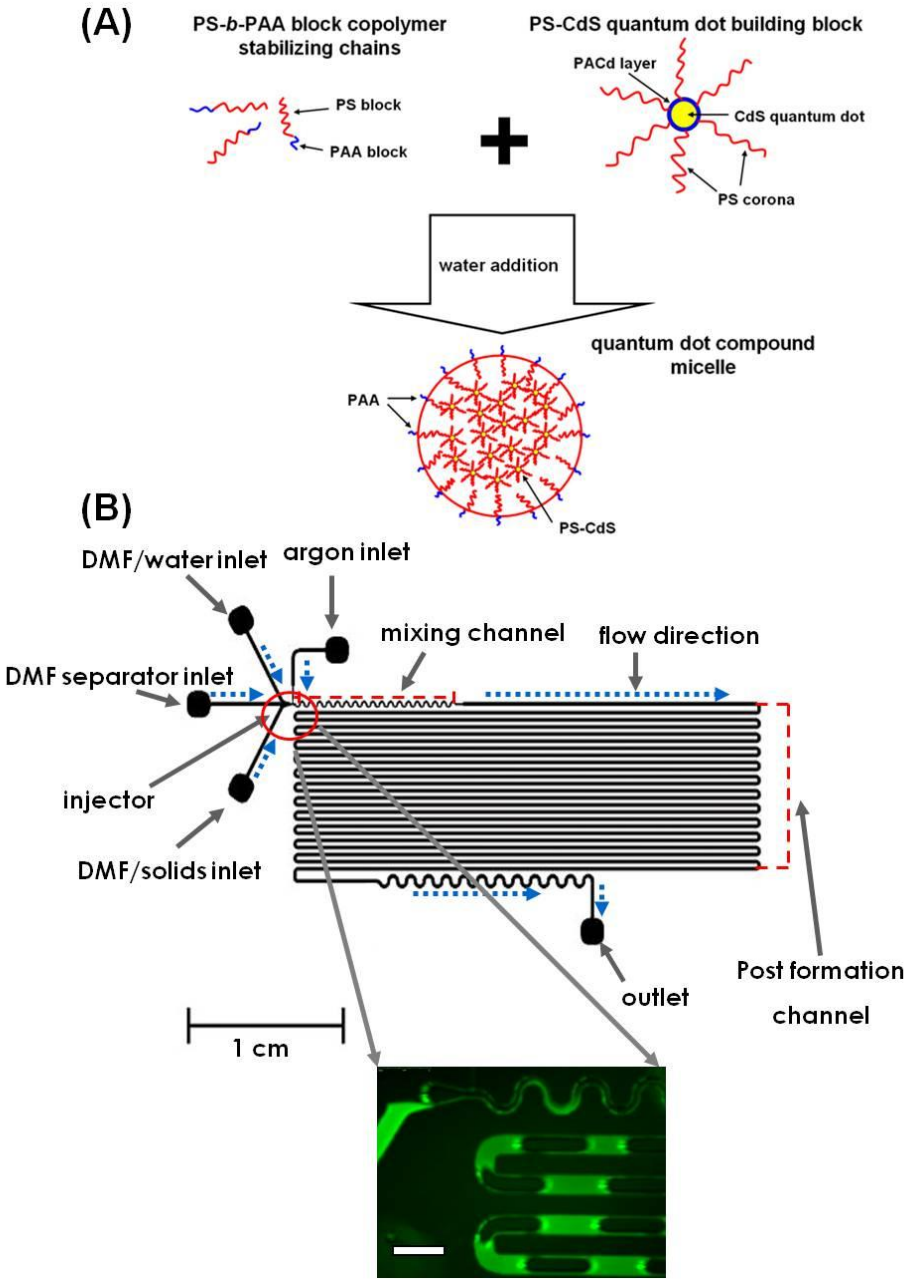

Figure 2.1. QDCM assembly process and multiphase microfluidic reactor approach. (A) Schematic of the QDCM assembly process. Red indicates hydrophobic blocks, while blue indicates hydrophilic blocks. (B) Schematic of the microfluidic reactor. The solid constituents and water-containing streams are combined with a separator solvent stream prior to injection of the argon gas bubbles, which compartmentalizes the liquid and facilitates rapid mixing and shearing of reactants and products. The inset of (B) shows a select fluorescence microscopy image of the reactor inlet. The white scale bar indicates 500 μm.

2.3.2. Tuning QDCM Mean Size via On-Chip Flow Parameters

Figure 2.2 shows representative TEM images of QDCMs prepared in the gas-liquid segmented reactor at a steady-state water concentration of 2 wt%, highlighting particle tunablity via different flow conditions. Figure 2.2A corresponds to the low flow rate case of Q = 3.1 μL/min, with the higher flow rate case of Q = 31.6 μL/min shown in Figure 2.2B. For QDCMs prepared at Q = 3.1 μL/min, the mean QDCM diameter is 76 nm with a relative standard deviation of SD = 12%, while for QDCMs prepared at Q = 31.6 μL/min the mean QDCM diameter is 42 nm with a relative standard deviation of SD = 15%. These results support a shear-induced particle break-up mechanism in which shear forces increase with flow rate. This is consistent with our previous study of QDCM formation in gas-liquid segmented flow reactors, in which we identified the ability to tune particle size via shear forces. The inset in Figure 2.2A shows a high magnification image of the same QDCM population without Pt/Pd shadowing prior to imaging, allowing the internal structure of QDCM to be visualized. As can be seen from the image, well-dispersed CdS QDs (dark dots) are distributed within the dark grey PS matrix. We note that the actual distances between self-assembled CdS QDs in three dimensions cannot be determined from this image, since TEM of a spherical ~80 nm QDCM will result in a projection through several layers of constituent PS-CdS particles. However, this inter-QD distance should be on the order of the diameter of a single PS-CdS nanoparticle in the bulk state. This dimension is estimated to be ~18 nm, using the molecular weight of PS-CdS determined from light scattering and assuming a density of bulk PS ~1 mg/mL.[27]

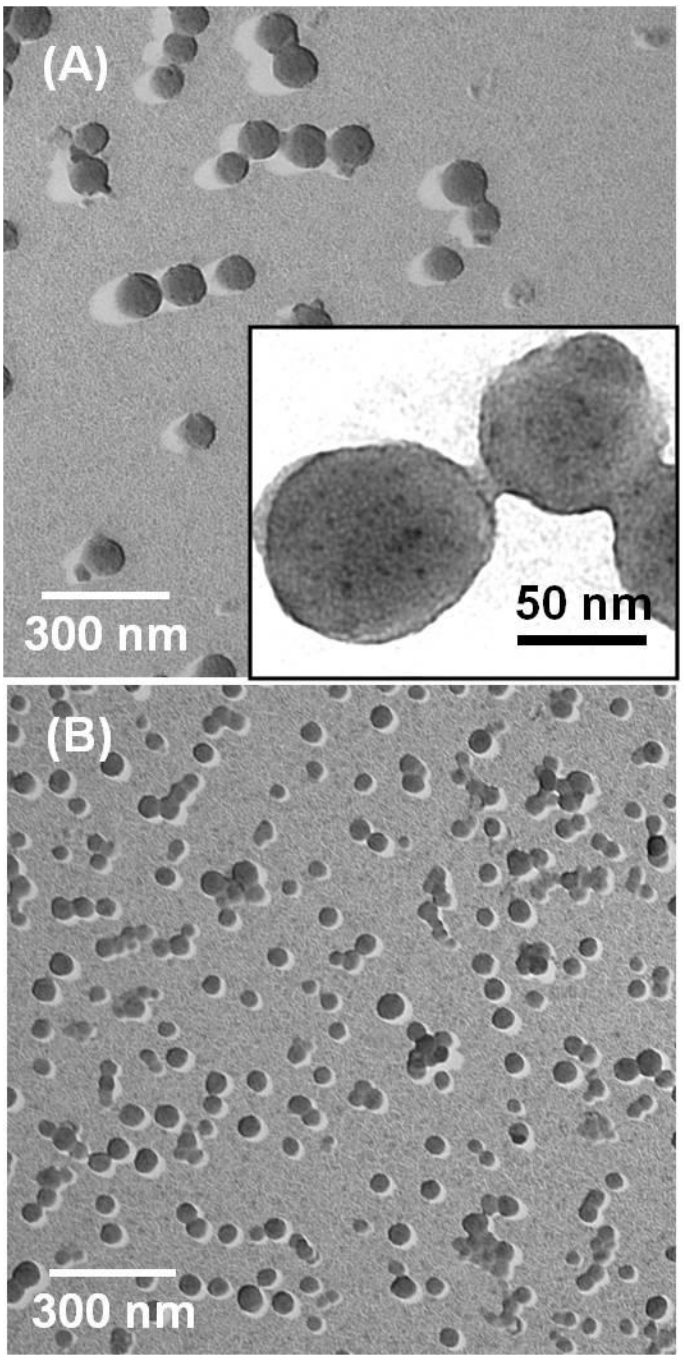

Figure 2.2. Representative TEM images of QDCMs prepared in a gas-liquid segmented reactor at a steady-state water concentration of 2 wt% and flow rates of Q = 3.1 μL/min (A) and Q = 31.6 μL/min (B), respectively. The particles in both images have been shadowed with Pt/Pd alloy prior to imaging. The inset in (A) shows QDCMs without shadowing, revealing the internal QDCM structure consisting of multiple QDs (dark dots).

The effect of varying the gas-to-liquid ratio at a given nominal flow rate (2 wt% steady-state water concentration) is shown in Figure 2.3. The limiting case of no gas is the single-phase reactor shown in Figure 2.3A. Figure 2.3B and 2.3C show gas-liquid segmentation resulting from increasing the gas-to-liquid ratio and demonstrating compartmentalization of reagents into liquid plugs. The uniformity of the plug size and spacing throughout the gas-liquid segmented reactors indicates stable flow conditions. In the single-phase reactor (Figure 2.3A), mixing is limited to cross-stream diffusion, similar to our previous work on single-phase reactors.[24] Figure 2.3D shows the QDCM size distribution from TEM analysis obtained for the limiting case of no gas corresponding to Figure 2.3A. As shown, the mean QDCM size was 54 nm with *SD* = 42%; it is also apparent from the size distribution that there is an additional small fraction of significantly larger particles. This size heterogeneity is characteristic of single-phase reactors, and can be attributed to a large residence time distribution in the no-gas case.[32, 33] Figure 2.3E and F show the QDCM size distributions corresponding to the gas-liquid segmented reactors in Figure 2.3B and 2.3C. Comparing Figure 2.3D and 2.3E, it is apparent that introducing gas to the system significantly increases the mean QDCM size from 54 nm to 137 nm, narrows the relative standard deviation, and results in a more normal distribution shape. These differences can be attributed to the effects of gas-liquid segmentation, which increases mixing due to circulating flow within the liquid plugs and narrows the residence time distribution through compartmentalization. Increased mixing increases the rate of particle collisions and hence the rate of coalescence, resulting in larger particles. The result of further increasing the gas-to-liquid ratio (from 0.8 to 1.6) is shown in Figures 2.3E and 2.3F. The mean particle size

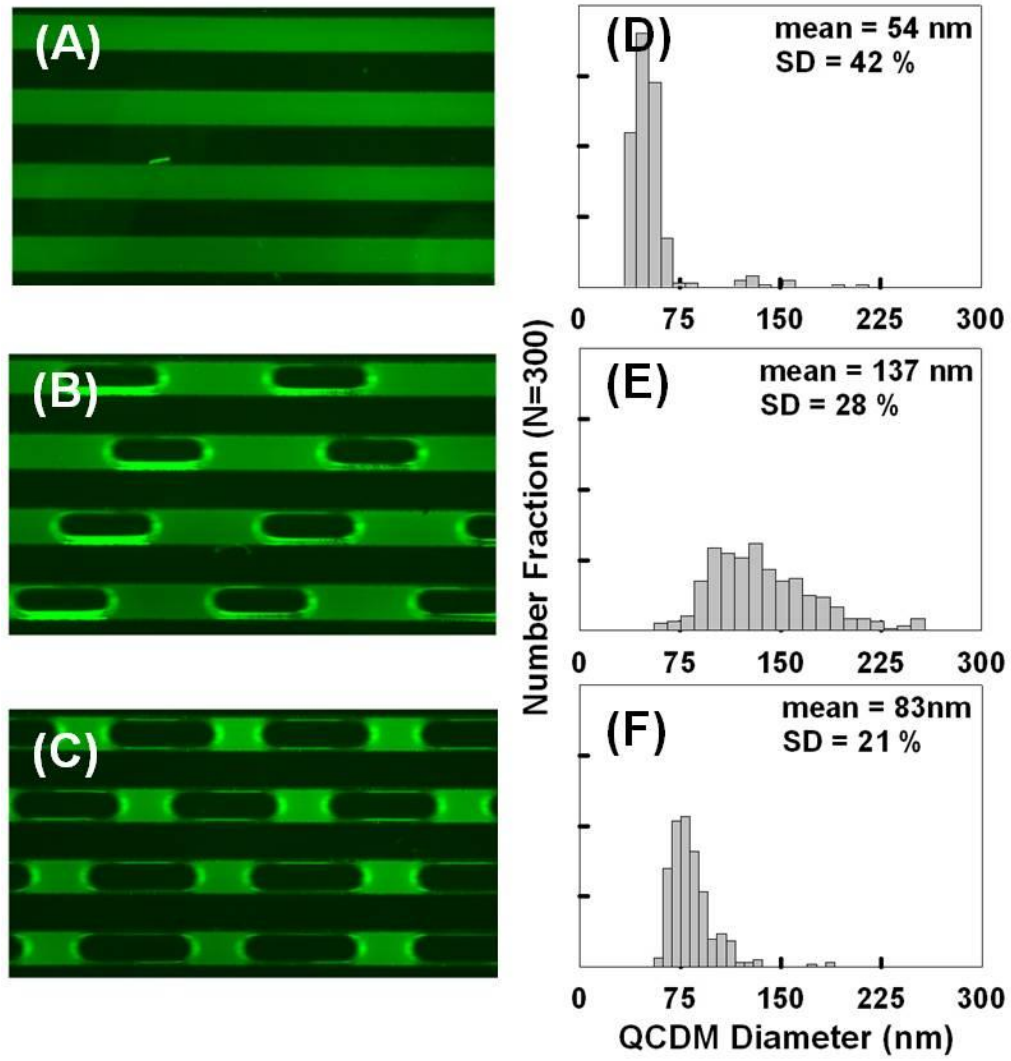

Figure 2.3. Effect of gas-to-liquid ratio at a steady-state water content of 2 wt%. (A), (B) and (C) are selected fluorescence images at three different gas-to-liquid ratios: Q_{gas}/Q_{liquid} = 0, 0.8, and 1.6 respectively, with corresponding size distributions shown in (D), (E), and (F). The calculated total flow rate for the three different gas-to-liquid ratios in (A), (B) and (C) are Q_{total} = 4.8, 4.4, and 3.2 μL/min, respectively.

decreased significantly from 137 nm to 83 nm, and the relative standard deviation further decreased. This reduction in particle size with increased gas flow is in contrast with the increase in particle size observed with the initial introduction of gas. We attribute the decrease in particle size from Figure 2.3E to 2.3F to shear-induced particle breakup within the two-phase reactors.

The conditions for shear-induced particle breakup in two-phase reactors can be defined by the capillary number *Ca*, which is describes the balance of viscous to interfacial forces for dispersed liquid droplets under shear.[25] Our previous calculations have shown that the high shear required for particle breakup is localized in the corners of the liquid plugs (which we referred to as "hot spots"),[25] whereas coalescence is expected to be operative throughout the liquid plugs. The hot spots, or high shear stress regions, have a complex three dimensional structure on each side of the bubble; however, these regions are similar from bubble to bubble, and the number of these high-shear regions is directly proportional to the number of bubbles in the system. Thus, the number of bubbles in the system was taken as the measure to quantify the number of high-shear hot spots. A**s** the gas-to-liquid ratio is increased (Figure 2.3B to 2.3C), a decrease in liquid plug size and an increase in the number of liquid plugs was observed. This results in a greater number of hot spots in the reactor. We propose that the increase in the number of hot spots increases the rate of particle breakup relative to the rate of coalescence, such that particle breakup becomes dominant as the gas flow rate is increased (Figure 2.3E and 2.3F).

In Figure 2.4, we present the data in Figure 2.3, along with two additional data points, as a plot of mean particle size vs. gas-to-liquid flow ratio for a constant nominal total flow rate and steady-state water concentration of 2 wt%. The observed trend shows particle size increasing, going through a maximum, and then decreasing as the gas-to-liquid ratio increases, which highlights the proposed competition between coalescence-driven growth and shear-induced particle breakup within the two-phase reactors. In the first part of the plot ($Q_{gas}/Q_{liquid} \approx$ 0-0.8), the observed increase in particle size suggests that particle growth is dominant in this regime ("growth regime"), with increased gas flow rate effecting increased mixing and coalescence within the liquid plugs. However, as the gas flow rate and the number of hot spots continues to increase, the relative effect of particle breakup becomes more important, eventually dominating over the effect of coalescence-driven growth. As a result, we see the particle size going through a maximum at $Q_{gas}/Q_{liquid} \approx 0.8$ under the present conditions of total flow rate and water concentration, and then decreasing in the second part of the plot ($Q_{gas}/Q_{liquid} > 0.8$, "breakup regime").

We note that the gas-segmented reactor has benefits such as increased mixing and reduced residence time distributions; however, the introduction of gas to the system results in some operational challenges. Specifically, the compressibility of the gas and the high gas/liquid interfacial tension gives rise to discrepancies between the actual flow rate and the nominal flow rate programmed with syringe pumps.[34] In light of these effects, we calculate and report the actual flow rates which are the sums of the liquid flow rates, as applied with the syringe pump, and the gas flow rates as determined from the fluorescence image data. A listing of component flow rates for each run is given in

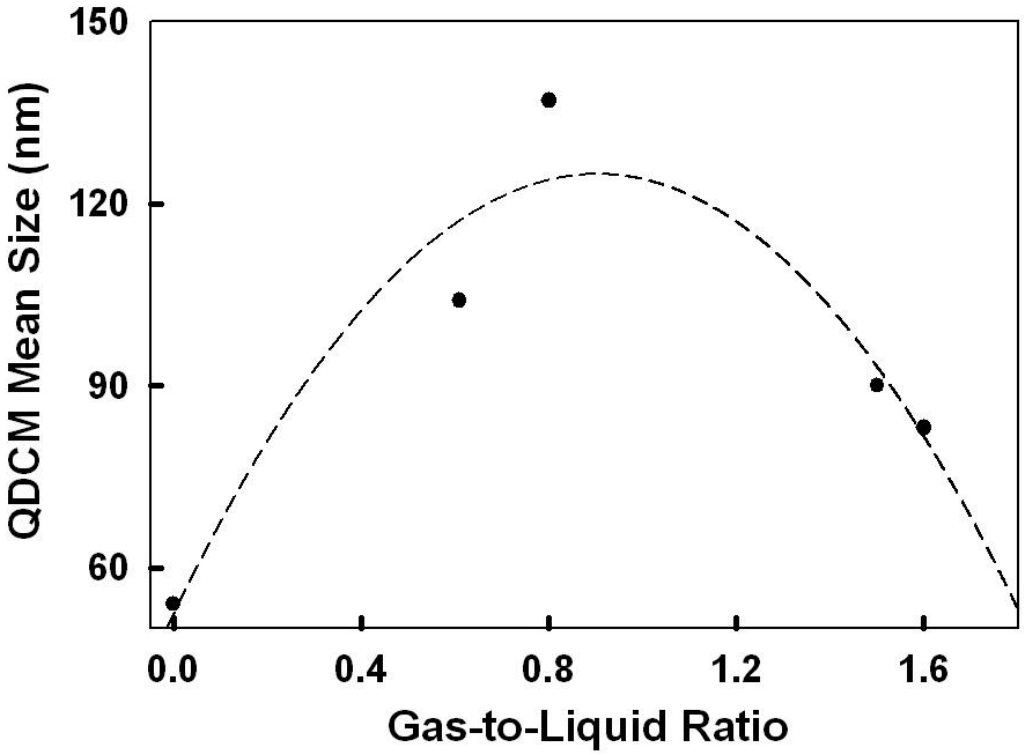

Figure 2.4. Plot of mean QDCM particle diameter versus gas-to-liquid ratio at a steady-state water content of 2 wt%. For the ratios Q_{gas}/Q_{liquid} = 0, 0.6, 0.8, 1.5 and 1.6 respectively, the calculated total flow rates are Q_{total} = 4.8, 3.9, 4.4, 4.5, and 3.2 μL/min, respectively. The dashed line represents a quadratic fit to the data, and is intended as a guide for the dye.

Table 2.1.[35] Also included in Table 2.1 are the average bubble lengths, plug lengths and the resulting number of high shear hot spots in each case. The number of hot spots scales with the number of liquid plugs, and increases, in general, with increasing gas-to-liquid flow ratio (e.g. Figure 2.3 series in Table 2.1). Calculation details for actual component and total flow rates, and number of hot spots, are provided in the experimental section.

Figure 2.5 shows the two-phase reactor in operation at 2 wt% steady-state water content and at varying total flow rate (Q_{total} = 3.1 μL/min to 31.6 μL/min). The goal was to investigate the effect of flow rate at a relatively constant gas-to-liquid ratio, although due to the aforementioned challenges the gas-to-liquid ratio varied somewhat (Q_{gas}/Q_{liq} = 1.6-1.8). We note that the experiment described in Figure 2.5A and 2.5D represents approximately the same experimental conditions as in Figure 2.3C and 2.3F, and the similar particle sizes demonstrate reproducibility. Fluorescence image data for each run are shown in Figure 2.5A-C. The images for Figure 2.5B and 2.5C are slightly blurred due to increased velocity and fixed exposure time (13 ms). In addition, there is a decrease in both the gas and liquid plug lengths (L_{gas} and L_{liquid}, Table 2.1) as the flow rate increases from 3.1 μL/min to 16.6 μL/min (Figure 2.5A-B), attributed to a decreased role of capillary pressure at higher flow rate and higher injector pressure. Corresponding particle size distributions are shown in Figure 2.5D-F. A significant decrease in the mean particle size is observed as the total flow rate increases. The initial decrease is most significant from 76 nm to 44 nm as the total flow rate increases from Q_{total} = 3.1 μL/min to 16.6 μL/min, with a more modest decrease to 42 nm with a further increase to Q_{total} = 31.6 μL/min. The overall trend is consistent with shear-induced particle break-up, since the maximum shear rate in the hot spots increases with flow rate.[25] However, we expect

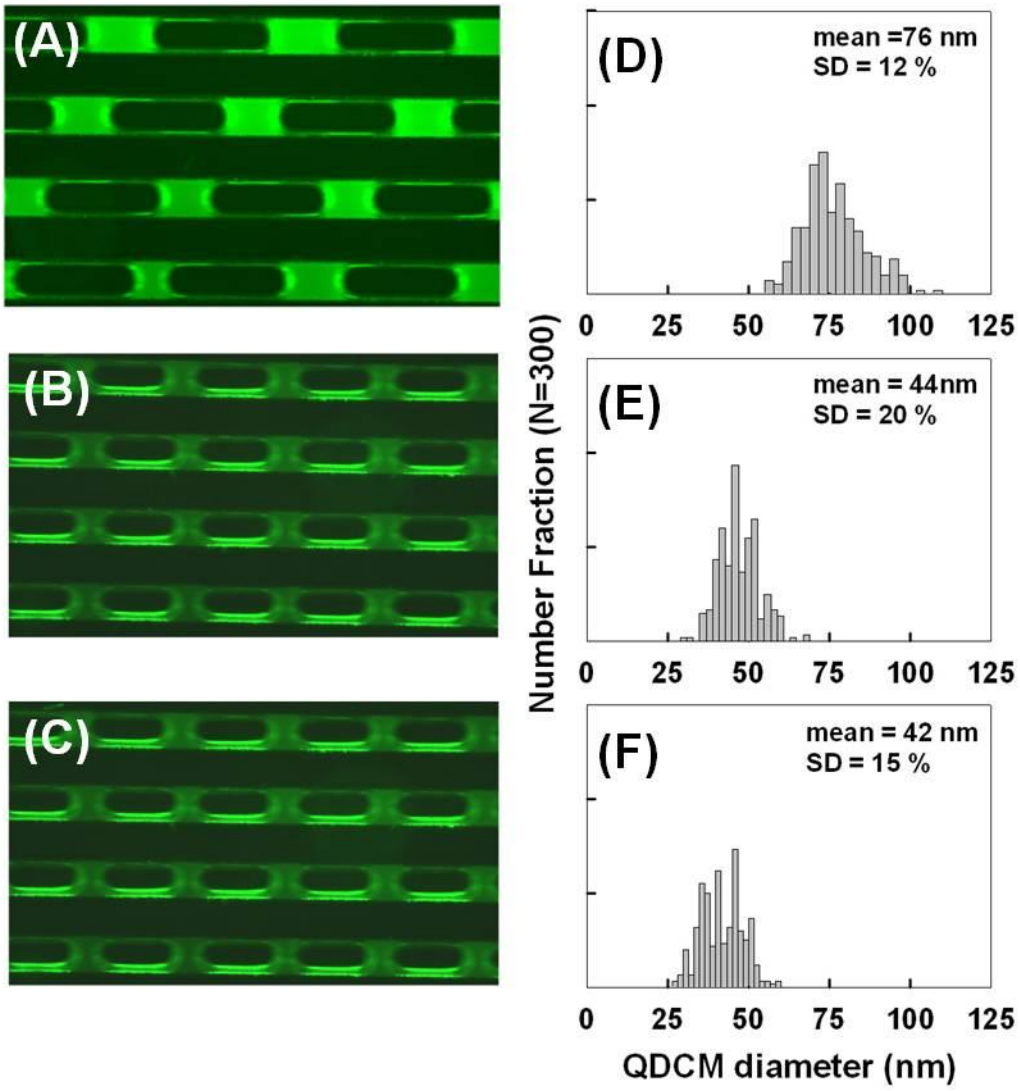

Figure 2.5. Effect of total flow rate at a steady-state water content of 2 wt%. (A), (B) and (C) are selected fluorescence images at three different total flow rates: Q_{total} = 3.1 16.6, and 31.6 μL/min, respectively, with corresponding size distributions shown in (D), (E), and (F). The calculated gas-to-liquid flow ratios for the three different total flow rates in (A), (B) and (C) are Q_{gas}/Q_{liquid} = 1.6, 1.8, and 1.6, respectively.

that the dramatic decrease in particle size during the initial increase in flow rate (Figure 2.5D-E) is a combination of increased maximum shear rate in the hot spots as well as an increase in the number of hot spots due to the decrease in liquid plug length (Figure 2.5A-B and Table 2.1).

In Figure 2.6, we show the effect of varying the flow rate (Q_{total} = 3.1 μL/min to 40.9 μL/min) for a higher steady-state water content (8 wt%). Water content is an important experimental handle on particle size in these systems, due to the combined effects of increased interfacial tension and decreased chain dynamics as the water content increases. Figure 2.6A-C show representative fluorescence images at each flow rate. In this case, the gas and liquid plug lengths remain relatively constant, resulting in a similar number of hot spots at each flow rate (Table 2.1). Corresponding particle size distributions are shown in Figure 2.6D-F. Similar to the 2 wt% water case, the mean particle size decreases with increasing flow rate. At low flow rate, we note the mean particle size (53 nm) is much smaller than in the 2 wt% case (76 nm). It is known that the steady-state water concentration will have a significant effect on chain dynamics within the polymer phase, due to differing extents of plasticization by the organic solvent.[28] In general, for a given particle collision frequency, a decreased rate of particle coalescence is expected at higher water contents. This is due to slower chain dynamics arising from a decreased degree of solvent swelling, such that fewer collisions result in coalescence. We propose that at low flow rate, the effect of shear-induced breakup is not strong, such that the particle size is dominated by the rate of coalescence, resulting in a smaller mean particle size at the higher water concentration. However, as the flow rate

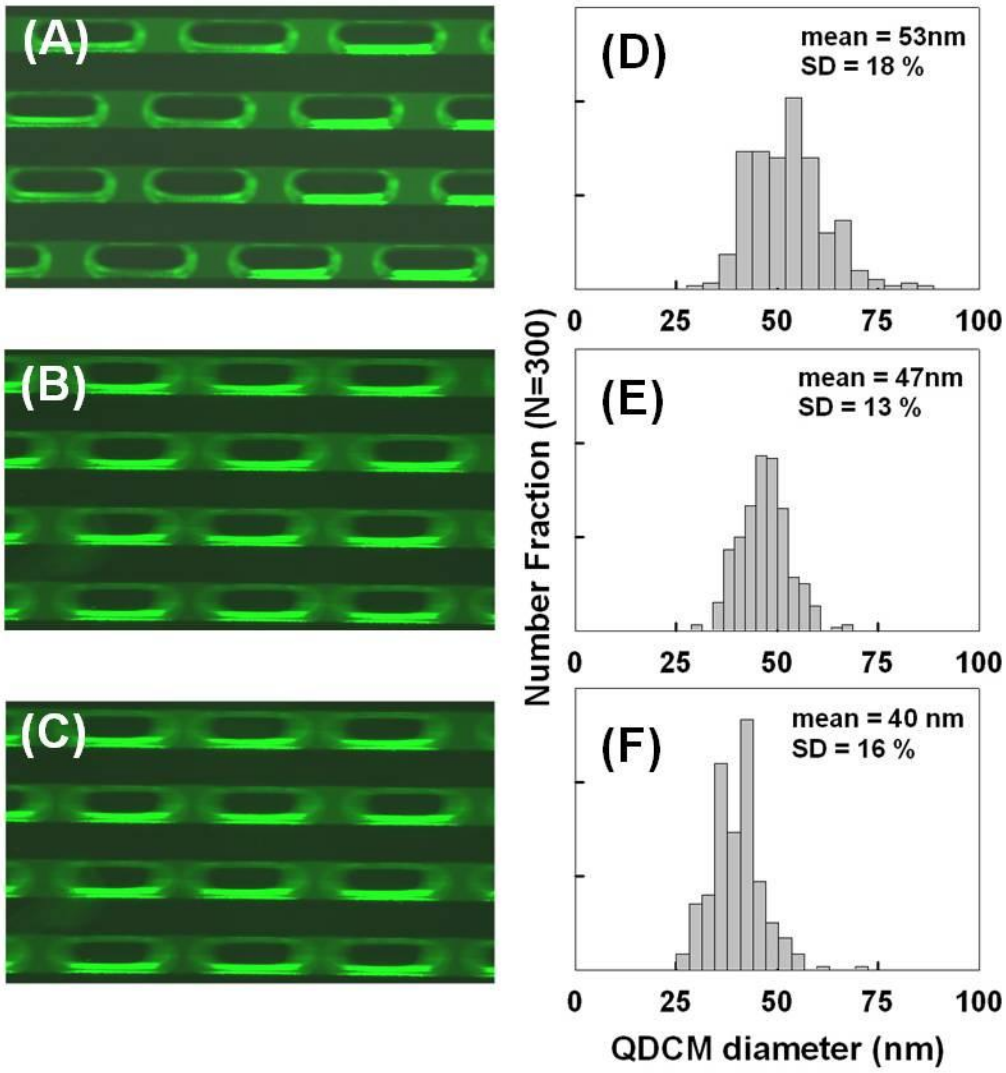

Figure 2.6. Effect of total flow rate at a steady-state water content of 8 wt%. (A), (B) and (C) are selected fluorescence images at three different total flow rates: Q_{total} = 3.1 19.1, and 40.9 μL/min, respectively, with corresponding size distributions shown in (D), (E), and (F). The calculated gas-to-liquid flow ratios for the three different total flow rates in (A), (B) and (C) are Q_{gas}/Q_{liquid} = 1.6, 2.2, and 2.4, respectively.

increases, particle breakup becomes more important relative to particle coalescence, such that the particle size decreases to a similar value (~40 nm) for both water contents.

2.3.3. Tuning QDCM Mean Size via Combined On-Chip Flow Parameters and Water Contents

Figure 2.7 provides a summary of QDCM particle size control achieved in the two-phase gas-liquid segmented reactor as a function of total flow rate and at different water contents. In addition to the 2 wt% and 8 wt% steady-state water concentrations discussed previously, the results from two intermediate water content series are plotted. We note that particle sizes at the lowest flow rate are dependent on the water content, with a general trend of increasing size with decreasing water content, ranging from 53 nm at 8 wt% to 76 nm at 2 wt%, consistent with the aforementioned effect of solvent swelling on the rate of coalescence. A marked exception to this trend is the 3 wt% case, which at the lowest flow rate exhibits a particle size of 53.7 nm, in between the values found at 4 and 8 wt%. We point out that water concentration will influence not only the kinetics, but also the thermodynamics, of particle growth, through its effect on the interfacial tension between solvent-swollen QDCMs and the surrounding mixed solvent. This interfacial tension has an estimated value of 2 dyn/cm at 4 wt% water,[25] and will increase as the water content increases. One possible explanation for the anomalous behavior at 3 wt% is that this case falls in a transition region between fast and slow coalescence kinetics compared to experimental time-scales, resulting in a thermodynamic contribution of interfacial tension that is large compared to the other water concentrations investigated.

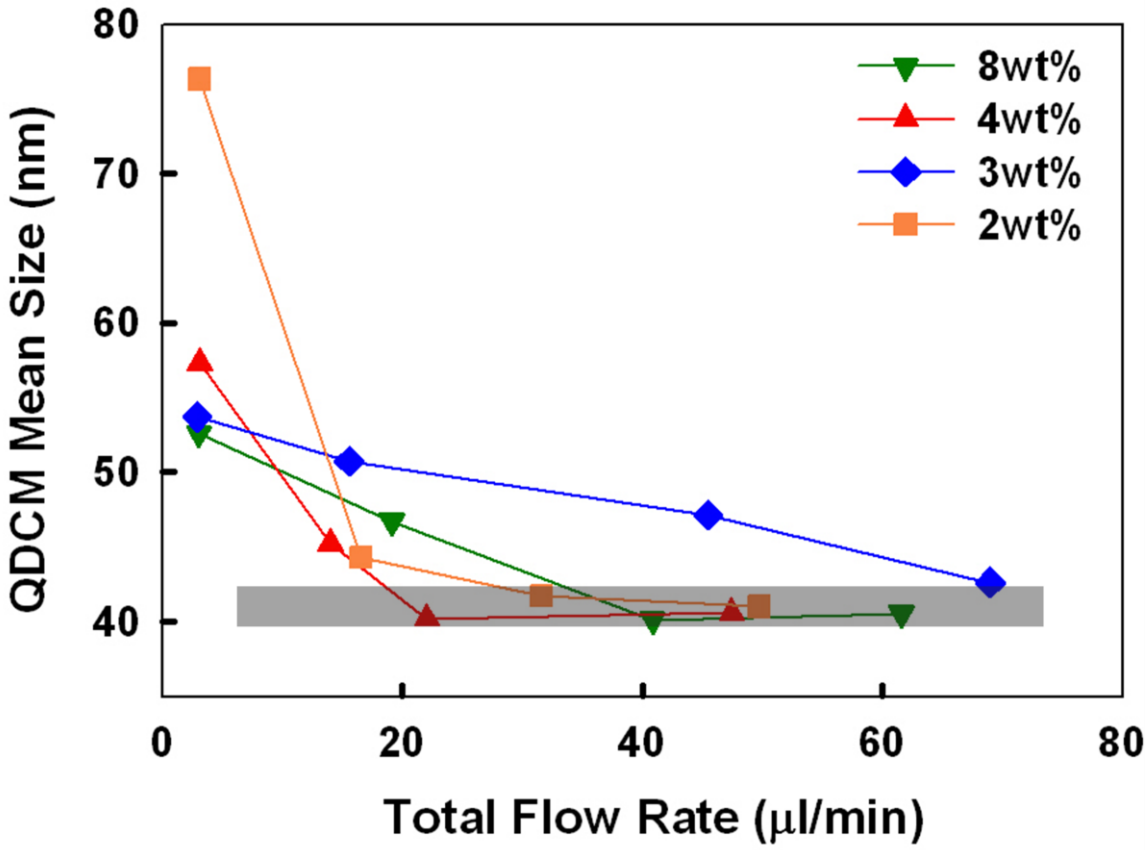

Figure 2.7. Influence of steady-state water content and total flow rate on the mean QDCM particle size. The grey shaded area represents the mean and standard deviation of minimum size obtained at different water contents (41 ± 1 nm).

All water concentration cases show a monotonic decrease with increasing total flow rate, approaching a common minimum size of 41 nm ± 1 nm, as indicated by the grey band. We note that for most water contents, particle sizes begin to level off in the region of the grey band as the flow rate increases to sufficiently high values. These trends suggest a common intrinsic minimum particle size, which we assign to the smallest thermodynamically-stable unit of a micelle of PS(665)-*b*-PAA(68) stabilizing chains with a single PS-CdS particle encapsulated in the PS core. The mean diameter of micelles formed from pure PS(665)-*b*-PAA(68) by water addition to DMF has been previously reported to be ~25 nm;[27] as well, the diameter of a single PS-CdS particle in the bulk state can be estimated at ~18 nm, as mentioned previously.[27] Considering that a single encapsulated PS-CdS particle should be localized in the center of the PS core, the sum of these two values, ~43 nm, gives a reasonable estimate of the size of the resulting smallest particle unit, in excellent agreement to the common minimum size in Figure 2.7. Therefore, for a given water content, the behavior of particle size as a function of increasing flow rate appears to be described by two distinct regions: 1) a steady decrease attributed to shear-induced particle breakup, followed by 2) a leveling off at a thermodynamically-determined minimum size.

Since the physical phenomena associated with these two regions are different, it is not useful to determine a single mathematical relationship over the entire range of flow rates. However, in order to quantify and compare the effect of flow rate on particle size for the various water concentration cases, we fit data points in the region of decreasing particle size, before the functions begin to level off at their common minimum value. The 3, 4, and 8 wt% cases provide sufficient data in this range, and could be described by the

general equation $D = C - AQ_{total}^{a}$ where D is particle diameter, C and A are constants, and a is a scaling exponent.[36] For all cases, the determined a values were found to be in the range of 0.90-0.96. This indicates that particle sizes show an initial approximately-linear decrease with increasing flow rate for all water contents, before leveling off in the neighborhood of the intrinsic minimum value. Considering that $a \approx 1$ in all cases, the constant A can be used to describe the rate of particle size decrease in response to flow rate; these values are A = 2.4, 0.27, 1.2, and 0.38 for the 2, 3, 4, and 8 wt% cases, respectively. With the exception of the 3 wt% case, which shows the smallest value, the other A values exhibit a monotonic decrease with increasing water concentration. This variability in the rate of size decrease in response to flow rate is attributed to the difference between water contents with respect to the number of hot spots and with respect to physical parameters such as interfacial tension and chain dynamics, all of which will influence the particle size. The data in Figure 2.7 therefore demonstrate the general utility of particle processing in gas-liquid segmented reactors, which provides a tunable shear-induced particle breakup mechanism that dominates over other thermodynamic and kinetic parameters at sufficiently high flow rate.

2.4. Conclusions

We have used a two-phase gas-liquid segmented microfluidic reactor system to control the self-assembly of polystyrene-coated quantum dots (PS-CdS) and a stabilizing PS-*b*-PAA block copolymer into quantum dot compound micelles (QDCMs) by varying various chemical and flow parameters. Mixing of water with polymeric constituents is greatly enhanced due to chaotic advection in the liquid plugs as they travel through the sinusoidal mixing channel. In addition, circulating flow within the liquid plugs provides two convenient handles for size control following initial self-assembly: shear-induced particle breakup, due to high shear in the corners of the plugs (hot spots), and collision-induced particle coalescence. The resulting particle size is a balance of the relative rates of these processes under a specific set of experimental conditions. Specifically, we studied the effects of the steady-state water concentration, the gas-to-liquid flow ratio, and the total flow rate. By changing these self-assembly conditions, the mean particle size was tuned in the range of 40 nm to 137 nm. In addition, we observed a common intrinsic minimum size of 41 nm ± 1 nm with increasing total flow rate at all steady-state water contents, which is attributed to the smallest thermodynamically-stable unit formed from the self-assembling constituents. The appearance of this common minimum size at all water contents clearly indicates the dominance of the particle breakup mechanism at high flow rates. These results point to new microfluidic strategies for the self-assembly of block copolymers and other colloids in which bottom-up intermolecular forces are coupled with top-down mixing and shear forces for improved structural control.

2.5. References

1. Wang, C. W.; Oskooei, A.; Sinton, D.; Moffitt, M. G., *Langmuir* **2010,** *26* (2), 716-723.

2. Caruso, F., *Adv Mater* **2001,** *13* (1), 11-22.

3. Faul, C. F. J.; Antonietti, M., *Adv Mater* **2003,** *15* (9), 673-683.

4. Kim, B. S.; Qiu, J. M.; Wang, J. P.; Taton, T. A., *Nano Lett.* **2005,** *5* (10), 1987-1991.

5. Lin, Y.; Skaff, H.; Emrick, T.; Dinsmore, A. D.; Russell, T. P., *Science* **2003,** *299* (5604), 226-229.

6. Murray, C. B.; Kagan, C. R.; Bawendi, M. G., *Annu Rev Mater Sci* **2000,** *30*, 545-610.

7. Pileni, M. P., *J. Phys. Chem. B* **2001,** *105* (17), 3358-3371.

8. Shenhar, R.; Norsten, T. B.; Rotello, V. M., *Adv Mater* **2005,** *17* (6), 657-669.

9. Tang, Z. Y.; Kotov, N. A., *Adv Mater* **2005,** *17* (8), 951-962.

10. Alivisatos, A. P., *Science* **1996,** *271* (5251), 933-937.

11. Boal, A. K.; Ilhan, F.; DeRouchey, J. E.; Thurn-Albrecht, T.; Russell, T. P.; Rotello, V. M., *Nature* **2000,** *404* (6779), 746-748.

12. Nie, Z. H.; Li, W.; Seo, M.; Xu, S. Q.; Kumacheva, E., *J. Am. Chem. Soc.* **2006,** *128* (29), 9408-9412.

13. Seo, M.; Nie, Z. H.; Xu, S. Q.; Mok, M.; Lewis, P. C.; Graham, R.; Kumacheva, E., *Langmuir* **2005,** *21* (25), 11614-11622.

14. Karnik, R.; Gu, F.; Basto, P.; Cannizzaro, C.; Dean, L.; Kyei-Manu, W.; Langer, R.; Farokhzad, O. C., *Nano Lett.* **2008,** *8* (9), 2906-2912.

15. Chan, E. M.; Alivisatos, A. P.; Mathies, R. A., *J. Am. Chem. Soc.* **2005,** *127* (40), 13854-13861.

16. Chan, E. M.; Mathies, R. A.; Alivisatos, A. P., *Nano Lett.* **2003,** *3* (2), 199-201.

17. Cottam, B. F.; Krishnadasan, S.; deMello, A. J.; deMello, J. C.; Shaffer, M. S. P., *Lab Chip* **2007,** *7* (2), 167-169.

18. Krishnadasan, S.; Tovilla, J.; Vilar, R.; deMello, A. J.; deMello, J. C., *J. Mater. Chem.* **2004,** *14* (17), 2655-2660.

19. Yang, H. W.; Luan, W. L.; Tu, S. T.; Wang, Z. M. M., *Lab Chip* **2008,** *8* (3), 451-455.

20. Yen, B. K. H.; Gunther, A.; Schmidt, M. A.; Jensen, K. F.; Bawendi, M. G., *Angew Chem Int Edit* **2005,** *44* (34), 5447-5451.

21. Steinbacher, J. L.; Moy, R. W. Y.; Price, K. E.; Cummings, M. A.; Roychowdhury, C.; Buffy, J. J.; Olbricht, W. L.; Haaf, M.; McQuade, D. T., *J. Am. Chem. Soc.* **2006,** *128* (29), 9442-9447.

22. Malmstadt, N.; Nash, M. A.; Purnell, R. F.; Schmidt, J. J., *Nano Lett.* **2006,** *6* (9), 1961-1965.

23. Jahn, A.; Vreeland, W. N.; Gaitan, M.; Locascio, L. E., *J. Am. Chem. Soc.* **2004,** *126* (9), 2674-2675.

24. Schabas, G.; Yusuf, H.; Moffitt, M. G.; Sinton, D., *Langmuir* **2008,** *24* (3), 637-643.

25. Schabas, G.; Wang, C. W.; Oskooei, A.; Yusuf, H.; Moffitt, M. G.; Sinton, D., *Langmuir* **2008,** *24* (19), 10596-10603.

26. Moffitt, M.; Vali, H.; Eisenberg, A., *Chem. Mater.* **1998,** *10* (4), 1021-1028.

27. Yusuf, H.; Kim, W. G.; Lee, D. H.; Guo, Y. Y.; Moffitt, M. G., *Langmuir* **2007,** *23* (2), 868-878.

28. Zhang, L. F.; Shen, H. W.; Eisenberg, A., *Macromolecules* **1997,** *30* (4), 1001-1011.

29. Yu, Y. S.; Zhang, L. F.; Eisenberg, A., *Macromolecules* **1998,** *31* (4), 1144-1154.

30. Yusuf, H.; Kim, W. G.; Lee, D. H.; Aloshyna, M.; Brolo, A. G.; Moffitt, M. G., *Langmuir* **2007,** *23* (10), 5251-5254.

31. Zhang, L. F.; Eisenberg, A., *J. Am. Chem. Soc.* **1996,** *118* (13), 3168-3181.

32. Song, H.; Tice, J. D.; Ismagilov, R. F., *Angew Chem Int Edit* **2003,** *42* (7), 768-772.

33. Gunther, A.; Jensen, K. F., *Lab Chip* **2006,** *6* (12), 1487-1503.

34. In general, the gas flow rates are less than the applied flow rates due to a combination of capillary pressure and compressibility. The discrepancy between nominal and actual gas flow rates decreases with increasing total flow rate as the capillary pressure at the injector becomes smaller relative to the local pressure.

35. In the case of Figure 3B and 3C, although the programmed nominal total flow rate was held constant as the gas-to-liquid flow ratio was increased, Table 2.1 shows that the actual total flow rate decreased. However, the observed decrease in particle size (Figure 3E to 3F) cannot be attributed to the incidental flow rate decrease, since the dominant effect of decreasing flow rate is an increase in particle size due to a decrease in shear-induced particle breakup (as described in reference 24).

36. We note that the constant C, which is the theoretical particle size in the limit of $Q_{total} = 0$, has no physical significance, since QDCMs in the absence of flow should grow continuously over time.

CHAPTER 3

FLOW-DIRECTED BLOCK COPOLYMER MICELLE MORPHOLOGIES VIA MICROFLUIDIC SELF-ASSEMBLY

3.1.Introduction

The solution self-assembly of amphiphilic block copolymers into colloidal nanostructures, termed block copolymer micelles, has spurred extensive fundamental and applied research in recent years.[2-21] Of particular interest is the plethora of diverse micelle morphologies, including spheres, cylinders and vesicles, that can spontaneously form in such systems, as a result of the exquisite and complex interplay of thermodynamic forces. A central focus of work in this area has been the understanding and control of these varied morphologies, since the size and shape of micellar structures will profoundly influence their effectiveness for specific applications, including drug delivery,[22, 23] sensing,[24] and medical imaging.[25-27] Under equilibrium conditions, the morphologies of block copolymer micelles are governed by a fine balance of interfacial tension, chain stretching within the micelle core, and repulsion among solubilized coronal chains.[2, 3, 6, 8, 9, 11] However, along with such thermodynamic factors, kinetic effects arising from a combination of slow chain dynamics and high interfacial tension can also contribute significantly to the products of self-assembly, often leading to structurally-complex and kinetically-stable morphologies that are not globally equilibrated.[6, 11, 14, 15]

Conventional experimental control of block copolymer morphologies involves variation in chemical parameters which are known to directly influence intermolecular interactions (e.g. block copolymer composition,[2, 3] choice of solvent,[9] polymer concentration,[12] pH and ionic strength[5]). In contrast to this bottom-up approach, the top-

down control of block copolymer morphologies through templates or external force fields (e.g. shear, magnetic and electric fields) opens the door to engineering micellar structures under a given set of chemical conditions by "dialing in" specific processing parameters. Although such directed assembly has been widely applied in block copolymer thin films using chemically- and topologically-defined patterned substrates,[28-33] there are very few examples of top-down morphological control in block copolymer colloids.[34, 35] In one example, Wu and coworkers extruded a block copolymer colloid through a nanoporous template to induce a sphere-to-cylinder micelle transition, with the resulting cylinders reverting back to spheres upon standing for several hours.[34] More recently, work from the Winnik group reported that block copolymer spherical micelles decorated with CdSe quantum dots could be converted to a wormlike network by rapid magnetic stirring, whereas similar stirring conditions yielded only spheres in the absence of quantum dots.[35]

Microfluidic reactors have been studied as environments for the self-assembly of polymers[36-44] and other molecular building blocks,[45-47] since the associated nanoscale volumes and laminar flow enable fine tuning of local concentrations of reagents, mixing rates, and shear forces. We recently applied a gas-liquid multiphase microfluidic reactor, in which compartmentalized liquid plugs are segmented by a regular stream of gas bubbles, in order to form spherical colloidal aggregates of polymer-coated quantum dots.[42, 43] In that work, we demonstrated that flow-variable high shear regions in the corners of the liquid plugs strongly influenced particle sizes via competing mechanisms of coalescence and particle break-up.[43] In this chapter, we demonstrate that the solution self-assembly of amphiphilic block copolymers in a similar multiphase reactor leads to flow-variable micelle morphologies that are different from equilibrium structures

produced by off-chip self-assembly under identical chemical conditions. The resulting shear-induced nanostructures are kinetically controlled by the on-chip flow environment, but are stabilized by kinetic trapping after transfer from the reactor into aqueous environments. This approach provides a convenient top-down handle on block copolymer morphologies through variation of microfluidic flow parameters, enabling facile processing control of colloidal nanostructures.

3.2. Experimental Section

3.2.1. Materials

The polystyrene-*block*-poly(acrylic acid) sample used in this study, PS(665)-*b*-PAA(68), was synthesized via anionic polymerization of the associated polystyrene-*block*-poly(*tert*-butyl acrylate) block copolymer, followed by hydrolysis of the ester block; numbers in parentheses refer to number-average degrees of polymerization of each block.[48, 49] Dimethylformamide (DMF) (Aldrich, 99.9+%, HPLC grade, $H_20 < 0.03\%$) and 1,4-dioxane Aldrich, 99.0%, reagent grade, $H_20 < 0.05\%$ were used as received without further purification.

3.2.2. Critical Water Content Determination

In order to accurately determine the critical water content (cwc) of PS(665)-*b*-PAA(68) for the polymer concentration and solvent mixture applied in this study, static light scattering measurements were carried out. Light scattering experiments were performed on a Brookhaven Instruments photon correlation spectrometer equipped with a BI-200SM goniometer, a BI-9000AT digital autocorrelator, and a Melles Griot He-Ne

Laser (632.8 nm) with a maximum power output of 75 mW. First, a stock solution was prepared by adding 75/25 (w/w) DMF/dioxane solvent mixture to a copolymer concentration of 0.66 wt %. The stock solution was then filtered through a Teflon syringe membrane filter with a nominal pore size of 0.45 μm (National Scientific Company) into pre-cleaned scintillation vials. Next, the stock solution was diluted with 75/25 (w/w) DMF/dioxane solvent mixture filtered through two Teflon syringe filters with nominal pore size of 0.20 μm (National Scientific Company) connected in series to give a polymer concentration of 0.33 wt %. Deionized water was next added dropwise to ~6 g of the solution in successive 0.02 - 0.05 g quantities via a microsyringe equipped with a membrane filter (Life Sciences) with nominal pore size of 0.20 μm. After each addition of water, the solution was agitated with a vortexer to aid mixing. The scattered light intensity was recorded 15 min after vortexing to allow the solution to equilibrate. All measurements were carried out at a scattering angle of 90^{o} and a temperature of 23 ^{o}C. The cwc thus obtained (Figure 3.2) was 3.2 ± 0.1 wt %.

3.2.3. Off-Chip Micelle Preparation

Morphologies formed on-chip under different chemical and flow conditions were compared to off-chip control experiments in which block copolymer micelles were prepared in the following manner. To three vials, each containing ~5 mL of 0.33 wt % PS(665)-*b*-PAA(68) in 75/25 (w/w) DMF/dioxane, deionized water was added dropwise at a rate of 20 μL every 10 s with moderate magnetic stirring (600 rpm) until the various target water concentrations were reached (4.2, 5.2 and 7.2 wt %). The resulting micelles were then allowed to equilibrate for 2 weeks without stirring, followed by kinetic

trapping via transfer into ~50 mL deionized water. The colloidal dispersions were finally dialyzed against deionized water to remove residual organic solvent.

In addition, to compare the effects of off-chip stirring-induced shear with the effects of on-chip shear, we prepared micelles at 5.2 wt % water in a manner similar to that described above, except for the following differences. Once the target water concentration was reached, the micelles were stirred rapidly at 1200 rpm for a period of time equivalent to the on-chip residence time at low flow rate (280 s), followed by immediate kinetic trapping into excess deionized water and dialysis. In Figure 3.4, this additional off-chip control experiment is referred to as "off-chip (rapid stirring)"

3.2.4. Microfluidic Chip Fabrication

Negative masters were fabricated on high-quality silicon wafers (Silicon Quest International, CA) using a negative photoresist, SU-8 100 (Microchem Inc., MA). Prior to use, new silicon wafers were heated on a hotplate to at 200 ºC for 20 minutes to remove all moisture. SU-8 films, 150 μm thick, were spin-coated onto the silicon wafers, then heated to 95 ºC for 60 minutes to remove residual SU-8 solvent. A photomask was placed over the film and the device was exposed to UV light for 180 s. After additional heating at 95 ºC for 20 minutes, the device was submerged in SU-8 developer (Microchem, MA) until all unexposed photoresist was removed. The reactor has a set channel depth of 150 μm, and consists of a sinusoidal mixing channel 100 μm wide and 100 mm in length, and a sinusoidal processing channel 200 μm wide and 740 mm in length.

For further stabilization of the bubble generation process, external resistor chips were employed in series between the Ar gas tank and the microfluidic chip. These

resistors were 1000 mm long, 400 μm wide and 150 μm deep. In operation, these high pressure drop resistors serve to efficiently dampen the pressure fluctuations caused by the Ar gas tank and the bubble generation process itself. The resistors were designed in a way that the total pressure drop in the resistors was at least one order of magnitude higher than the pressure drop in the reaction channel.

Microfluidic chips were fabricated from poly(dimethylsiloxane) (PDMS) using a SYLGARD 184 silicon elastomer kit (Dow Corning, MI) with an elastomer base-to-curing agent ratio of 10:1. The elastomer and curing agent were mixed together and degassed in a vacuum chamber. The degassed PDMS was poured onto the negative master in a petri dish and then degassed again until all remaining air bubbles in the PDMS were removed. The PDMS was then heated at 85 ºC until cured (~ 50 mins). The microfluidic chips were peeled off the master, and holes were punched through its reservoirs to allow for the insertion of tubing. A thin PDMS film was formed on a glass slide by spin-coating and was permanently bonded to the base of the microfluidic reactor after both components were exposed to oxygen plasma for 30 s.

3.2.5. Flow Delivery and Control

Pressure-driven flow of liquids to the inlets of the reactors was provided using 250 μL gastight syringes (Hamilton, NV) mounted on syringe pumps (Harvard Apparatus, MA). The microchip was connected to the syringes with 1/16th inch (OD) Teflon tubing (Scientific Products and Equipment, ON). Gas pressure was controlled by the Ar tank regulator as well as a downstream regulator for fine adjustments (Johnson Controls Inc.). For gas flow, connections were joined using Teflon tubing of 1/16 inch (OD) and 100 μm (ID) (Upchurch Scientific, WA). The liquid flow rate (Q_{liq}) was

programmed via the syringe pumps and the gas flow rate (Q_{gas}) was varied by tuning the pressure regulator. Due to the compressible nature of the gas and the high gas/liquid interfacial tension, discrepancies arise between the nominal (programmed) and actual values of Q_{gas}, Q_{gas}/Q_{liq}, and the total flow rate (Q_{total}). Therefore, actual gas flow rates were calculated from the frequency of bubble formation and the average volume of gas bubbles, determined from image analysis of the mean lengths of liquid and gas plugs, L_{liq} and L_{gas}, respectively, under a given flow set of conditions. This method of flow calculation has been previously employed in the context of gas-liquid multiphase flow in microfluidic device.[43, 50, 51] Actual flow parameters pertaining to the gas-liquid segmented microfluidic reactor experiments are described in Table 3.1. For all experiments, the relative gas-to-liquid flow ratio (Q_{gas}/Q_{liq}.) was ~1, and two different nominal total flow rates were investigated: Q_{total} = ~5 μL / min (low flow rate case) and ~50 μL / min (high flow rate case) (see Table 3.1 for actual values).

Table 3.1. Actual gas and liquid flow rates for the various on-chip experiments described in the text.

Conditions (water content, nominal flow rate)	L_{liq} **(x 10^{-2} μm)**	L_{gas} **(x 10^{-2} μm)**	Q_{gas} **(μL/min)**	Q_{liq}[a] **(μL/min)**	Q_{gas}/Q_{liq}	Q_{total} **(μL/min)**
4.2 wt %, 5 μL/min	14.9	16.4	2.9	2.4	1.2	5.3
5.2 wt %, 5 μL/min	12.4	12.6	2.7	2.4	1.1	5.1
7.2 wt %, 5 μL/min	11.0	10.7	2.6	2.4	1.1	5.0
4.2 wt %, 50 μL/min	9.1	9.3	27.7	24	1.2	51.7
5.2 wt %, 50 μL/min	11.2	8.4	20.4	24	0.8	44.4
7.2 wt %, 50 μL/min	10.6	7.7	19.8	24	0.8	43.8

[a] The liquid flow rate is assumed to be same as the value programmed at the syringe pump.

3.2.6. On-Chip Micelle Preparation

For microfluidic self-assembly experiments, three separate liquid streams were combined at equal flow rate to form gas-separated liquid plugs within the reactor: 1. a 1.0 wt % solution of PS(665)-*b*-PAA(68) single chains in 75/25 w/w DMF/dioxane; 2. a separator stream containing 75/25 w/w DMF/dioxane only; and 3. a solution of 75/25 w/w DMF/dioxane containing 12.6, 15.6, or 21.6 wt % deionized water. Combination of the three liquid streams yielded steady-state on-chip concentrations of 0.33 wt % polymer, identical to the off-chip control experiments, and either 4.2, 5.2, or 7.2 wt % water— 1.0, 2.0 and 4.0 wt % above the cwc (3.2 wt %), respectively. Microfluidic flow conditions were selected as described in the previous section.

For off-chip analysis of micelle morphologies prepared within the reactor, micellar dispersions were generally collected from the chip following the processing

channel into vials containing a large excess (~250 μL) of deionized water, where the particles immediately became kinetically frozen due to the high water content. For experiments tracking the off-chip relaxation of micellar morphologies formed on-chip, micellar dispersions were collected from the chip following the processing channel into empty vials; the solutions were then allowed to sit off-chip without shear or stirring for various times, before kinetic trapping by dumping into excess deionized water. For both types of micelle collection (immediate trapping or annealing), the solids content of the final mostly-aqueous solution was ~0.25 mg/mL.

Flow visualization of microfluidic experiments and quantification of all the flow conditions was performed with an inverted fluorescence microscopy system operating in transmission mode. Optical images of the reactor were capture using a CCD camera (AF6000 Orca, Hamamatsu, NJ) installed on the inverted microscope (DMI 6000B, LEICA, NJ).

3.2.7. TEM and Image Analysis

Transmission electron microscopy (TEM) of various aqueous micellar dispersions was performed at a Hitachi H-700 electron microscope, operating at an accelerating voltage of 75 kV. For TEM imaging, a 10 μL drop of micellar dispersion was deposited onto either a carbon-coated or carbon-coated Formvar 300 mesh copper grid, and then shadowed with Pt/Pd wire for imaging. For TEM imaging of on-chip prepared samples, the small quantity of dioxane remaining in the final solutions was found to dissolve Formvar substrates, and so carbon-coated grids without Formvar were required for these samples.

Analysis of micelle size distributions and statistics of both spherical and non-spherical aggregates were carried on images randomly selected from various regions of the TEM grid. To assemble size histograms of spherical micelle populations for each sample, the diameters of 150 spheres were measured with a caliper (Mastercraft, FL), from printouts of multiple regions of the TEM grid where the particles appeared 40,000 to 50,000 times their actual size.

To quantify the percentage of non-spherical micelles in a given sample, we determined their areal percentage relative to the total micelle area in TEM images. Assuming a constant density and constant height of different micelle morphologies on the TEM grids, the areal percentage of non-spherical micelles gives a reasonable estimate of their weight percentage relative to total micelles in a given sample. The areal percentage of non-spherical micelles on a TEM grid was averaged from values determined from 4-5 randomly-selected regions. When a grid region was selected, a low-magnification (10k) image was first taken, followed by higher-magnification (20k) imaging of four quadrants of the larger area to allow for accurate image analysis. The higher magnification images were processed with scientific image analysis software (ImageProPlus v. 6.1, Media Cybernetics). Appropriate brightness, contrast and sharpness levels were selected for each image; after image binarization, threshold levels were set to allow particles to be counted and analyzed by the software. By visual inspection, non-spherical objects were then selected and their areal percentage was calculated. For each sample, the process was repeated for two other TEM grids prepared using the same micelle dispersion, in order to arrive at an average value and experimental error (standard deviation of the three grids)

for the sample. The experimental errors on values of the areal percentage of non-spherical micelles in various samples were ~15-20%.

It was found that dynamic light scattering (DLS) analysis of many of the micelle populations prepared on-chip was not practical for two reasons. First, the samples could not be effectively filtered to remove dust without also removing many of the larger non-spherical micelles in the sample. Second, the small number fractions and very slow diffusion times for the large network micelles observed in many on-chip prepared samples did not allow them to be effectively sampled in typical collections of the DLS autocorrelation function.

3.2.8. Zeta Potential Measurements

Zeta potentials of various samples were measured using a Zeta PALS Analyzer (Brookhaven Instruments Corporation, USA). Zeta potential values were computed from electrophoretic mobility values at 25°C using the Smoluchowski equation.

3.3. Results and Discussion

3.3.1. PS-*b*-PAA Self-Assembly Process and Multiphase Microfluidic Reactor Approach

The specific amphiphilic block copolymer used for this study is polystyrene-*block*-poly(acrylic acid), PS(665)-*b*-PAA(68), where numbers in brackets indicate number average degrees of polymerization for the respective blocks. For all on-chip and off-chip (control) experiments, solutions of 0.33 wt % PS(665)-*b*-PAA(68) in the solvent mixture 75/25 (w/w) *N*,*N*-dimethylformamide/1,4-dioxane (DMF/dioxane) serve as the

initial state for block copolymer self-assembly. Subsequent water addition to the solution in the microfluidic device (on-chip) or in vials (off-chip) increases the polarity of the solvent and decreases the solubility of the hydrophobic PS blocks until micelles with PS cores and soluble PAA coronae are formed (Fig. 3.1A). In both bulk and microfluidic environments, micelle formation is thermodynamically favorable above the critical water concentration (cwc),[8] which is determined to be 3.2 ± 0.1 wt % for the copolymer solution employed here (Fig. 3.2). Therefore, to investigate the effect of the chemical environment on self-assembly, three different water contents, 1, 2, and 4 wt % above the cwc, were selected for on-chip and off-chip experiments: that is, 4.2, 5.2 and 7.2 wt % water in DMF/dioxane.

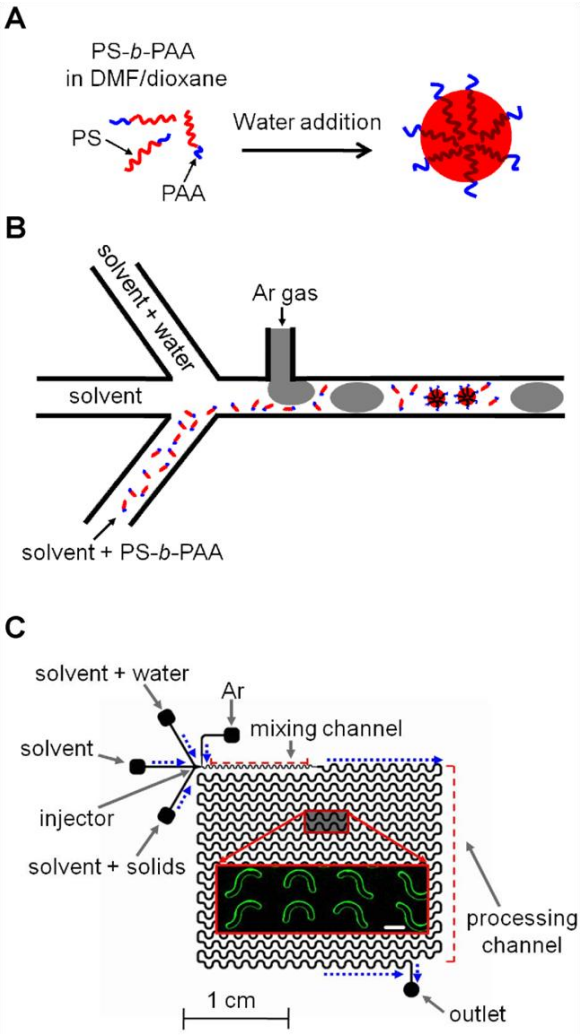

Figure 3.1. PS-*b*-PAA self-assembly process and multiphase microfluidic reactor approach. (A) Schematic of the PS-*b*-PAA assembly process. Red indicates hydrophobic PS blocks, while blue indicates hydrophilic PAA blocks. (B) Cartoon representation of the self-assembly of PS-*b*-PAA into micelles in the multiphase microfluidic reactor. The self-assembly is initiated by mixing of the three liquid stream contents within segmented plugs, which leads to an average cross-stream water content above the critical water content (cwc). (C) Schematic of the microfluidic reactor, showing liquid and gas inlets at the injector, followed by the mixing channel (represented in B); in the subsequent processing channel, the formed micelles experience the shear-induced collisions and morphological transformations discussed in the text, which are trapped by collection into pure water after the outlet. The inset of (C) shows a select optical microscopy image of the reactor under stable operation. The white scale bar indicates 500 μm.

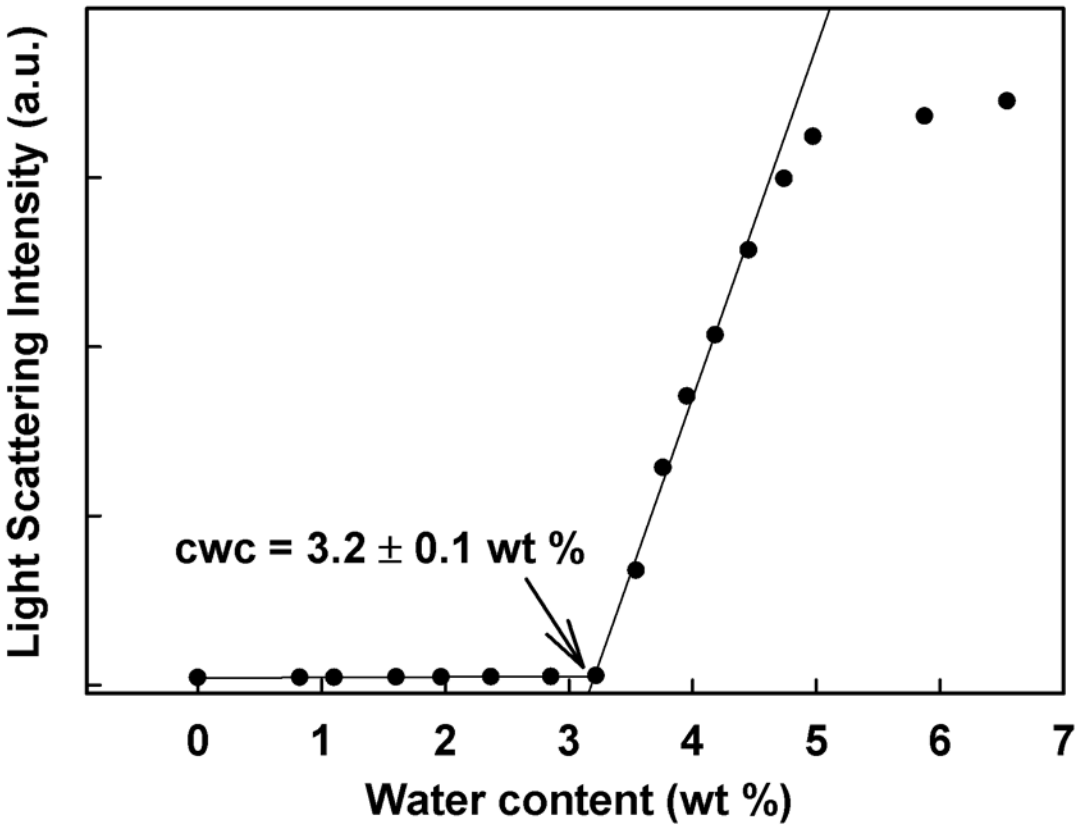

Figure 3.2. Critical water concentration (cwc) determination of 0.33 wt % PS(665)-*b*-PAA(68) in 75/25 w/w DMF/dioxane using the static light scattering method. The cwc is determined from the plotted light scattering data to be 3.2 ± 0.1 wt %, as shown.

Microfluidic self-assembly in the gas-liquid segmented reactor is depicted in Fig. 3.1B. A stream of the DMF/dioxane solvent mixture containing PS(665)-*b*-PAA(68) copolymer is combined with a DMF/dioxane separator stream and a DMF/dioxane/water stream; the concentrations of copolymer and water in the corresponding inlet streams are selected to give a cross-sectional average copolymer concentration of 0.33 wt % and a cross-sectional average water concentration of 4.2, 5.2 or 7.2 wt %. The streams are then joined with argon gas at the injector, which compartmentalizes the co-laminar flow into liquid plugs. The resulting chaotic advection in the sinusoidal mixing channel enables fast mixing of water with the copolymer solution (~1 s), triggering micelle formation shortly after the injector.[42, 43, 52, 53]

A detailed schematic of the reactor is shown in Fig. 3.1C. The reactor has a set channel depth of 150 μm, and consists of a sinusoidal mixing channel 100 μm wide and 100 mm in length, and a sinusoidal processing channel 200 μm wide and 740 mm in length. Following initial formation, block copolymer micelles are exposed to continuous mixing as the liquid plugs proceed through the mixing and processing channels, until the colloidal dispersion is collected at the outlet for off-chip characterization by transmission electron microscopy (TEM). Unless otherwise stated, micelles formed on-chip are kinetically trapped immediately upon exiting the chip by collection into a vial containing a large excess of deionized water; under these conditions, the amount of organic solvent in the PS phase becomes negligibly small, and micelle cores that were highly dynamic on-chip as a result of solvent swelling become suddenly vitrified, "freezing" the on-chip colloidal morphologies for off-chip characterization. For all experiments, the gas-to-liquid flow ratio is ~1, and two different nominal total flow rates are investigated: Q = ~5

μL/min (low flow rate case) and ~50 μL/min (high flow rate case).[54] An optical image of part of the reactor (Fig. 3.1C, inset) demonstrates typical stable operation in which uniform and regularly-spaced gas bubbles are produced.

The dramatic effect of the microfluidic environment on micelle morphologies produced by block copolymer self-assembly is shown in Fig. 3.3. In the off-chip control experiment, water is added dropwise to a solution of PS(665)-*b*-PAA(68) up to 5.2 wt %, and the resulting dispersion is allowed to equilibrate for 2 weeks, generating exclusively spherical micelles (Fig. 3.3A, mean diameter, d = 35 nm). In contrast, block copolymer self-assembly at the same water content in the microfluidic device operating at low flow rate (Q = ~5 μL/min) gives a mixture of spherical micelles (d = 41 nm) and several higher order, non-spherical morphologies (Fig. 3.3, B to D). The representative images highlight the broad range of morphologies that are generated on-chip under these conditions, including linear and looped cylinders, Y-junctions, spherical caps, bilayer sheets, and dense networks of loops and cylinders. Several of the larger micelles consist of hybrid morphologies described by abrupt changes in local interfacial curvature. For example, the micellar aggregate in Fig. 3.3C possesses interconnected bilayer regions with appendages of linear and looped cylinders, while Fig. 3.3D shows a flat bilayer sheet embedded within a network of looped cylinders and Y-junctions.

On the basis of their uniformity and low polydispersity, we expect that the spherical micelles formed off-chip (Fig. 3.3A) are close to thermodynamic equilibrium. Conversely, the various non-spherical morphologies (Fig. 3.3, B to D) formed under identical chemical conditions but in the microfluidic device appear to be kinetic products of the unique on-chip environment. Our previous work on similar two-phase

microfluidic reactors has shown that recirculating flow in the liquid plugs gives rise to localized regions of extremely high shear (~ 10^4 - 10^5 s^{-1}) in the plug corners.[42] Moreover, we have demonstrated that the associated shear fields can induce both coalescence and breakup of suspended, solvent-swollen polymeric particles, with shear-induced coalescence dominating at low flow rate (~ 5 μL/min) and shear-induced breakup becoming increasingly important at higher flow rates.[43] In the current work, we attribute the various non-spherical micelle morphologies formed at 5 μL/min (Fig. 3.3) to shear-induced coalescence of smaller, more thermodynamically stable, spherical micelles within the microfluidic reactor.

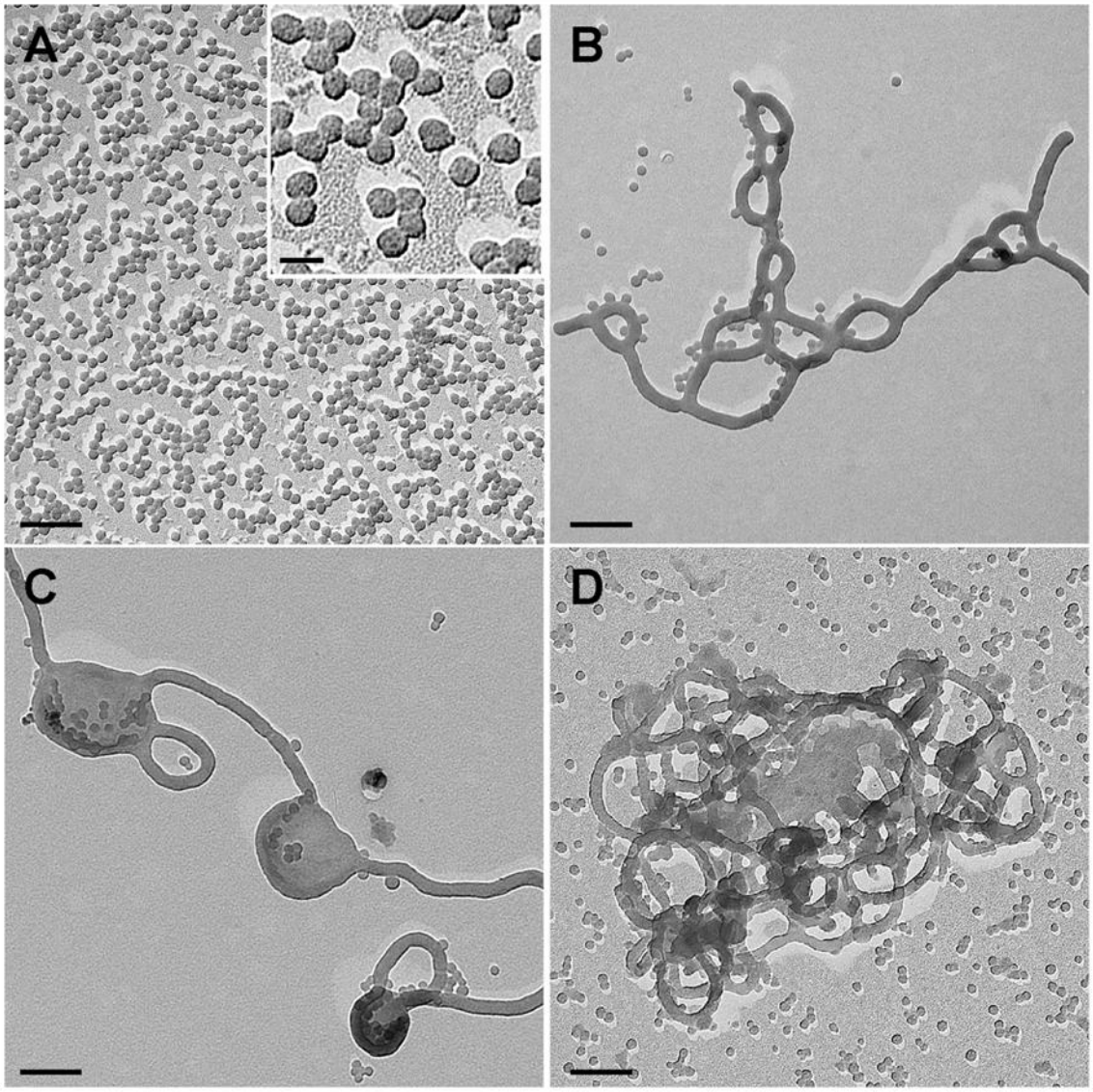

Figure 3.3. TEM images comparing off-chip (A) and on-chip, Q = ~5 μL/min (B to D), morphologies of PS-*b*-PAA micelles formed in DMF/dioxane mixtures containing 5.2 wt % water. Only the equilibrium spherical morphology was formed off-chip (A). However, the on-chip experiment yielded a mixture of morphologies in addition to spheres, including linear and looped cylinders (B, C and D), Y-junctions (B and D), spherical caps (B), bilayer sheets (C and D), and networks (D). All scale bars = 200 nm, except the higher-magnification inset to A (scale bar = 50 nm).

3.3.2. Proposed Energy Pathway For On-Chip Shear-Induced Morphological Transitions

The free energy pathway for such on-chip shear-induced morphology transitions is represented in Scheme 3.1. First, spherical micelles are generated shortly after the injector, as fast mixing of water (< 1 s) brings the average solvent composition above the cwc (Scheme 3.1, State A). Next, as the liquid plugs travel through the reactor, continuous recirculating flow moves micelles in and out of the high-shear corners, resulting in shear-induced micelle coalescence to form larger micelles with elevated free energies compared to the global equilibrium state (Scheme 3.1, State B). Finally, internal chain rearrangements, driven by localized free energy lowering within coalesced micelles, give rise to the various non-spherical morphologies (Scheme 3.1, State C).

Shear-induced aggregation of solid colloidal particles (or coalescence of liquid drops) is a well-known phenomenon occurring in both natural and industrial systems, with examples ranging from the deterioration of dispersed pigments to the formation of strong silk fibers within a spider's spinneret.[55] Recent theoretical work by Zaccone and workers describes shear-induced aggregation as an activated-rate process, using an Arrhenius-type rate equation to show that shear both increases the particle collision rate and also supplies energy to overcome repulsive interparticle potentials, thus increasing the fraction of adhesive collisions.[56] In general, the relative effects of shear and Brownian motion on aggregation rates of colloidal particles can be described by the dimensionless Peclet number:

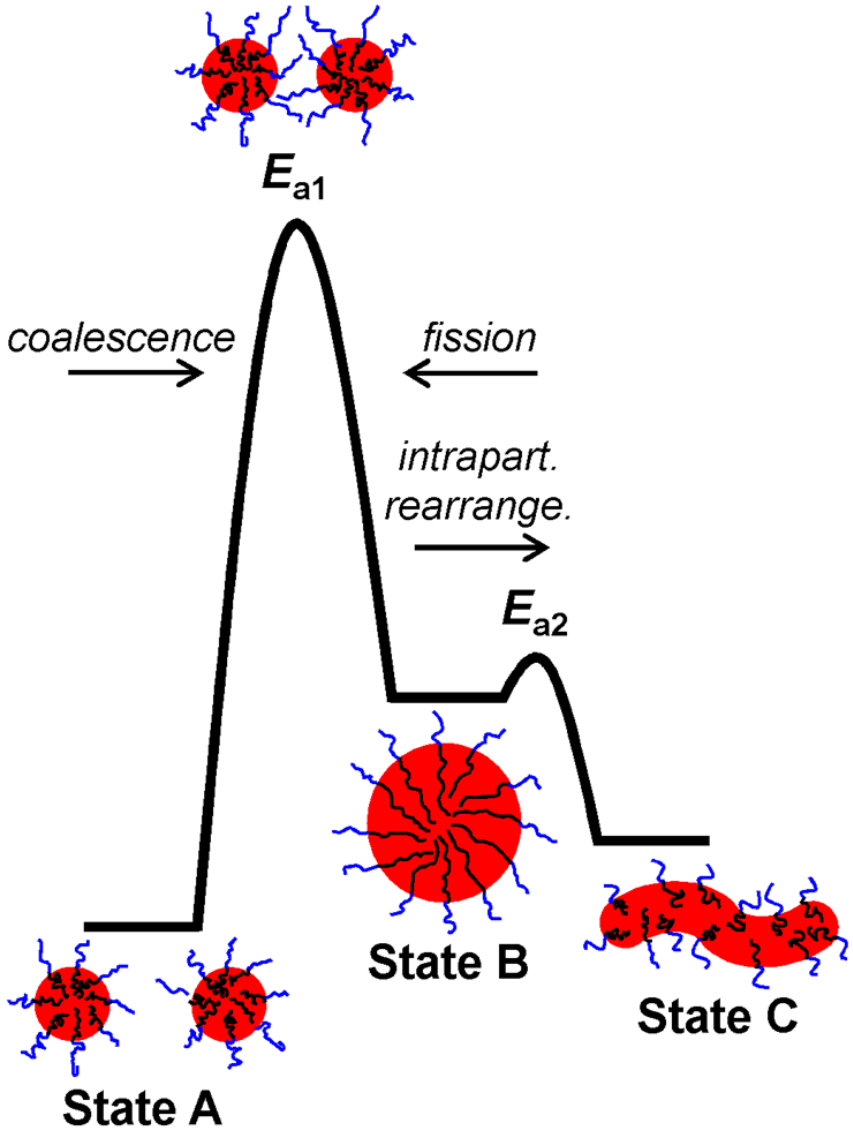

Scheme 3.1. Proposed energy diagram for on-chip shear-induced morphological transitions.

$$Pe = \frac{\dot{\gamma} a^2}{D_0} \quad \textbf{(3.1)}$$

where $\dot{\gamma}$ is the shear rate, a is the particle size and D_0 is the particle diffusion coefficient.[57] For low Peclet numbers ($Pe << 1$) thermal diffusion has a dominant effect on particle aggregation, whereas shear forces have a stronger influence on aggregation rates as Peclet numbers increase.[58]

From Eq. 3.1, the initially-formed spherical micelles (a = ~40 nm) in the high-shear corners of the liquid plugs at low flow rate ($\dot{\gamma}$ = ~10^4 s^{-1}) are described by a Peclet number of Pe = ~10.[59] Although the specific dependence of shear-induced aggregation on Pe depends on the nature of the interparticle interactions,[57] Pe numbers on the order of ~10 have been found to give rise to shear-induced aggregation in related systems.[56-58] It is therefore reasonable to propose that micelles will experience multiple shear-induced collisions as they circulate through the high-shear hot spots of the plug corners, with some of these collisions being sufficiently energetic to overcome E_{a1} (Scheme 3.1) and activate micelle coalescence.[56] The collision of two primary micelles, represented in Scheme 3.1, is only one of many statistical possibilities, which will also include collisions between one or more larger micelles (with higher Peclet numbers, Eq. 3.1) that have experienced at least one previous instance of collision-coalescence.

A key component of the activation energy E_{a1} is the repulsion between the overlapping coronae of colliding micelles (Scheme 3.1).[60] Even at the relatively low water contents in DMF/dioxane employed on-chip (~4-7 wt%), PS-*b*-PAA micelles will exhibit polyelectrolyte character, due to preferential accumulation of water within the

PAA corona.[61] This means that the PAA chains will be partially ionized and negatively charged, with the extent of ionization increasing at higher water contents; this was confirmed by off-chip zeta-potential measurements of PAA-*b*-PAA micelles at the same solvent conditions as on-chip experiments, which gave ζ = -15 ± 3, -21 ± 1, and -24 ± 2 mV in DMF/dioxane at 4.2, 5.2, 7.2 wt % water, respectively.

To estimate the contribution of intercoronal repulsion to E_{a1}, we employ a recent model by Jusufi et al. describing repulsive interactions between spherical polyelectrolyte brushes.[60] According to this model, the confinement of counterions within the brush layers results in negligible electrostatic interparticle forces. As well, it is assumed that chains in the approaching brushes retract from each other (or "dent") rather than interdigitating. The dominant term of the resulting electrosteric pair potential is attributed to the decreased entropy of counterions in the overlapping polyelectrolyte brushes. The analytical form of their result is a pair potential that increases from zero as approaching brushes begin to overlap, and reaches a maximum value of $0.2kT$ per unit counterion when the cores come into contact. From this result, we take $0.2kT$ x ($Q/|e|$) as the electrosteric contribution to E_{a1}, where Q is the effective charge of counterions in the corona and e is the elementary charge. For spherical micelle cores with a = ~40 nm, an aggregation number of Z = ~250 is determined, or ~2 x 10^4 COOH units per micelle. Assuming a maximum degree of ionization of ~10% (calculated from a pKa of 4.25 in water),[61] and two-thirds condensed counterions,[60] we obtain an effective charge of counterions in the corona of Q = ~700 $|e|$, which yields an E_{a1} value on the order of ~100kT if electrosteric effects dominate the coalescence energy barrier.

Another potential contribution to E_{a1} is the viscosity of the PS micelle cores, which will govern the rate of core coalescence if the electrosteric barrier described above is overcome. It is well established that block copolymer intermicellar and intramicellar chain dynamics are a strong function of the water content in polar organic solvents; at low water contents, the micelle cores are highly swollen by the organic solvent, becoming increasingly viscous until eventual kinetic freezing as the water content increases.[9, 11] For PS-*b*-PAA in DMF, fast micelle equilibration kinetics on experimental time scales for water contents less than ~6.5% have been found, suggesting highly swollen and dynamic PS blocks in this range of solvent composition;[11] based on this result, and considering that dioxane is an even better solvent for the PS core than DMF,[9] it is reasonable to conclude that core viscosities do not contribute significantly to E_{a1} in DMF/water mixtures at the two lowest water contents of 4.2 and 5.2 wt %. However, as the water content increases, the solvent content in the core, along with the chain dynamics, will drop off significantly; we therefore cannot rule out a considerable, and possibly even dominant, contribution of core viscosity to the coalescence rate at the highest water content (7.2 wt %).

From the Arrhenius expression for the rate of shear-activated coalescence,[56] a critical shear rate $\dot{\gamma}^*$ can be defined such that the activation barrier becomes vanishingly small, and the rate of coalescence becomes equal to the collision rate, when $\dot{\gamma} >> \dot{\gamma}^*$:

$$\dot{\gamma}^* = \frac{E_{a1}}{6\pi\alpha\mu a^3} \qquad \textbf{(3.2)}$$

In this expression, α is a numerical coefficient describing the flow (e.g. $\alpha = 1/3\pi$ for simple shear) and μ is the dynamic viscosity. Using $E_{a1} = 100kT$, $\alpha = 1/3\pi$, $\mu = 0.001$ Pa

s, and a = 40 nm, we obtain $\dot{\gamma}^*$ = 6 x 10^6 s^{-1} for primary spherical PS-*b*-PAA micelles in DMF/water with electrosteric repulsion. Since in the high-shear hot spots on chip $\dot{\gamma}^*$ >> $\dot{\gamma}$ = ~10^4 s^{-1}, we conclude that the magnitude of E_{a1} will strongly influence the kinetics, such that the rate of shear-induced coalescence is expected to increase as E_{a1} decreases either by changes in the corona charge or core viscosity.[56]

As the average micelle size increases through statistical collision-coalescence events, increased PS chain stretching stores accumulated shear energy in micelles with elevated free energies (Scheme 3.1, State B). Outside of the high-shear regions, coalesced micelles in State B will therefore have a thermodynamic tendency to return to their lowest free energy state via micelle fission (Scheme 3.1). However, if a sufficiently high E_{a1} results in a fission rate that is comparable or slow compared to the rate of shear-induced coalescence, then on-chip relaxation to global equilibrium will be precluded. Under this kinetic constraint, a significant number of micelles in State B will lower their free energy via the alternative pathway of intramicellar chain rearrangements, leading to localized morphology transitions (State C). The energy barrier E_{a2} is expected to be a function of the viscous resistance to intramicellar chain diffusion within the PS cores; at low water contents (4-5 wt %), the PS cores will be highly swollen with solvent, with estimated core polymer concentrations of ~50 wt %.[9] Using literature values for the activation energy of viscous flow for PS-toluene solutions of similar concentrations,[62] we estimate E_{a2} to be ~10kT, an order of magnitude lower than E_{a1}. This explains why the intramicellar pathway to the observed non-spherical morphologies is kinetically favored over a return to global equilibrium. Therefore, as a combined result of the statistical nature of shear-induced collisions and the kinetic constraints of relaxation processes in

the microfluidic device, we obtain a potpourri of spherical and non-spherical morphologies that are not globally equilibrated, but nonetheless represent a tendency of micelles to locally minimize their internal free energy.

Although the detailed mechanisms of these on-chip morphological transformations are currently unknown, copolymer chains are assumed to redistribute after a coalescence event following microphase separation principles, with internal curvature optimized to reduce stretching within the constraints of high chain packing densities required to lower interfacial tension.[2, 3, 14, 35] In general, micelle morphologies will change from spheres to cylinders to bilayer structures (in order of decreasing internal curvature), as a means of relieving stretching of core-forming blocks in response to chemical variables that increase the chain packing density at the interface.[2, 3] In the present case, it is shear-induced coalescence, rather than chemical forces, that locally increase aggregation numbers, triggering localized transitions from spheres to mainly cylindrical structures in order to lower internal curvature and reduce PS stretching. However, despite the predominance of cylinders under the current chemical and flow conditions, we point out that other non-spherical morphologies with even lower internal curvature are also observed, suggesting significant variability in local conditions due to the statistical nature of collision-coalescence events. For instance, the observed hybrid morphologies discussed earlier (e.g. Fig. 3.3, C and D) are explained by intraparticle morphology transitions (e.g. from cylinders to bilayers) that become kinetically trapped during off-chip collection.

Recently, Winnik and coworkers showed that a sphere-to-wormlike network transition could be induced in polystyrene-*block*-poly(4-vinyl pyridine) (PS-*b*-P4VP)

block copolymer micelles with PS cores and P4VP coronae by conventional rapid magnetic stirring at 1200 rpm, but only in the presence of in CdSe quantum dots, which were proposed to form bridging interactions between coronae of assembling spherical micelles.[30] Therefore, to confirm the important role of the extremely strong shear fields enabled by the on-chip environment in the current system,[42] we investigate the effect of micelle formation under off-chip vigorous magnetic stirring conditions similar to those employed in the Winnik's work.[35] In this experiment, micelles are formed by drop-wise addition of water to 5.2 wt %, and then stirred at 1200 rpm for 280 s (equivalent to the on-chip residence time at low flow rate). Although the solution mixing will be much improved, the maximum shear rates in this experiment are on the order of 1 s^{-1}, which are negligible compared to local maximums experienced on-chip. In contrast to on-chip self-assembly under the same chemical conditions, no non-spherical micellar structures are formed in these more conventional shear fields, and the resulting spherical micelles are similar in size (d = 37 nm) to micelles formed off-chip at 5.2 wt % water without vigorous stirring (d = 35 nm, Fig. 3.4). We conclude that nanoscale velocity gradients in the plug corners are germane to increasing the rate of on-chip collision-coalescence events relative to normal diffusive motion in the bulk, thus enabling the morphology transformations described above.

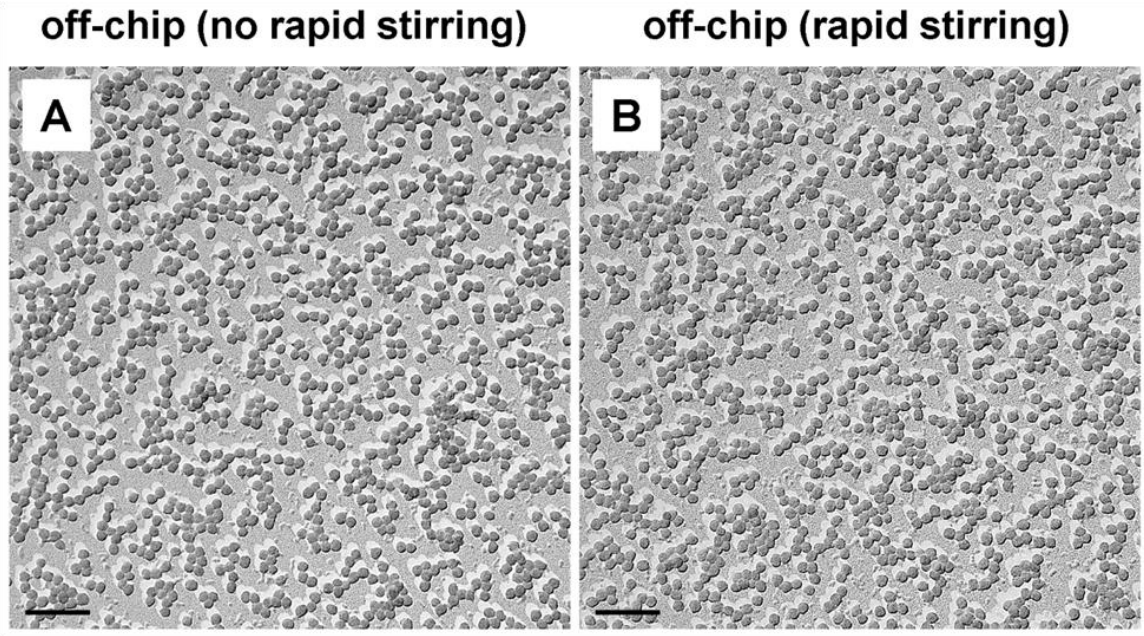

Figure 3.4. Comparison of PS-*b*-PAA micelles formed off-chip in DMF/dioxane at 5.2 wt % water, with and without vigorous magnetic stirring. (A) Micelles produced without vigorous stirring, "off-chip". (B) Micelles produced by vigorous magnetic stirring at 1200 rpm for 280 s following water addition, "off-chip (rapid stirring)". The mean sizes (*d*) and relative standard deviations (*sd*) in these samples are (A) *d* = 35 nm, *sd* = 6%; (B) *d* = 37 nm, *sd* = 8%. All scale bars = 200 nm.

3.3.3. The Effect of Water Content on On-Chip PS-*b*-PAA Micelle Morphologies

Fig. 3.5 describes the effect of chemical conditions on the on-chip formation of flow-directed block copolymer micelle morphologies at low flow rate. In Figs. 3.5A, C, and D, representative micelles are shown for solvent mixtures with 4.2, 5.2, and 7.2 wt % water, with associated spherical micelle size distributions shown in Fig. 3.5, B, D, and F. Not shown in the figure are the results of the associated off-chip control experiments, which give rise to uniform and low-polydispersity spherical micelles for all three water contents, with monotonically increasing mean sphere sizes of 29 nm, 35 nm, and 39 nm for 4.2, 5.2 and 7.2 wt % water, respectively (Table 3.2). Comparing 4.2 and 5.2 wt % water on-chip (Fig. 3.5, A and C), both images reveal a mixture of spheres and non-spherical morphologies, indicating that shear-induced morphological transformations are operative at both water contents. In addition, both samples show spherical micelle populations with the same mean size (d = 41 nm), larger than the associated off-chip equilibrium sizes (d =29 and 35 nm for 4.2 and 5.2 wt % water, respectively), although with very different distribution shapes and widths (Fig. 3.5, B and D). We also find that the higher water content results in significantly larger network structures (Fig. 3.6), as well as a higher areal percentage of non-spherical micelles relative to the total micelle area (*areal percentage* = 5 % and 24 % at 4.2 and 5.2 wt % water, respectively).[63] This indicates that a significantly larger percentage of spherical micelles are converted into non-spherical nanostructures by the on-chip environment at 5.2 wt % compared to 4.2 wt % water. Interestingly, the opposite trend is found upon further increasing the water content to 7.2 wt % (Fig. 3.5E), which results in uniform spherical micelles with mean size

Table 3.2. Mean spherical micelle diameters and relative standard deviations under various on-chip and off-chip preparation conditions.

Conditions	**4.2 wt% water**	**5.2 wt% water**	**7.2 wt% water**
off-chip	29 nm; 10%	35 nm; 6%	39 nm; 10%
on-chip, ~5 μL/min			
t = 0	41 nm; 10%*	41 nm; 24%*	33 nm; 9%
t = 2 hrs	41 nm; 15%*	36 nm; 14%*	-
t = 10 hrs	45 nm; 9%*	36 nm; 14%*	-
t = 48 hrs	49 nm; 10%*	35 nm; 11%*	-
t = 7 days	49 nm; 8%	35 nm; 17%*	-
t = 28 days	49 nm; 8%	35 nm; 14%	-
on-chip, ~50 μL/min	37 nm; 8%	32 nm; 9%	30 nm; 13%

*indicate samples containing non-spherical micelles, in addition to spherical micelles measured here.

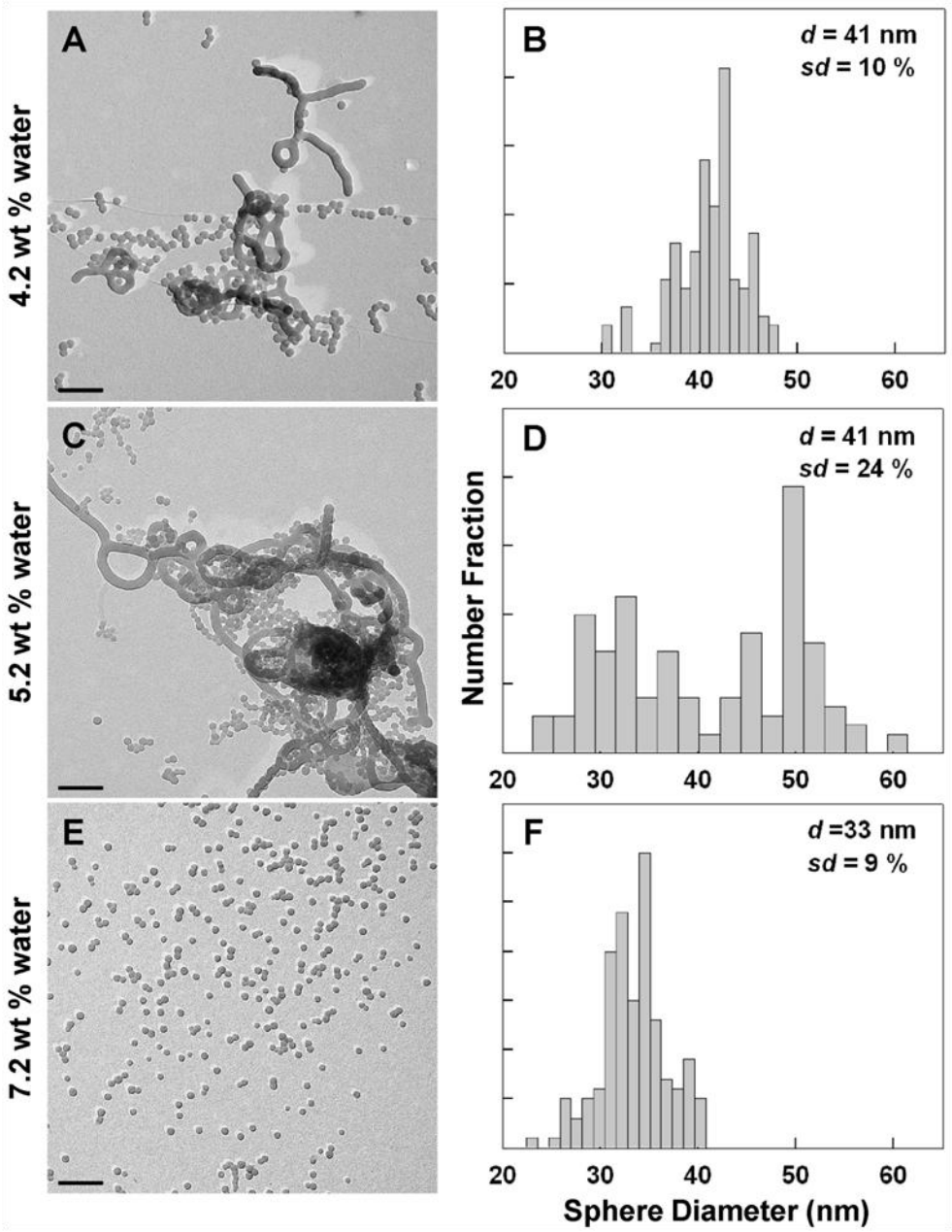

Figure 3.5. The effect of water content on on-chip PS-*b*-PAA micelle morphologies (A, C, and E) and spherical micelle size distributions (B, D, and F) formed in DMF/dioxane mixtures, Q = ~5 μL/min. A, C and D show TEM images of representative micelles formed at 4.2, 5.2 and 7.2 wt % water, respectively; B, D and F show size histograms of spherical micelle populations formed at the corresponding water contents. All scale bars = 200 nm.

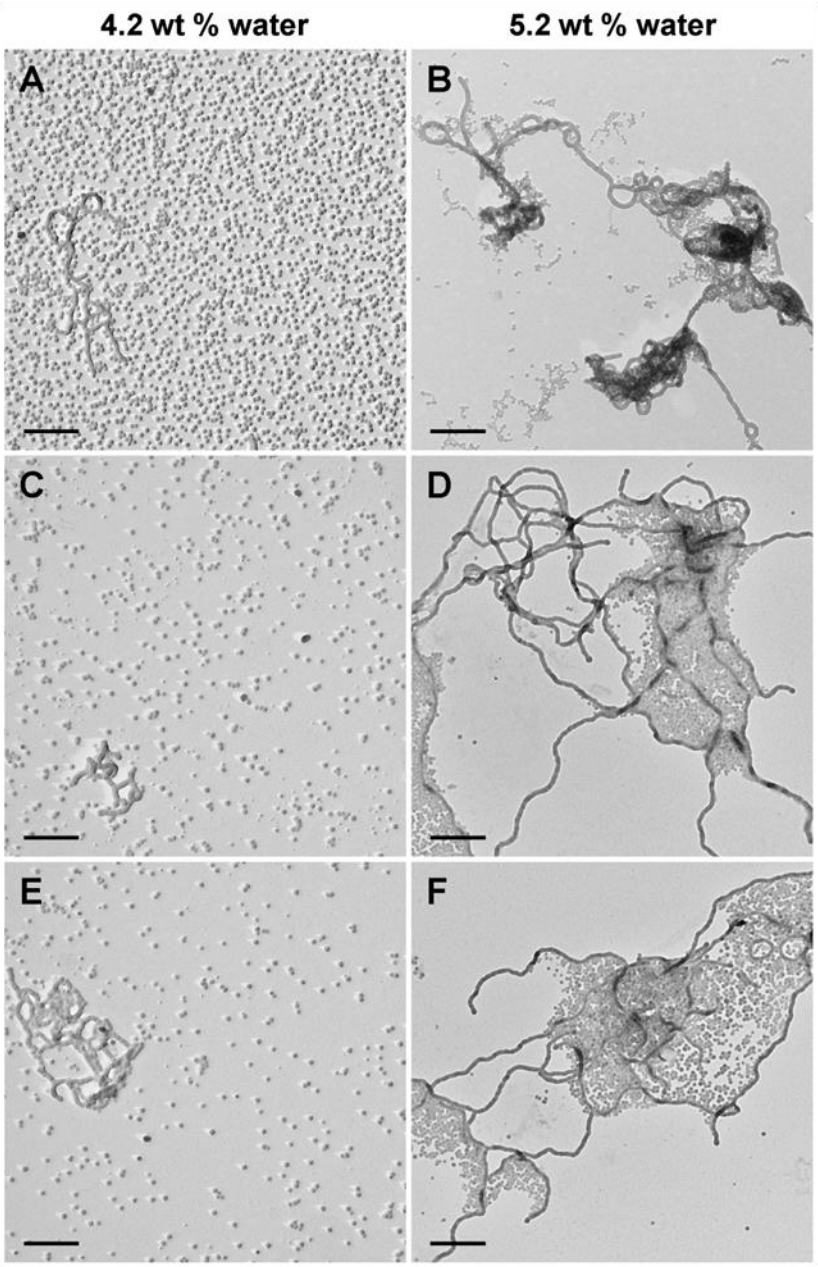

Figure 3.6. Representative low-magnification images comparing the sizes of non-spherical aggregates formed on-chip (Q = ~5 μL/min) at 4.2 wt % water (A, C, and E) and 5.2 wt % water (B, D, and F). All scale bars = 500 nm.

d = 33 nm (Fig. 3.5F), smaller than the associated equilibrium value (d = 39 nm), with no observable non-spherical micelles.

The influence of water content on the on-chip morphologies can be understood in terms of its effect on activation barriers in Scheme 3.1. The activation energy for the coalescence/fission process, E_{a1}, is a function of intercoronal electrosteric repulsion and core viscosity for two colliding micelles, which represents the transition state between States A and B.[64] With increasing water content, intercoronal repulsion and core viscosity will both increase, as the PAA chains become increasingly ionized and the solvent quality for the PS core decrases.[11] Both effects will therefore contribute to an increase in E_{a1}, and the later effect will also contribute to an increase in E_{a2}. The increase in electrosteric interactions will dominate at the two lowest water contents (4.2 and 5.2 wt %), where the electrosteric barrier for coalescence is ~10 x greater than the barrier for viscous flow within the core. However, the increase in core viscosity is expected to play a more significant role at 7.2 wt % water, based on the demonstrated sharp decrease in PS-*b*-PAA chain dynamics for water contents >6.5 wt %.[11]

For an intermediate value of E_{a1}, sufficiently low for shear-induced coalescence to be activated but sufficiently high to significantly inhibit the reverse fission process, a large number of high-energy micelles will be trapped on the right-hand-side of the coalescence/fission activation barrier. This situation is consistent with the bimodal nature of the spherical micelle distribution at 5.2 wt % (Fig. 3.5D), in which two distinct populations of smaller and larger particles correspond to micelles in States A and B, respectively. In contrast, when E_{a1} is lowered by decreasing the water content (e.g. to 4.2 wt % water), a faster fission rate leads to a more dynamic exchange between States A and

B, resulting in a single averaged population of spherical micelles (Fig. 3.5B). As well, the larger barrier E_{a1} at 5.2 wt % compared to 4.2 wt % forces a greater number of micelles in State B to follow the relatively fast intraparticle relaxation pathway through E_{a2}, explaining the larger quantity of non-spherical micelles in the former case. Conversely, when the water content is increased to the point where E_{a1} is too high for micelle coalescence to be activated (e.g. to 7.2 wt % water), the formation of non-spherical morphologies is precluded, and only spherical micelles are observed (Fig. 3.5E).

The effect of flow rate on microfluidic block copolymer self-assembly was also determined, by investigating micelles prepared at the same three water contents but at high flow rate (~50 μL / min, Fig. 3.7). In contrast to the low flow rate case, only unimodal populations of spherical micelles, with no additional morphologies, are observed for all three water contents. According to our previous results on kinetic polymeric particles formed in similar reactors, the on-chip competition between shear-induced particle coalescence and shear-induced particle breakup favors coalescence at low flow rates and breakup as the flow rate increases.[43] Therefore, for the 4.2 wt % and 5.2 wt % water contents, when the flow rates are increased to ~50 μL / min, the shear-induced coalescence that gives rise to non-spherical morphologies at ~5 μL / min (Fig. 3.5, A and C, respectively) is countered by the dominant mechanism of shear-induced particle breakup, such that cylinders and other higher-aggregation structures cannot form.

Based on the current results, we believe that two alternative mechanisms for the on-chip morphology transformations can be ruled out. The first of these is a shear-induced micellization picture, described in the theoretical work of Jones et al,[65] in which

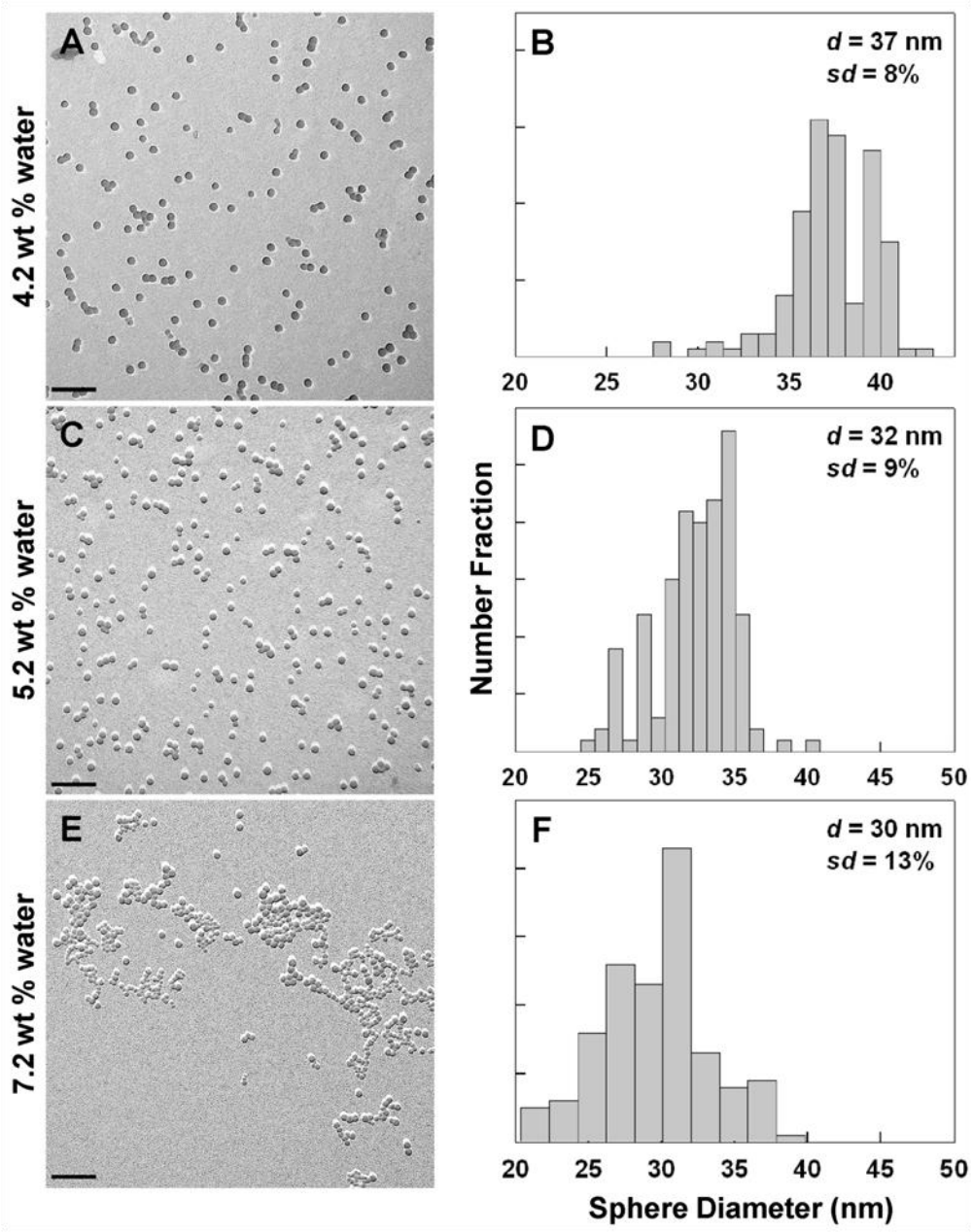

Figure 3.7. The effect of water content on on-chip PS-*b*-PAA micelle morphologies (A, C, and E) and spherical micelle size distributions (B, D, and F) formed in DMF/dioxane mixtures, Q = ~50 μL/min. A, C and D show TEM images of representative micelles formed at 4.2, 5.2 and 7.2 wt % water, respectively; B, D and F show size histograms of spherical micelle populations formed at the corresponding water contents. All scale bars = 200 nm.

micelle aggregation numbers (or their morphologies in the present case) are determined by shear forces at the stage of unimer self-assembly. To eliminate this possible mechanism, we consider that only a very small percentage of micelles will initially form under significant shear, due to the strong localization of high-shear regions in the plug corners. Specifically, a conservative calculation shows that less than 2 % of the liquid plug volume is exposed to the high shear regions during the initial mixing/micellization process.[66] The large percentages of non-spherical structures that we observe under certain conditions (up to 25 % of the total micelle volume) cannot, therefore, be accounted for by micellization under shear. While it is not possible to completely shelter the bulk liquid from high shear during the short mixing process, the rapid mixing achieved with the multiphase microfluidic system effectively separates the mixing function, which initiates micelle formation, from the downstream shear processing function, which induces the morphological transformation.

A second mechanism that merits consideration is one in which the directionality of shear forces templates the formation of specific micelle morphologies. For example, cylindrical micelles could be formed via the one-dimensional assembly of spherical micelles along the direction of shear. However, we eliminate such a "shear-templating" mechanism based on the presence of other, non-directional, morphologies such as bilayer sheets (Fig. 3.3, C and D) which also form as a result of shear exposure. Rather, as described above, our results strongly support a mechanism in which the role of on-chip shear forces is simply to increase the rate of micelle coalescence in a statistical manner, such that colloids with aggregation numbers well above the mean equilibrium value are generated. The subsequent relaxation of these aggregates via intramicellar pathways is

then guided by internal molecular forces (and not shear forces), ultimately forming the micelle morphology that allows the greatest decrease in local free energy relative to the initial shear-induced aggregation state.

3.3.4. Non-Spherical Micelles with Mirror Image Symmetry From On-Chip Self-Assembly

Several of the on-chip morphologies formed at low flow rate, including looped cylinders, Y-junctions, and networks of linear and looped cylinders, are very reminiscent of nonergodic micelles of poly(1,2-butadiene)-*block*-poly(ethylene oxide) (PB-*b*-PEO) in aqueous solution described previously by Bates and coworkers.[14] Although micelles in that work were not formed in the presence of strong external shear fields, the morphological similarities with our system are consistent with on-chip micelles being nonergodic on the time scale of our microfluidic experiments. In the work of Bates, complex micelles with unusual mirror symmetry are attributed to network fragmentation by stirring or sonication followed by intraparticle redistribution of molecules to balance the free energy, under conditions where interparticle exchange of material cannot occur on experimental time scales.[14] Interestingly, in addition to cylinder network fragments of various sizes formed on-chip (e.g., Fig. 3.8A), we find a number of compelling complex micelles with mirror symmetry (Fig. 3.8, B to E). This further highlights the importance of intraparticle chain rearrangements in the on-chip formation of the observed micelle morphologies.

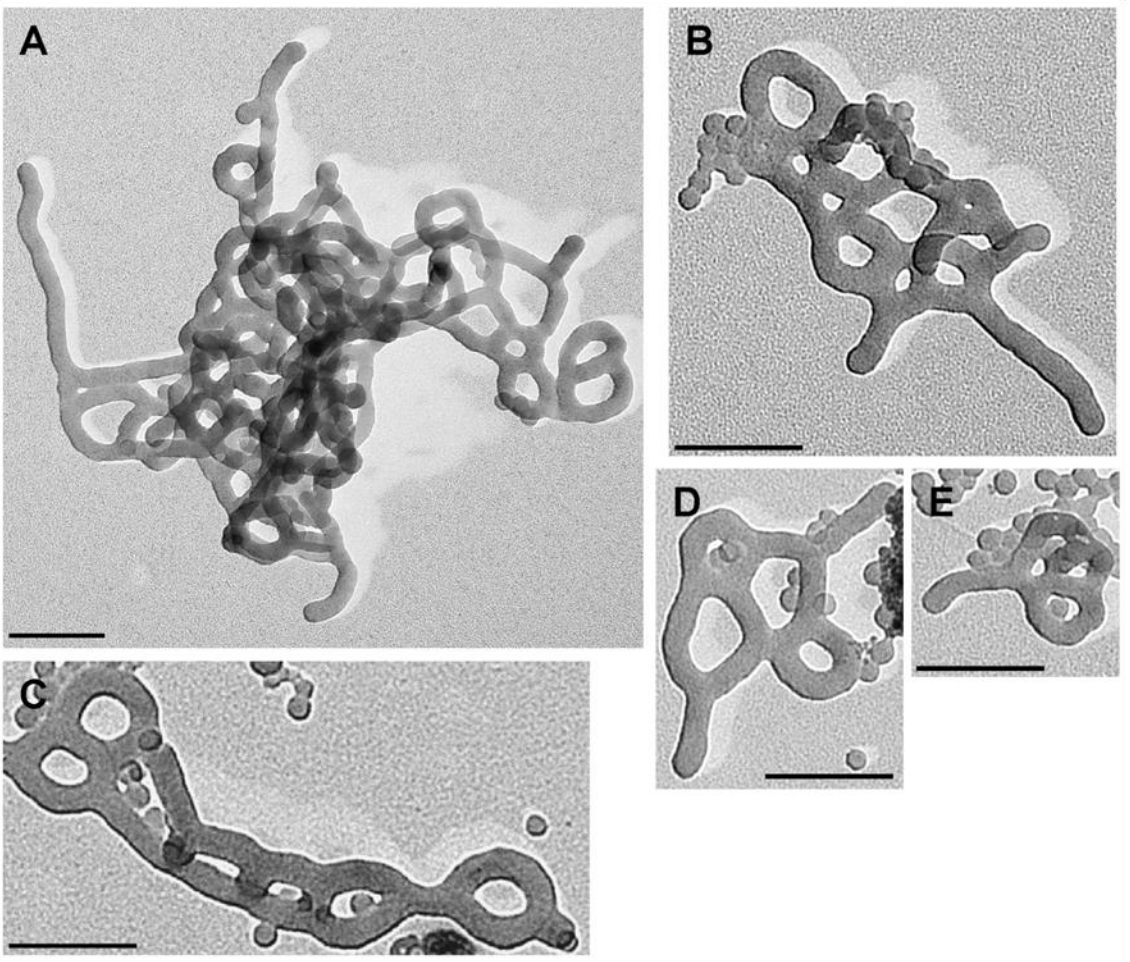

Figure 3.8. Further examples of PS-*b*-PAA micellar structures formed on-chip, Q = ~5 μL/min, in DMF/dioxane mixtures containing 4.2 wt % water (A,B, D, and E) or 5.2 wt % water (C). TEM images B to E highlight the prominent occurrence of non-spherical micelles with mirror image symmetry from on-chip self-assembly. All scale bars = 200 nm.

In contrast to PB-*b*-PEO micelles in water, which showed nonergodic behavior over a time scale of months to years, the off-chip relaxation of PS-*b*-PAA micelles formed on-chip can be monitored over a time scale of days to weeks (Fig. 3.9). For relaxation studies, micellar dispersions are collected from the chip and allowed to sit for various times (t) before kinetic trapping by dumping into excess water; $t = 0$ represents samples collected with immediate off-chip trapping, giving a mixture of spherical and non-spherical morphologies as discussed above (Fig. 3.9, A and C for 4.2 and 5.2 wt % water, respectively). As shown in Fig. 3.9, B and D, after sufficient off-chip time for both water contents, $t = 7$ days for 4.2 wt % (Fig. 3.9B) and $t = 28$ days for 5.2 wt % (Fig. 3.9D), the non-spherical micelles disappear completely, leaving only uniform populations of spheres. Since spherical micelles have been shown to be the equilibrium morphology at both of these water contents, the disappearance of non-spherical micelles is consistent with the relaxation of shear-induced structures toward global equilibrium, following their transfer to off-chip quiescent conditions. It is worth noting that the times required for the disappearance of cylindrical structures, on the time scale of days, are extremely long compared to the on-chip residence time (280 s); this explains why significant on-chip relaxation does not occur, such that shear-induced morphologies could be kinetically trapped off-chip for observation.

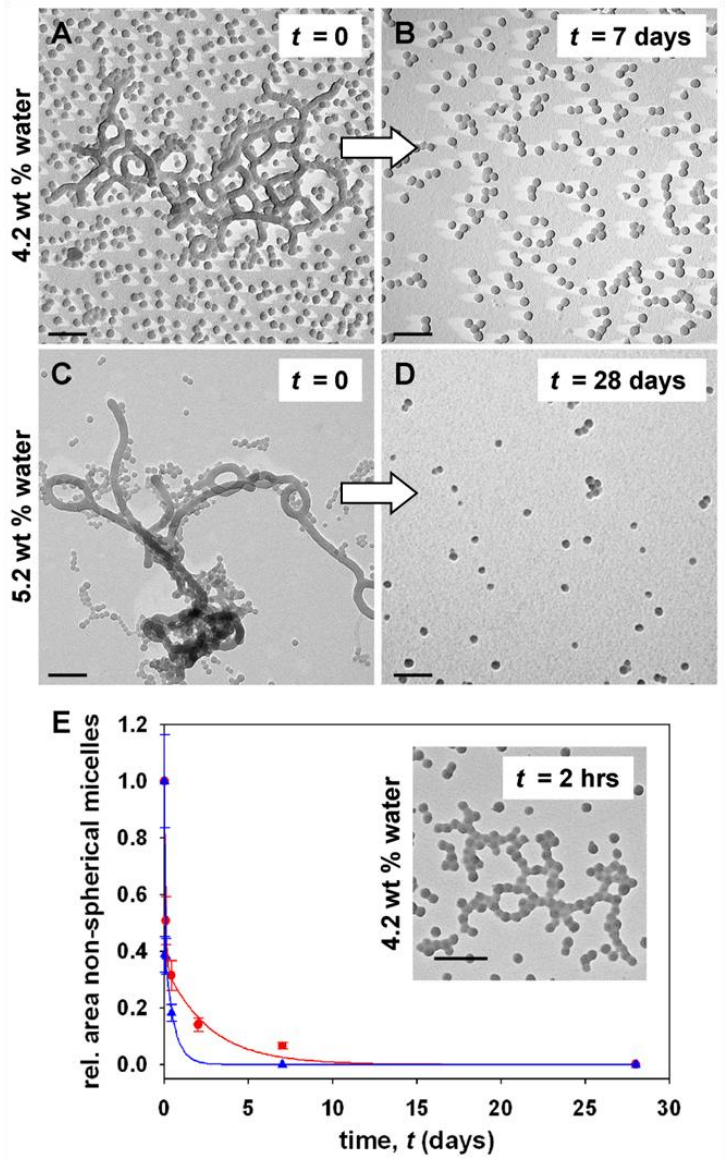

Figure 3.9. Off-chip relaxation kinetics of non-spherical micelles formed on-chip (Q = ~5 μL/min) at two different water contents. A and C show TEM images of immediately-trapped (t = 0) mixtures of spherical and non-spherical micelles formed at 4.2 and 5.2 wt % water, respectively. TEM images in B and D indicate that only spherical micelles remain at both water contents after sufficient off-chip relaxation time (t = 7 and 28 days for 4.2 and 5.2 wt % water, respectively). In E, the relative area of non-spherical micelles is plotted vs. t for 4.2 wt % water (blue triangles) and 5.2 wt % water (red circles), with mean decay times of 26 s and 5200 s, respectively, determined from fits to bi-exponential decay functions (solid blue and red curves). The inset to E shows an example of transition structures suggesting break-up of cylinders into spheres during off-chip relaxation at 4.2 wt % water. All scale bars = 200 nm.

3.3.5. Off-Chip Relaxation Kinetics of Non-Spherical Micelles Formed On-Chip

The off-chip relaxation kinetics of non-spherical micelles can be quantified by tracking the time-dependent decrease of their relative area for 4.2 and 5.2 wt % water dispersions. Since these samples show different initial percentages of non-spherical micelles, as discussed earlier, the two decay functions are compared by normalizing each data point with respect to the initial areal percentage value at t = 0. Fig. 3.9E shows the resulting decay plots for 4.2 and 5.2 wt % water cases, indicating slower off-chip disappearance of non-spherical structures at higher water content. We found that neither data set could be fit to a single exponential decay, although both plots fit reasonably well to biexponential decay functions:

$$rel.\ area\ nonspherical\ micelles = ae^{-t/\tau_1} + be^{-t/\tau_2} \quad \textbf{(3.3)}$$

The individual fast and slow decay times from the fit, τ_1 and τ_2, are probably not physically meaningful, although they characterize the distribution of decay times in the collected samples. Mean decay times for each fit were calculated using

$$\bar{\tau} = \left(\frac{a}{a+b}\right)\tau_1 + \left(\frac{b}{a+b}\right)\tau_2, \quad \textbf{(3.4)}$$

giving 26 s for the 4.2 wt % water sample and 5200 s (~2 h) for the 5.2 wt % water sample.

Along with different relaxation rates, a more detailed analysis of TEM images provides evidence for different off-chip relaxation mechanisms following on-chip micelle formation at 4.2 and 5.2 wt % water. The inset to Fig. 3.9E shows an example of prominent aggregates observed between t = 10 min and t = 120 min in dispersions formed at 4.2 wt % water, which appear to be transition structures formed by cylinder networks

breaking into spheres in the manner of Rayleigh instabilities in liquid strands.[67] The absence of similar structures during relaxation of the 5.2 wt % water sample suggests that cylinder breakup is not a prominent relaxation mechanism in that case, presumably due to stronger electrosteric repulsion between proximal spheres. This difference implies that the off-chip transition between non-spherical and spherical micelles at 5.2 wt % water occurs via the alternative relaxation mechanism of unimer exchange, with larger aggregates progressively releasing block copolymer chains into solution which then reassemble into more stable spheres.

Additional support for these different relaxation mechanisms comes from following the evolution of spherical micelle size distributions as a function off-chip time (Fig. 3.10). Size distributions for 4.2 and 5.2 wt % water are shown on the left-hand and right-hand sides of the figure, respectively, for increasing off-chip times, *t*, moving down each column. The equilibrium (off-chip) mean sphere sizes for both water contents are indicated as a dashed line in the histograms. For 4.2 wt % water, no changes in the position and shape of the distribution are observed in the first 2 hours off-chip (d = 41 nm), although by 10 hours a clear shift to larger spherical micelles has occurred (d = 45 nm), away from the equilibrium sphere size (d = 29 nm). This unexpected shift can be explained by the process of cylinder breakup and the resulting generation of daughter spheres, whose sizes are governed by local wave instabilities that develop in the cylinder during relaxation rather than by a global free energy minimum. Following the near-complete disappearance of non-spherical micelles within ~1 day at 4.2 wt % water (Fig. 3.9), the resulting spheres show no evidence of approaching their equilibrium size even after 28 days (Fig. 3.10). We conclude that the relatively fast off-chip relaxation process

of cylinder breakup leads to nonergodic spherical micelles kinetically trapped within a local free energy minimum. In contrast, the size distributions of spherical micelles show very different off-chip evolution at 5.2 wt % water. In this case, the bimodal distribution discussed previously (t = 0) rapidly converges to a unimodal sphere population (t = 2 hours, d = 36 nm) centered close to the equilibrium size (d = 35 nm), which then persists for the remainder of the monitored time off-chip. This trend corroborates the off-chip relaxation mechanism of unimer exchange at this water content. By this pathway, the cylinder networks disappear more gradually than by cylinder breakup (Fig. 3.9), although in a manner that allows global equilibrium to be reached on a shorter time scale.

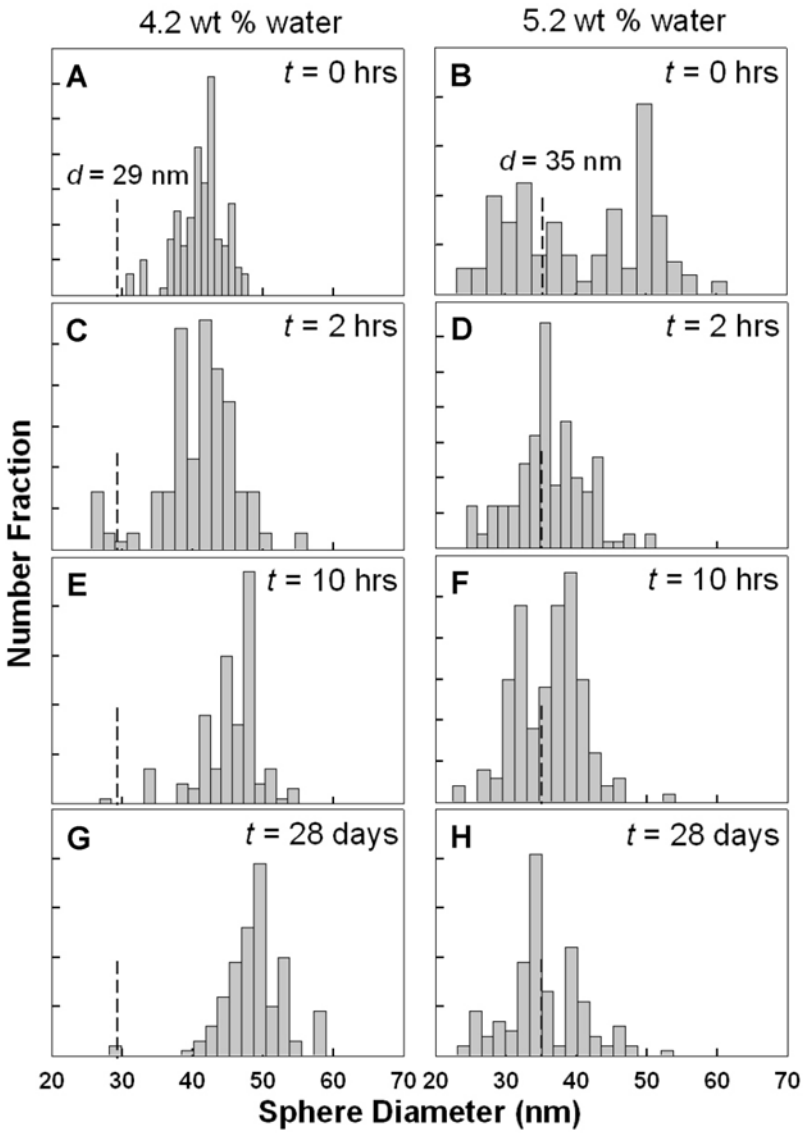

Figure 3.10. Evolution of spherical micelle size distributions as a function off-chip relaxation time, *t*, for the two on-chip samples (4.2 and 5.2 wt % water) described in Figure 3.9. The expected equilibrium mean size of spherical micelles under the same chemical conditions, based on off-chip micellization experiments at 4.2 or 5.2 wt % water followed by two weeks equilibration (Table 3.2), is indicated as a dashed line in the histograms.

3.4. Conclusions

In this chapter, we have demonstrated that the solution self-assembly of amphiphilic block copolymers in a gas-liquid multiphase microfluidic reactor provides flow-directed variation of micelle morphologies due to the unique on-chip shear environment. Under chemical conditions that form equilibrium spherical micelles off-chip, a range of non-spherical nanostructures, including bilayer lamellae and networks of cylinders, can be generated on-chip. The resulting nanostructures are varied using a combination of chemical (bottom-up) and flow (top-down) parameters, and can be kinetically trapped off-chip by collection into excess water. A micelle formation mechanism of shear-induced collision-coalescence followed by intraparticle chain rearrangements is proposed for microfluidic self-assembly. Finally, the off-chip micelle relaxation processes are analyzed under different chemical conditions. Top-down directed molecular self-assembly in microfluidic reactors opens up new opportunities for processing control of functional colloidal nanostructures for a wide range of applications ranging from imaging to drug-delivery.

3.5. References

1. Wang, C. W.; Sinton, D.; Moffitt, M. G., *J. Am. Chem. Soc.* **2011,** *133* (46), 18853-18864.

2. Zhang, L. F.; Eisenberg, A., *Science* **1995,** *268* (5218), 1728-1731.

3. Zhang, L. F.; Eisenberg, A., *J. Am. Chem. Soc.* **1996,** *118* (13), 3168-3181.

4. Yu, K.; Zhang, L. F.; Eisenberg, A., *Langmuir* **1996,** *12* (25), 5980-5984.

5. Zhang, L. F.; Yu, K.; Eisenberg, A., *Science* **1996,** *272* (5269), 1777-1779.

6. Shen, H. W.; Zhang, L. F.; Eisenberg, A., *J. Phys. Chem. B* **1997,** *101* (24), 4697-4708.

7. Yu, Y. S.; Eisenberg, A., *J. Am. Chem. Soc.* **1997,** *119* (35), 8383-8384.

8. Zhang, L. F.; Shen, H. W.; Eisenberg, A., *Macromolecules* **1997,** *30* (4), 1001-1011.

9. Yu, Y. S.; Zhang, L. F.; Eisenberg, A., *Macromolecules* **1998,** *31* (4), 1144-1154.

10. Discher, B. M.; Won, Y. Y.; Ege, D. S.; Lee, J. C. M.; Bates, F. S.; Discher, D. E.; Hammer, D. A., *Science* **1999,** *284* (5417), 1143-1146.

11. Zhang, L. F.; Eisenberg, A., *Macromolecules* **1999,** *32* (7), 2239-2249.

12. Shen, H. W.; Eisenberg, A., *J. Phys. Chem. B* **1999,** *103* (44), 9473-9487.

13. Discher, D. E.; Eisenberg, A., *Science* **2002,** *297* (5583), 967-973.

14. Jain, S.; Bates, F. S., *Science* **2003,** *300* (5618), 460-464.

15. Cui, H. G.; Chen, Z. Y.; Zhong, S.; Wooley, K. L.; Pochan, D. J., *Science* **2007,** *317* (5838), 647-650.

16. Wang, X. S.; Guerin, G.; Wang, H.; Wang, Y. S.; Manners, I.; Winnik, M. A., *Science* **2007,** *317* (5838), 644-647.

17. Forster, S.; Plantenberg, T., *Angew Chem Int Edit* **2002,** *41* (5), 689-714.

18. Liu, G. J., *Self-Assembled Nanomaterials Ii: Nanotubes* **2008,** *220*, 29-64.

19. Li, Z. B.; Kesselman, E.; Talmon, Y.; Hillmyer, M. A.; Lodge, T. P., *Science* **2004,** *306* (5693), 98-101.

20. Li, Z. B.; Hillmyer, M. A.; Lodge, T. P., *Nano Lett.* **2006,** *6* (6), 1245-1249.

21. LaRue, I.; Adam, M.; Pitsikalis, M.; Hadjichristidis, N.; Rubinstein, M.; Sheiko, S. S., *Macromolecules* **2006,** *39* (1), 309-314.

22. Allen, C.; Maysinger, D.; Eisenberg, A., *Colloids and Surfaces B-Biointerfaces* **1999,** *16* (1-4), 3-27.

23. Geng, Y.; Dalhaimer, P.; Cai, S. S.; Tsai, R.; Tewari, M.; Minko, T.; Discher, D. E., *Nat. Nanotechnol.* **2007,** *2* (4), 249-255.

24. Gonzalez, D. C.; Savariar, E. N.; Thayumanavan, S., *J. Am. Chem. Soc.* **2009,** *131* (22), 7708-7716.

25. Torchilin, V. P., *Adv. Drug Delivery Rev.* **2002,** *54* (2), 235-252.

26. Nasongkla, N.; Bey, E.; Ren, J. M.; Ai, H.; Khemtong, C.; Guthi, J. S.; Chin, S. F.; Sherry, A. D.; Boothman, D. A.; Gao, J. M., *Nano Lett.* **2006,** *6* (11), 2427-2430.

27. Wu, W. C.; Chen, C. Y.; Tian, Y. Q.; Jang, S. H.; Hong, Y. N.; Liu, Y.; Hu, R. R.; Tang, B. Z.; Lee, Y. T.; Chen, C. T.; Chen, W. C.; Jen, A. K. Y., *Adv. Funct. Mater.* **2010,** *20* (9), 1413-1423.

28. Rockford, L.; Mochrie, S. G. J.; Russell, T. P., *Macromolecules* **2001,** *34* (5), 1487-1492.

29. Kim, S. O.; Solak, H. H.; Stoykovich, M. P.; Ferrier, N. J.; de Pablo, J. J.; Nealey, P. F., *Nature* **2003,** *424* (6947), 411-414.

30. Segalman, R. A.; Hexemer, A.; Kramer, E. J., *Macromolecules* **2003,** *36* (18), 6831-6839.

31. Cheng, J. Y.; Mayes, A. M.; Ross, C. A., *Nat. Mater.* **2004,** *3* (11), 823-828.

32. Stoykovich, M. P.; Muller, M.; Kim, S. O.; Solak, H. H.; Edwards, E. W.; de Pablo, J. J.; Nealey, P. F., *Science* **2005,** *308* (5727), 1442-1446.

33. Cheng, J. Y.; Rettner, C. T.; Sanders, D. P.; Kim, H. C.; Hinsberg, W. D., *Adv Mater* **2008,** *20* (16), 3155-3158.

34. Chen, Q. J.; Zhao, H.; Ming, T.; Wang, J. F.; Wu, C., *J. Am. Chem. Soc.* **2009,** *131* (46), 16650-16651.

35. Zhang, M.; Wang, M. F.; He, S.; Qian, J. S.; Saffari, A.; Lee, A.; Kumar, S.; Hassan, Y.; Guenther, A.; Scholes, G.; Winnik, M. A., *Macromolecules* **2010,** *43* (11), 5066-5074.

36. Nie, Z. H.; Xu, S. Q.; Seo, M.; Lewis, P. C.; Kumacheva, E., *J. Am. Chem. Soc.* **2005,** *127* (22), 8058-8063.

37. Xu, S. Q.; Nie, Z. H.; Seo, M.; Lewis, P.; Kumacheva, E.; Stone, H. A.; Garstecki, P.; Weibel, D. B.; Gitlin, I.; Whitesides, G. M., *Angew Chem Int Edit* **2005,** *44* (5), 724-728.

38. Seo, M.; Nie, Z. H.; Xu, S. Q.; Mok, M.; Lewis, P. C.; Graham, R.; Kumacheva, E., *Langmuir* **2005,** *21* (25), 11614-11622.

39. Karnik, R.; Gu, F.; Basto, P.; Cannizzaro, C.; Dean, L.; Kyei-Manu, W.; Langer, R.; Farokhzad, O. C., *Nano Lett.* **2008,** *8* (9), 2906-2912.

40. Xu, Q. B.; Hashimoto, M.; Dang, T. T.; Hoare, T.; Kohane, D. S.; Whitesides, G. M.; Langer, R.; Anderson, D. G., *Small* **2009,** *5* (13), 1575-1581.

41. Schabas, G.; Yusuf, H.; Moffitt, M. G.; Sinton, D., *Langmuir* **2008,** *24* (3), 637-643.

42. Schabas, G.; Wang, C. W.; Oskooei, A.; Yusuf, H.; Moffitt, M. G.; Sinton, D., *Langmuir* **2008,** *24* (19), 10596-10603.

43. Wang, C. W.; Oskooei, A.; Sinton, D.; Moffitt, M. G., *Langmuir* **2010,** *26* (2), 716-723.

44. Brown, L.; McArthur, S. L.; Wright, P. C.; Lewis, A.; Battaglia, G., *Lab Chip* **2010,** *10* (15), 1922-1928.

45. Jahn, A.; Vreeland, W. N.; Gaitan, M.; Locascio, L. E., *J. Am. Chem. Soc.* **2004,** *126* (9), 2674-2675.

46. Steinbacher, J. L.; Moy, R. W. Y.; Price, K. E.; Cummings, M. A.; Roychowdhury, C.; Buffy, J. J.; Olbricht, W. L.; Haaf, M.; McQuade, D. T., *J. Am. Chem. Soc.* **2006,** *128* (29), 9442-9447.

47. Malmstadt, N.; Nash, M. A.; Purnell, R. F.; Schmidt, J. J., *Nano Lett.* **2006,** *6* (9), 1961-1965.

48. Hautekeer, J. P.; Varshney, S. K.; Fayt, R.; Jacobs, C.; Jerome, R.; Teyssie, P., *Macromolecules* **1990,** *23* (17), 3893-3898.

49. Zhong, X. F.; Varshney, S. K.; Eisenberg, A., *Macromolecules* **1992,** *25* (26), 7160-7167.

50. Yen, B. K. H.; Gunther, A.; Schmidt, M. A.; Jensen, K. F.; Bawendi, M. G., *Angew Chem Int Edit* **2005,** *44* (34), 5447-5451.

51. Oskooei, S. A. K.; Sinton, D., *Lab Chip* **2010,** *10* (13), 1732-1734.

52. Khan, S. A.; Gunther, A.; Schmidt, M. A.; Jensen, K. F., *Langmuir* **2004,** *20* (20), 8604-8611.

53. Gunther, A.; Jensen, K. F., *Lab Chip* **2006,** *6* (12), 1487-1503.

54. Due to discrepancies between actual and programmed (nominal) gas flow rates arising from the compressible nature of the gas and the high gas/liquid interfacial tension, actual gas flow rates were calculated from from image analysis of the flow and are reported in Supporting Information (Table 3.1).

55. Zaccone, A.; Gentili, D.; Wu, H.; Morbidelli, M., *J. Chem. Phys.* **2010,** *132* (13), 1349031-1309036.

56. Zaccone, A.; Wu, H.; Gentili, D.; Morbidelli, M., *Phys Rev E* **2009,** *80* (5), 0514041-0514048.

57. Melis, S.; Verduyn, M.; Storti, G.; Morbidelli, M.; Baldyga, J., *AIChE J.* **1999,** *45* (7), 1383-1393.

58. Zinchenko, A. Z.; Davis, R. H., *Phys. Fluids* **1995,** *7* (10), 2310-2327.

59. For calculating P_e, D_0 was estimated from off-chip dynamic light scattering data of similar sized PS-*b*-PAA micelles under the same temperature and solvent conditions.

60. Jusufi, A.; Likos, C. N.; Ballauff, M., *Colloid Polym. Sci.* **2004,** *282* (8), 910-917.

61. Zhang, L. F.; Eisenberg, A., *Macromolecules* **1996,** *29* (27), 8805-8815.

62. Grishchuk, A. A.; Estrin, Y. I., *Russ J Appl Chem+* **2007,** *80* (11), 1940-1944.

63. Assuming that the internal densities and heights of spherical and nonspherical micelles are the same, the areal percentage of non-spherical micelles in TEM images should be roughly equivalent to their weight percentage relative to the entire micelle population.

64. Dormidontova, E. E., *Macromolecules* **1999,** *32* (22), 7630-7644.

65. Jones, J. L.; Marques, C. M.; Joanny, J. F., *Macromolecules* **1995,** *28* (1), 136-142.

66. This mixing channel geometry run under similar conditions resulted in complete mixing of the liquid plug within 2 mm of the 10 mm mixing chamber, or 0.5 s at the low flow rate. While this short channel length (and short duration) is sufficient to mix the reactants in the liquid plug, it is not sufficient to expose a significant volume of the liquid to the high shear hot spots in the corners of the liquid plug.

67. Reiter, G., *Phys. Rev. Lett.* **1992,** *68* (1), 75-78.

CHAPTER 4

DEPENDENCE OF CHEMICAL PARAMETERS ON FLOW-DIRECTED BLOCK COPOLYMER MICELLE MORPHOLOGIES IN TWO-PHASE MICROFLUIDIC REACTORS

4.1. Introduction

Conventional morphological control over block copolymer self-assembly in solution is from the bottom-up, as has been demonstrated via variation of chemical parameters that are known to directly influence intermolecular interactions.[1-28] In particular, various groups have investigated the effect of block copolymer composition,[10-12, 18] polymer concentration,[17, 22] choice of solvent,[15, 21, 28] pH and ionic strength[9, 13, 17, 23] on structures obtained by micelle formation. For example, Eisenberg and co-workers observed that PS-*b*-PAA micelle morphologies transformed from spheres, to cylinders, to vesicles as the THF content in mixtures of THF/DMF/water was increased, due to increased contributions from PS chain stretching with increased core swelling by the less-polar solvent.[15, 21, 28] The same group showed that in similar systems of PS-*b*-PAA, adding various amounts of salt, acid or base lead dramatic differences in micelle morphologies, attributed to changes in the extent of electrostatic repulsion between PAA chains.[9, 13, 17] In many cases, these chemically-induced morphological transformations are found to be reversible, suggesting that the structures are controlled by thermodynamics.[14, 17, 26] In fact, empirical equilibrium phase diagrams for block copolymer micelle morphologies as a function of chemical conditions have been determined. However, under conditions where interfacial tension between the microphase-separated blocks is extremely high, or chain dynamics are extremely slow, the sluggish reversibility of block copolymer self-assembly leads to strong kinetic contributions to the observed micelle morphologies.[14, 17, 26]

In the last chapter, we investigated the self-assembly of PS-*b*-PAA block copolymers under specific chemical conditions (75/25 DMF/dioxane, various water

contents) on a multiphase gas-liquid microfluidic chip. We showed that an array of non-spherical morphologies (cylinders, Y-junctions, bilayers, and networks) were formed on-chip under chemical conditions that produced only spherical micelles in the bulk. These results indicated that top-down control of block copolymer micelle morphologies could be exerted through the localized high-shear environment of the liquid plugs in the gas-liquid microfluidic reactor. Specifically, we proposed a two-part mechanism in which shear-induced collision/coalescence of thermodynamically-stable micelle structures produced high-free energy aggregates which then relaxed to various kinetically-stable morphologies via intramicellar chain rearrangements.

Despite this demonstrated influence of shear forces on-chip, it is reasonable to suggest that chemical forces should also play an important role in morphologies formed by on-chip self-assembly. In the previous chapter, some direct evidence for the interplay of both bottom-up (intermolecular) and top-down (external shear) forces was provided by the observed influence of water content on the relative amounts of shear-induced morphologies on-chip. The effects of water content in that chapter were explained by the influence of the amount of water on the kinetics of on-chip processes of interparticle collision/coalescence and intraparticle rearrangements. In addition, chemical forces should also have a thermodynamic influence on global equilibrium states,[14, 17, 26] and consequently on the local free energy minima that will be reached via intraparticle rearrangements following collision/coalescence.

In this chapter, we provide a systematic study of chemical parameters on the observed on-chip morphologies, with comparison to the structures formed off-chip under equivalent chemical conditions. Specifically, we investigate the effects of different

solvent mixtures, water contents, polymer concentrations and added salt. We show that these chemical parameters have a considerable influence on the thermodynamics and kinetics of on-chip micelle formation, which in turn governs the resulting micelle morphologies. More significantly, by investigating these chemical parameters, the toolbox of morphological control by combining chemical (bottom-up) and shear (top-down) forces using microfluidics is expanded considerably. We rationalize our findings based on a combination of kinetic considerations and the position of micelles on an empirical phase diagram determined from bulk self-assembly under different chemical conditions. A notable result in this chapter is the formation of vesicles on-chip under chemical conditions that form no vesicles off-chip. Vesicles are extremely appealing colloidal structures due to their potential applications in drug delivery, sensing and medical imaging,[27, 29, 30] and this work provides the first example of polymer vesicles (polymersomes) generated as a result of processing in external force fields.

4.2. Experimental Section

4.2.1. Materials

The composition of the polystyrene-*block*-poly(acrylic acid) sample used in this study was PS(665)-*b*-PAA(68). Anionic polymerization was employed to synthesize the associated polystyrene-*block*-poly(*tert*-butyl acrylate) block copolymer, followed by hydrolysis of the ester block. Numbers in parentheses refer to number-average degrees of polymerization of each block. The reagents, Dimethylformamide (DMF) (Aldrich, 99.9+%, HPLC grade, H_20 < 0.03%) and 1,4-dioxane Aldrich, 99.0%, reagent grade, H_20 < 0.05% were used as received without further purification.

4.2.2. Critical Water Content Determination

Static light scattering measurements were carried out in order to accurately determine the critical water content (cwc) of PS(665)-*b*-PAA(68) for different chemical variables (polymer concentrations, solvent mixtures and salt contents) applied in this study,. Light scattering experiments were performed on a Brookhaven Instruments photon correlation spectrometer equipped with a BI-200SM goniometer, a BI-9000AT digital autocorrelator, and a Melles Griot He-Ne Laser (632.8 nm) with a maximum power output of 75 mW. For instance, to determine the cwc of 0.33 wt % PS(665)-*b*-PAA(68) in pure DMF, stock solution was prepared by adding DMF solvent to a copolymer concentration of 0.66 wt %. The stock solution was then filtered through a Teflon syringe membrane filter with a nominal pore size of 0.45 μm (National Scientific Company) into pre-cleaned scintillation vials. Next, the stock solution was diluted DMF solvent mixture filtered through two Teflon syringe filters with nominal pore size of 0.20

μm (National Scientific Company) connected in series to give a polymer concentration of 0.33 wt %. Deionized water was next added dropwise to ~6 g of the solution in successive 0.02 - 0.05 g quantities via a microsyringe equipped with a membrane filter (Life Sciences) with nominal pore size of 0.20 μm. After each addition of water, the solution was agitated with a vortexer to aid mixing. The scattered light intensity was recorded 15 min after vortexing to allow the solution to equilibrate. All measurements were carried out at a scattering angle of 90^{o} and a temperature of 23 ^{o}C. The cwc thus obtained DMF (Figure 4.2) was 2.8 ± 0.1 wt %. The cwc determinations of other solvent mixtures were carried out in similar fashion. We also carried out cwc determinations for solutions under different chemical conditions, such as different polymer concentration and salt contents. For both of these measurements, the solvent used was the same as the last chapter (75/25 w/w DMF/Dioxane) which serves as a basis for comparisons. To determine the cwc for 1.0 wt % of PS(665)-*b*-PAA(68) in 75/25 w/w DMF/Dioxane, a stock solution of 2 wt % in 75/25 w/w DMF/Dioxane was used. It was diluted down to 1.0 wt % polymer solution in 75/25 w/w DMF/Dioxane using similar method. The cwc determination for the added salt effect in 75/25 w/w DMF/Dioxane was carried out using stock solution of 0.66 wt%. The stock solution was treated with filtered 0.2 M NaCl solution in deionized water until salt contents of 20% equivalent of the polyacrylic acid unit (R = 0.20) has been added. Then the stock solution was diluted down to 0.33 wt% with filtered 75/25 w/w DMF/Dioxane for cwc measurement.

4.2.3. Off-Chip Micelle Preparation

Morphologies formed on-chip (Fig. 4.1A) under different chemical and flow conditions were compared to off-chip control experiments in which block copolymer

micelles were prepared in the following manner. Three water contents (cwc + 1, 2 and 4 wt% water) were investigated for each solvent compositions. For instance, to prepare off-chip micelle solution in pure DMF, water contents of 1, 2 and 4 wt% above its respective cwc were used. To the three vials, each containing ~5 mL of 0.33 wt % PS(665)-*b*-PAA(68) in DMF, deionized water was added dropwise at a rate of 20 μL every 10 s with moderate magnetic stirring (600 rpm) until the various target water concentrations were reached (1, 2 and 4 wt % above cwc). The resulting micelles were then allowed to equilibrate for 2 weeks without stirring, followed by kinetic trapping via transfer into ~50 mL deionized water. The colloidal dispersions were finally dialyzed against deionized water to remove residual organic solvent.

In addition, to compare the effects of polymer concentrations and salt contents, we prepared micelles at 2 wt % above the cwc in 75/25 w/w DMF/Dioxane in a manner similar to that described above.

4.2.4. Microfluidic Chip Fabrication

High-quality silicon wafers (Silicon Quest International, CA) and negative photoresist, SU-8 100 (Microchem Inc., MA) were used to fabricate negative masters. Prior to use, new silicon wafers were heated on a hotplate to at 200 ºC for 20 minutes to remove all moisture. 150 μm thick of SU-8 films were spin-coated onto the silicon wafers, followed by heating at 95 ºC for 60 minutes to remove residual SU-8 solvent. A photomask was placed over the film for exposure under UV light for 180 s. The device was heated for additional 20 minutes at 95 ºC. After that, the device was submerged in SU-8 developer (Microchem, MA) until all unexposed photoresist was removed. The

reactor has a set channel depth of 150 μm, and consists of a sinusoidal mixing channel 100 μm wide and 100 mm in length, and a sinusoidal processing channel 200 μm wide and 740 mm in length.

To further stabilize the process of bubble generation, we employed external resistor chips, which were connected in series between the Ar gas tank and the microfluidic chip. These resistors were 1000 mm long, 400 μm wide and 150 μm deep. In operation, these high pressure drop resistors serve to effectively dampen the pressure fluctuations caused by the Ar gas tank and the bubble generation process itself. The resistors were designed in a way that the total pressure drop in the resistors was at least one order of magnitude higher than the pressure drop in the reaction channel.

Microfluidic chips were fabricated from poly(dimethylsiloxane) (PDMS) using a SYLGARD 184 silicon elastomer kit (Dow Corning, MI) with an elastomer base-to-curing agent ratio of 10:1. The elastomer and curing agent were mixed together and degassed in a vacuum chamber. The degassed PDMS was poured onto the negative master in a petri dish and then degassed again until all remaining air bubbles in the PDMS were removed. The PDMS was then heated at 85 ºC until cured (~ 50 mins). The microfluidic chips were cut and peeled off the master, and holes were punched through its reservoirs to allow for the insertion of tubing. A thin PDMS film was formed on a glass slide by spin-coating and was permanently bonded to the base of the microfluidic reactor after both components were exposed to oxygen plasma for 30 s.

4.2.5. Flow Delivery and Control

Pressure-driven flow of liquids to the inlets of the reactors was provided using 250 μL and 1 mL gastight syringes (Hamilton, NV) mounted on syringe pumps (Harvard Apparatus, MA). The microchip was connected to the syringes with 1/16th inch (OD) Teflon tubing (Scientific Products and Equipment, ON). Gas pressure was adjusted by a Ar tank regulator as well as a downstream regulator for fine adjustments (Johnson Controls Inc.). For gas flow, connections were joined using Teflon tubing of 1/16 inch (OD) and 100 μm (ID) (Upchurch Scientific, WA). The liquid flow rate (Q_{liq}) was programmed via the syringe pumps and the gas flow rate (Q_{gas}) was varied by tuning the pressure regulator. Due to the compressible nature of the gas and the high gas/liquid interfacial tension, discrepancies arise between the nominal (programmed) and actual values of Q_{gas}, Q_{gas}/Q_{liq}, and the total flow rate (Q_{total}). Therefore, actual gas flow rates were calculated from the frequency of bubble formation and the average volume of gas bubbles, determined from image analysis of the mean lengths of liquid and gas plugs, L_{liq} and L_{gas}, respectively, under a given flow set of conditions. This method of flow determination has been previously employed in the context of gas-liquid multiphase flow in microfluidic device.[31-33] For all experiments in this chapter, the relative gas-to-liquid flow ratio (Q_{gas}/Q_{liq}.) was ~1, and single nominal total flow rate was investigated: Q_{total} = ~5 μL / min (low flow rate case).

4.2.6. On-Chip Micelle Preparation (Fig 4.1B and C)

For microfluidic self-assembly experiments, three separate liquid streams were combined at equal flow rate to form gas-separated liquid plugs within the reactor: 1. a 1.0

wt % solution of PS(665)-*b*-PAA(68) single chains in DMF/dioxane 2. a separator stream containing DMF/dioxane only; and 3. a solution of DMF/dioxane containing differing deionized water contents. The particular DMF/dioxane w/w ratio depends on the individual runs. Combination of the three liquid streams yielded steady-state on-chip concentrations of 0.33 wt % polymer, identical to the off-chip control experiments, and either 1.0, 2.0 and 4.0 wt % above the cwc, respectively. Microfluidic flow conditions were selected as described in the previous section.

For off-chip analysis of micelle morphologies prepared within the reactor, micellar dispersions were generally collected from the chip following the processing channel into vials containing a large excess (~250 μL) of deionized water, where the particles immediately became kinetically frozen due to the high water content. The solids content of the final mostly-aqueous solution was ~0.25 mg/mL.

Flow visualization of microfluidic experiments and quantification of all the flow conditions was performed with an inverted fluorescence microscopy system operating in transmission mode. Optical images of the reactor were capture using a CCD camera (AF6000 Orca, Hamamatsu, NJ) installed on the inverted microscope (DMI 6000B, LEICA, NJ).

4.2.7. TEM and Image Analysis

Transmission electron microscopy (TEM) of various aqueous micellar dispersions was performed at a Hitachi H-7000 electron microscope operating at 75 kV and a JEOL JEM-1400 microscope operating 80 kV. For TEM imaging, a 10 μL drop of micellar dispersion was deposited onto either a carbon-coated or carbon-coated Formvar 300 mesh

copper grid, and then shadowed with Pt/Pd wire for imaging. For TEM imaging of on-chip prepared samples, the small quantity of dioxane remaining in the final solutions was found to dissolve Formvar substrates, and so carbon-coated grids without Formvar were required for these samples.

Analysis of micellar features (spherical diameters, cylinders' diameters and vesicles' wall thickness and etc.) were carried on images randomly selected from various regions of the TEM grid. They were measured from printouts of multiple regions of the TEM grid where the particles appeared 40,000 to 50,000 times their actual size.

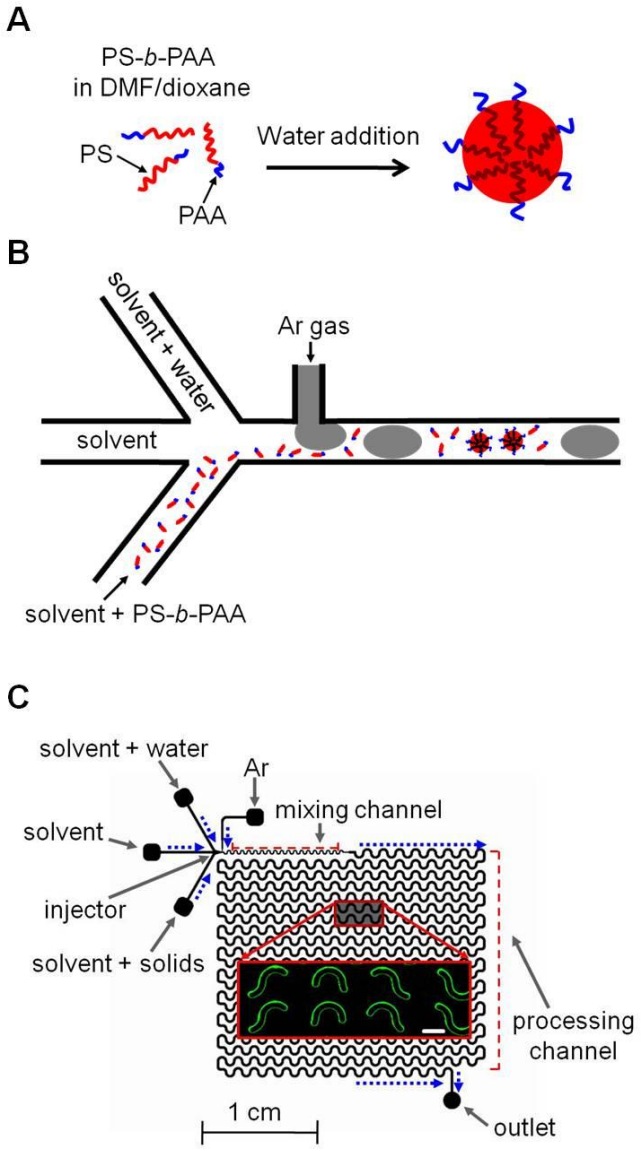

Figure 4.1. PS-*b*-PAA self-assembly process and multiphase microfluidic reactor approach. (A) Schematic of the PS-*b*-PAA assembly process. Red indicates hydrophobic PS blocks, while blue indicates hydrophilic PAA blocks. (B) Cartoon representation of the self-assembly of PS-*b*-PAA into micelles in the multiphase microfluidic reactor. The self-assembly is initiated by mixing of the three liquid stream contents within segmented plugs, which leads to an average cross-stream water content above the critical water content (cwc). (C) Schematic of the microfluidic reactor, showing liquid and gas inlets at the injector, followed by the mixing channel (represented in B); in the subsequent processing channel, the formed micelles experience the shear-induced collisions and morphological transformations discussed in the text, which are trapped by collection into pure water after the outlet. The inset of (C) shows a select optical microscopy image of the reactor under stable operation. The white scale bar indicates 500 μm.

4.3. Results and Discussion

4.3.1. Effect of Solvent Composition on PS-*b*-PAA Morphologies Formed Off-Chip

Before understanding the effect of solvent composition on the on-chip morphologies, it is first necessary to discuss the influence of solvent composition on equilibrium (off-chip) morphologies of PS-*b*-PAA micelles. The morphogenic effect of the organic solvent composition and the water content on PS-*b*-PAA crew-cut micelle morphologies in various mixtures of organic solvents and water has been extensively researched. Two physical parameters that have been used to gauge the polymer-solvent interactions are the solubility parameters of solvent and polymer and the dielectric constant of the solvent. A closer match between the solubility parameters of the solvent and the PS core-forming block will lead to more extensive solvent swelling of the core, contributing greater stretching of the insoluble PS blocks within the resulting micelles, and thus favouring morphologies with lower internal curvature in order to reduce the PS stretching. For this reason, a progressively closer match in solubility parameter between PS and the solvent has been found to lead to morphology transformations from spheres, to cylinders, and then vesicles. On the other hand, the solvent dielectric constant describes the strength of interaction between the solvent and the soluble PAA block. As the dielectric constant decreases, the degree of dissociation of PAA is reduced, leading to a decreased extent of ionization and weaker repulsive interactions between PAA chains; the resulting increase in aggregation number also effects an increase in PS chain stretching, further contributing to morphology transformations from spheres, to cylinders, to vesicles.

For the "crew-cut" copolymer employed in this study, PS(665)-*b*-PAA(68), the above trends were confirmed by investigating off-chip self-assembly in various mixtures of DMF/dioxane at various water contents. The relevant solubility parameters and dielectric constants for this system are given in Table 4.1. Clearly, as the dioxane content

Table 4.1. Some Physical Parameters of Solvents and Polymers.

material	**solubility parameter (δ) ([MPa]$^{1/2}$)**	**dielectric constant (ε)**
DMF	24.8	38.2
Dioxane	20.5	2.2
PS	18.7	

of DMF/dioxane increases, the solubility parameter of the mixture will become closer to the value for the PS block, while the dielectric constant of the mixture will decrease. One result of the increased solvent quality for the PS block with increasing dioxane content is the concomitant increase in the critical water content (cwc) for micelle formation: as the PS blocks are more strongly solvated by the organic solvent, more water is required to precipitate them from the solvent phase. This is shown by the results in Fig. 4.2. The cwc values for PS(668)-*b*-PAA(65) in different DMF/dioxane compositions were carefully determined using the well-established light scattering technique, in which sharp increases in scattering intensity with increasing water content indicate the cwc (Fig. 4.2A).[17] As shown in Fig. 4.2B, the general trend of increasing cwc with increasing dioxane content is exhibited by the data, as expected based on the solubility parameters

and the arguments presented above. In this chapter, we retain the convention adopted in the previous chapter of investigating self-assembly at three different water contents above the cwc for each solvent mixture: cwc + 1, 2, and 4 wt %; however, due to the different cwc values for the different solvent systems (Fig. 4.2B), the absolute water contents for self-assembly are different for each mixture of DMF/dioxane.

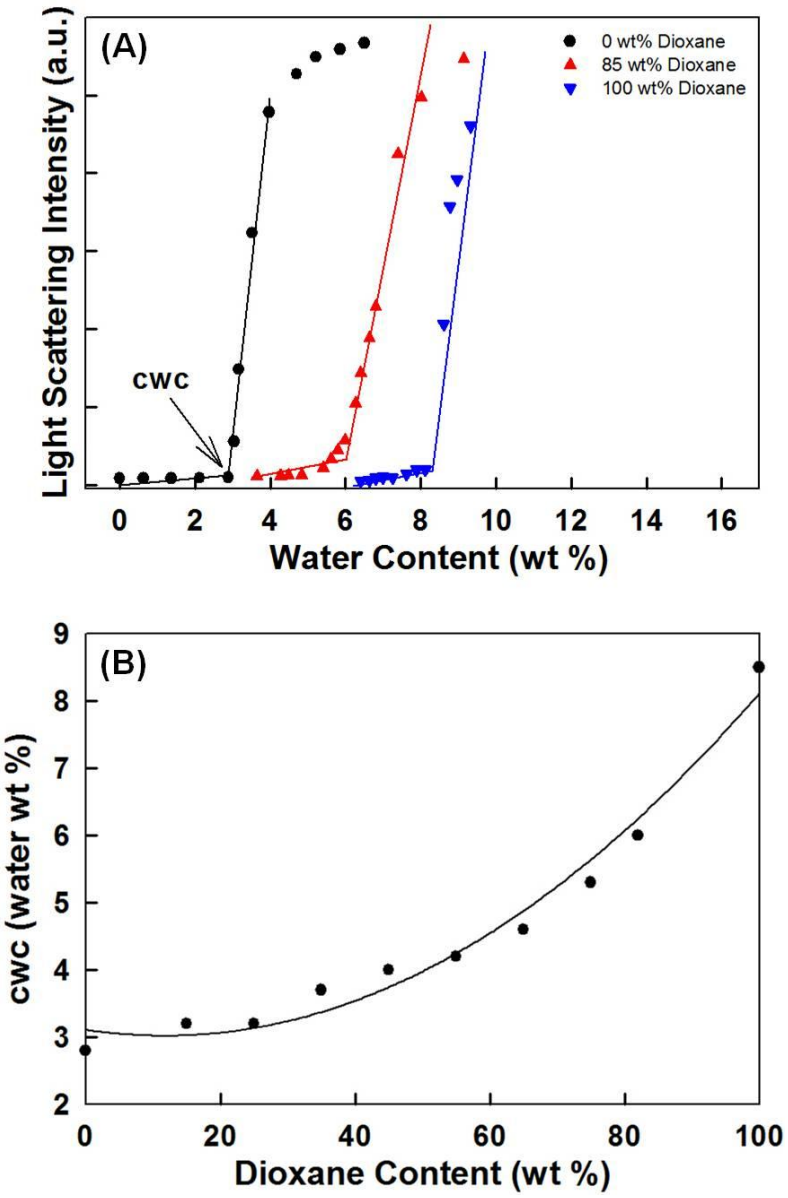

Figure 4.2. Critical water determination of 0.33 wt% PS(665)-*b*-PAA(68) various DMF/dioxane mixed solvent systems using static light scattering method. (A) A example of cwc determination of 0.33 wt% PS (665)-*b*-PAA(68) in DMF. The cwc is determined to be 2.8 ± 0.1 wt%. (B) A plot showing cwc as a function of dioxane content in the DMF/dioxane mixed solvent systems.

The effect of solvent composition on the resulting micelle morphologies is clearly demonstrated in Fig 4.3, which shows TEM images for off-chip self-assembly in DMF/dioxane (w/w) mixtures of 100/0, 35/65, 25/85, and 0/100, each at a relative water content of cwc + 2 wt %. At lower dioxane contents, the sole morphology is spherical (Fig 4.3, A and B) with the mean size of spheres increasing from 33 ± 2 nm (Fig. 4.3A) to 40 ± 2 nm (Fig. 4.3B) as the dioxane content increases from DMF/dioxane compositions of 100/0 to 35/65. A further increase in the dioxane content to 25/85 transforms spherical micelles to long cylinders and vesicles (Fig. 4.3C). Finally, the micelle morphology progresses to pure vesicles in the 0/100 case (pure dioxane, Fig. 4.3D). The observed trends are consistent with the results for similar PS-*b*-PAA copolymers described in refs,[21] and can be explained by a combination of increased solvent swelling of the PS cores and decreased repulsion between PAA chains as the dioxane content of the solvent mixture increases. The resulting increase in PS stretching first effects an increase in core diameter (Fig. 4.3, A and B), followed by a morphological transformation to micelles with progressively lower internal curvature: first to cylinders (Fig. 4.3C), and then to vesicles (Fig. 4.3D).

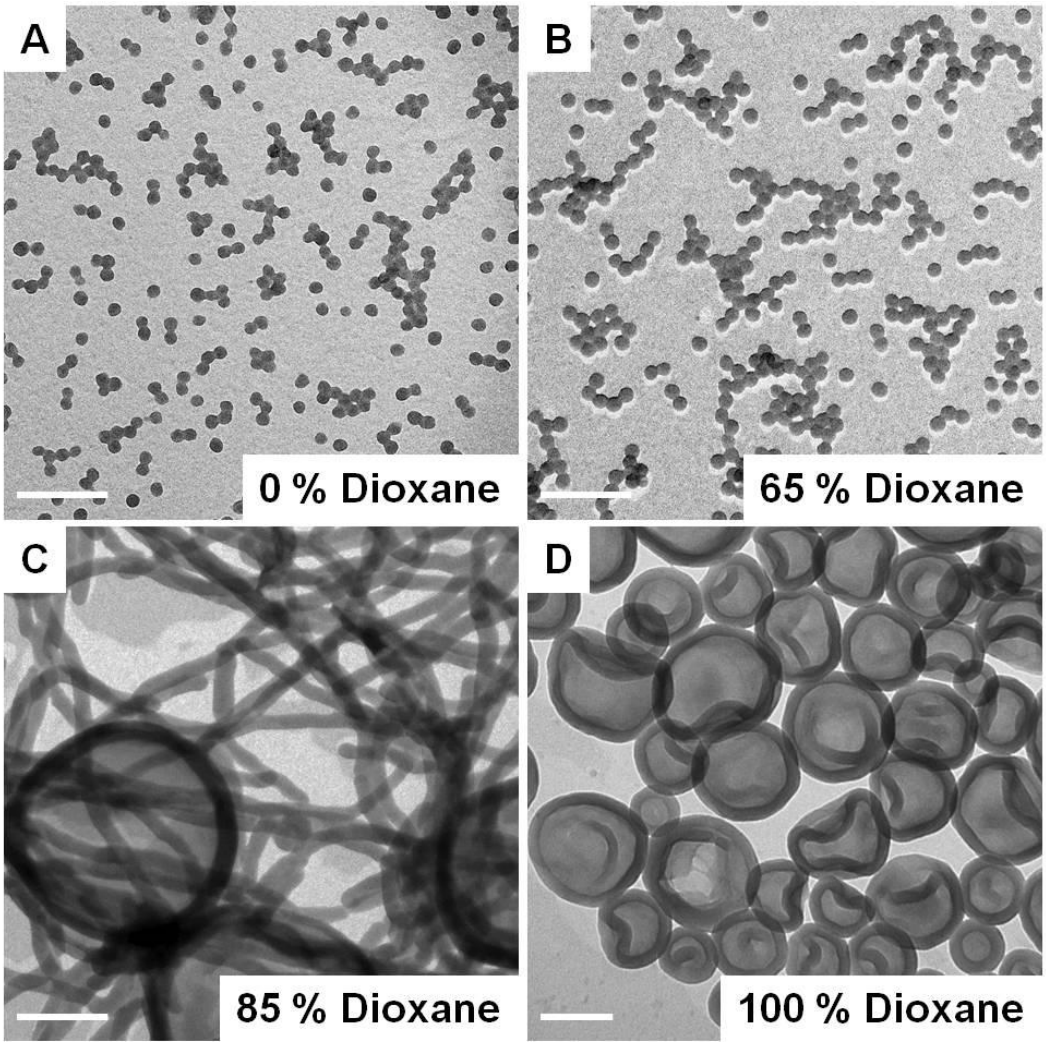

Figure 4.3. TEM images of 0.33 wt% PS(665)-*b*-PAA(68) self-assembled at 2.0 wt% above cwc at different solvent systems. (A) Pure DMF, (B) 35/65 w/w DMF/Dioxane, (C) 15/85 w/w DMF/dioxane and (D) pure dioxane. The scale bars indicate 200 nm.

Table 4.2. Summary of Morphologies via Off-Chip Self-Assembly.

DMF/dioxane (w/w) → cwc + x wt %	100/0	85/15	75/25	65/35	55/45	45/55	35/65	25/75	15/85	0/100
cwc (wt %)	2.8	3.2	3.2	3.7	4.0	4.2	4.6	5.3	6.0	8.5
1.0	S	S	S	S	S	S	S	S	S	S + L
2.0	S	S	S	S	S	S	S	S + C	C + V	V
4.0	S	S	S	S	S	S	S	S*	S*+ V	V

Note: S = spheres and S* represent kinetically-trapped spheres; C = cylinders; L = lamella; V = vesicles. The polymer concentration c_o in all cases is 0.33 wt% and the cwc was determined using light scattering. The micelle morphologies were determined from TEM.

In addition to the specific mixtures described in Fig. 4.3, we investigated the morphologies obtained for several other DMF/dioxane mixtures at water contents of cwc + 1, 2 and 4 wt %. For the DMF/dioxane = 0/100 case (pure dioxane), an additional water content of cwc + 0.5 wt % was also investigated. Table 4.2 compiles the main micelle morphologies observed in each of these cases. Spheres are observed at all water contents for solvent mixtures with dioxane contents up to 35/65. However, at dioxane contents of 25/75 and higher, cylinders and vesicles start to appear as the water content increases. In the 25/75 mixtures, the morphology is spherical at a water content of cwc + 1 wt %, although the increased thermodynamic driving force for micellization with an increase in water content to cwc + 2 wt % gives rise to a mixture of spheres and cylinder; the reversion to spheres as the water content further increases to cwc + 4 wt % is believed

to be a kinetic effect, representing trapped morphologies as the viscosity of the core increases. For the 15/85 mixture, a similar transformation from spheres to a mixture of cylinders and vesicles occurs as the water content increases from cwc + 1 wt % to cwc + 2 wt %. Further increasing water content to cwc + 4 wt % results in mostly smaller vesicles along with some spheres, owing to slow chain dynamics at higher water content, forbidding micelles from reaching their most thermodynamically favourable state. In pure dioxane (0/100), the transformation is from spheres to a mixture of spheres and lamellae (a structural precursor to vesicles) as the water content increases from cwc + 0.5 wt % to cwc + 1 wt %, and then to pure vesicles at both cwc + 2 wt % and cwc + 4 wt %. Considering that, for the most part (and with the notable exception of the 25/75, cwc + 4 wt % case), the resulting off-chip self-assembled micelles should represent equilibrium morphologies, we used the data in Table 4.2 to construct a solvent composition vs. water content phase diagram (Fig. 4.4). The boundaries between morphological regions are estimated, and in the 25/75, cwc + 4 wt % case, where the observed morphology is believed to be kinetically trapped, the thermodynamic phase region is inferred from the general trends. The phase boundary between the unimer phase and the spherical phase is simply determined from the locus of cwc values described previously. This equilibrium phase diagram serves as an important starting point for understanding the non-equilibrium on-chip morphologies under different solvent conditions.

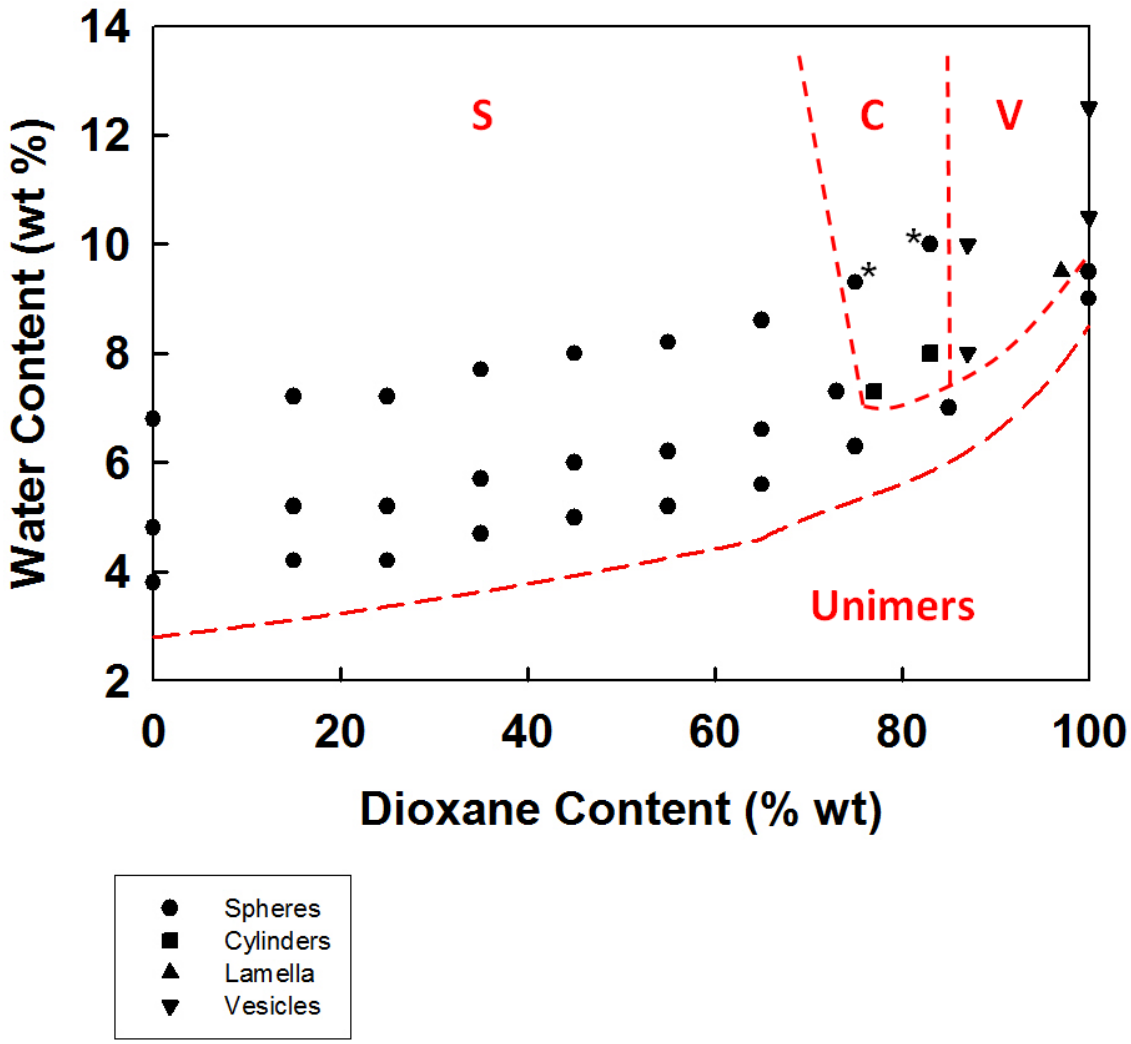

Figure 4.4. Phase diagram of PS(665)-*b*-PAA(68) (c_0 = 0.33 wt%) in various DMF/dioxane/water mixtures. The cwc for each solvent mixture is carefully determined by light scattering and for each solvent composition, three water contents are investigated: 1.0, 2.0 and 4.0 wt% above cwc. The dashed lines represent phase boundaries; the boundary line between micelles and unimers is the cwc.

4.3.2. Effect of Solvent Composition on PS-*b*-PAA Morphologies Formed On-Chip

In the previous chapter, morphologies were described for on-chip self-assembly of PS(668)-*b*-PAA(65) in a single DMF/dioxane solvent mixture of 75/25 (w/w) composition, at water contents of cwc + 1, 2 and 4 wt %. Under those solvent conditions, the equilibrium off-chip morphologies were found to be spheres at all three water contents, with different quantities of primarily cylindrical structures generated at cwc + 1 and 2 wt % as a result of shear-induced processes on-chip. Herein, we study on-chip self-assembly for various DMF/dioxane compositions and water contents of cwc + 1, 2 and 4 wt % in each solvent mixture. We compare the resulting on-chip micellar structures with morphologies formed under equilibrium conditions in the bulk under the corresponding chemical conditions, as described in the phase diagram in Fig. 4.4.

Along with the 75/25 DMF/dioxane solutions discussed in the last chapter, three other compositions showed similar general trends in the relationship between bulk (off-chip) and on-chip micelle morphologies; these are, in order of increasing dioxane content: 100/0 (pure DMF, Fig. 4.5), 85/15 (Fig. 4.6), and 35/65 (Fig. 4.8). The 75/25 solvent mixture is also represented here for completeness (Fig. 4.7). Comparison of these figures shows that in all four DMF/dioxane mixtures, only spherical micelles were formed in the bulk at all investigated water contents, whereas cylindrical morphologies were generated on-chip at certain water contents. In the 100/0 (Fig. 4.5) and 85/15 (Fig. 4.6) mixtures, shear-directed cylinders are generated on-chip at cwc + 2 wt %, but not at cwc + 1 wt %; however, at higher dioxane contents, 75/25 (Fig. 4.7) and 35/65 (Fig. 4.8), on-chip cylinders formed at both cwc + 1 wt % and cwc + 2 wt %. All four solvent compositions formed only spheres on-chip at cwc + 4 wt %, although in most cases the

resulting spheres appear to be highly aggregated compared to the bulk. The nature of the shear-induced morphologies is slightly different at the different solvent compositions, although all are dominated by cylindrical micelles: the 100/0 solvent forms only highly interconnected networks of cylinders (Fig. 4.5D); the 85/15 (Fig. 4.6D) and 75/25 (Fig. 4,7, B and D) mixtures form mainly branched and network cylinders, along with a few lamellae; the 35/65 (Fig. 4.8, B and D) mixture forms branched and network cylinders, along with a few vesicles.

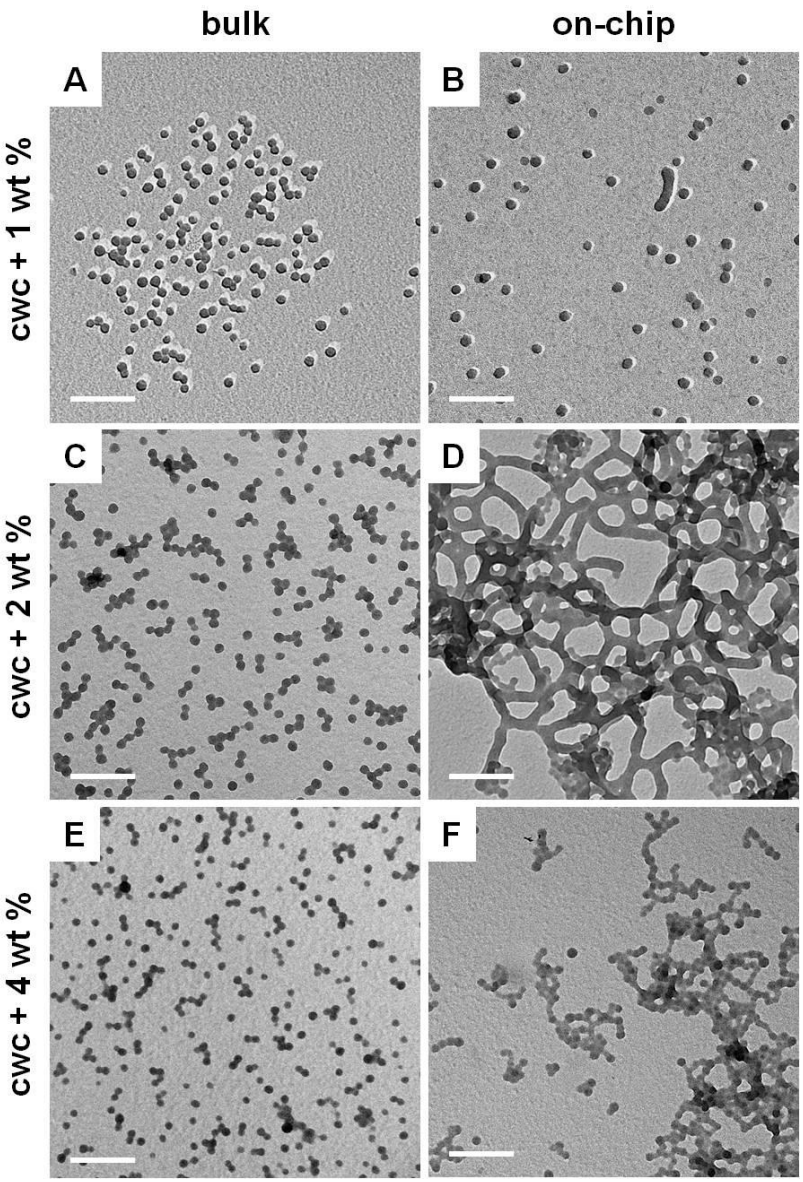

Figure 4.5. Bulk and on-chip TEM images of PS(665)-*b*-PAA(68) self-assembled in DMF. A, C and D are the morphologies of PS(665)-*b*-PAA(68) self-assembled in the bulk at 1.0 wt%, 2.0 wt% and 4.0 wt% above cwc, respectively, while B, D and F are the same the corresponding TEM images of the same water content self-assembled on microfluidic chips. The polymer concentration c_0 = 0.33 wt% in all cases, and cwc = 2.8 wt% H_2O. The on-chip flow rate is ~ 5 µL/min. The scale bars indicate 200 nm.

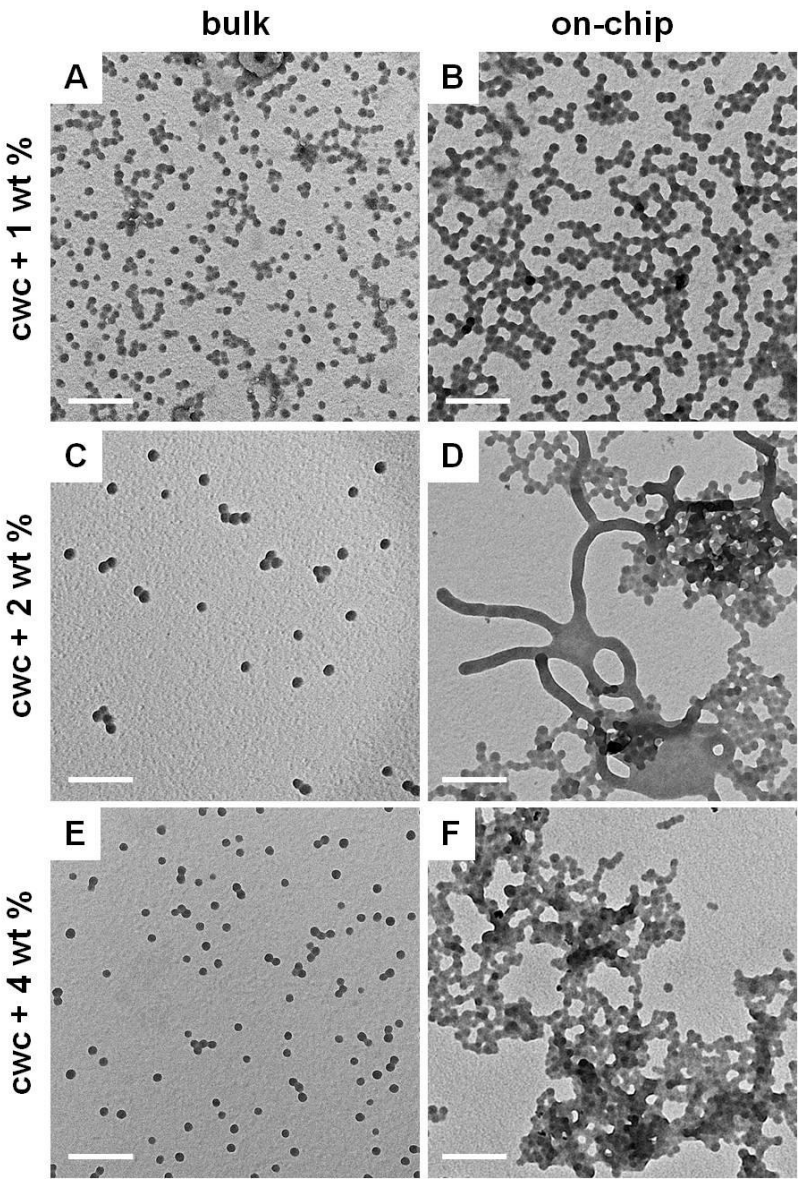

Figure 4.6. Bulk and on-chip TEM images of PS(665)-*b*-PAA(68) self-assembled in 85/15 DMF/dioxane. A, C and D are the morphologies of PS(665)-*b*-PAA(68) self-assembled in the bulk at 1.0 wt%, 2.0 wt% and 4.0 wt% above cwc, respectively, while B, D and F are the same the corresponding TEM images of the same water content self-assembled on microfluidic chips. The polymer concentration is c_0 = 0.33 wt% in all cases and cwc = 3.2 wt% H_2O. The on-chip flow rate is ~5 µL/min. The scale bars indicate 200 nm.

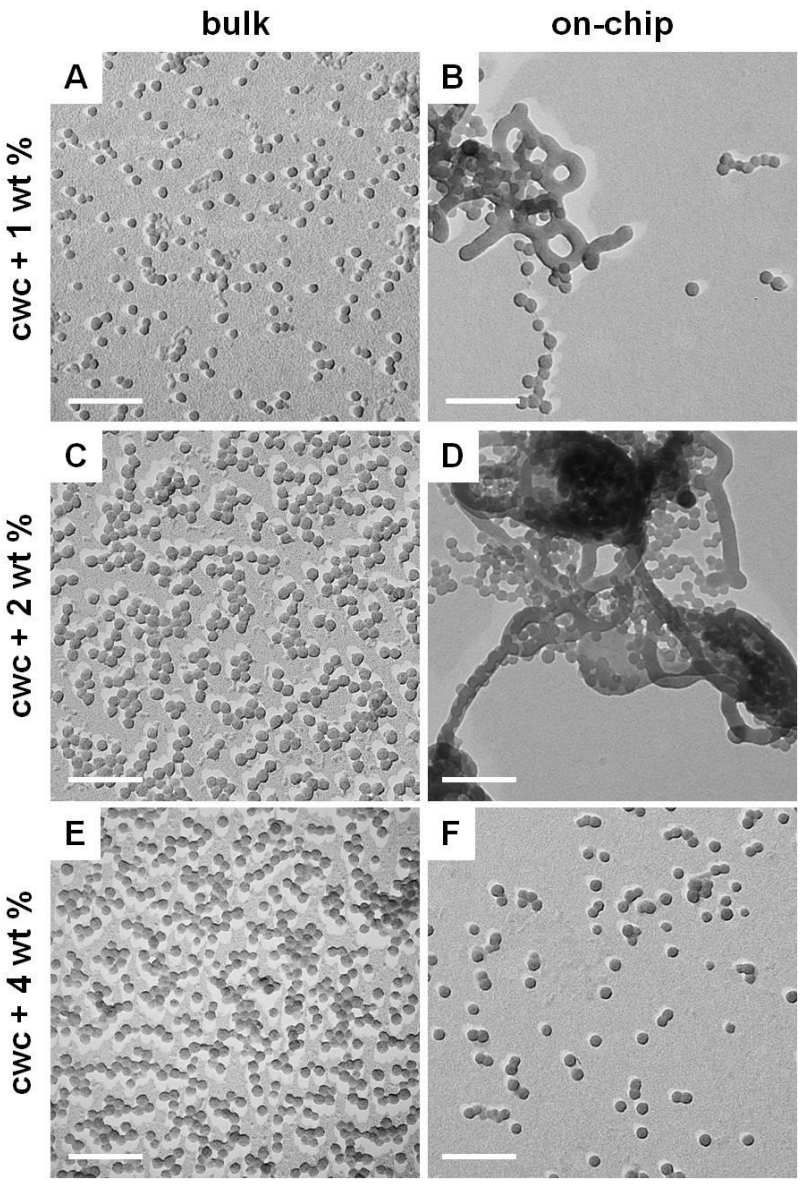

Figure 4.7. Bulk and on-chip TEM images of PS(665)-*b*-PAA(68) self-assembled in 75/25 DMF/dioxane A, C and D are the morphologies PS(665)-*b*-PAA(68) self-assembled in the bulk at 1.0 wt%, 2.0 wt% and 4.0 wt% above cwc, respectively, while B, D and F are the same the corresponding TEM images of the same water content self-assembled on microfluidic chips. The polymer concentration is c_0 = 0.33 wt% in all cases and cwc = 3.2 wt% H_2O. The on-chip flow rate is ~5 µL/min. The scale bars indicate 200 nm.

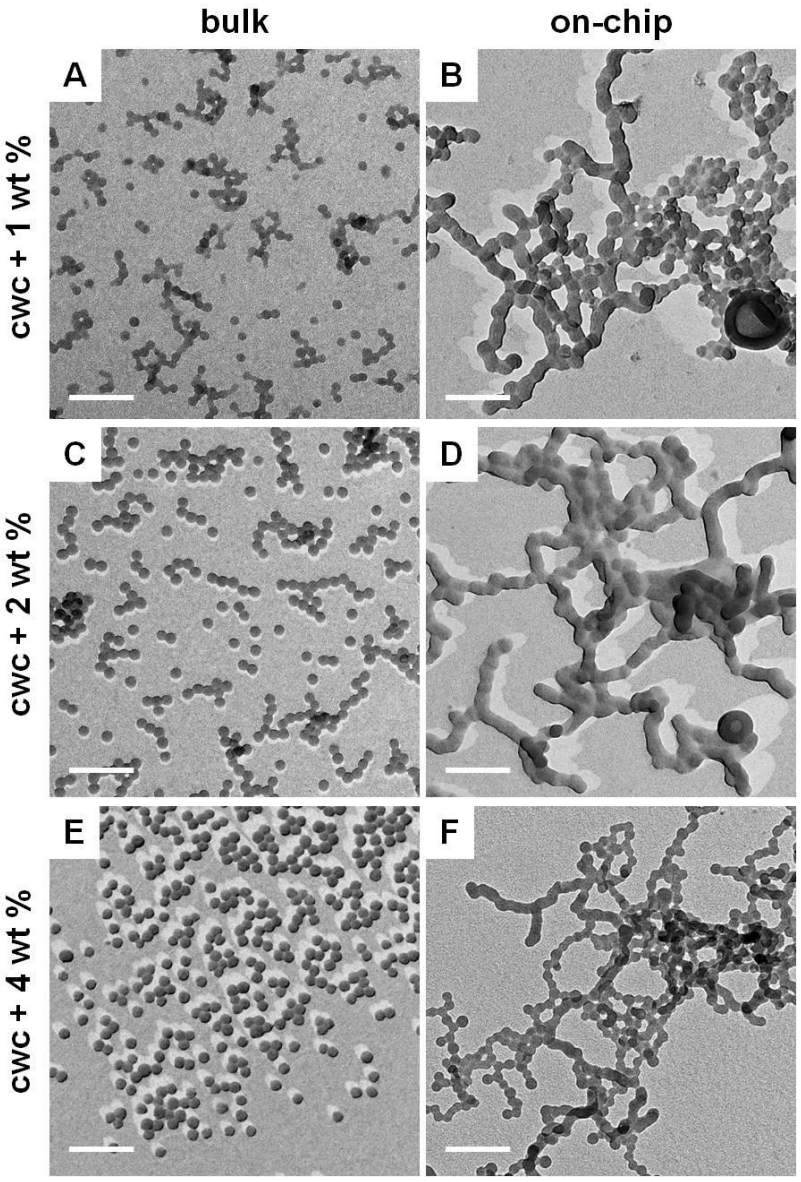

Figure 4.8. Bulk and on-chip TEM images of PS(665)-*b*-PAA(68) self-assembled in 35/65 DMF/dioxane A, C and D are the morphologies PS(665)-*b*-PAA(68) self-assembled in the bulk at 1.0 wt%, 2.0 wt% and 4.0 wt% above cwc, respectively, while B, D and F are the same the corresponding TEM images of the same water content self-assembled on microfluidic chips. The polymer concentration is c_0 = 0.33 wt% in all cases and cwc = 4.6 wt% H_2O. The on-chip flow rate is ~ 5 µL/min. The scale bars indicate 200 nm.

Considering the equilibrium phase diagram (Fig 4.4), and the mechanism of on-chip morphology transformations developed in the previous chapter (Scheme 4.1), we can understand why cylinders are the most prominent non-spherical structures generated in the microfluidic channel at the four compositions 100/0, 85/15, 75/25, and 35/65. In these mixtures, global equilibrium favours spheres, and so fast mixing with water generates spheres near the injector (State A). Subsequent shear-induced coalescence of spheres in the high-shear corners of the liquid plugs locally increases aggregation numbers to generate high-energy aggregates (State B). These transition structures then relax via the kinetically-favoured pathway of intramicellar chain rearrangements to form the morphology (State C) that represents a local free energy minimum, within the kinetic constraint of local aggregation numbers in the absence of interparticle exchange. Since the effect of shear-induced coalescence on-chip is to increase aggregation numbers, it exerts a force locally that is morphogenically equivalent to the chemical force exerted by an increase in dioxane and/or water content (both of which will globally increase aggregation numbers). As a result, the equilibrium spheres are pushed by on-chip shear into the nearest morphological region with higher aggregation number, which is cylinders. In Scheme 4.2, this process is represented by Path 1, in which the purple oval designates the equilibrium morphology (spheres, S), and the dotted arrow represents the morphogenic transformation (to cylinders, C) effected by on-chip shear processes. This analysis also explains why a small number of lamellae (a transition structure in vesicle formation, e.g. Fig 4.6D) and then some vesicles (Fig 4.8, B and D), are observed by on-chip self-assembly as the dioxane content increases; as the equilibrium composition moves closer to the sphere-cylinder phase boundary, a small number of particles will

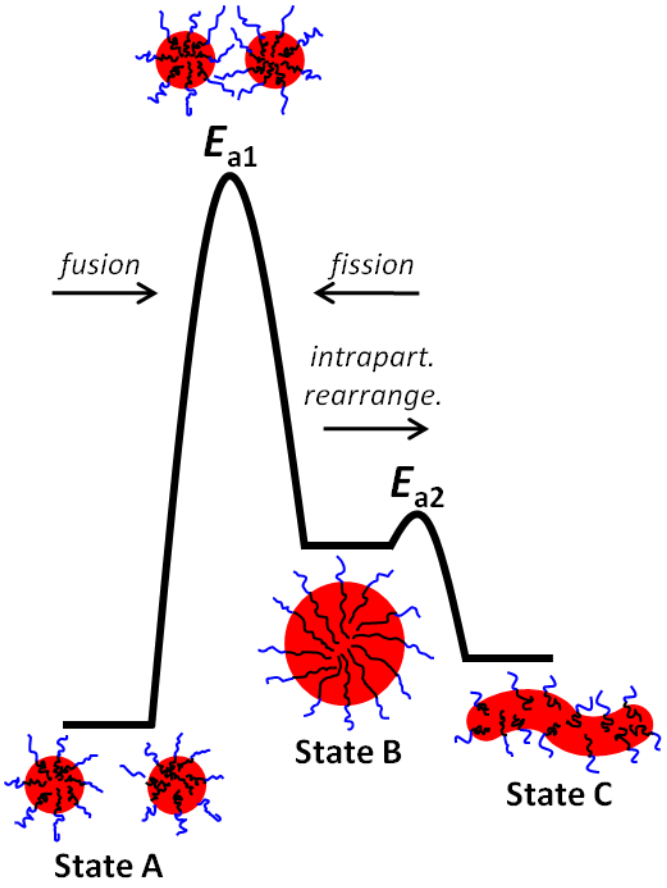

Scheme 4.1. Proposed energy diagram for on-chip shear-induced morphological transitions.

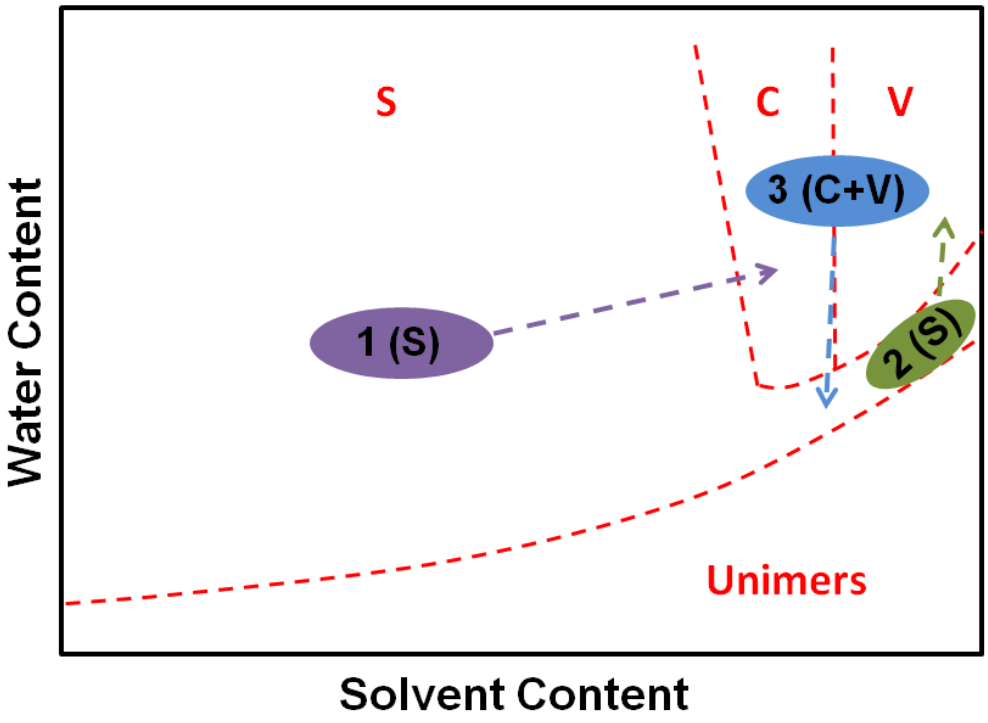

Scheme 4.2. Carton representation of the Phase diagram of PS(665)-*b*-PAA(68) (c_0 = 0.33 wt%) in various DMF/dioxane mixtures. The dashed lines represent phase boundary; the boundary line between micelles and unimers is the cwc.

experience a sufficient increase in local aggregation number under shear to cross two phase boundaries into the vesicle region.

Under equilibrium (off-chip) conditions, the solvent composition 15/85 DMF/dioxane (Fig. 4.9) lies in the sphere region just below the cylinder/vesicle phase boundary at cwc + 1 wt % (Fig. 4.9A), and at different points along the cylinder/vesicle phase boundary at cwc + 2 wt % (Fig. 4.9C) and cwc + 4 wt % (Fig. 4.9E). The small number of spheres present along with vesicles at cwc + 4 wt % (Fig. 4.9E), far from the equilibrium sphere region, are almost certainly kinetic structures trapped as a result of the high water content. On-chip, this solvent composition shows a rich variety of shear-induced morphogenic behaviour that is strongly dependent on the water content and thus the initial equilibrium morphologies that form immediately after the injector. At cwc + 1 wt %, solely spheres are present under off-chip equilibrium conditions (Fig. 4.9A), whereas on-chip, spheres along with a significant number of shear-induced vesicles, are formed (Fig. 4.9B). The formation of shear-induced vesicles from equilibrium spheres, instead of the shear-induced cylinders observed at compositions with lower dioxane content, is attributed to the close proximity of spherical micelles under these conditions to the vesicle region of the phase diagram; thus, the local increases in aggregation number as a result of shear-induced coalescence push spherical aggregates into the vesicle region, as portrayed by Path 2 in Scheme 4.2.

In sharp contrast to the equilibrium spheres at cwc + 1 wt %, the chemical conditions at 15/85 DMF/dioxane and cwc + 2 wt % give rise to an equilibrium mixture of long cylinders and large vesicles off-chip (Fig. 4.9C); on-chip, the dominant effect of downstream shear is particle breakup rather than coalescence, since the capillary number

governing shear-induced breakup will be significantly higher for these large aggregates compared to small spherical micelles. As a result, the shear-induced on-chip morphologies (Fig. 4.9D) have lower, rather than higher, aggregation numbers than their off-chip counterparts (Fig. 4.9C), in the form of spheres (likely from the breakup of cylinders) and smaller vesicles (likely from the breakup of larger vesicles). We represent this type of on-chip transition—from larger equilibrium aggregates (e.g. cylinders and vesicles) to smaller aggregates (e.g. spheres) as a result of shear-induced breakup at high capillary number— by Path 3 in Scheme 4.2. Finally, the cwc + 4 wt % morphologies on-chip (Fig. 4.9F) and off-chip (Fig. 4.9E) are consistent with other solvent compositions at high water content, in that the small particle size and large activation energy do not allow either significant breakup or coalescence under shear, such that the on-chip morphologies are not dramatically different from those formed off-chip under the same chemical conditions. However, we do note that a few cylindrical-like aggregates appear to form on-chip (Fig. 4.9F) as a result of coalescence of the kinetically-trapped spheres formed off-chip (Fig. 4.9E); this suggests that under chemical conditions where off-chip structures are trapped away from equilibrium, on-chip shear may provide sufficient energy to allow micelles to move closer to their lowest-free energy morphology.

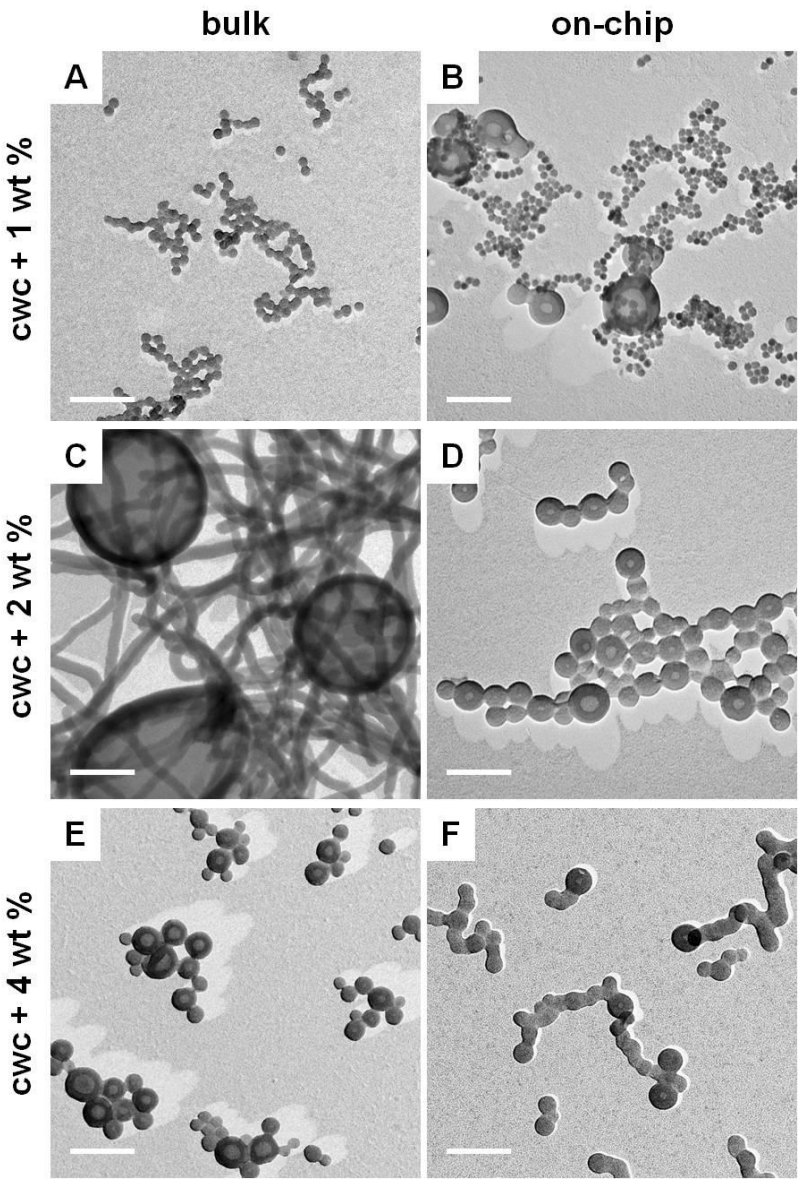

Figure 4.9. Bulk and on-chip TEM images of PS(665)-*b*-PAA(68) self-assembled in 15/85 DMF/dioxane. A, C and D are the morphologies of PS(665)-*b*-PAA(68) self-assembled in the bulk at 1.0 wt%, 2.0 wt% and 4.0 wt% above cwc, respectively, while B, D and F are the same the corresponding TEM images of the same water content self-assembled on microfluidic chips. The polymer concentration c_0 = 0.33 wt% in all cases and cwc = 6.0 wt% H_2O. The on-chip flow rate is ~ 5 µL/min. The scale bars indicate 200 nm.

The on-chip generation of vesicles under chemical conditions in which vesicles are not thermodynamically favoured, such as demonstrated in the 15/85 DMF/dioxane mixture at cwc + 1 wt % (Fig. 4.9, A and B), represents the first example of block copolymer vesicles formed as a direct result of top-down shear forces. The applied and fundamental importance of block copolymer vesicles for drug delivery,[27, 29, 30] encapsulation,[27, 29, 34] and biomimetic studies,[27] makes this on-chip, shear-induced sphere-to-vesicles transition (Path 2, Scheme 4.2) of particular interest for further study and optimization. Specifically, we note that although some vesicles are generated from spheres on-chip in the 15/85, cwc + 1 wt % case, the majority of micelles remain spherical (Fig. 4.9B); however, by carrying out self-assembly in pure dioxane (0/100 composition) at relatively low water contents above the cwc, we have identified chemical conditions that generate no vesicles under off-chip equilibrium conditions, but lead to either a majority of vesicles or a pure vesicle population on-chip. For instance, in pure dioxane just above the cwc, cwc + 0.5 wt %, off-chip self-assembly generated only spheres (Fig. 4.10A), as indicated in the equilibrium phase diagram (Fig. 4.4). In contrast, the same chemical conditions on-chip generated a nearly-pure population of vesicles via shear-induced coalescence (Fig. 4.10B, C and D); the vesicle population is quite polydisperse, with sizes ranging from ~50-500 nm, and a few spherical micelles (without internal water pools) can also be identified—although clearly vesicles are the dominant morphology formed on-chip. Compared to the 15/85, cwc + 1 wt % case, where only a few shear-induced vesicles are generated on-chip, the presence of pure dioxane as the organic solvent appears to adjust the coalescence activation barrier (E_{a1}, Scheme 4.1) to a level that maximizes coalescence while at the same time minimizes

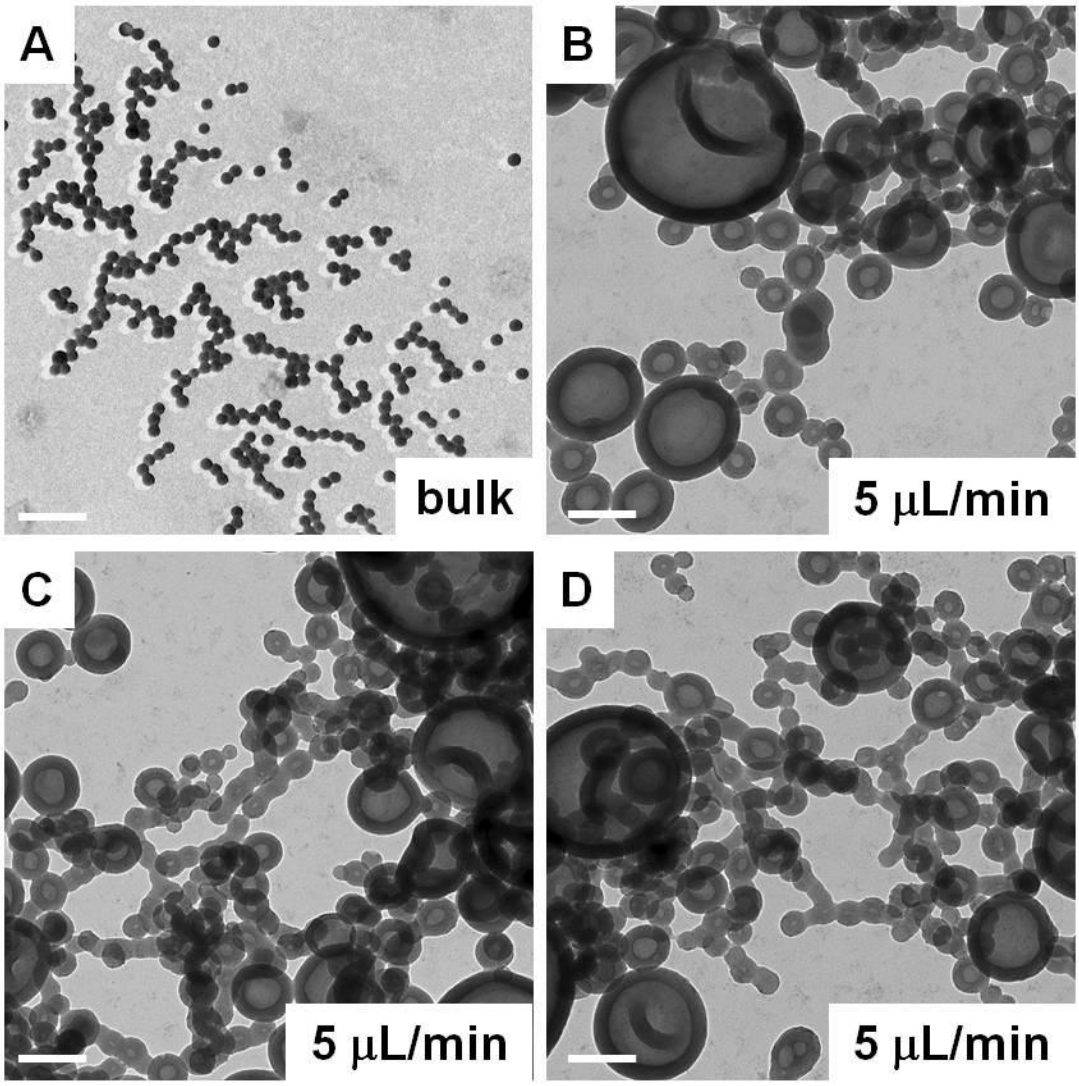

Figure 4.10. Bulk and on-chip TEM images of PS(665)-*b*-PAA(68) self-assembled in dioxane. A is morphologies of PS(665)-*b*-PAA(68) self-assembled at 0.50 wt% above cwc in the bulk and while B, C and D are from on-chip self-assembly under identical chemical conditions. The polymer concentration is c_0 = 0.33 wt% in all cases and cwc = 8.5 wt% H_2O. The on-chip flow rate is ~ 5 μL/min. The scale bars indicate 200 nm.

fission in favour of intraparticle rearrangements. The effect of increasing the dioxane content would be to lower the core viscosity component to the coalescence activation barrier by increasing the degree of solvent swelling in the PS core; at the same time, increasing dioxane should increase the electrosteric activation energy, since the water content at the cwc is higher, leading to a higher concentration of water localized in the PAA corona and thus increasing the charge density of the brush.

Fig. 4.11 shows off-chip and on-chip morphologies in pure dioxane at the three water contents cwc + 1 wt %, cwc + 2 wt % and cwc + 4 wt %. Similar to cwc + 0.5 wt %, the cwc + 1 wt % condition forms no vesicles off-chip (Fig. 4.11A) but leads to vesicles on-chip (Fig. 4.11B) through shear-induced coalescence. The bulk morphology (Fig. 4.11A) shows a mixture of spheres and flat lamellar structures, which are precursors to vesicles, indicating an equilibrium condition on the phase boundary between spheres and vesicles (Fig. 4.4); in comparison with on-chip vesicles generated at cwc + 0.5 wt %, the vesicles formed at this slightly higher water content (Fig. 4.11B) are less polydisperse as well as being morphologically "pure"—i.e. no spherical micelles are observed within the population of on-chip structures. This indicates that under the appropriate chemical conditions on-chip, a morphologically pure population of kinetic vesicles can be generated using top-down shear forces from an equilibrium condition containing no vesicles. Such a processing route to pure vesicles, to our knowledge, is unprecedented, and opens the door to a new level of top-down control in which morphologies can be "dialled in" via flow rate for specific applications, e.g. on-chip vesicle generation for drug delivery applications requiring an encapsulated water pool.[27, 29, 30, 34] By increasing the water content to cwc + 2 wt%, the equilibrium morphology moves into the vesicle

region, and a pure population of vesicles are obtained off-chip (Fig. 4.11C); on-chip, vesicles are also observed, although characterized by a population of very large vesicles (up to a micron in diameter) that apparently formed from the shear-induced coalescence of smaller vesicles (Fig. 4.11D). Finally, at the highest water content of cwc + 4 wt %, a pure population of small vesicles is observed in the off-chip case (Fig. 4.11E); the vesicles generated in the same chemical conditions on-chip are very similar in size, although they are accompanied by a population of spherical micelles that are not present in the bulk (Fig. 4.11F). These spheres may have formed as a result of shear-induced breakup of some of the small vesicles that form upon water mixing; another possibility is that they represent trapped transition structures that are locked in during vesicle formation as a result of the fast on-chip mixing.

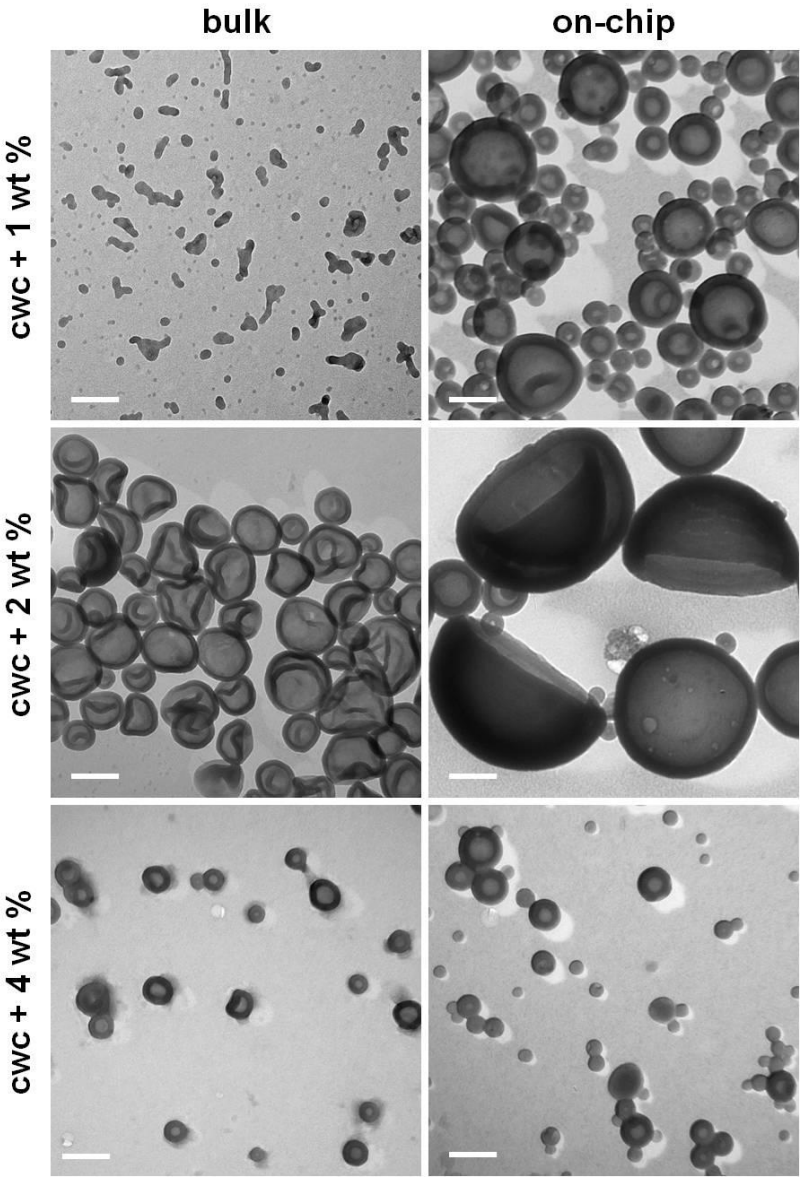

Figure 4.11. Bulk and on-chip TEM images of PS(665)-*b*-PAA(68) self-assembled in dioxane. A, C and D are the morphologies of PS(665)-*b*-PAA(68) self-assembled in the bulk at 1.0 wt%, 2.0 wt% and 4.0 wt% above cwc, respectively, while B, D and F are the same the corresponding TEM images of the same water content self-assembled on microfluidic chips. The polymer concentration c_0 = 0.33 wt% in all cases and cwc = 8.5 wt% H_2O. The on-chip flow rate is ~ 5 µL/min. The scale bars indicate 200 nm.

In summary, three main paths for on-chip morphological transitions are observed, depending on the solvent composition and water content and thus on the equilibrium morphology (Scheme 4.2). These are: Path 1: sphere-to-cylinder transition via shear-induced coalescence and intraparticle rearrangement (e.g. all on-chip morphology changes at dioxane contents up to 35/65 DMF/dioxane); Path 2: sphere-to-vesicle transition via shear-induced coalescence and intraparticle rearrangement (e.g. 25/85 DMF/dioxane, cwc + 1 wt %; 0/100 DMF/dioxane, cwc + 0.5 wt % and cwc + 1.0 wt %). Path 1 and Path 2 both follow the energy diagram represented in Scheme 4.1, with the main difference being the morphology that forms as a result of intraparticle rearrangement, which we have shown depends on the proximity of the initial equilibrium state to other morphological regions on the phase diagram. Finally, Path 3: cylinder- or vesicle-to-sphere transition via shear-induced breakup of large equilibrium micelle morphologies under high capillary number conditions (e.g. 25/85 DMF/dioxane, cwc + 2 wt %). The determination of operative conditions for these various on-chip pathways, demonstrated here, highlights the immense potential of on-chip self-assembly as a means of combining chemical forces with shear processing to effect fine control over nanoscale colloidal structure.

4.3.3. Effect of Polymer Concentration and Added Salt on On-Chip PS-*b*-PAA Morphologies

In the previous section, we investigated chemical parameters (solvent composition and water content) that influence the observed on-chip morphologies through the equilibrium state of the initially formed micelles at the injector. In some cases, these

parameters were also shown to influence the energy barrier of micelle coalescence, and thus vary the relative amounts of shear-induced structures that formed; however, as previously discussed, actual morphology differences on-chip as a result of different solvent composition or water content are generally attributed to thermodynamic, rather than kinetic effects. By contrast, in this section we investigate the effect of polymer concentration and salt addition on the on-chip morphology, and find dramatic differences that we attribute mainly to increased rates of coalescence, suggesting a kinetic rather than thermodynamic effect.

In Fig. 4.12, we compare off-chip and on-chip morphologies for the 75/25 DMF/dioxane, cwc + 2 wt % system at two different polymer concentrations: our standard concentration of c_0 = 0.33 wt % and an elevated polymer concentration 3x higher: c_0 = 1.0 wt %. Note that the c_0 = 0.33 wt % condition is identical to that in two experiments described in the previous section (Fig. 4.7, C and D). At both polymer concentrations, the off-chip experiments yield spherical micelles (Fig.4.12, A and C), indicating that polymer concentration does not have an influence on the micelle morphology in this range off-chip. However, on-chip, the morphologies are dramatically different at the two polymer concentrations. A discussed previously, the lower polymer concentration yields a mixture of spheres and shear-induced branched cylinders and cylinder networks, along with a few lamellae (Fig. 4.12B). On the other hand, the higher polymer concentration generates surprising and impressively large extended aggregates (Fig. 4.12D), which appear to consist of a network of cylinders encapsulated and interconnected with large lamellar sheets. In some cases, these large bilayer networks, which we jauntily term “dinosomes” (similar aggregates have been called large

compound vesicles elsewhere in the literature),[13] extend for several microns (further examples in Fig. 4.13) and often appear broken or damaged by deposition and water evaporation, indicative of the large volumes of water that were encapsulated by the extensive bilayer sheets in the colloid state.

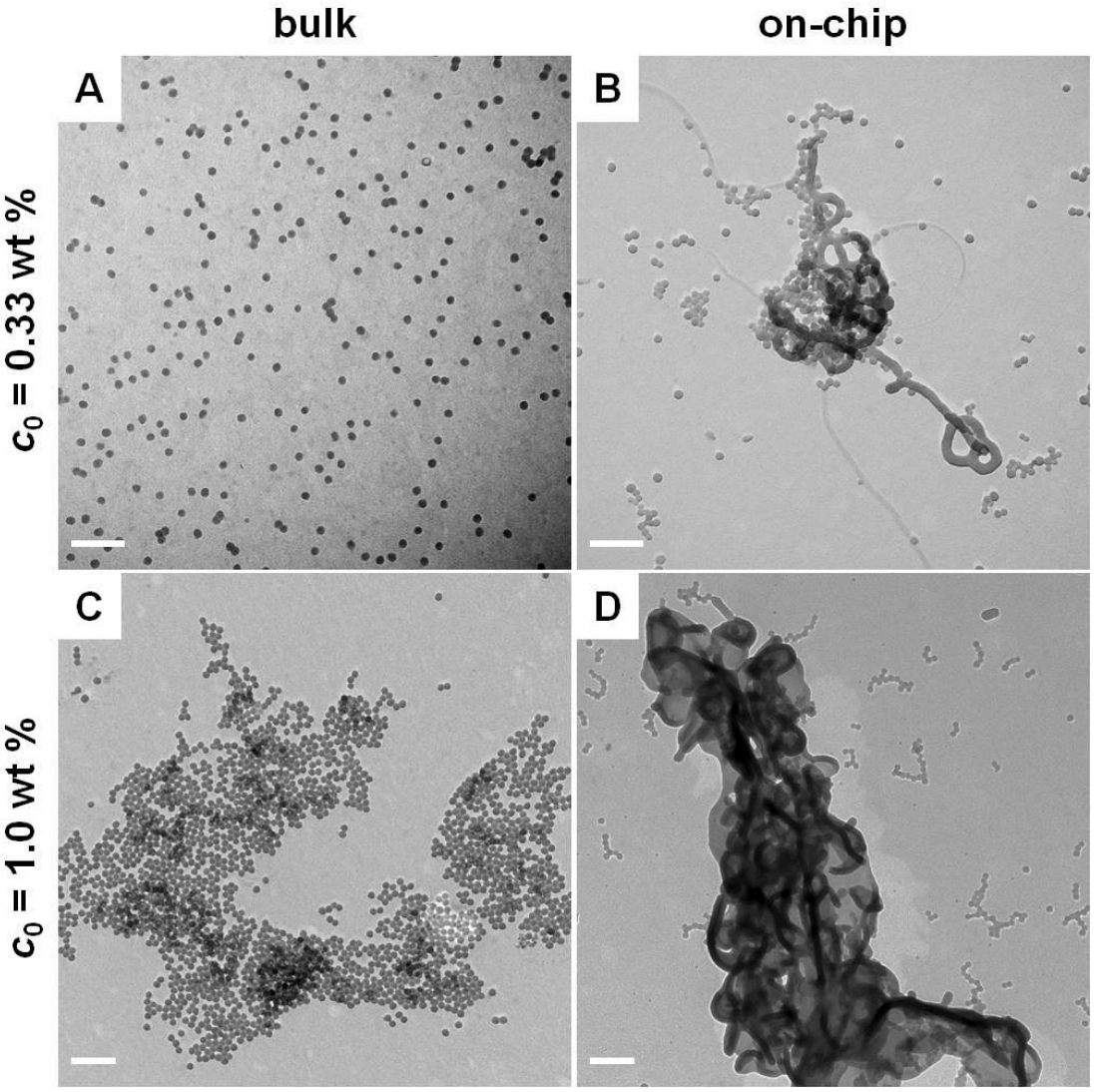

Figure 4.12. Effect of polymer concentration on the self-assembled morphology of PS(665)-*b*-PAA(68) in 75/25 DMF/dioxane solvent system at 2.0 wt% above cwc. A and C are the morphologies formed in the bulk at initial polymer concentration c_0 = 0.33 wt% and c_0 = 1.0 wt%, while B and D are the corresponding TEM images of self-assembled morphologies formed on-chip at the same initial polymer concentrations as A and D, respectively. The on-chip flow rate is ~ 5 µL/min. The scale bars indicate 200 nm.

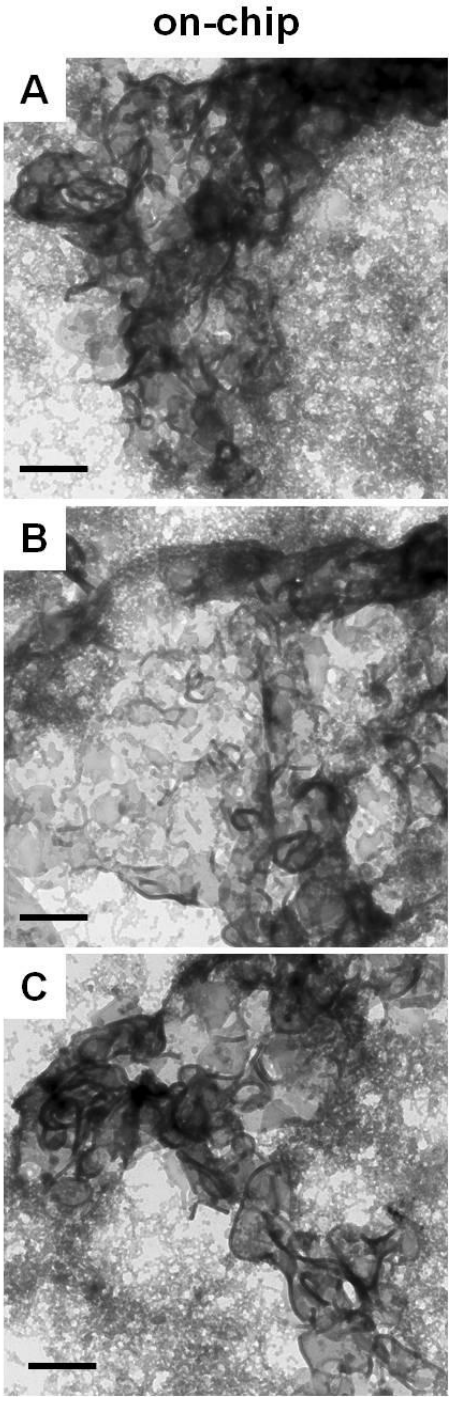

Figure 4.13. More TEM images at low magnification of effect of polymer concentration on the self-assembled morphology of c_0 = 1.0 wt % PS(665)-*b*-PAA(68) in 75/25 DMF/dioxane solvent system at 2.0 wt% above cwc. A, B and C are the TEM images showing the gigantic sizes of these dinosomes. The on-chip flow rate is ~ 5 μL/min. The scale bars indicate 500 nm.

Although block copolymer concentration is known to influence the equilibrium morphology of block copolymer micelles, the effect is generally quite weak, as obviated by the very steep morphological phase boundaries in the polymer concentration-water content phase diagram determined for the PS(310)-*b*-PAA(52) copolymer in dioxane/water mixtures.[22] This weak thermodynamic effect, in addition to the large size difference in the aggregates obtained at the two polymer concentrations, suggests that the most important result of increasing the copolymer concentration is to increase the concentration of micelles and thus increase the on-chip collision/coalescence rate dramatically. As a result, a much larger number of primary spherical micelles effectively coalesce into a single giant aggregate as the liquid plugs travel through the chip, with the resulting bilayer structure governed by the resulting high local concentration of copolymer chains. Thus we view the demonstrated polymer concentration effect on the on-chip morphology to be kinetic, rather than thermodynamic, in origin.

Interestingly, we can effect a very similar morphology change on-chip to that obtained by increasing the polymer concentration by adding a small amount of salt (R_{NaCl} = 0.2 mol NaCl per mol acrylic acid repeat unit) to the self-assembly mixture prior to inducing micellization by adding water above the cwc. In both off-chip and on-chip experiments, the salt was added to the DMF/dioxane/copolymer solution via a concentrated 0.2 M NaCl aqueous solution, resulting in an initial water content well below the cwc; the remaining water was then added either dropwise off-chip or via mixing with the water-containing stream on-chip. The off-chip and on-chip morphologies (also in the solvent mixture 75/25 DMF/dioxane, cwc + 2 wt %), with and without added salt are shown in Fig. 4.14. Off-chip, the small amount of added salt does

not influence the morphology, with spheres observed in both cases (Fig. 4.14, A and C). Eisenberg and co-workers have studied the influence of added salt on morphologies of PS-*b*-PAA block copolymers, and observed dramatic morphology transitions, but only for salt contents $R_{NaCl} > 0.4$;[13] therefore, the spheres we observe via off-chip self-assembly both with and without added salt are consistent with their results. On-chip, the added salt gives rise to similar dinosome aggregates (although not as large) to those obtained at elevated polymer concentration, along with vesicles (Fig. 4.14D), in contrast to the cylindrical aggregates generated on-chip without added salt (Fig. 4.14B).

The observed effect of added salt on the on-chip morphologies can be explained by a combination of kinetic and thermodynamic effects. Similar to increasing the polymer concentration, the addition of salt will increase the rate of on-chip coalescence events, not by increasing the collision rate, as in the case of elevated polymer concentration, but by decreasing the electrosteric contribution to the activation barrier E_{a1} (Scheme 4.1). The short-range electrosteric repulsion between charged polymer brushes, described in the previous chapter, has previously been shown to decrease as the ionic strength increases,[35] leading in the present case to an increased rate of successful collisions with added salt. As a result of this increased rate of coalescence, similar large dinosome structures are generated to those observed at the higher polymer concentration. In addition to this kinetic effect, adding salt has been shown by Eisenberg and coworkers[9, 13, 17] to change the free energy of the self-assembling system by effectively screening electrostatic repulsive interactions between proximal charged PAA chains, leading to morphological transitions from spheres to cylinders to vesicles as the salt content is increased. Although the small degree of screening present at $R_{NaCl} = 0.2$ is not

significant enough to effect a change in morphology off-chip, it does change the equilibrium position of the system, effectively moving the spherical micelles closer to the vesicle region of an appropriate phase diagram. Thus, when coalescence induces increases in aggregation number, the resulting intraparticle rearrangements to locally minimize free energy give rise to vesicles (Fig. 4.14D), rather than the cylinders formed in the absence of added salt (Fig. 4.14C).

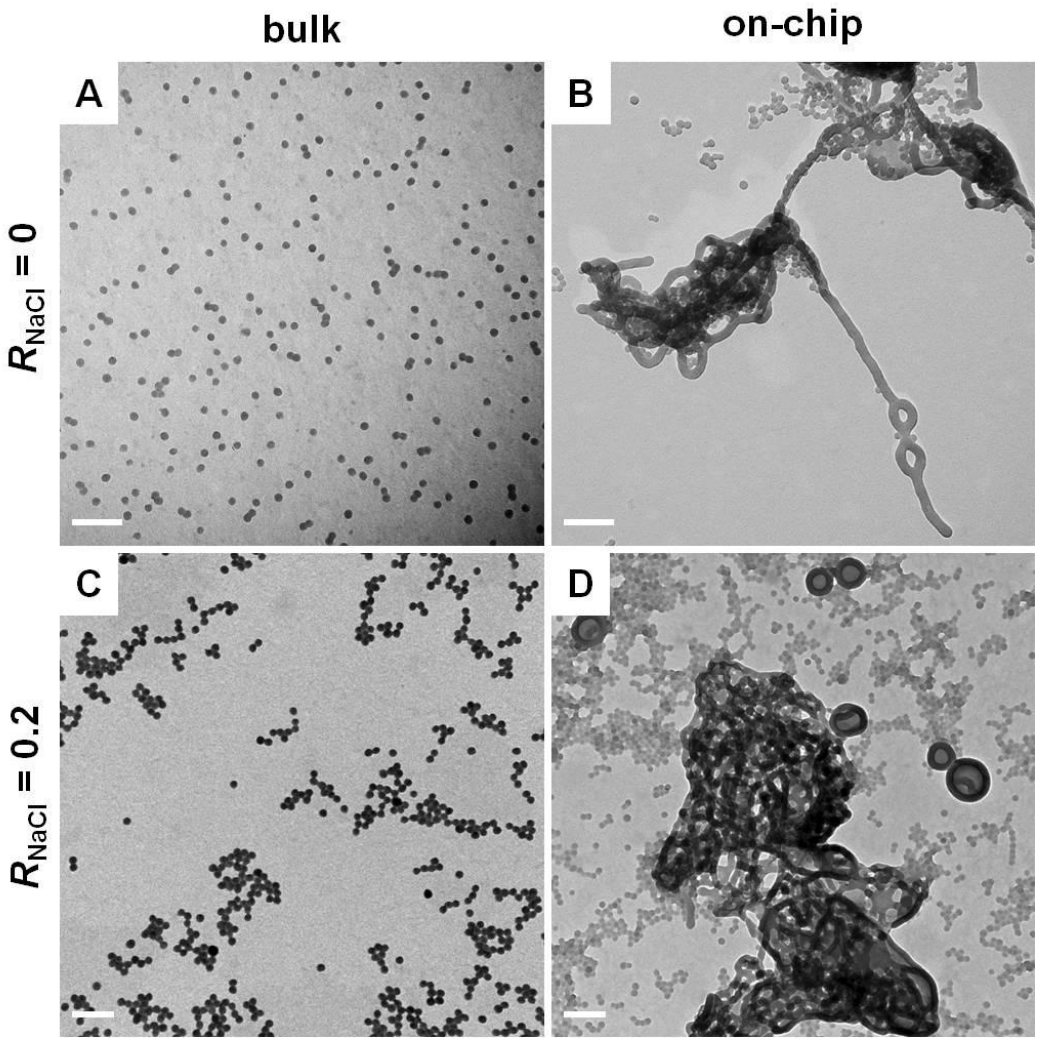

Figure 4.14. Effect of added salts on the self-assembled morphology of 0.33 wt% PS(665)-*b*-PAA(68) in 75/25 DMF/dioxane solvent system at 2.0 wt% above cwc. A and C are the morphologies formed in the bulk at R_{NaCl} = 0 and R_{NaCl} = 0.2 salt contents, while B and D are the corresponding TEM images of the morphologies formed on chip at the same contents as A and D, respectively. The on-chip flow rate is ~ 5 μL/min. The scale bars indicate 200 nm.

4.4. Conclusions

In this chapter, we have investigated the effect of various chemical conditions (solvent composition, water content, polymer concentration and added salt) on the morphologies formed by PS-*b*-PAA in DMF/dioxane/water mixtures on a two-phase gas-liquid segmented microfluidic reactor. The resulting morphological trends are explained by a combination of top-down shear effects (such as shear-induced coalescence, particle breakup and mixing) and bottom-up chemical forces. Using off-chip morphology results, an equilibrium phase diagram of the present block copolymer system in various DMF/dioxane/water mixtures was constructed. In many cases, the on-chip morphologies could be explained by one of three identified shear-induced paths from a particular equilibrium position on the phase diagram. In addition, polymer concentration and salt content were found to have a dramatic kinetic effect on micelle morphology when combined with on-chip shear forces, due to the increased rate of coalescence that was effected by changes in these parameters. Top-down directed molecular self-assembly in microfluidic devices offers immense potential for a variety of applications, as it promises new and convenient handles on colloidal morphology and size at the nanoscale.

4.5. References

1. Discher, B. M.; Won, Y. Y.; Ege, D. S.; Lee, J. C. M.; Bates, F. S.; Discher, D. E.; Hammer, D. A., *Science* **1999,** *284* (5417), 1143-1146.

2. Jain, S.; Bates, F. S., *Science* **2003,** *300* (5618), 460-464.

3. Jain, S.; Bates, F. S., *Macromolecules* **2004,** *37* (4), 1511-1523.

4. Won, Y. Y.; Davis, H. T.; Bates, F. S., *Science* **1999,** *283* (5404), 960-963.

5. Cui, H. G.; Chen, Z. Y.; Wooley, K. L.; Pochan, D. J., *Soft Matter* **2009,** *5* (6), 1269-1278.

6. Cui, H. G.; Chen, Z. Y.; Zhong, S.; Wooley, K. L.; Pochan, D. J., *Science* **2007,** *317* (5838), 647-650.

7. Li, Z. B.; Chen, Z. Y.; Cui, H. G.; Hales, K.; Qi, K.; Wooley, K. L.; Pochan, D. J., *Langmuir* **2005,** *21* (16), 7533-7539.

8. Li, Z. B.; Chen, Z. Y.; Cui, H. G.; Hales, K.; Wooley, K. L.; Pochan, D. J., *Langmuir* **2007,** *23* (9), 4689-4694.

9. Zhang, L. F.; Yu, K.; Eisenberg, A., *Science* **1996,** *272* (5269), 1777-1779.

10. Zhang, L. F.; Eisenberg, A., *Science* **1995,** *268* (5218), 1728-1731.

11. Yu, K.; Zhang, L. F.; Eisenberg, A., *Langmuir* **1996,** *12* (25), 5980-5984.

12. Zhang, L. F.; Eisenberg, A., *J. Am. Chem. Soc.* **1996,** *118* (13), 3168-3181.

13. Zhang, L. F.; Eisenberg, A., *Macromolecules* **1996,** *29* (27), 8805-8815.

14. Shen, H. W.; Zhang, L. F.; Eisenberg, A., *J. Phys. Chem. B* **1997,** *101* (24), 4697-4708.

15. Yu, Y. S.; Eisenberg, A., *J. Am. Chem. Soc.* **1997,** *119* (35), 8383-8384.

16. Yu, Y. S.; Zhang, L. F.; Eisenberg, A., *Langmuir* **1997,** *13* (9), 2578-2581.

17. Zhang, L. F.; Shen, H. W.; Eisenberg, A., *Macromolecules* **1997,** *30* (4), 1001-1011.

18. Yu, G. E.; Eisenberg, A., *Macromolecules* **1998,** *31* (16), 5546-5549.

19. Yu, K.; Bartels, C.; Eisenberg, A., *Macromolecules* **1998,** *31* (26), 9399-9402.

20. Yu, K.; Eisenberg, A., *Macromolecules* **1998,** *31* (11), 3509-3518.

21. Yu, Y. S.; Zhang, L. F.; Eisenberg, A., *Macromolecules* **1998,** *31* (4), 1144-1154.

22. Shen, H. W.; Eisenberg, A., *J. Phys. Chem. B* **1999,** *103* (44), 9473-9487.

23. Shen, H. W.; Zhang, L. F.; Eisenberg, A., *J. Am. Chem. Soc.* **1999,** *121* (12), 2728-2740.

24. Yu, K.; Bartels, C.; Eisenberg, A., *Langmuir* **1999,** *15* (21), 7157-7167.

25. Zhang, L. F.; Eisenberg, A., *Journal of Polymer Science Part B-Polymer Physics* **1999,** *37* (13), 1469-1484.

26. Zhang, L. F.; Eisenberg, A., *Macromolecules* **1999,** *32* (7), 2239-2249.

27. Soo, P. L.; Eisenberg, A., *Journal of Polymer Science Part B-Polymer Physics* **2004,** *42* (6), 923-938.

28. Choucair, A.; Eisenberg, A., *European Physical Journal E* **2003,** *10* (1), 37-44.

29. Kataoka, K.; Harada, A.; Nagasaki, Y., *Adv. Drug Delivery Rev.* **2001,** *47* (1), 113-131.

30. Allen, C.; Maysinger, D.; Eisenberg, A., *Colloids and Surfaces B-Biointerfaces* **1999,** *16* (1-4), 3-27.

31. Wang, C. W.; Oskooei, A.; Sinton, D.; Moffitt, M. G., *Langmuir* **2010,** *26* (2), 716-723.

32. Yen, B. K. H.; Gunther, A.; Schmidt, M. A.; Jensen, K. F.; Bawendi, M. G., *Angew Chem Int Edit* **2005,** *44* (34), 5447-5451.

33. Oskooei, S. A. K.; Sinton, D., *Lab Chip* **2010,** *10* (13), 1732-1734.

34. Kwon, G.; Naito, M.; Yokoyama, M.; Okano, T.; Sakurai, Y.; Kataoka, K., *J. Controlled Release* **1997,** *48* (2-3), 195-201.

35. Carambassis, A.; Rutland, M. W., *Langmuir* **1999,** *15* (17), 5584-5590.

CHAPTER 5

ON-CHIP LOADING OF FLUOURESCENT PROBES INTO BLOCK COPOLYMER MICELLES USING MULTIPHASE MICROFLUIDIC REACTORS

5.1. Introduction

Microfluidic reactors are well-suited for numerous applications due their ability to rapidly mix reagents, maintain a homogenous reaction environment, add reagents at precise time intervals, and continuously vary reaction conditions.[1-6] Furthermore, microfluidic devices also enable screening of a variety of reaction conditions by systemically varying reagent concentrations, temperature, and flow rates in order to produce high quality products using a minimum amount of reagents.[1-6] Microfluidic reactors have been widely used in material synthesis, including semiconducting nanoparticles (CdS, CdSe, and CdSe/ZnS core-shell),[7-15] metal nanoparticles (Au, Ag, Cu and Co),[16-18] titanium oxide nanorods,[19] janus and ternary polymeric particles[20-22]

In parallel, there has been considerable interest in using polymeric micelles in applications such as sensing, medical imaging and drug delivery. Particularly, block copolymer micelles have been found to be well-suited as drug delivery vehicles because they can be made biodegradable and biocompatible, and have tunable morphologies.[23-27] The morphologies of polymeric drug delivery vehicles have been shown to play a significant role in bio-transport, biodistribution and circulation times.[24, 27] Furthermore, in comparison with surfactant micelles, polymeric micelles generally have higher thermodynamic and kinetic stabilities, with much lower critical micelle concentrations (cmcs) (surfactants: 10^{-3} mole/L and block copolymers: 10^{-8} to 10^{-9} mole/L),[28] and lower rates of dissociation, which allow retention of drugs for a longer period of time, and eventually higher accumulation of drugs at a target site.[29] Typical methods for introducing drugs or probe molecules into polymeric micelles involve slow and time-

consuming drop-wise addition of water to a blend solution containing the copolymer and drug, followed by a long period of dialysis to remove the residual solvent.[27]

Microfluidics approaches to loading various colloidal nanostructures with drugs or small probe molecules have already been investigated by several researchers,[30-33] spurred by the potential for a small, fast and efficient portable devices for point-of-care drug loading.[34, 35] In addition, as shown in previous chapters, shear forces have been shown to strongly influence self-assembly via shear-induced breakup and coalescence of particles. In chapter 2, these two competing mechanisms have been utilized to effectively tune the size of quantum dot compound micelles (QDCMs); in chapter 3, the same competing mechanisms have been used to guide to solution self-assembly of block copolymers. Herein we anticipate that these two mechanisms can influence the loading efficiencies due to the following reasons. In general, loading efficiencies represent a balance between the thermodynamic partition coefficient and the kinetic restrictions to diffusion of small molecules into the core, both of which are influenced by water content. Slow addition provides the advantage of allowing more time for diffusion into the core at the expense of long preparation times. On-chip mixing has the advantage of being faster but at the potential cost of loading efficiency. However, increased shear and resulting on-chip processes of breakup and coalescence should improve exchange of material between micelles and between micelles and the surrounding solvent, which could mitigate the detrimental effects of fast mixing. Therefore, experiments to find out how the potential advantages balance the potential disadvantages of on-chip self-assembly and loading under various conditions are essential to moving forward with this technology.

In general, loading and release studies involving therapeutic drugs such as anti–cancers drugs doxorubicin (DXR) and docetaxel (Dtxl) are somewhat restricted by the high cost of the drugs.[36] Therefore, as an alternative, various probes are often used as stand-ins for drug encapsulation studies in block copolymers. These probes are not only cheaper and more accessible, but also they can be quantified by methods with greater sensitivity (e.g. fluorescence). For instance, many studies in the literatures used fluorescence spectroscopy to study the loading and release of fluorescent hydrophobic probes into/from micellar cores self-assembled from bio-compatible block copolymer.[37-43] These fluorescence experiments provide valuable feedback on essential parameters in drug delivery including the loading efficiency, the partition coefficient and the release profile.

In this chapter, as models for drug encapsulation, we will study the on-chip self-assembly and simultaneous loading of two fluorescent hydrophobic probes, pyrene and naphthalene, into PS-*b*-PAA crew-cut micelles using gas-liquid reactors. The block copolymer used is identical to that used for self-assembly studies in previous chapters. These two hydrophobic compounds were chosen because they have been well studied in the literature and also because one has a higher affinity for the PS-core (pyrene) than the other so that they should allow us to evaluate the practicality of the on-chip loading approach for molecules with different solubilities in the micelles core.[44, 45] The on-chip loading efficiency of each of the probes is evaluated for different chemical and flow conditions and compared to values obtained using a conventional bulk method involving dropwise water addition to a solution of block copolymer and dye molecules. While PS-*b*-PAA is not a biocompatible system, we employ it here due to the knowledge and

experience gained in the previous chapters. Together with the hydrophobic fluorescent probes, this system should serve as a model system that will provide some preliminary information for future studies on microfluidic self-assembly of biocompatible block copolymers.

5.2. Experimental Section

5.2.1. Materials

The composition of the polystyrene-*block*-poly(acrylic acid) sample used in this study was the same as in previous chapters, PS(665)-*b*-PAA(68), where numbers in brackets indicate number-average degrees same as in the previous chapters. Therefore, the relevant characterization information will not be repeated here. The reagents, dimethylformamide (DMF) (Aldrich, 99.9+%, HPLC grade, H_20 < 0.03%) and 1,4-dioxane Aldrich, 99.0%, reagent grade, H_20 < 0.05% were used as received without further purification. The dyes, pyrene (Aldrich, ≥ 99.0% (GC), fluorescence grade) and naphthalene (Aldrich, ≥ 99.7% (GC), analytical standard) were also used as received without further purification. The micro dialysis tubes (D-tube, Dialyzer Midi, MWCO 6-8 k Da) were purchased from Novagen.

5.2.2. Off-Chip Probe Loading

The copolymer PS(665)-*b*-PAA(68) was dissolved in DMF to a concentration of 1 wt % and allowed to stir overnight to form the copolymer stock solution. Pyrene or naphthalene were also dissolved in DMF to form appropriate dye stock solutions. The

dye and copolymer stock solutions were blended to give a ratio of 1 x 10^{-2} g dye/g polymer. This ratio was selected since in previous study it was found to yield the maximum loading efficiencies of hydrophobic probes in polycaprolactone-*block*-poly(ethylene oxide) (PCL-*b*-PEO) micelles.[37] The blend dye/copolymer solutions were diluted with pure DMF to a copolymer concentration of 0.33 wt % and allowed to stir for 4 hours in the dark. To induce micellization and probe loading, deionized water (D.I. H_2O) was added dropwise to the dye/copolymer solutions at a constant rate of 20 μL every 10 s with moderate magnetic stirring (600 rpm) until a target water concentration of 80 wt % was reached. The micelle/dye solutions were allowed to stir overnight in the dark. They were then dialyzed against pure deionized water to remove organic solvent and unincorporated dyes. During dialysis, water was changed every hour for the first 8 hours, and then micelle/dye solutions were allowed to dialyze overnight. The loading in dioxane was carried out using the same procedure outlined above. The dialyzed micelle/dye solutions were weighed on an analytical balance to determine the copolymer concentration in the final solutions.

5.2.3. On-Chip Probe Loading

The fabrication of microfluidic chips as well as flow control and fluid delivery followed the same procedure as outlined in Chapters 3 and 4; therefore, it will not be repeated here. The copolymer was dissolved in DMF to a concentration of 5.0 wt % and allowed to stir overnight to form the copolymer stock solution. Pyrene or naphthalene were also dissolved in DMF to form appropriate dye stock solutions. The dye and copolymer stock solutions were blended to give a ratio of 1.0 x 10^{-2} g dye/g polymer

(identical ratio to that employed in off-chip loading). To form solutions for the copolymer/dye stream, blend solutions were diluted with pure DMF to yield copolymer concentrations of 1.0 wt %. The blend solutions were stirred for 4 hours in the dark. As well, to form solutions for the water-containing stream, suitable amounts of water were added to pure DMF, taking into account the on-chip dilution factors.

For on-chip micellization/probe probe loading experiments, three streams were combined at equal flow rates to form gas-separated liquid plugs within the reactor: 1. a 1.0 wt % of PS(665)-*b*-PAA(68) single chains with dye concentration of 1.0 x 10^{-2} g dye/g polymer in DMF or dioxane 2. a separator stream containing DMF or dioxane only; and 3. a solution of DMF or dioxane containing different amounts of deionized water. Combination of the three liquid streams yielded a steady-state on-chip concentration of 0.33 wt % polymer with 1.0 x 10^{-2} g dye/g polymer ratio, identical to the off-chip loading experiments, but with various final water contents.

When a steady-state on-chip water content of 80 wt % was targeted in some cases, the water/solvent stream was replaced by a pure water stream; also the concentration of the copolymer was increased 3 fold to 3.0 wt %. To obtain a steady-state on-chip water content of 80 wt %, the flow rates of three liquid streams were adjusted accordingly. For all on-chip experiments, 50 μL solution produced on-chip was collected into 200 μL D.I. H_2O such that the same final polymer concentration was obtained as in the off-chip experiment. For all experiments, the relative gas-to-liquid flow ratio (Q_{gas}/Q_{liq}.) was ~1, and two different nominal total flow rates were investigated: Q_{total} = ~5 μL / min (low flow rate case) and ~50 μL / min (high flow rate case). All on-chip samples were dialyzed using micro dialysis tubes following the same dialysis procedure for the off-chip

experiments. The dialyzed micelle/dye solutions were weighed on an analytical balance to determine the copolymer concentration in the final solutions.

5.2.4. Determination of Probe Loading Efficiency

Absorption spectra were recorded on a Cary 50-scan UV – vis spectrophotometer. Static fluorescence measurements were recorded on an Edinburgh Instruments FLS 920 instrument equipped with a Xe 450W arc lamp and a red-sensitive PMT (R928-P). To determine the probe loading efficiency, probe-loaded micelles were broken down into singles chains and free probes by adding a small weighed aliquot of micelle solution (1-2 drops) to a known quantity of DMF and stirring for 4 hours in the dark to dissolve the micelles. PL intensity-concentration calibration curves for pyrene and naphthalene in DMF were determined in the linear range. Under identical conditions and within 5 min of obtaining the calibration curves, the fluorescence intensities of dissolved micelle solutions were measured. All spectra were run on air-equilibrated solutions. For fluorescence emission spectra, λ_{ex} was 337 nm for pyrene and 278 nm for naphthalene. Before calculating integrated photoluminescence intensities, a solvent background was subtracted and a correction for the detector response was applied to each sample and reference measurement. The dye concentrations were then determined from the calibration curves. After correcting for the dilution factors and taking into account of the original volume of the probe/micelle solution, the loading efficiency was determined. One way of expressing the loading of probe molecules into the micelles is through the loading efficiency. Riley et al. defined the loading efficiency (or drug entrapment as he called it) though the following expression:[46]

$$\text{loading efficiency (\%)} = \frac{\text{mass of probe in micelles (g)}}{\text{total mass of probe used (g)}} \times 100\%$$

The various steps in the loading and characterization of loading efficiency are depicted in Scheme 5.1. The errors were determined from multiple loading experiments under the same conditions.

5.2.5. Imaging of Micellar Morphologies.

Transmission electron microscopy (TEM) of various aqueous micellar dispersions was performed at a Hitachi H-700 electron microscope, operating at an accelerating voltage of 75 kV. For a typical TEM imaging, a 10 μL drop of dialyzed probe loaded micellar dispersion was deposited onto carbon-coated Formvar 300 mesh copper grid, and then shadowed with Pt/Pd wire for imaging.

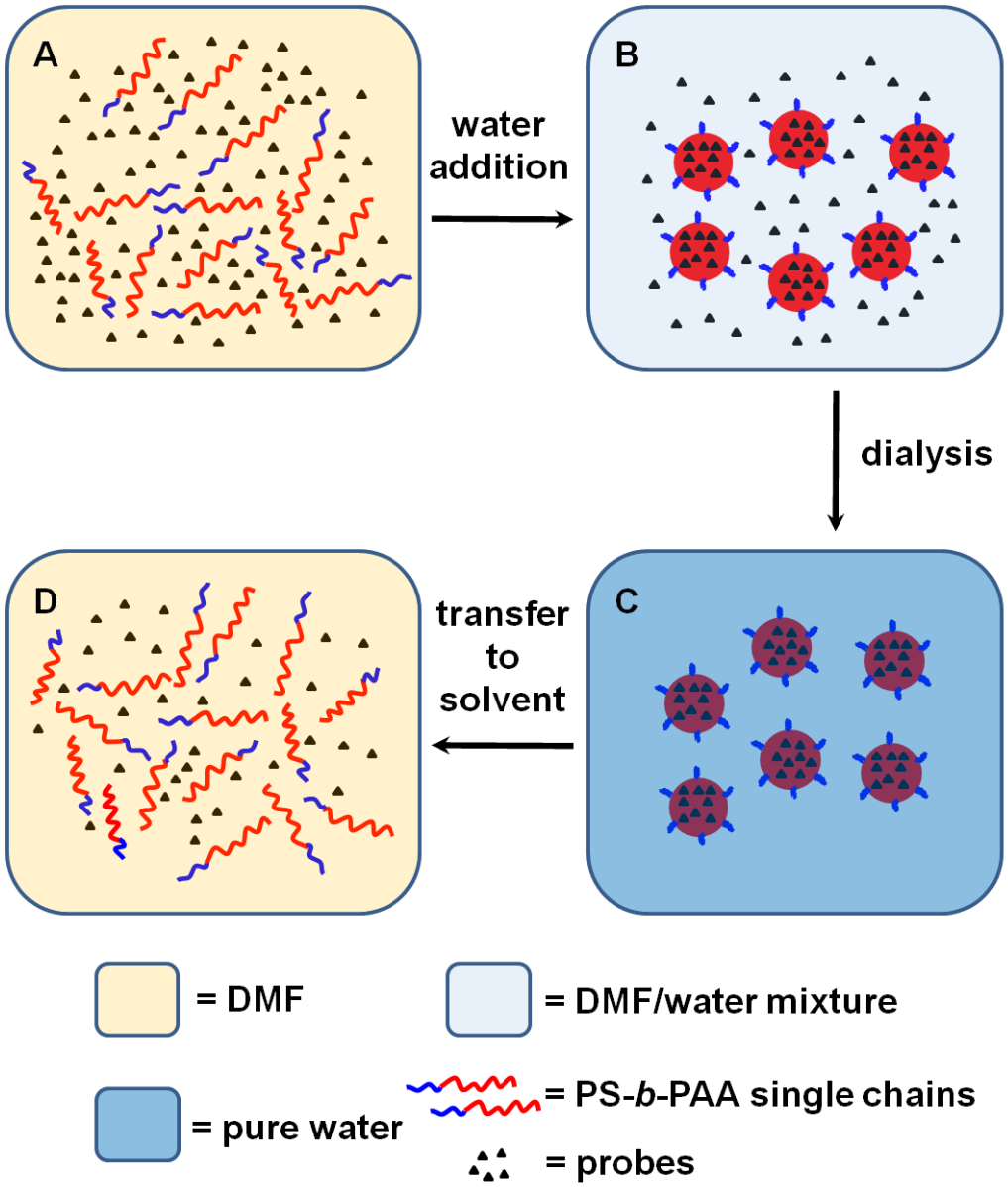

Scheme 5.1. Cartoon representations of the probe loading process in polymeric micelles and subsequent micelles break up to release probes for loading efficiency measurement. (A) The probes and single chains are co-dissolved in a common solvent (e.g. DMF). (B) Water addition causes micellization/probe encapsulation when water content is above the critical water content (cwc). (C) The micelles/loaded probes are dialyzed to remove organic solvent as well as unincorporated dyes. (D) The micelles are broken up to release the incorporated dyes for fluorescence measurements.

5.3. Results and Discussion

5.3.1. Off-Chip and On-Chip Dye Loading Efficiencies in DMF

The critical water content (cwc) for the present system of c_o = 0.33 wt % PS(665)-*b*-PAA(68) in DMF was determined in chapter 4 to be 3.0 wt %. As water is added above this value, the PS forms the core phase and the hydrophobic dye partitions into the core according to the partition coefficient, which is a measure of differential solubility of the compound between two immiscible phases (PS/solvent core and solvent/water medium). As the water content increases, the partition coefficient increases, but the core viscosity increases and the diffusion kinetics of the dye into the core decreases. Furthermore, in order to understand the loading results from both on-chip and off-chip experiments, it is important to have an understanding of the difference between the two loading environments. In the on-chip environment, fast mixing of water (~1 s) with the self-assembling constituents (polymer chains and probes) initiate the self-assembly/loading process when the average cross-stream water content is above cwc. In comparison, the off-chip loading experiments involve slow addition of water (20 μL/10 s) to a solution containing co-dissolved polymer chains and probes. The water addition is continued well past the cwc until 80 wt % water content is reached to ensure maximum loading efficiency. All the off-chip loading experiments were done in the same way.

For loading experiments, we choose two model hydrophobic compounds, one which has a higher affinity for the PS-core than the other. The partition coefficients for pyrene and naphthalene, between PS-based micelles and water have been determined to be 10^5 and 10^2, respectively.[44, 45] These two model hydrophobic compounds have been a popular choice in many loading studies involving polymeric micelles, including PEO-*b*-

PPO-PEO,[47] PCL-*b*-PEO,[48] PS-*b*-PEO,[42] and PS-*graft*-poly(2-vinylpyridine) (P2VP).[44, 45] We choose these two dyes due to their large difference in the partition coefficient for the PS-core which should allow us evaluate on-chip loading for hydrophobic molecules with different partition coefficients.

For the first set of experiments, we looked at the loading of pyrene, which has the higher affinity for the PS-core relative to DMF of the two dyes. Fig. 5.1 shows the loading efficiency determined at various off-chip and on-chip chemical conditions (i.e., different water contents) while Fig. 5.2 shows the corresponding micelles morphologies formed under the different conditions described in Fig. 5.1. The off-chip and on-chip loading morphologies were consistent with those obtained without the probe (from chapter 4 under the same water content), indicating that the small amount of dye does not strongly influence the self-assembly, as expected. The off-chip pyrene loading into PS-*b*-PAA micelles resulted in a loading efficiency of 81 ± 6 %, while the same water content on-chip gave loading efficiencies of 60 ± 4 % and 63 ± 3 % for the low and high flow rate cases, respectively; the on-chip loading efficiencies at the two different flow rates are the same within error. Water content will influence the partition coefficient of the dye into the core as well as the viscosity of the core. As mentioned previously, with increasing water content, the partition coefficient increases; however, at the same time, the core becomes more viscous as DMF is forced out from the core by the chemical potential gradient, and the rate of diffusion of the dye into the core also decreases. In the off-chip loading case, since water is added slowly at a constant rate (20 µL/ 10 s), the dye partitioning has more time to equilibrate and so thermodynamics dominate over kinetics.

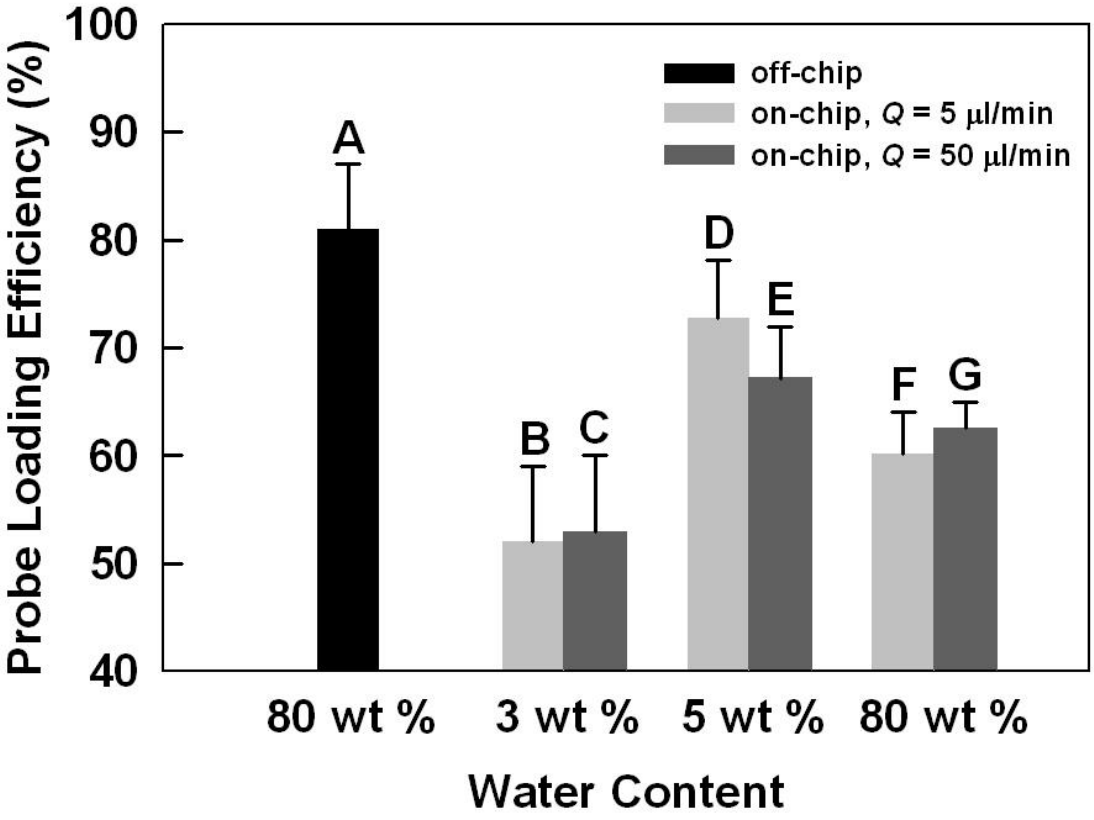

Figure 5.1. Off-chip and on-chip loading efficiencies for pyrene incorporation into PS(665)-*b*-PAA(68) micelles via self-assembly in DMF at various water contents and flow rates.

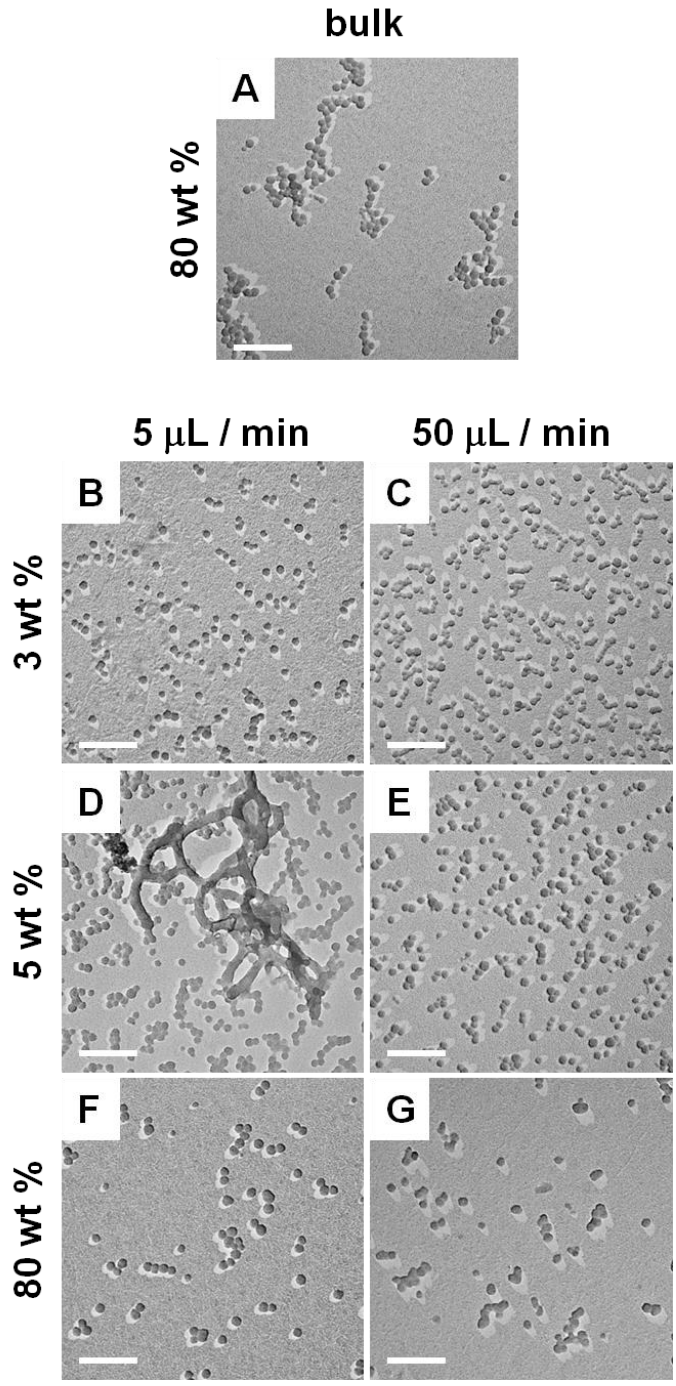

Figure 5.2. Off-chip and on-chip morphologies of PS(665)-*b*-PAA(68) micelles containing pyrene self-assembled in DMF at various water contents and flow rates. All scale bars represent 200 nm.

In the on-chip case, fast mixing of water with the self-assembling constituents (polymer chains and dyes) (~1 s) initiates micelle formation/probe loading near the injector.[5, 34, 35, 49] Fast mixing not only initiates faster micelle formation compared to the off-chip experiment, but also increases the rate at which the viscosity of the core increases. In this case, the amount of dye that diffuses into the core becomes limited by the fast increase in viscosity, which occurs before the equilibrium concentration of dye in the core is reached. In addition, flow rates seem to have a minimum effect on the on-chip loading efficiencies at high water content, which can be attributed to high viscosity in the PS-core, such that shear has a limited effect in influencing on-chip loading efficiency.

As shown in Fig. 5.1, we also investigated loading at two other water contents on-chip, one at the cwc (3.0 wt % water) and the other at cwc + 2 wt % (5.0 wt % water). The loading efficiencies at the cwc are the lowest of the on-chip results (52 ± 7 % for low flow rate and 53 ± 7 % for high flow rate) (Fig. 5.1 B and C) and this can be attributed to a lower percentage of copolymers existing as micelles at the cwc as well as a relatively low partition coefficient for the dye into the solvent-swollen core at low water content. Among the three water contents investigated, the on-chip loading efficiencies are the highest at 5.0 wt % water content (73 ± 6 % for low flow rate and 67 ± 5 % for high flow rate) (Fig. 5.1 D and E). This is a combined effect of increasing partition coefficient with increasing water content while the viscosity of the core still remains low (in comparison with the 80 wt % case on-chip) to permit the diffusion of dyes into the core.

In addition to giving the highest on-chip loading efficiencies, loading at 5.0 wt % water also shows the largest dependence on the flow rate. Based on the accompanying TEM data (Fig. 5.2, D and E) this difference appears to correspond with different shear-

induced morphologies at the two flow rates. The loading efficiency at low flow rate is higher than that at high flow rate. At low flow rate, the PS-*b*-PAA micelles in DMF have cylindrical morphologies due to the predominance of shear-induced coalescence; at high flow rate, the micelles have spherical morphologies due to predominance of shear-induced breakup (Fig 5.2 D and E). The results are consistent with identical conditions in the absence of dye (chapter 4, under identical conditions). The higher loading efficiency in the case of low flow rate might be attributed to that the incorporation of the dyes take place during the formation of spherical micelles, but shear-induced coalescence of sphere and subsequent rearrangement to form cylinder facilitate the diffusion of the dye into the core. It is likely that during the chain rearrangements, there is improved exchange of dyes between micelles and between micelles and the surrounding solvent

We will now investigate the loading of the other dye (naphthalene), which has a lower partition coefficient for the PS-core. The loading efficiencies and the corresponding morphologies are shown in Fig. 5.3 and 5.4, respectively. The morphologies are consistent with chapter 4 (under the inertial water content and without dye) . In the off-chip loading, naphthalene has lower loading efficiency (48 ± 2 %) than pyrene (80 ± 6 %) as is expected from the lower thermodynamic tendency of naphthalene to partition into the PS core relative to pyrene. In the on-chip loading, loading efficiency in general is low, owing to a combined effect of poor solubility as reflected in the off-chip value and kinetic constraints due to fast mixing. The general trends observed for on-chip naphthalene loading are similar to the pyrene case. The loading efficiency on-chip is the lowest at 80 wt % water, which can be attributed to the fast increase in viscosity (as a result of high water content) which occurs before the equilibrium concentration of dye

in the core is reached. The loading efficiency is the highest at 5 wt % water content owing to a combined effect of increasing partition coefficient with increasing water content as well as low viscosity of the core (in comparisons with 80 wt % on-chip case). In addition, loading at this water content shows similar flow rate dependent effects as observed in the pyrene case. The loading efficiency is higher at low flow rates and is attributed to the same morphological transformation effect that facilitates the diffusion of the dyes into the cores as mentioned in the case of pyrene in DMF.

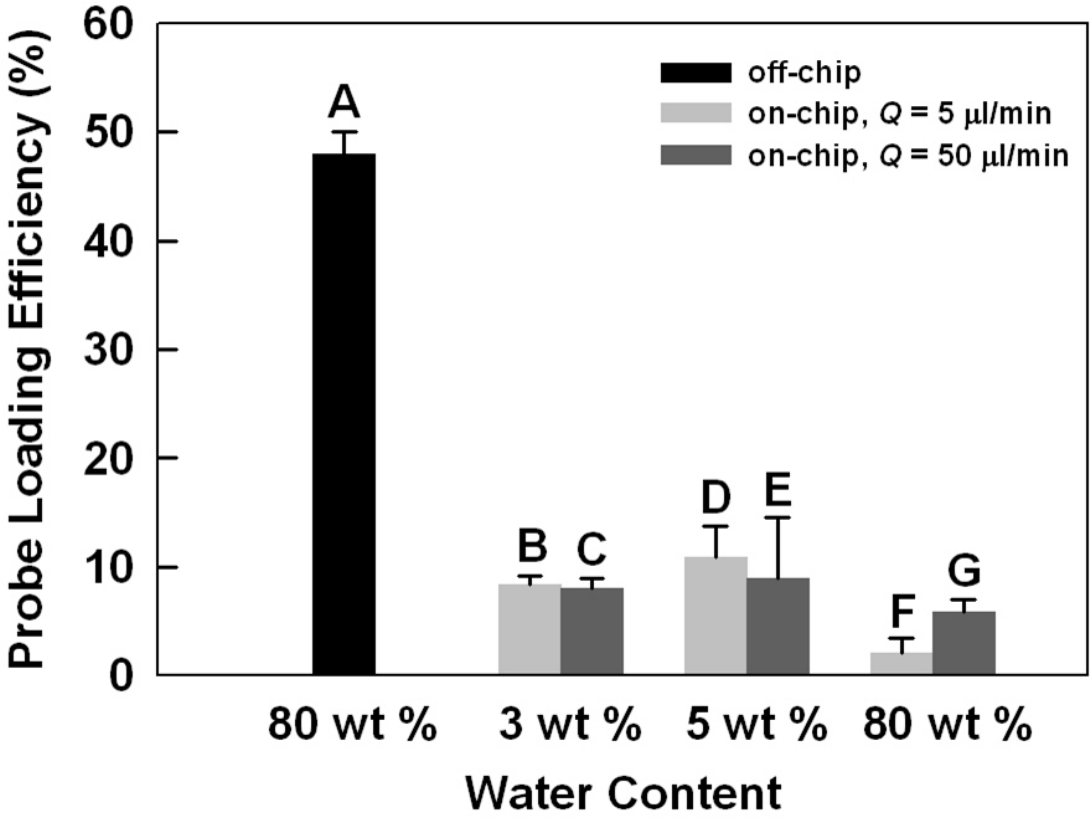

Figure 5.3. Off-chip and on-chip loading efficiencies for naphthalene incorporation into PS(665)-*b*-PAA(68) micelles via self-assembly in DMF at various water contents and flow rates.

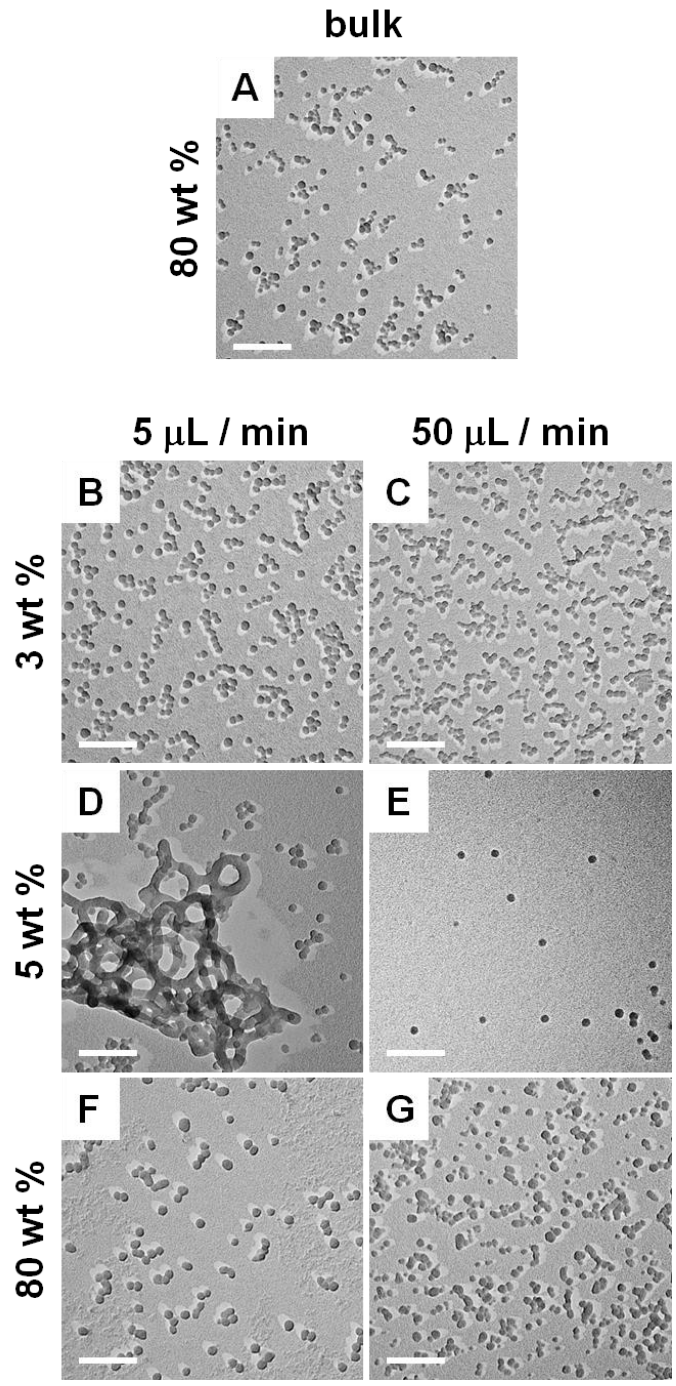

Figure 5.4. Off-chip and on-chip morphologies of PS(665)-*b*-PAA(68) micelles containing naphthalene self-assembled in DMF at various water contents and flow rates. All scale bars represent 200 nm.

5.3.2. Off-Chip and On-Chip Dye Loading Efficiencies in Dioxane

The choice of micellization/loading solvent will have a strong influence on the partition coefficient of probes into the micelle core, due to the strong dependence of the thermodynamic partitioning on the relative interactions between the probe and the dispersing medium (solvent + water) and the probe and the micelle core (PS + solvent). Also, the extent of solvent swelling of the core, which will depend on the affinity of the solvent for PS, will influence the chain dynamics, and thus the extent to which diffusion of dye into the core is kinetically restricted. Finally, we have shown in previous chapters that the micelle morphology and size both on-chip and off-chip are influenced by the choice of solvent; it is reasonable to expect that morphology and size will influence the loading efficiency, due to different interfacial areas and encapsulation geometries. Therefore, it was of interest to compare dye loading in DMF, described in the last section, with dye loading in another solvent. For this we chose dioxane, which is a less polar solvent than DMF with a higher affinity for the PS core.

The cwc for the present system of c_0 = 0.33 wt % PS(665)-*b*-PAA(68) in dioxane, which was determined by light scattering as described in chapter 4, is 8.5 wt %. We chose a single water content for the on-chip experiments in dioxane: 2.0 wt % above cwc (i.e., 10.5 wt % water content); the off-chip loading still follows the same methodology as described in the previous section. The loading efficiencies and the corresponding morphologies are shown in Figure 5.5 and 5.6, respectively. Off-chip loading of pyrene into micelles in dioxane/water results in 94 ± 2 % loading efficiency, compared to 81 ± 6 % for the same dye into micelles in DMF/water under the same off-chip conditions. Compared to DMF, the micellar cores are more swollen in dioxane,[50-52] and solvent

swelling should decrease the partition coefficient since the core and surroundings are chemically similar. However, solvent swelling also increases chain dynamics, which makes the kinetics of reaching the equilibrium partitioning faster. In off-chip loading results of pyrene in DMF and dioxane, the kinetic factor has played a dominant role in contributing to the higher loading efficiency is dioxane.

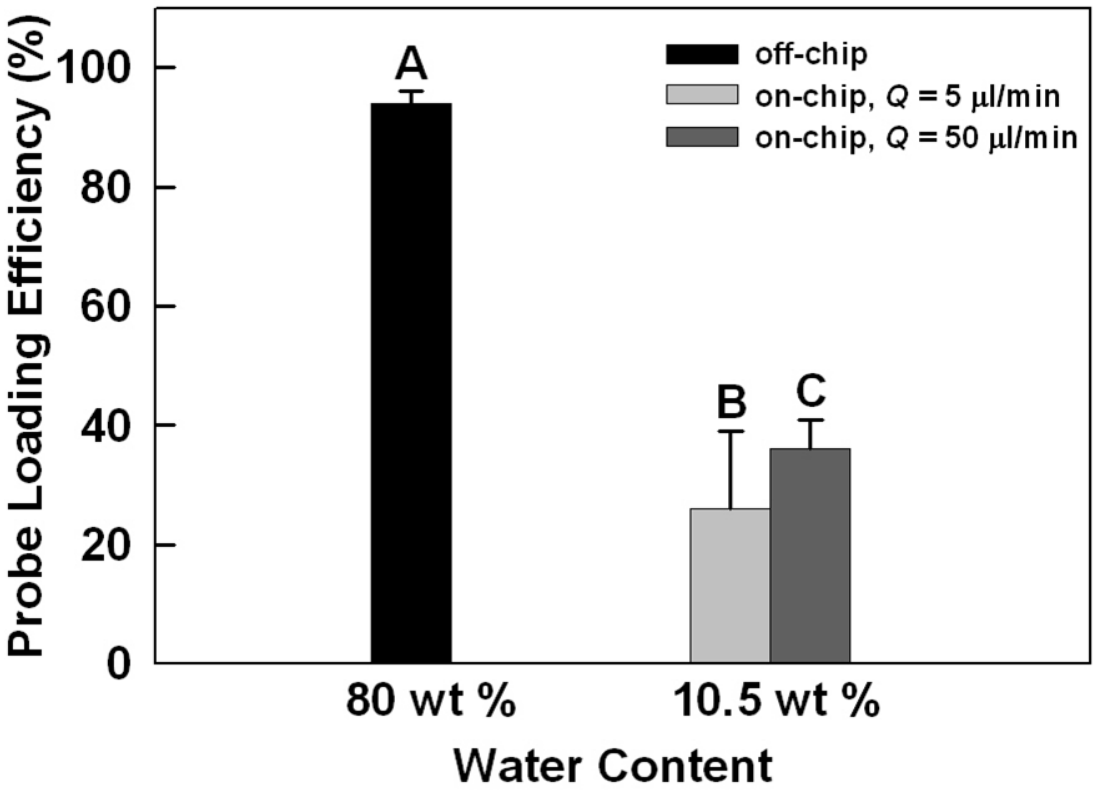

Figure 5.5. Off-chip and on-chip loading efficiencies for pyrene incorporation into PS(665)-*b*-PAA(68) micelles via self-assembly in dioxane at various water contents and flow rates.

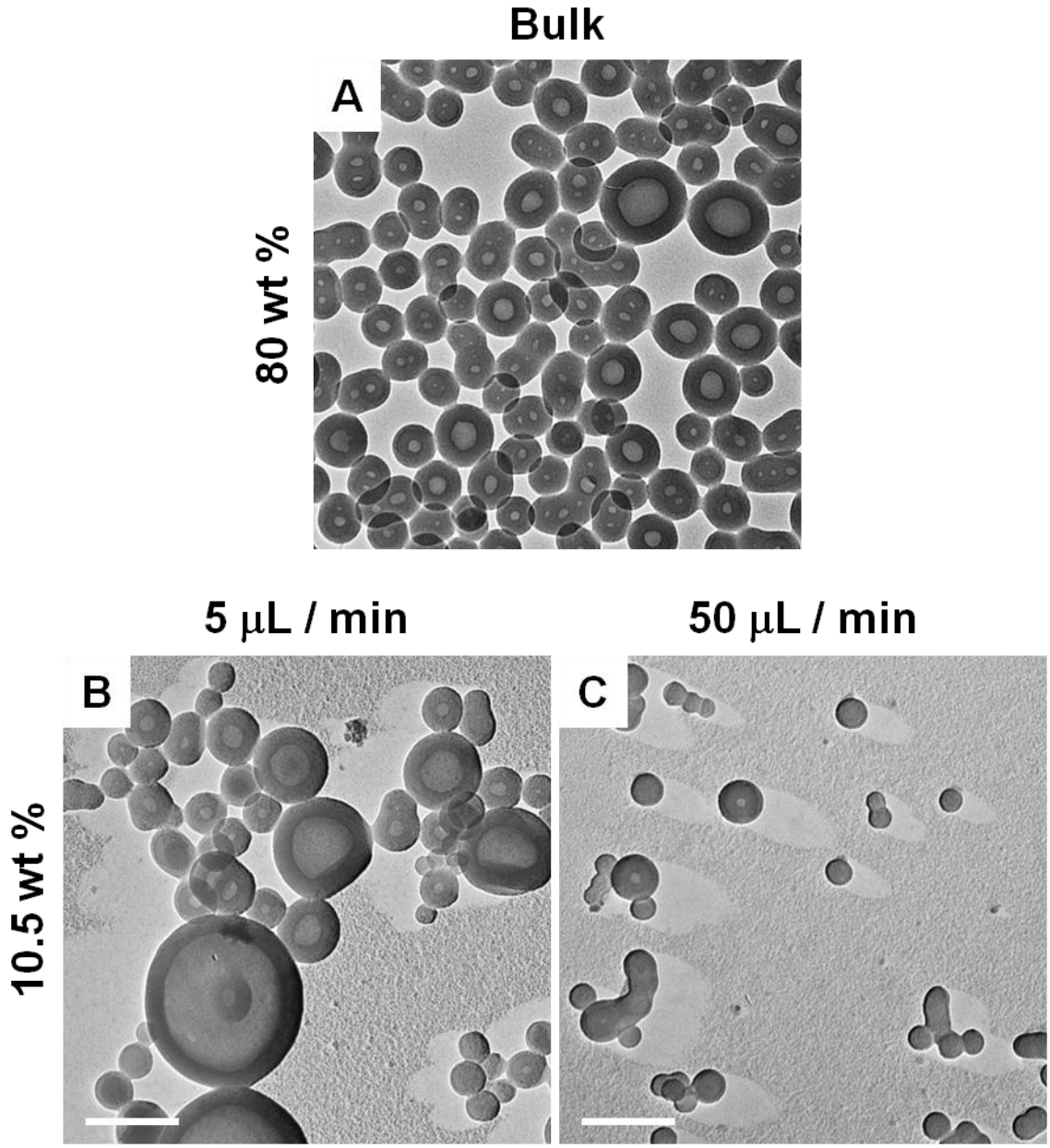

Figure 5.6. Off-chip and on-chip morphologies of PS(665)-*b*-PAA(68) micelles containing pyrene self-assembled in dioxane at various water contents and flow rates. All scale bars represent 200 nm.

On-chip loading of pyrene in dioxane at 10.5 wt % water content (cwc + 2 wt %) water shows lower loading efficiency at both low and high flow rates (30 ± 10 % and 36 ± 5 %, respectively) than the off-chip loading in the same solvent. This can be attributed to lower thermodynamic driving for the probes to partition into the PS-cores in the case of on-chip loading due to lower water content. In addition, the higher on-chip loading efficiency at high flow rate as compared to low flow rate is likely related to an increased interfacial area of the micelles, since the vesicles are shown to be broken down via shear into spherical micelles at fast flow rate (Fig. 5.6 B and C). The increased micellar interfacial area under shear-induced breakup should increase the diffusion rate of dyes into the cores, increasing the loading efficiencies relative to the lower flow rate case.

The loading efficiency and the corresponding morphologies for naphthalene loading in micelles formed in dioxane are shown in Figure 5.7 and 5.8, respectively. The morphologies are similar to other probe both off-chip and on-chip. In dioxane, the off-chip loading efficiency of naphthalene (2 ± 1 %) is very low compared to the off-chip loading of naphthalene in the DMF (48 ± 2 %). However, this is not entirely unexpected considering the micellar cores are very swollen in dioxane compared with DMF; solvent swelling should decrease the partition coefficient since the cores and the surroundings are energetically similar. In addition, when comparing off-chip loading of naphthalene (2 ± 1 %) in dioxane with the off-chip loading of pyrene in the same solvent (94 ± 2 %), the higher partition coefficient of pyrene has played in key role in contributing the high loading efficiency. The on-chip loading of naphthalene in dioxane shows loading efficiency of 2 ± 2 % and 6.0 ± 0.8 % for the low and high flow rates, respectively. While the on-chip loading efficiency at low flow rate is similar to that in the bulk in the

same solvent, the on-chip loading efficiency at high flow rates shows significantly higher loading efficiency than both the off-chip and on-chip at low rates. The increased on-chip loading efficiency of naphthalene in dioxane at high flow rate compared to the low rate rates is attributed to the same phenomenon observed in the on-chip loading of pyrene in dioxane: increased interfacial area should provide improved loading pathways of probes into the micellar cores. This highlights that fact that there are conditions under which shear can improve the loading efficiency.

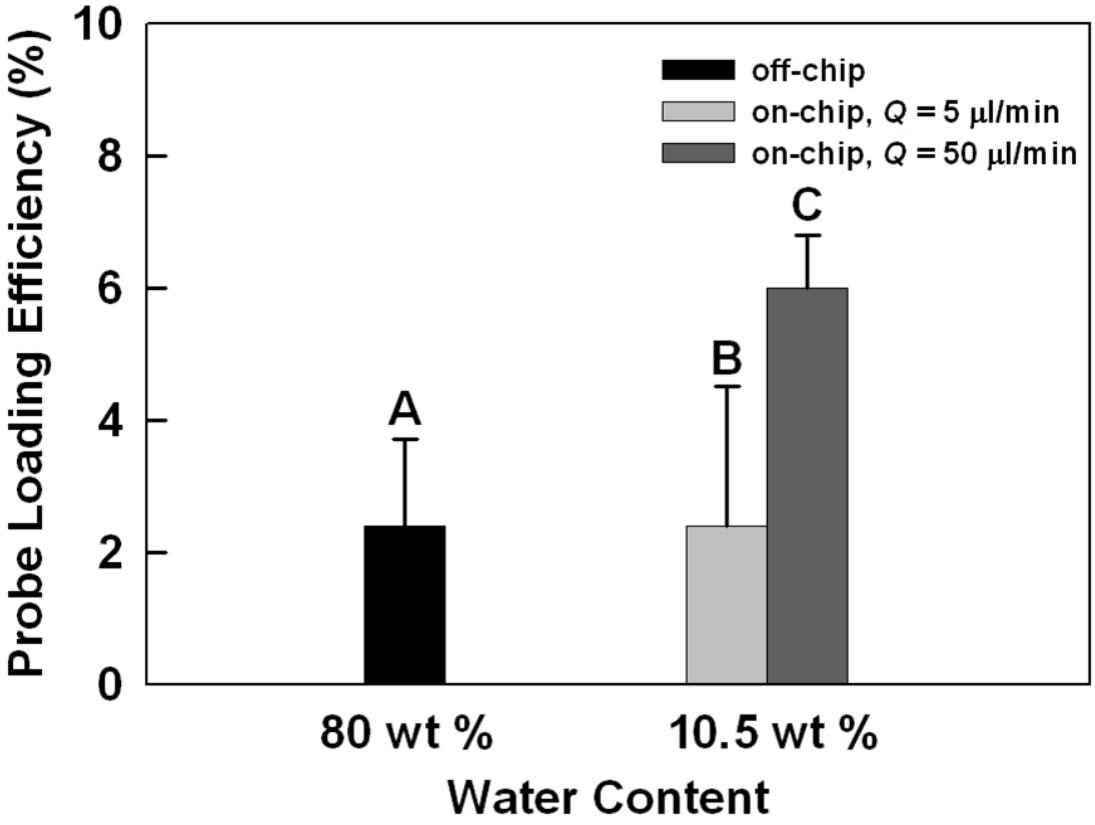

Figure 5.7. Off-chip and on-chip loading efficiencies for naphthalene incorporation into PS(665)-*b*-PAA(68) micelles via self-assembly in dioxane at various water contents and flow rates.

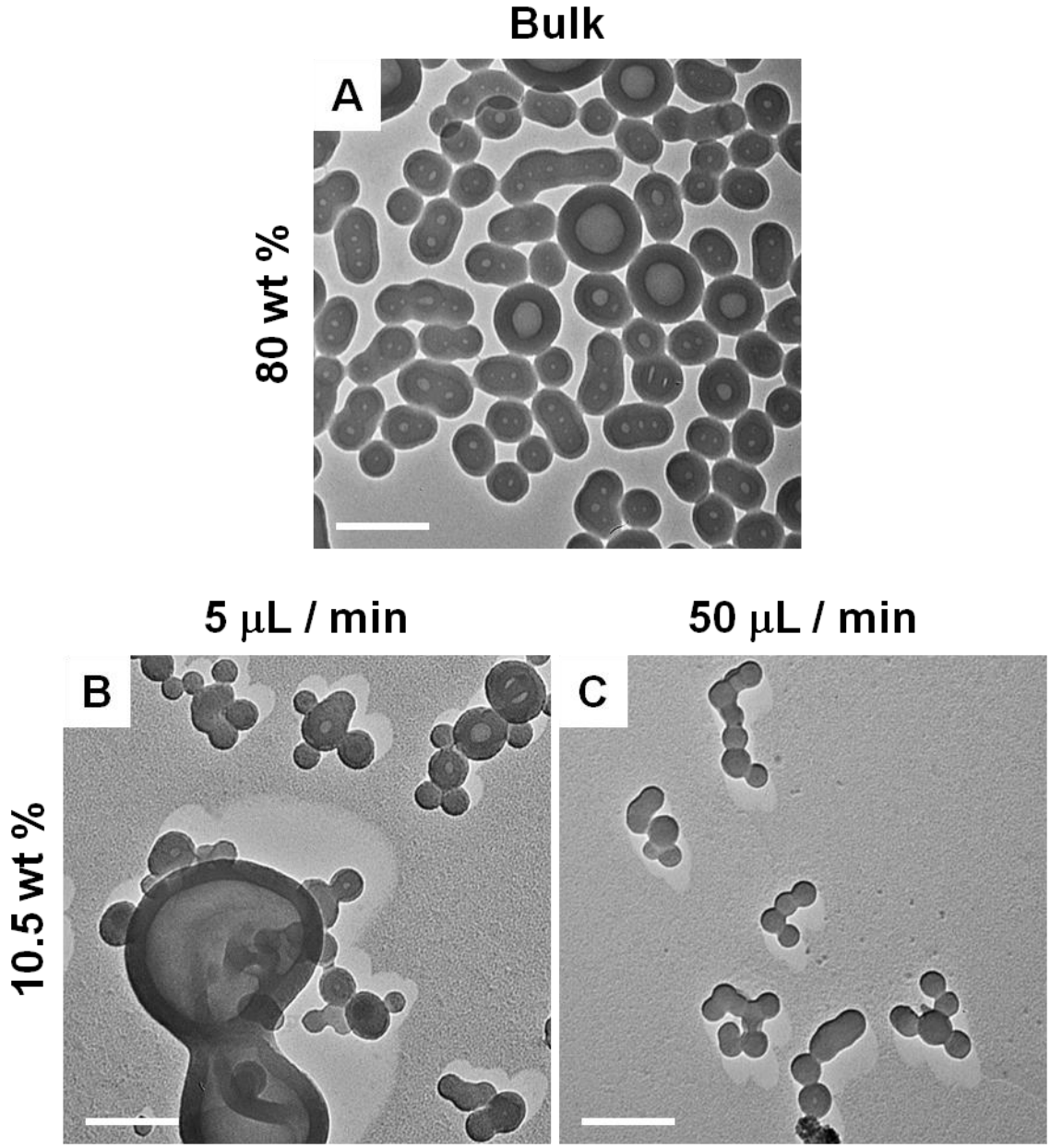

Figure 5.8. Off-chip and on-chip morphologies of PS(665)-*b*-PAA(68) micelles containing naphthalene self-assembled in dioxane at various water contents and flow rates. All scale bars represent 200 nm.

5.4. Conclusions

In this chapter, the loading of two hydrophobic probes in PS-*b*-PAA micelles on gas-liquid segmented microfluidic reactors were studied; the on-chip loading results were compared with off-chip loading results which involved slow drop-wise water addition. The dependence of loading efficiency on several on-chip characteristics unique to two-phase flow were explored: fast mixing, shear-induced micelle break-up and coalescence. In addition, the effect of solvents on loading efficiency were explored. In general when loading was carried out in DMF, the on-chip loading efficiency is lower than that in the bulk, which is a result of the kinetic constraint of the diffusion of dyes into the micellar cores as a result of fast mixing. Nonetheless, in certain cases the on-chip loading efficiency is comparable (within 10 % difference) to that produced in the bulk with significant reduction in loading times (for the low rate case). When the solvent was switched from DMF to dioxane, we found that in certain case, the off-chip loading is higher than in the bulk, possibly due to shear-induced morphology changes leading to improved loading pathways of probes into the micellar cores. Through this work, we demonstrated that on-chip shear force can be used to influence loading efficiency, and we also gain understanding of the various thermodynamic and kinetic factors that are critical to improving on-chip loading. In general, on-chip loading of probes offers immense potential: the on-chip loading percentage is near that in the bulk (in the best case scenario) with significant reduction in loading times (from hrs to min); in certain case, on-chip loading is better than off-chip due to shear-induced morphological effects; as well, on-chip loading strategy can be effectively coupled with the potential of point-of care-strategy that microfluidic devices offer such that it produces ready to administer formulations.

5.5. References

1. Song, H.; Bringer, M. R.; Tice, J. D.; Gerdts, C. J.; Ismagilov, R. F., Appl. Phys. Lett. **2003,** 83 (22), 4664-4666.

2. Song, H.; Chen, D. L.; Ismagilov, R. F., Angew Chem Int Edit **2006,** 45 (44), 7336-7356.

3. Song, H.; Tice, J. D.; Ismagilov, R. F., Angew Chem Int Edit **2003,** 42 (7), 768-772.

4. Song, Y. J.; Hormes, J.; Kumar, C. S. S. R., Small **2008,** 4 (6), 698-711.

5. Gunther, A.; Jensen, K. F., Lab Chip **2006,** 6 (12), 1487-1503.

6. Gunther, A.; Khan, S. A.; Thalmann, M.; Trachsel, F.; Jensen, K. F., Lab Chip **2004,** 4 (4), 278-286.

7. Edel, J. B.; Fortt, R.; deMello, J. C.; deMello, A. J., Chem Commun **2002,** (10), 1136-1137.

8. Chan, E. M.; Mathies, R. A.; Alivisatos, A. P., Nano Lett. **2003,** 3 (2), 199-201.

9. Krishnadasan, S.; Tovilla, J.; Vilar, R.; deMello, A. J.; deMello, J. C., J. Mater. Chem. **2004,** 14 (17), 2655-2660.

10. Wang, H. Z.; Li, X. Y.; Uehara, M.; Yamaguchi, Y.; Nakamura, H.; Miyazaki, M. P.; Shimizu, H.; Maeda, H., Chem Commun **2004,** (1), 48-49.

11. Chan, E. M.; Alivisatos, A. P.; Mathies, R. A., J. Am. Chem. Soc. **2005,** 127 (40), 13854-13861.

12. Wang, H. Z.; Nakamura, H.; Uehara, M.; Yamaguchi, Y.; Miyazaki, M.; Maeda, H., Adv. Funct. Mater. **2005,** 15 (4), 603-608.

13. Krishnadasan, S.; Brown, R. J. C.; deMello, A. J.; deMello, J. C., Lab Chip **2007,** 7 (11), 1434-1441.

14. Sounart, T. L.; Safier, P. A.; Voigt, J. A.; Hoyt, J.; Tallant, D. R.; Matzke, C. M.; Michalske, T. A., Lab Chip **2007,** 7 (7), 908-915.

15. Yang, H. W.; Luan, W. L.; Tu, S. T.; Wang, Z. M. M., Lab Chip **2008,** 8 (3), 451-455.

16. Kohler, J. M.; Abahmane, L.; Wagner, J.; Albert, J.; Mayer, G., Chem. Eng. Sci. **2008,** 63 (20), 5048-5055.

17. Song, Y. J.; Modrow, H.; Henry, L. L.; Saw, C. K.; Doomes, E. E.; Palshin, V.; Hormes, J.; Kumar, C. S. S. R., Chem. Mater. **2006,** 18 (12), 2817-2827.

18. Song, Y. J.; Doomes, E. E.; Prindle, J.; Tittsworth, R.; Hormes, J.; Kumar, C. S. S. R., J. Phys. Chem. B **2005,** 109 (19), 9330-9338.

19. Cottam, B. F.; Krishnadasan, S.; deMello, A. J.; deMello, J. C.; Shaffer, M. S. P., Lab Chip **2007,** 7 (2), 167-169.

20. Nie, Z. H.; Xu, S. Q.; Seo, M.; Lewis, P. C.; Kumacheva, E., J. Am. Chem. Soc. **2005,** 127 (22), 8058-8063.

21. Nie, Z. H.; Li, W.; Seo, M.; Xu, S. Q.; Kumacheva, E., J. Am. Chem. Soc. **2006,** 128 (29), 9408-9412.

22. Seo, M.; Nie, Z. H.; Xu, S. Q.; Mok, M.; Lewis, P. C.; Graham, R.; Kumacheva, E., Langmuir **2005,** 21 (25), 11614-11622.

23. Geng, Y.; Dalhaimer, P.; Cai, S. S.; Tsai, R.; Tewari, M.; Minko, T.; Discher, D. E., Nat. Nanotechnol. **2007,** 2 (4), 249-255.

24. Sentjurc, M.; Vrhovnik, K.; Kristl, J., J. Controlled Release **1999,** 59 (1), 87-97.

25. Coldren, B.; van Zanten, R.; Mackel, M. J.; Zasadzinski, J. A.; Jung, H. T., Langmuir **2003,** 19 (14), 5632-5639.

26. Pereira-Lachataignerais, J.; Pons, R.; Panizza, P.; Courbin, L.; Rouch, J.; Lopez, O., Chem. Phys. Lipids **2006,** 140 (1-2), 88-97.

27. Allen, C.; Maysinger, D.; Eisenberg, A., Colloids and Surfaces B-Biointerfaces **1999,** 16 (1-4), 3-27.

28. Khougaz, K.; Gao, Z. S.; Eisenberg, A., Macromolecules **1994,** 27 (22), 6341-6346.

29. Kataoka, K.; Harada, A.; Nagasaki, Y., Adv. Drug Delivery Rev. **2001,** 47 (1), 113-131.

30. Kolishetti, N.; Dhar, S.; Valencia, P. M.; Lin, L. Q.; Karnik, R.; Lippard, S. J.; Langer, R.; Farokhzad, O. C., Proc. Natl. Acad. Sci. U. S. A. **2010,** 107 (42), 17939-17944.

31. Xu, Q. B.; Hashimoto, M.; Dang, T. T.; Hoare, T.; Kohane, D. S.; Whitesides, G. M.; Langer, R.; Anderson, D. G., Small **2009,** 5 (13), 1575-1581.

32. Zhang, Y.; Sinha-Ray, S.; Yarin, A. L., J. Mater. Chem. **2011,** 21 (23), 8269-8281.

33. Karnik, R.; Gu, F.; Basto, P.; Cannizzaro, C.; Dean, L.; Kyei-Manu, W.; Langer, R.; Farokhzad, O. C., Nano Lett. **2008,** 8 (9), 2906-2912.

34. Schabas, G.; Wang, C. W.; Oskooei, A.; Yusuf, H.; Moffitt, M. G.; Sinton, D., Langmuir **2008,** 24 (19), 10596-10603.

35. Wang, C. W.; Oskooei, A.; Sinton, D.; Moffitt, M. G., Langmuir **2010,** 26 (2), 716-723.

36. Choucair, A.; Soo, P. L.; Eisenberg, A., Langmuir **2005,** 21 (20), 9308-9313.

37. Soo, P. L.; Luo, L. B.; Maysinger, D.; Eisenberg, A., Langmuir **2002,** 18 (25), 9996-10004.

38. Bromberg, L.; Temchenko, M., Langmuir **1999,** 15 (25), 8627-8632.

39. Bromberg, L.; Temchenko, M., Langmuir **1999,** 15 (25), 8633-8639.

40. Yokoyama, M.; Kwon, G. S.; Okano, T.; Sakurai, Y.; Naito, M.; Kataoka, K., J. Controlled Release **1994,** 28 (1-3), 59-65.

41. Cao, T.; Munk, P.; Ramireddy, C.; Tuzar, Z.; Webber, S. E., Macromolecules **1991,** 24 (23), 6300-6305.

42. Wilhelm, M.; Zhao, C. L.; Wang, Y. C.; Xu, R. L.; Winnik, M. A.; Mura, J. L.; Riess, G.; Croucher, M. D., Macromolecules **1991,** 24 (5), 1033-1040.

43. Zhao, J. X.; Allen, C.; Eisenberg, A., Macromolecules **1997,** 30 (23), 7143-7150.

44. Njikang, G. N.; Gauthier, M.; Li, J. M., Polymer **2008,** 49 (25), 5474-5481.

45. Njikang, G.; Gauthier, M.; Li, J. M., Polymer **2008,** 49 (5), 1276-1284.

46. Riley, T.; Govender, T.; Stolnik, S.; Xiong, C. D.; Garnett, M. C.; Illum, L.; Davis, S. S., Colloids and Surfaces B-Biointerfaces **1999,** 16 (1-4), 147-159.

47. Kabanov, A. V.; Nazarova, I. R.; Astafieva, I. V.; Batrakova, E. V.; Alakhov, V. Y.; Yaroslavov, A. A.; Kabanov, V. A., Macromolecules **1995,** 28 (7), 2303-2314.

48. Allen, C.; Yu, Y. S.; Maysinger, D.; Eisenberg, A., Bioconjugate Chem. **1998,** 9 (5), 564-572.

49. Khan, S. A.; Gunther, A.; Schmidt, M. A.; Jensen, K. F., Langmuir **2004,** 20 (20), 8604-8611.

50. Zhang, L. F.; Shen, H. W.; Eisenberg, A., Macromolecules **1997,** 30 (4), 1001-1011.

51. Zhang, L. F.; Eisenberg, A., Macromolecules **1999,** 32 (7), 2239-2249.

52. Shen, H. W.; Zhang, L. F.; Eisenberg, A., J. Phys. Chem. B **1997,** 101 (24), 4697-4708.

CHAPTER6

CONCLUSIONS, CONTRIBUTIONS TO ORIGINAL KNOWLEDGE AND SUGGESTIONS FOR FUTURE WORK

6.1. Conclusions, Contributions to Original Knowledge

In this thesis, we have shown that block copolymer solution self-assembly processes in microfluidic devices are strongly influenced by the flow field of the solvent medium. The effect of extremely high shear on block copolymer self-assembly has never been thoroughly investigated until now. We have shown that extremely high shear on-chip can strongly influence self-assembly results, in terms of particle size, morphology, and small molecule loading as a result of shear-induced pathways. The influence of shear on solution self-assembly at the nanoscale has not been extensively investigated in the past. Part of the reason for this is that under typical bulk conditions, large volumes are not conducive to high shear rates (which are required for influencing particles at the nanoscale), even under extreme stirring conditions. As well, in the bulk any shear energy imposed on the system is quickly dissipated to the environment due to large volume.[1] However, as we show in this thesis, the microscale environment of two-phase microfluidic reactors provide access to shear that is sufficiently high to strongly influence nanoscale self-assembly, even with the relatively low driving energy provided by syringe pumps, providing a unique platform for investigating these effects for the first time.

Microfluidic environments have been widely employed in materials synthesis because crucial process parameters such as flow characteristics, flow rates, temperature, residence time and residence time distribution can be controlled with ease.[2] In particular, in two phase reactors, mixing is greatly enhanced as a result of chaotic advection due to compartmentalization of reagents plugs.[3-9] The mixing advantage has been the focus of application for these reactors. That is, the unique flow fields in two-phase reactors have been applied to achieve rapid mixing of molecular reagents;[3-9] however, the high fluid

shear rates that develop at the two-phase interfaces in these flows and the resulting influence on particle collisions and breakup has not been fully studied. Until now, the flow-tunable shear forces in the gas-liquid segmented reactors have not been fully characterized, nor has the full potential of these shear fields been demonstrated. For the first time, this work demonstrates that extremely high shear fields in two-phase microfluidic reactors can effect top-down influence on nanoscale structures formed by self-assembly. In the process, this thesis provides new insights into the effect of shear on the size and morphology of self-assembly products via the mechanisms of shear-induced particle coalescence and breakup.

This section provides a summary of the significant findings discussed in this thesis, emphasizing contributions to original knowledge. Our goal in this thesis was to develop new methodologies to combine highly tunable top-down microfluidic processes with the efficient bottom-up self-assembly of block copolymers, in order to achieve a high level of control over the resulting nanostructures. Specifically, the extremely strong and flow-variable shear forces in the corners of the liquid plugs of gas-liquid microfluidic reactors was utilized as a versatile top-down handle on self-assembly. The organization of section 6.1 will mirror the three major research topics presented in this thesis and is accordingly divided into three sub-sections. Section 6.1.1 summarizes chapter 2, and thus describes the most pertinent aspects of the on-chip self-assembly of polystyrene-coated cadmium sulfide quantum dots (PS-CdS) with amphiphilic stabilizing chains into mesoscale quantum dot compound micelles (QDCMs). Section 6.1.2 describes chapters 3 and 4, which explore unprecedented top-down morphology control of block copolymer micelles using two-phase microfluidic reactors. Finally, section 6.1.3 summarizes the

findings of chapter 5, which takes the first steps into exploring the potential of our top-down microfluidic process for loading hydrophobic molecules into the cores of block copolymer micelles, with future applications such as point-of-care preparation of drug-delivery formulations in mind.

6.1.1. On-Chip Size Control of Quantum Dot Compound Micelles (QDCMs)

Chapter 2 examined a directed self-assembly strategy using the flow-variable shear forces in gas-liquid microfluidic reactors to control the mean size and size distributions of quantum dot compound micelles (QDCMs). This represents an application of a top-down approach, in which high shear corners effect an influence on the resulting particle sizes.

Self-assembly was initiated by fast mixing of polymer/QD constituents with water via chaotic advection within the liquid plugs as the plugs travelled down a sinusoidal mixing channel. The resulting QDCMs then entered a post-formation channel where they were subject to processing via high-shear regions in the corners of the liquid plugs, followed by off-chip kinetic quenching and analysis by TEM. We investigated the effects of flow parameters (i.e. gas-to-liquid ratio, Q_{gas}/Q_{liquid}, and total flow rate, Q_{total}) and a single chemical parameter (i.e. water content) on the final size distributions of QDCMs.

In the limit of $Q_{gas}/Q_{liquid} = 0$, which described a single-phase liquid reactor without chaotic advection, the mean QDCM diameter was 54 nm with a comparatively broad distribution (SD = 42 %) which was attributed to the large particle residence time distribution due to the absence of gas-liquid segmentation. We showed that the effect of gas-liquid segmentation was dramatic: when the gas to liquid flow ratio was increased

above a zero value, Q_{gas}/Q_{liquid} = 1.6, the mean particle size went up to 137 nm and the size distribution narrowed to SD = 28 %. The increase in size was attributed to high shear in the plug corners increasing the rate of particle collisions and hence the rate of coalescence; the narrowing of the size distribution was attributed to liquid compartmentalization with the introduction of the gas phase, which lowered the particle residence time distribution.

We found that the effect of the gas-to-liquid ratio could be divided into two regimes: the growth regime of $Q_{gas}/Q_{liquid} \approx$ 0-0.8 and the breakup regime of $Q_{gas}/Q_{liquid} >$ 0.8. In the growth regime, the dominant on-chip mechanism is shear-induced particle coalescence, whereas in the breakup regime, the dominant on-chip mechanism is shear-induced particle breakup, which becomes prominent above a critical capillary number.

Finally, we described on-chip QDCM particle size control in a master graph of particle size at constant Q_{gas}/Q_{liquid} as a function of both total flow rate and water content. There were two general trends observed in these plots. At the lowest flow rates, where shear-induced particle coalescence is dominant, the particles sizes were highly dependent on the water content, with a general trend of increasing size with decreasing water content; this trend was due to the lower core viscosities (via solvent swelling) and thus decreasing activation energies for coalescence as the water content decreased. In this case, the dominant on-chip shear effect is shear-induced particle coalescence. It was found that for all water concentrations, the particle sizes showed a monotonic decrease and became more similar with increasing total flow rate, due to the increasing contribution of shear-induced particle breakup.

In the area of polymer self-assembly, precise control over the sizes of nanoscale structures has been a challenging research topic because the resulting sizes are often controlled by a complex interplay between various thermodynamic and kinetic factors.[10-19] However, this area still continues to attract enormous amount of research efforts due both to its fundamental and applied importance.[16, 17, 20] In order to take full advantage of the efficiency of self-assembly and to make the best use of the resulting nanoscale structures, the lack of precise control over the sizes of nanoscale structures influenced by kinetics must be addressed. Herein, we demonstrated how flow-tunable shear forces influenced the sizes of self-assembled nanostructures via competing mechanisms of particle coalescence and breakup. The knowledge that we obtained should have fundamental and applied interest for the field of self-assembly.

6.1.2. On-Chip Morphology Control of Block Copolymer Micelles

Block copolymer solution self-assembly has been extensively researched in the last twenty years, owing to the enormous fundamental and applied importance of block copolymer micelles.[10, 11, 15, 21-29] Significant advancements and understanding in the field have been accomplished as a result. Early research in the field focused heavily on chemical methods (the bottom-up approach) to direct the self-assembly.[10, 11, 15, 21-29] Nonetheless, due to advancements in lithographic technologies,[2, 30-33] we envision a growing interest in guiding block copolymer solution self-assembly via top-down methods; the addition of top-down manipulation of external forces to control nanoscale structure adds another dimension of control to various fast and efficient self-assembly processes.

Chapter 3 introduced an on-chip strategy to direct morphologies of self-assembled PS-*b*-PAA crew-cut micelles using flow-tunable shear forces unique to gas-liquid two phase reactors. The control over block copolymer morphologies using flow-variable shear has been remarkable as it allows us to generate completely different kinetic morphologies under the same chemical conditions that generate equilibrium morphologies in the bulk. To our knowledge, this result represents the first application of top-down control using shear over block copolymer morphologies in solution.

The on-chip environment has dramatic effect on the micelle morphologies, yielding various non-spherical morphologies (linear and looped cylinders, Y-junctions, spherical caps, bilayer sheets, and dense networks of loops and cylinders) under the same chemical conditions that produced only equilibrium spherical micelles off-chip. The various non-spherical structures formed on-chip were found to represent trapped kinetic states, which relaxed off-chip back to equilibrium spheres with a decay rate and mechanism that depended on the chemical conditions. We explain the kinetic on-chip morphologies using a mechanism of shear-induced coalescence of initially-formed spheres, followed by intraparticle rearrangement to reach a lowest local free energy state under nonergodic conditions.

Motivated by the findings in chapter 3, we decided to further systematically explore this chemical variable effect on the on-chip flow-directed morphologies. This combined top-down and bottom up approach might open new avenues, leading to a new level of morphology control in block copolymer self-assembly.

Specifically, in chapter 4, chemical variables such as solvent compositions, water contents, polymer concentrations and salt contents were studied. We constructed a

solvent composition vs. water content phase diagram, from the TEM result of the bulk morphologies obtained. This equilibrium phase boundary is the foundation of our understanding of the non-equilibrium on-chip morphologies under different solvent conditions. Three different shear-operating pathways were identified on the phase diagram. Path 1 included four investigated solvent DMF/Dioxane (w/w) compositions: 100/0, 85/15, 75/25, and 35/65 where the equilibrium favours spheres are being push into the next phase boundary, cylinder. Since the effect of shear-induced coalescence on-chip is to increase aggregation numbers, it exerts a force locally that is morphogenically equivalent to the chemical force exerted by an increase in dioxane and/or water content (both of which will globally increase aggregation numbers). Path 2 on the phase diagram represents the transformation of equilibrium morphology (15/85) of cylinders and larger vehicles by on chip shear into the nearest morphological region with lower-curvature, which is spheres and smaller vesicles. Finally, in Path 3 (0/100), we showed for the first time the transformation of pure spheres to pure vesicles using a guided top-down approach.

It is known that collision and coalescence rates will also increase with an increase in the particle concentration. Therefore we set out to investigate the role of polymer concentration on the observed morphologies. It was found that a threefold increase in the concentration (from c_0 = 0.33 to 1 wt %) drastically transformed the on-chip morphologies of primarily cylindrical micelles in addition to spheres to some incredibly large compound vesicles that we termed “dinosomes”. Finally chemical variable such as salt which would change the degree of repulsion among PAA corona chains had a similar effect on the shear-induced morphologies, producing large compound vesicles.

In previous chapters it was established that shear provides a handle on particle breakup and coalescence, which could be a very important top-down control handle for other self-assembling nanostructures. Taking this approach a step further, this chapter showed that morphology can also be controlled by shear. Controlling morphology is a main focus of material science and self-assembly.[10, 11, 16, 19, 21, 22, 25, 34-40] The broader implication of the results presented in this chapter is that top-down processes can serve as a viable way for controlling bottom-up self-assembly processes; this type of top-down control via shear is not just limited to block copolymers but can be easily extended to other processes (e.g. surfactant systems). As well, microfluidics through its small scale volumes and dimensions provides convenient access to making shear fields strong enough to influence self-assembly at the nanoscale. However, there are other practical limitations with this approach as well, such as the scale-up issue (mass production of samples) and the precise control of flow parameters. With respect to scale-up, the in-channel process is amenable to scaling, the issue is rather the lack of volume utilization. In other words, the current reactors are largely, by volume, plastic. Increasing the volume-density of fluid channels, perhaps in multiple dimensions is one route to achieve higher density in future.

6.1.3. On-Chip Loading of Hydrophobic Probes into Block Copolymer Micelles

The final contribution in this thesis is the application of the developed tools for the control of nanoparticle self-assembly to encapsulation of drugs. Block copolymer micelles have shown significant promise as drug delivery vehicles.[40, 41] Key features that are critical to drug delivery such as control over the shape of the drug delivery vesicles,

stability of the drug delivery vehicles and loading efficiency can be easily manipulated using block copolymer micelles as drug delivery vehicles.[40, 41]

Microfluidic devices have shown promise for drug loading due their potential for point-of-care (small and portable) loading platforms and fast mixing.[16] In general, low off-chip drug loading efficiencies may be attributed to limited diffusion rates of drug into the micelle resulting in drugs being kinetically trapped outside.[40, 41] Shear-induced breakup and coalescence could provide improved pathways for exchange of probe between micelles and between the micelles and the solvent. However, fast mixing could also be detrimental to loading due to an increased rate of micelle formation which could lead to cores becoming highly viscous too quickly for sufficient loading to occur.

In chapter 5, we set out to study the practicality and advantages/disadvantages of the microfluidic environment for drug loading. As a stand-in for drugs, two hydrophobic fluorescent probes were used. The on-chip and off-chip loading efficiency of pyrene and naphthalene in PS-*b*-PAA crew cut micelles were compared. When the loading environment was carried in DMF, the on-chip loading efficiency is generally lower than that in the bulk, which is most likely a result of fast mixing of water with the polymer and probe. However, it should be noted that in some cases (pyrene in DMF at 5 wt % water content), the on-chip loading efficiency is comparable to that generated in the bulk, with significant reduction in loading time. When loading of probes was conducted in dioxane, we found that in certain case, the on-chip loading efficiency is higher than that in the bulk, which we attributed to the shear-induced morphological effect. The major contributions from this work is that it demonstrated the potential of drug-loading using

microfluidic devices and helped us understood various factors that important to loading efficiency on-chip.

The broad scope of the results in this chapter is that shear not only can be used as a handle in controlling sizes and morphologies of nanoscale structures formed by self-assembly, but also in doing so influencing exchange pathways for loadings. The results have significant implications for any systems in which slow kinetics provide a limitation on loading efficiency. However, the shear-induced loading pathways are still not clearly understood and will need to be carefully studied in order to embrace the strategy.

6.2. Suggestions for Future Work

As with Section 6.1, this section is divided into three subsections focusing on the three central aspects of this thesis. Section 6.2.1 discusses possible directions of the QDCM work in the context of their potential sensing/imaging applications using the microfluidic "lab-on-a-chip" concept. Section 6.2.2 suggests potential future directions for the self-assembly of block copolymers in microfluidic reactors. Finally, Section 6.2.3 discusses potential future chip designs that could improve the loading efficiency of probes in block copolymer micelles and improve the integration of point-of-care drug encapsulation devices.

6.2.1. Suggested Research on QDCMs Self-Assembly in Microfluidic Devices

One of the appealing properties of our QDCMs systems is its potentials in medical imaging/sensing. However, this aspect of the QDCMs was not explored in this thesis. In addition, the "lab-on-a-chip" concept has certainly been gaining increased

attention in the microfluidic community. Therefore, to take advantages of the versatility of microfluidic reactors, it is possible to utilize a chip design where the first portion of the chip allows for the QDCMs self-assembly, follows by a portion of the chip that allows for bio-conjunctions (e.g. streptavidin-biotin) for medical imaging/sensing purpose and finally a portion that allows for on-chip separation and detection of the analyte of interest.

6.2.2. Suggested Research on Block Copolymer Self-Assembly in Microfluidic Devices

In Chapter 3 and 4, we looked various flow and chemical variables and found these variables have profound effects on the resulting on-chip shear-induced morphologies. However, one aspect of this work still remained to be explored; that is, the effect of channel geometry on the flow-induced morphologies. Since these morphologies are kinetic products, it is reasonable to speculate that they will be strongly influenced by the flow field within the reactors. One possible design is to couple a geometry that allows for confinement effect (such as a nanopore or nanofilter) following the on-chip self-assembling/process region to effectively control the shape and size distributions. That is, we would like to use some sort of size-exclusion filter to select specific morphologies formed by shear based on their size. It is possible this type of chip design could produce extremely uniform structures (such as highly mondisperse vesicles) that are important in many applications.

6.2.3. Suggested Research on On-chip Probe Loading in PS-*b*-PAA Crew-Cut Micelles

Chapter 5 explored the effect of on-chip shear on probe loading in PS-b-PAA crew-cut micelles. The loading efficiency data indicated that shear does have an influence on the loading efficiency. However, the fast-mixing property characteristic of two-phase reactors might be detrimental to obtaining high loading efficiency on-chip. This fast-mixing problem could be tackled by using a distributive channel geometry. A distributive channel design has several side channels that are connected to the main channel of the microfluidic device. The essence of this type of design is that water or probes can be added in sequential fashion, while it still allows for the system to be influenced by the high shear regions. Furthermore, if additional drugs are introduced near the wall where shear is the highest, it is possible that the shear could introduce other pathways for exchange of dye between particles and between particles and the solvent, which might improve the loading efficiencies. This can also be similarly done by using a distributive channel design where additional drugs are introduced from the distributive channel after the first stage of micelle formation/probe loading has taken place. In addition, it is certainly possible to engineer a chip design where the dialysis membrane is being coupled to the chip such that it can remove all of the organic solvent from the system before the outlet so that the chip produces ready to administer formulations.

6.3. References

1. Probstein, R. F., *Physicochemical hydrodynamics: an introduction*. 2nd ed.; John Wiley&Sons: New York, 1994.

2. Whitesides, G. M., *Nature* **2006,** *442* (7101), 368-373.

3. Bringer, M. R.; Gerdts, C. J.; Song, H.; Tice, J. D.; Ismagilov, R. F., *Philos T Roy Soc A* **2004,** *362* (1818), 1087-1104.

4. Song, H.; Chen, D. L.; Ismagilov, R. F., *Angew Chem Int Edit* **2006,** *45* (44), 7336-7356.

5. Song, Y. J.; Hormes, J.; Kumar, C. S. S. R., *Small* **2008,** *4* (6), 698-711.

6. Gunther, A.; Jensen, K. F., *Lab Chip* **2006,** *6* (12), 1487-1503.

7. Gunther, A.; Khan, S. A.; Thalmann, M.; Trachsel, F.; Jensen, K. F., *Lab Chip* **2004,** *4* (4), 278-286.

8. Khan, S. A.; Gunther, A.; Schmidt, M. A.; Jensen, K. F., *Langmuir* **2004,** *20* (20), 8604-8611.

9. Yen, B. K. H.; Gunther, A.; Schmidt, M. A.; Jensen, K. F.; Bawendi, M. G., *Angew Chem Int Edit* **2005,** *44* (34), 5447-5451.

10. Cui, H. G.; Chen, Z. Y.; Zhong, S.; Wooley, K. L.; Pochan, D. J., *Science* **2007,** *317* (5838), 647-650.

11. Jain, S.; Bates, F. S., *Science* **2003,** *300* (5618), 460-464.

12. Yu, Y. S.; Zhang, L. F.; Eisenberg, A., *Macromolecules* **1998,** *31* (4), 1144-1154.

13. Zhang, L. F.; Eisenberg, A., *Macromolecules* **1999,** *32* (7), 2239-2249.

14. Zhang, L. F.; Shen, H. W.; Eisenberg, A., *Macromolecules* **1997,** *30* (4), 1001-1011.

15. Kabanov, A. V.; Bronich, T. K.; Kabanov, V. A.; Yu, K.; Eisenberg, A., *J. Am. Chem. Soc.* **1998,** *120* (38), 9941-9942.

16. Karnik, R.; Gu, F.; Basto, P.; Cannizzaro, C.; Dean, L.; Kyei-Manu, W.; Langer, R.; Farokhzad, O. C., *Nano Lett.* **2008,** *8* (9), 2906-2912.

17. Valencia, P. M.; Basto, P. A.; Zhang, L. F.; Rhee, M.; Langer, R.; Farokhzad, O. C.; Karnik, R., *ACS Nano* **2010,** *4* (3), 1671-1679.

18. Yusuf, H.; Kim, W. G.; Lee, D. H.; Aloshyna, M.; Brolo, A. G.; Moffitt, M. G., *Langmuir* **2007,** *23* (10), 5251-5254.

19. Yusuf, H.; Kim, W. G.; Lee, D. H.; Guo, Y. Y.; Moffitt, M. G., *Langmuir* **2007,** *23* (2), 868-878.

20. Wacker, J.; Parashar, V. K.; Gijs, M. A. M., *Procedia Chem* **2009,** *1* (1), 377-380.

21. Zhang, L. F.; Yu, K.; Eisenberg, A., *Science* **1996,** *272* (5269), 1777-1779.

22. Zhang, L. F.; Eisenberg, A., *Science* **1995,** *268* (5218), 1728-1731.

23. Won, Y. Y.; Davis, H. T.; Bates, F. S., *Science* **1999,** *283* (5404), 960-963.

24. Wang, X. S.; Guerin, G.; Wang, H.; Wang, Y. S.; Manners, I.; Winnik, M. A., *Science* **2007,** *317* (5838), 644-647.

25. Discher, D. E.; Eisenberg, A., *Science* **2002,** *297* (5583), 967-973.

26. Discher, B. M.; Won, Y. Y.; Ege, D. S.; Lee, J. C. M.; Bates, F. S.; Discher, D. E.; Hammer, D. A., *Science* **1999,** *284* (5417), 1143-1146.

27. Zhang, L. F.; Eisenberg, A., *J. Am. Chem. Soc.* **1996,** *118* (13), 3168-3181.

28. Shen, H. W.; Zhang, L. F.; Eisenberg, A., *J. Am. Chem. Soc.* **1999,** *121* (12), 2728-2740.

29. Liu, F. T.; Eisenberg, A., *J. Am. Chem. Soc.* **2003,** *125* (49), 15059-15064.

30. Duffy, D. C.; McDonald, J. C.; Schueller, O. J. A.; Whitesides, G. M., *Anal. Chem.* **1998,** *70* (23), 4974-4984.

31. McDonald, J. C.; Duffy, D. C.; Anderson, J. R.; Chiu, D. T.; Wu, H. K.; Schueller, O. J. A.; Whitesides, G. M., *Electrophoresis* **2000,** *21* (1), 27-40.

32. Ng, J. M. K.; Gitlin, I.; Stroock, A. D.; Whitesides, G. M., *Electrophoresis* **2002,** *23* (20), 3461-3473.

33. Whitesides, G. M.; Stroock, A. D., *Phys Today* **2001,** *54* (6), 42-48.

34. Boal, A. K.; Ilhan, F.; DeRouchey, J. E.; Thurn-Albrecht, T.; Russell, T. P.; Rotello, V. M., *Nature* **2000,** *404* (6779), 746-748.

35. Nie, Z. H.; Li, W.; Seo, M.; Xu, S. Q.; Kumacheva, E., *J. Am. Chem. Soc.* **2006,** *128* (29), 9408-9412.

36. Schabas, G.; Wang, C. W.; Oskooei, A.; Yusuf, H.; Moffitt, M. G.; Sinton, D., *Langmuir* **2008,** *24* (19), 10596-10603.

37. Seo, M.; Nie, Z. H.; Xu, S. Q.; Mok, M.; Lewis, P. C.; Graham, R.; Kumacheva, E., *Langmuir* **2005,** *21* (25), 11614-11622.

38. Shenhar, R.; Norsten, T. B.; Rotello, V. M., *Adv Mater* **2005,** *17* (6), 657-669.

39. Wang, C. W.; Oskooei, A.; Sinton, D.; Moffitt, M. G., *Langmuir* **2010,** *26* (2), 716-723.

40. Allen, C.; Maysinger, D.; Eisenberg, A., *Colloids and Surfaces B-Biointerfaces* **1999,** *16* (1-4), 3-27.

41. Soo, P. L.; Eisenberg, A., *Journal of Polymer Science Part B-Polymer Physics* **2004,** *42* (6), 923-938.